Durham University

Durham E-Theses

The development of gas scintillation counters for high count rate x-ray detection

Al-Dargazelli, Shetha Selman

How to cite:

Al-Dargazelli, Shetha Selman (1979) *The development of gas scintillation counters for high count rate x-ray detection*, Durham theses, Durham University. Available at Durham E-Theses Online: http://etheses.dur.ac.uk/8411/

Use policy

The full-text may be used and/or reproduced, and given to third parties in any format or medium, without prior permission or charge, for personal research or study, educational, or not-for-profit purposes provided that:

- a full bibliographic reference is made to the original source
- a link is made to the metadata record in Durham E-Theses
- the full-text is not changed in any way

The full-text must not be sold in any format or medium without the formal permission of the copyright holders.

Please consult the full Durham E-Theses policy for further details.

Academic Support Office, The Palatine Centre, Durham University, Stockton Road, Durham, DH1 3LE
e-mail: e-theses.admin@durham.ac.uk Tel: +44 0191 334 6107
http://etheses.dur.ac.uk

The copyright of this thesis rests with the author.
No quotation from it should be published without
his prior written consent and information derived
from it should be acknowledged.

THE DEVELOPMENT OF GAS SCINTILLATION COUNTERS FOR HIGH COUNT RATE X-RAY DETECTION

BY

SHETHA SELMAN AL-DARGAZELLI, B.Sc., M.Sc.

A thesis submitted to the University of Durham,
for the degree of Doctor of Philosophy.

Being an account of the work carried out at the University of Durham
during the period October 1975 to March 1979.

Durham Uni
SCIENCE
SECTION
Library

بسم الله الرحمن الرحيم

Bismillāh Al-Raḥman Al-Raḥīm

In The Name Of God The Compassionate The Merciful

To My Mother

Ramaḍān 1399 H

ABSTRACT

This Thesis describes a study of a new type of detector, the gas scintillation counter. The counter is a development of the multiwire proportional chamber and the drift chamber with superior energy resolution and count rate capability.

A study of multiwire proportional chambers with a delay-line readout technique, as well as a conventional readout technique, is described. The limitations of this type of detector for high rate experiments are studied and discussed.

Measurements and a theoretical study of electron drift velocities in different argon-nitrogen mixtures are presented.

The study of the equipotential ~~counters~~ contours of the electric field inside multiwire proportional chambers and drift chambers, revealed the effect of the chamber dimensions and the applied drift and anode voltages on the field, and consequently on the performance of the chambers. This made it possible to select the most appropriate dimensions and applied voltages.

The investigation of the general properties and capabilities of this counter with the detailed study of each parameter helped the choice of suitable parameters for high count rate experiments.

Further development work on the detector is proposed and the applications of gas scintillation counters are discussed with particular reference to the new results and characteristics obtainable from this counter.

CONTENTS

		Page Nos
ABSTRACT		i
CHAPTER ONE	INTRODUCTION	1
1.1	Introduction	1
1.2	Absorption of X-rays in Material	2
1.3	X-ray Detectors	5
	1.3.1 Detectors classification	5
	1.3.2 Scintillation counters	6
	1.3.3 Multiwire proportional chamber	7
	1.3.4 Drift chamber	9
1.4	Energy Resolution and Count Rate	10
1.5	Present Work	12
References		13
CHAPTER TWO	SCINTILLATION COUNTERS	16
2.1	The Scintillation Process and Light Collection	16
2.2	Summary of the Main Characteristics of Scintillators	20
2.3	Photomultipliers	21
	2.3.1 Windows	21
	2.3.2 Photoemissive materials and photocathodes	21
	2.3.3 Dynodes	24
	2.3.4 Gain	25
	2.3.5 Photomultiplier circuit	26
2.4	The Performance of Photomultipliers at High Rates	29
	2.4.1 RCA 8575 photomultiplier tube	29
	2.4.2 Passive network dynode connections	31
	2.4.3 Active network dynode connections	32

Page Nos

2.5 Gas Scintillation Counters 34

2.5.1 Gas scintillators 34

2.5.2 Gas scintillation counters 35

2.6 Construction of Gas Scintillation Counters 38

2.6.1 Introduction 38

2.6.2 General descriptions 38

2.6.3 Gas flow system 39

2.6.4 Gas scintillation proportional counter 40

2.6.5 Gas scintillation drift counter 41

References 43

CHAPTER THREE EXCITATION, IONIZATION AND DRIFT 46

3.1 Introduction 46

3.2 Excitation and Ionization 46

3.2.1 Initial processes 46

3.2.2 The gas mixture 49

3.2.3 Light emission from Ar and N_2-mixtures 51

3.3 The Drift Process 53

3.3.1 In pure gases 53

3.3.2 In gas mixtures 55

3.3.3 Processes accompanying drift 58

A. Diffusion 58

B. Attachment and recombination 59

3.4 Drift Velocity Measurements in Ar-N_2 Mixtures 60

3.4.1 Experimental arrangement 60

3.4.2 Drift field 62

(i) The effect of the sense wire voltage 62

(ii) The effect of the drift voltage 63

(iii) Measured and calculated drift velocity 64

3.4.3 Drift distance 65

3.4.4 Nitrogen concentration 65

3.5 Conclusions 66

References 67

Page Nos

CHAPTER FOUR	CHARACTERISTICS AND LIMITATIONS OF MULTIWIRE PROPORTIONAL CHAMBERS	69
4.1	Introduction	69
4.2	The Multiplication Process and Space Charge Limitations	69
	4.2.1 The effect of the electric field on multiplication	69
	4.2.2 The effect of chamber parameters on multiplication	71
4.3	Construction of MWPC's	73
4.4	Performance of MWPC's	76
	4.4.1 Delay line readout techniques	76
	4.4.2 Theory of the pulse delay	77
	4.4.3 Test of transmission lines	79
	4.4.4 Spatial resolution and two dimensional images	80
	4.4.5 Energy resolution	82
4.5	A MWPC For High Count Rate Experiments	84
	4.5.1 Space charge limitations and high rate effect on multiplication	84
	4.5.2 Experimental arrangement	87
	4.5.3 Dead time	88
	4.5.4 High rate detection	89
	4.5.5 Effect of high rate on peak position and energy resolution	90
4.6	Conclusions	91
References		93

Page Nos

CHAPTER FIVE ELECTRIC FIELD CALCULATIONS IN MWPC'S AND DC'S 96

5.1 Introduction 96

5.2 The Method 96

5.3 The Program 97

5.4 Fields in MWPC's 100

5.4.1 Sense wire spacing(s) 101

5.4.2 Anode-Cathode separation(L) 103

5.5 Fields in Drift Chambers 104

5.5.1 Drift distance (D) 106

5.5.2 Drift wire-earth plane spacing (d) 106

5.5.3 Anode-drift wire plane separation (L) 107

5.5.4 Drift wire spacing (s) 108

5.5.5 Anode voltage (V_a) 109

5.5.6 Drift voltage (V_k) 109

5.6 Conclusions 110

References 111

CHAPTER SIX GAS SCINTILLATION COUNTERS 112

6.1 Introduction 112

6.2 Charge and Light Gain 112

6.2.1 Anode voltage and nitrogen concentration 113

6.2.2 Anode wire diameter 116

6.3 Plateaus and Energy Resolution 119

6.3.1 The drift voltage (V_k) 119

6.3.2 Photomultiplier voltage (V_{pm}) 121

6.3.3 Nitrogen concentration 122

6.3.4 Drift wire-earth plane separation (d) and the geometry factor 124

6.3.5 Sense wire diameter 125

Page Nos

6.4 The Pulse Shape 127

6.4.1 Anode voltage 127

6.4.2 The drift voltage 128

6.4.3 Source position 129

6.4.4 Nitrogen concentration 131

6.4.5 Drift wire-earth plane distance 132

6.5 High Rate Tests 133

6.5.1 Experimental arrangement 133

6.5.2 Effect of electronics on chambers performance 135

6.5.3 Peak shift and energy resolution 136

6.6 Conclusions 139

References 141

CHAPTER SEVEN CONCLUDING REMARKS AND FUTURE WORK 143

7.1 Summary of GSC's Performance 143

7.2 Applications of GSC's 144

7.3 High Rate Applications 146

7.4 Further Developments and Future Work 149

References 151

Acknowledgements 152

CHAPTER ONE

1.1 INTRODUCTION

One of the main aspects of modern experimental physics is the detection of radiation. The various types of detector available illustrate the extensive work which has been carried out over the years to detect radiation with high precision. Detectors of early workers were limited by the technology of that period but the fast development of electronics in recent years has helped to improve the detection capability.

The basis of nearly all detectors depends on the passage of particles through a material, which may be a gas, a liquid or a solid and in which, directly or indirectly, excitation and ionization of the atoms occur. The various detectors not only differ in the material within which the ionization is produced but also in the way in which it is observed or measured. Hence, the wide range of techniques available for particle detection makes it possible to choose a suitable detector for the requirements of a specified experiment.

The Nuclear Instrumentation group in Durham University, has maintained a line of research in an attempt to study and develop nuclear detectors for use in research and industry. As part of this continuing line of research, the study and development of gas scintillation counters (GSC) was started following a detailed study of multiwire proportional chambers (MWPC) and drift chambers (DC). The reason for working on GSC's is not only a desire to study this novel type of detector, but also because of the great demand for a detector with high count rate capability and modest energy resolution. For example, research in Extended X-ray Absorption Fine Structure (EXAFS) using synchrotron radiation requires the

Durham University
SCIENCE
- 3 OCT
SECTION
Library

total detector counting rate to be at least 10^7 sec^{-1}. Semiconductors with their excellent energy resolution are limited to a rate of about 10^5 sec^{-1}[1]. Scintillation counters, another candidate for high count rate experiments, have a serious defect of very poor energy resolution at high rates[2]. The conjunction of a MWPC or a DC with a photomultiplier to form a GSC appeared as a possible new detector with applications to research and industry.

1.2 ABSORPTION OF X-RAYS IN MATERIAL

Radiations can be divided into three categories : charged particles such as electrons or alpha particles, uncharged particles such as neutrons or neutrinos and electromagnetic radiation in particular gamma and X-rays. Uncharged particles and electromagnetic radiation produce ionization indirectly by secondary processes. One of the main differences between the various types of radiation is the difference in their penetration power through media. Beta rays are much more penetrating than alpha rays but the ionization density produced in a gas by beta rays is much less intense than that produced by alpha rays. The ionization produced per cm by alpha, beta and gamma rays, is roughly in the ratio of 10,000, 100 and 1. The penetration power of radiation depends on the medium as well as on the nature of the radiation. This thesis is concerned principally with X-rays and so more details are given below concerning X-ray interaction with matter.

Both gamma and X-rays are of the same nature and form part of the electromagnetic spectrum. They have short wavelengths and in general, gamma rays have higher energies and shorter wavelengths than X-rays, but there is no definite boundary between them. The real distinction is in their origins. Gamma rays are produced by transitions between energy levels in the nucleus and X-rays are produced by transitions of electrons between energy levels outside the nucleus.

The three major processes responsible for absorption of gamma rays in matter are the photoelectric effect, the Compton effect and pair production. For energies much less than the rest mass energy of an electron, i.e. $h\nu \ll 0.51$ MeV, (the region of interest to us), the first process is dominant. Pair production is important only for large $h\nu$ values ($h\nu > 1.02$ MeV). Compton effect is dominant in the intermediate energy range. Low energy X-rays (<10 keV) are of particular interest to us, hence only the photoelectric effect will be considered in detail.

The photoelectric effect is an interaction of the incident photons with the atomic electron cloud of the medium, in which an electron (usually from the K or L shell) is ejected with a kinetic energy equals to the difference between the binding energy of the electron and the energy of the incident photon. Whenever the energy of the photon is high enough, the probability of expelling a K-electron is higher than it is for any of the other electrons. At a photon energy equals to the K or L-electron binding energy, there is a sharp step in the cross section for photoelectric emission as shown in Fig 1.1 for lead $E_K = 88$ keV and $E_L = 15.86$ keV.

A study of absorption coefficients is necessary in order to choose the correct medium for absorbing the radiation in a detector. Many workers[3] have measured and calculated absorption coefficients of gamma rays for different elements over a wide range of energies. Fig.1.1 covers the range of 1-1000 keV.

The probability of absorption can be given in terms of the cross-section σ by

$$I = I_o \exp(-\sigma N x) \qquad (1.1)$$

where N is the number of molecules per unit volume of the medium and x is

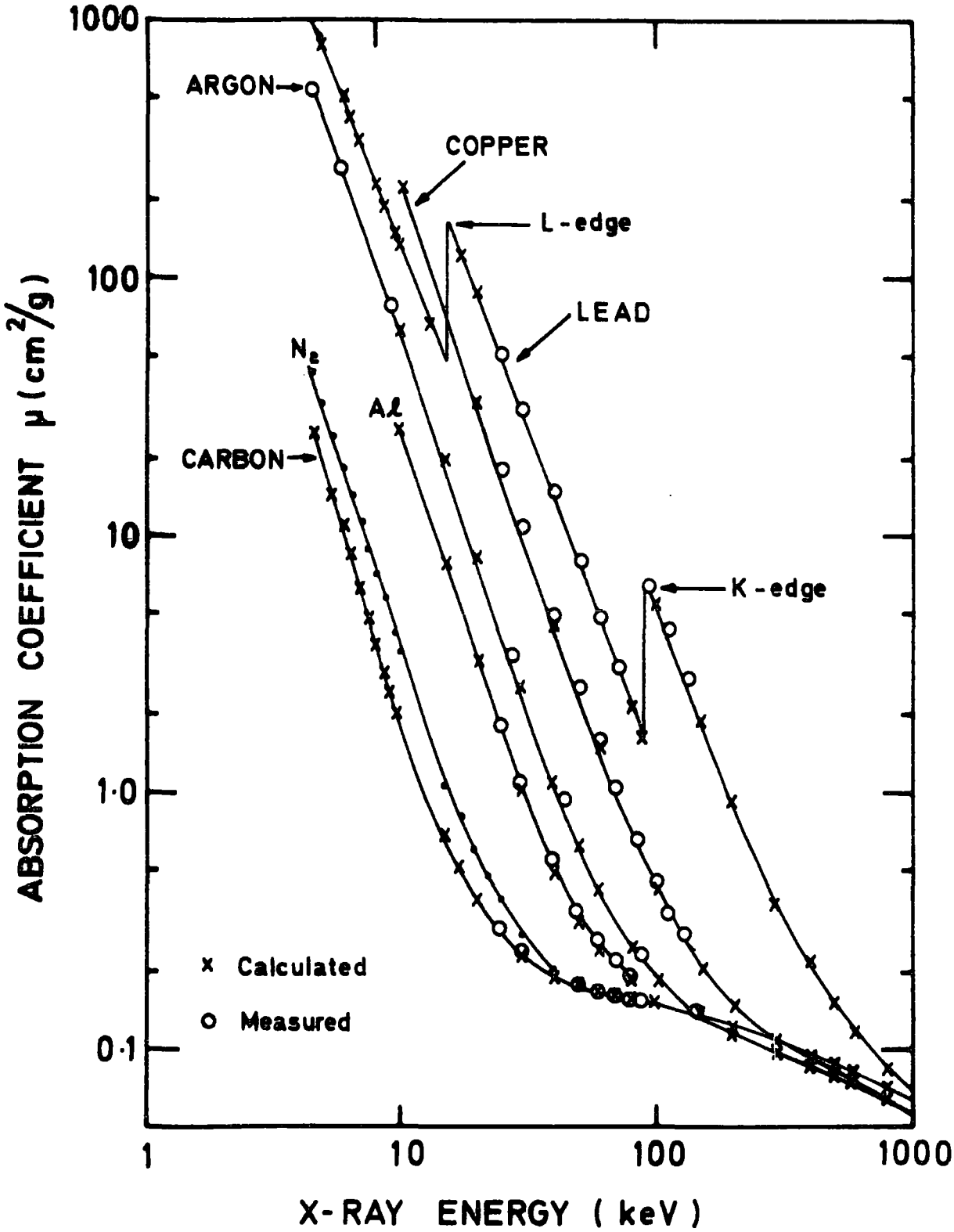

FIG. 1·1 Absorption Coefficients for different elements.

the medium thickness traversed by the beam of photons. In terms of the mass absorption coefficient $\mu(cm^2/g)$, equation 1.1 can be written as

$$I = I_o \exp(-\mu\rho x)$$

and for a mixture of gases

$$\mu_m = {}_1\mu a_1 + {}_2\mu a_2 + \ldots\ldots\ldots {}_i\mu a_i \qquad (1.2)$$

where a_i is the fractional amount by weight of the ith element in the mixture. The values of μ in the 4-15 keV energy range are shown in Fig.1.2 for different gases and gas mixtures. The values for the mixtures were obtained by substituting the values of μ for pure gases in equation 1.2. The gas mixtures used in this work are mainly argon-methane and argon-nitrogen. The addition of nitrogen to pure argon decreases the absorption coefficient, and this decrease is proportional to the nitrogen percentage. In Fig.1.3 it is shown that the addition of 10% nitrogen decreases μ by 9.3% at an energy of 5.9 keV (this particular energy is very relevant to the discussion because it is the X-ray energy from F_e^{55}, and it is used very considerably in the work described in this thesis).

From the absorption coefficients, the suitable gas depth, for the radiation to be absorbed in a chamber, can be calculated. Fig.1.4 shows the percentage of absorption with different depth values for pure argon and argon-methane mixtures for X-rays of 5.9 keV. Therefore it follows that a thick chamber will be needed to obtain a high percentage of absorption when large methane percentages are used. The addition of nitrogen to argon will produce a similar curve to that of methane with argon, due to the high absorption coefficient of argon compared with that

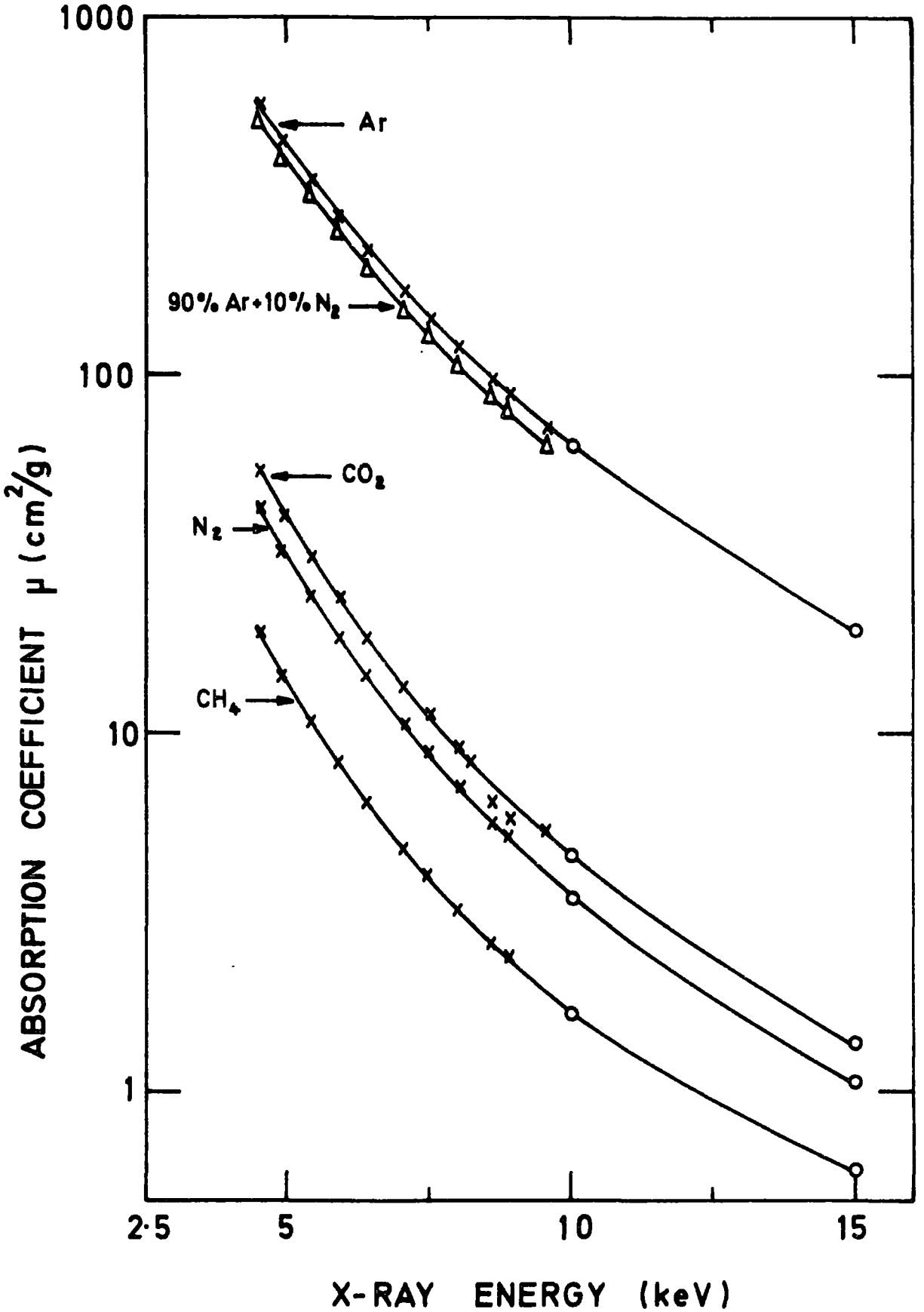

FIG. 1·2 Absorption Coefficients for different gases and gas mixtures.

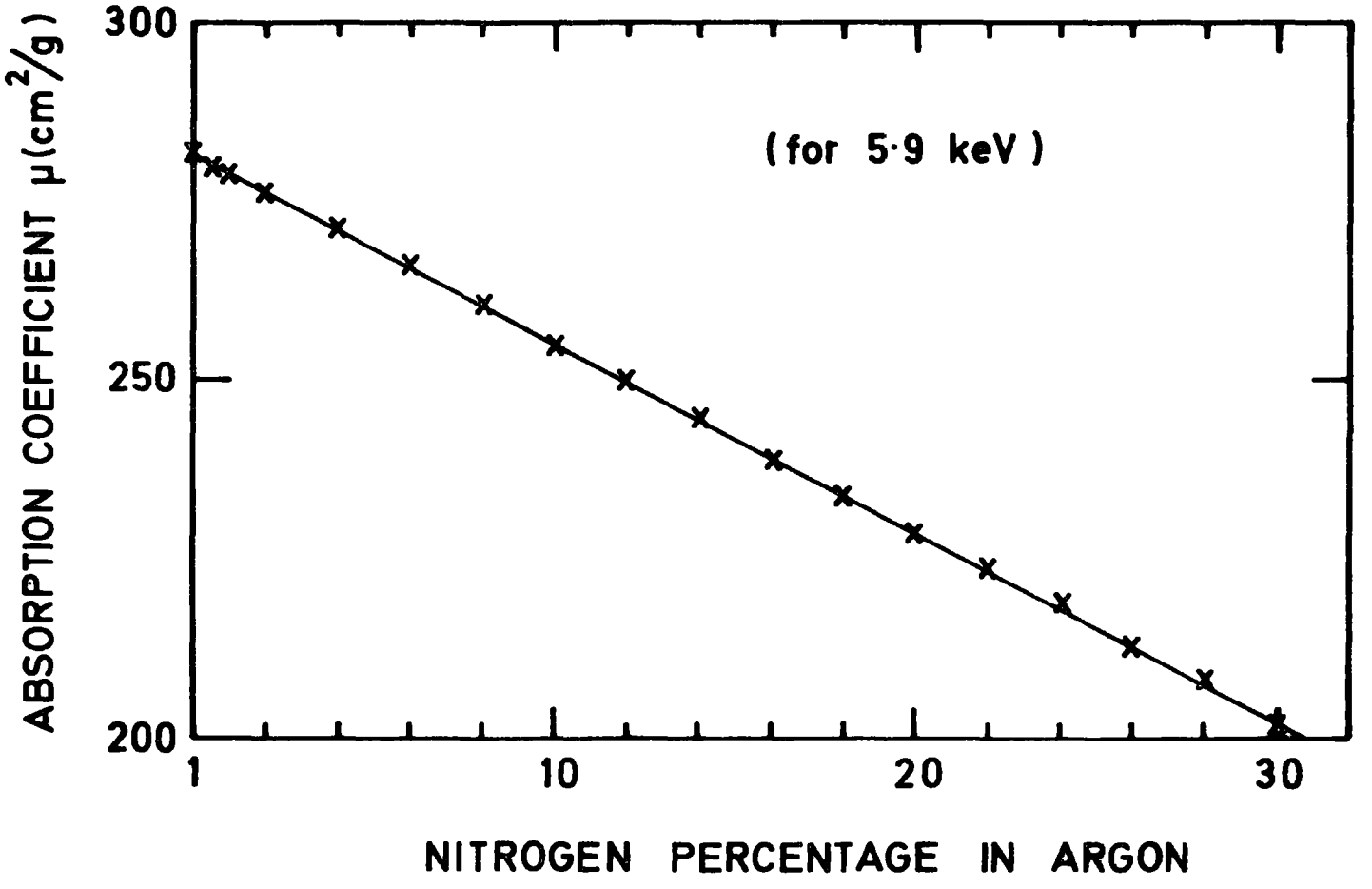

FIG. 1·3 Absorption Coefficients for Argon with different percentages of Nitrogen.

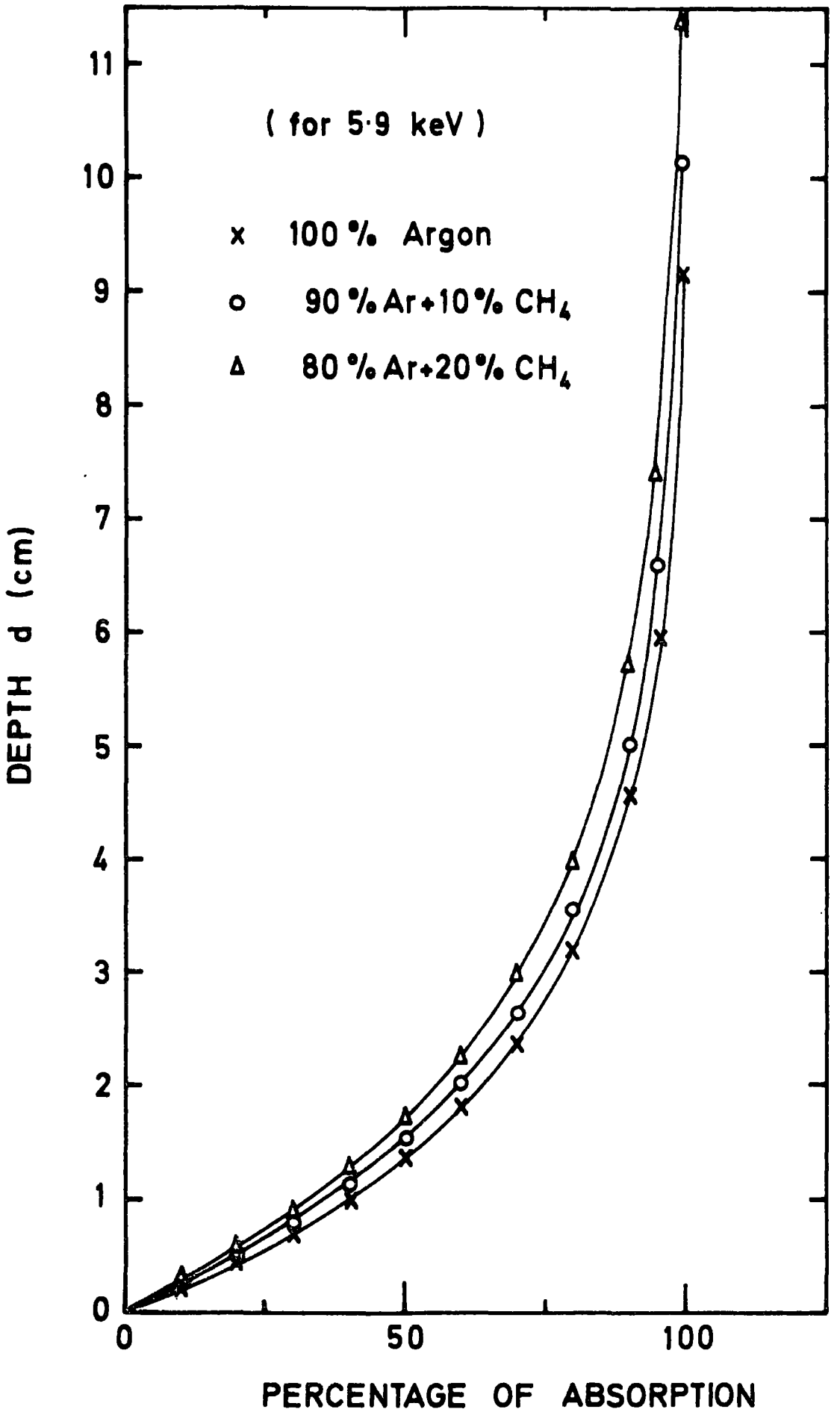

FIG. 1·4 Percentage of Absorption for Argon and Argon Mixtures at different depth values (for 5·9 keV)

of methane or nitrogen. The depth needed for nitrogen will be less than 1% lower than that for methane for the same absorption percentage.

1.3 X-RAYS DETECTORS

1.3.1 Detectors Classification

A historical treatment of detection chambers is a very vast subject to summarize, and as Rice-Evans[4] suggested, a whole book could deal with the history of this branch of science, starting from 1908 when Rutherford and Geiger[5] built their first detector until the present day.

Detector classification differs with different authors, Rossi and Staub[6] classified them according to the type of radiation to be detected, Price[7] classified detectors according to the medium used in the chamber, such as gas filled detectors, semiconductors, etc. A more recent classification[8] is according to the output mode of the detector. Most detectors fall into the category of either visual detectors (photographic emulsion, cloud chambers and bubble chambers) or electronic detectors. This second group may include spark chambers which in fact can be included as visual detectors or as sonic detectors. Hence to define a detector, three main characteristics should be stated as indicated by the above mentioned classification ; the type of radiation with its energy range, the medium of ionization and the output mode. Several detectors are identical in certain properties and each has its own advantages and disadvantages. Hence a close study of similar detectors such as streamer and bubble chambers[9], flash tubes and spark chambers[10], MWPC's with spark chambers and scintillators[11], will be useful for deciding the most appropriate detector for a particular experiment. On the other hand it may be best to choose a combination or hybrid of two detectors as in the hybrid of proportional and spark chamber[12], where the good time resolution of the proportional chamber is combined with the good spatial resolution of the spark chamber.

The main X-ray detectors which are relevant to this work will be described briefly in the following section.

1.3.2 Scintillation Counters

A scintillation counter generally consists of two main parts : the medium in which the light is produced by incident radiation and a photomultiplier tube in which the light is converted to electrons which are then amplified to a detectable signal. The medium of light production is either solid, liquid or gas. One of the main characteristics of scintillation counters is the possibility of using a large sensitive area, for example a plastic scintillator disc of approximately one meter diameter and 9 cm thickness[13] and liquid scintillators of 420 litre volume[14] have been used. A second property of importance is the possibility, in some cases, of obtaining small decay times which therefore give rise to a short resolving time, and consequently the short resolving time means a high count rate capability (100 MHz is possible[8]). A decay time of a few nanoseconds is obtainable[15] from some plastic or liquid phosphors. In general the energy resolution of scintillators is worse than that of other detectors. The major factors affecting resolution are the statistical variations of five separate processes, namely (a) light production in the scintillator itself, (b) light collection at the photocathode, (c) production of electrons at the photocathode, (d) collection of photoelectrons on the first dynode, (e) multiplication in the photomultiplier dynode structure. These and some non-statistical effects are discussed briefly by Neiler and Bell[16]. The deterioration in energy resolution with high count rates was attributed by Von Leishout et al[2] to the photomultiplier tube and they suggested that the resolution itself does not change with the counting rate, but the apparent width of a photopeak will increase due to the photomultiplier gain shift.

1.3.3 Multiwire Proportional Chamber (MWPC)

The first MWPC was developed at the Los Alamos laboratories in the 1940's[6] but the MWPC in its present form was developed by Charpak et al[17] in 1968 at Cern and since then the chamber has been under continuous development and use in a wide range of applications. The reason for the 20 year gap, according to Charpak[18], was the belief that the capacitive coupling between adjacent wires would prevent the localisation of the avalanche on one single wire - an induced pulse, with the same polarity, would be created on adjacent wires. However, it was discovered later that a positive induced pulse appears on both adjacent wires when a negative pulse is created on a wire by an electron avalanche. The induced positive pulse formation is due to the movement of electrons away from the wires and to the movement of positive ions towards the wires. The magnitude of the pulse is greater than the capacitively coupled negative pulse, and if the amplifier used is sensitive to negative pulses only, then the wires in a MWPC act as independent proportional counters.

To describe the MWPC, it is convenient to start with a description of the proportional counter. This consists of a fine anode wire mounted on the central axis of a cylinder (the cathode) with a high potential difference between the anode and the cathode, (see Fig.1.5). The filling gas is usually argon with some quenching gas such as methane. The field (E) inside the chamber depends on the geometry of the chamber and on the voltage (V) applied to the anode :

$$E = \frac{V}{r \ln (r_2/r_1)} \qquad (1.3)$$

where r_1 and r_2 are the radii of the wire and the cylinder respectively. The passage of an ionizing particle through the chamber will produce ion

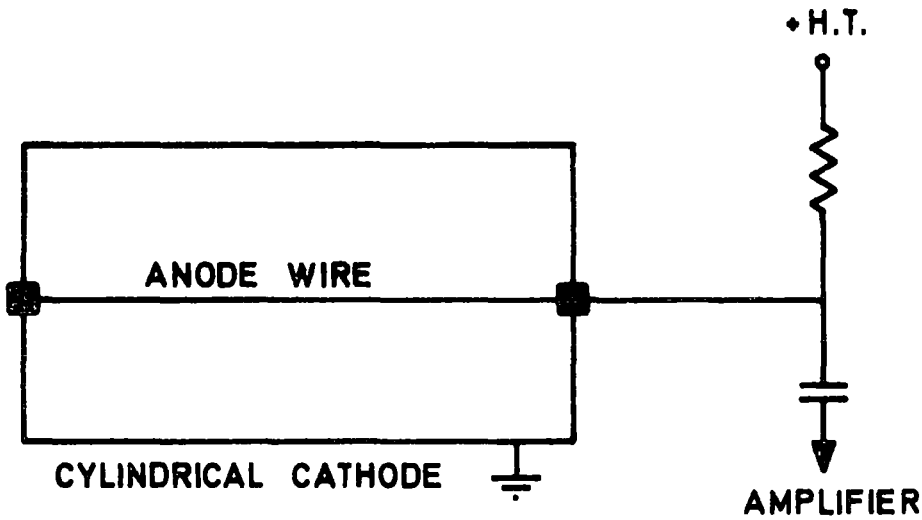

FIG. 1·5

Proportional Counter Configuration.

pairs in the gas. The positive potential on the anode will attract the electrons and hence a pulse will be produced which can be amplified and detected by the electronics connected to the counter. In the MWPC, the anode wire was replaced by a number of wires separated normally by not less than 2 mm. This wire plane lies between two outer plane electrodes (replacing the cylindrical cathode) these two cathodes are usually wire planes also, but with 1 mm spacing. However, it is possible to use thin foils instead of wire planes. Each wire in the anode plane can be used as an individual counter by connecting it to an amplifier. This was only made feasible by the development of transistors and integrated circuits of small size. Fig.1.6 shows the configuration of a MWPC. The field inside the chamber can be described using Erskine's equation[19]

$$V = q \ln \left[\sin^2 \left(\frac{\pi x}{s} \right) + \sinh^2 \left(\frac{\pi y}{s} \right) \right] \qquad (1.4)$$

where q is the charge per unit length on each wire, s is the anode wire spacing and the coordinates x and y relate to an origin centred on one wire, in a practical case when L>>s>>d, an approximated formula enables one to calculate the charge on the wire from the applied potential V_o and the dimensions of the chamber

$$q = \frac{V_o}{2\left[\left\{ \frac{\pi L}{s} \right\} - \ln \left\{ \frac{\pi d}{s} \right\} \right]} \qquad (1.5)$$

The field is very high near the wire as in the cylindrical proportional counter and the equipotentials circle concentrically near the wire. Field plots in MWPC's are given in more detail in a later chapter. The field in MWPC's as in proportional counters, depends on the dimensions

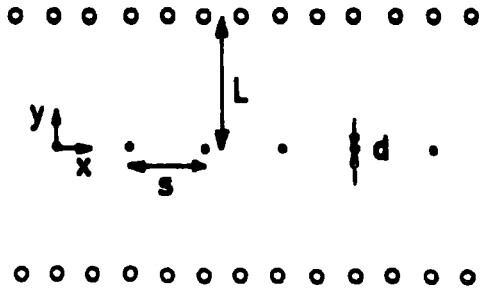

FIG. 1·6

The M.W.P.C. Configuration.

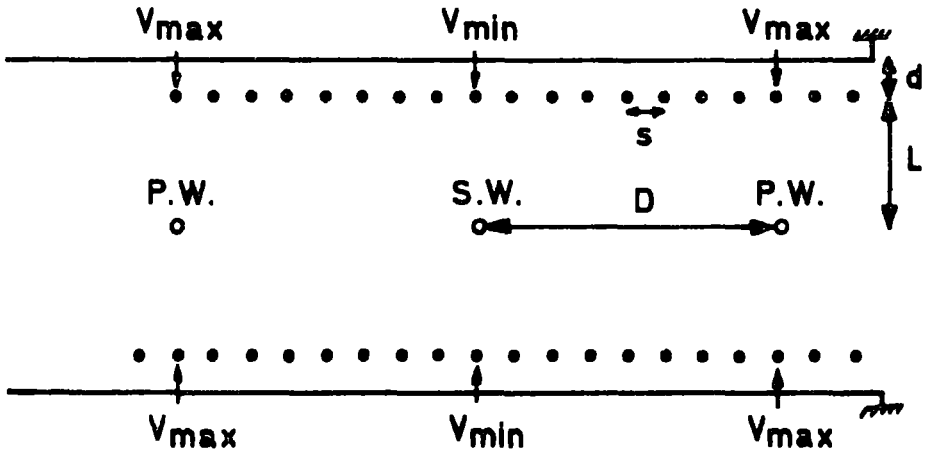

FIG. 1·7

Drift Chamber Wires Arrangement.

of the chamber and on the applied voltage. Hence the gas amplification which is a function of the field, can be defined in terms of measurable quantities and the choice of suitable dimensions for higher gas amplification is possible. The expensive cost of extracting the data from each single wire (an amplifier and a discriminator are required per wire) has led to the development of other readout techniques in particular the delay line technique[20]. This uses either a helical[21] or a plane[22] transmission line. A very good spatial resolution has been obtained[23] using delay line-techniques (∿ 60 μm). More details will be given in a later chapter.

1.3.4 Drift Chamber

The drift chamber is a development of the MWPC introduced in 1969 by Bressani et al[24] and by Charpak et al in 1970[25]. The idea of long drift distance (> 10 mm) was first introduced by Walenta in 1971[26].

The drift chamber is based on drifting the electrons, liberated by the passing ionizing particles, through the gas to a collecting electrode. Fig.1.7 shows the arrangement of the wires in a D.C. One of the main components is the sense wire, (or many in the case of multiwire drift chambers), which is set at a high positive potential and provides the high field around the sense wire and hence the region of excitation, ionization and multiplication. The two cathode planes each consist of a set of parallel wires with negative potentials decreasing gradually towards the sense wire. The voltages on the cathode wires provide the drift field. The cathode wires near to the sense wire also contribute to the high field around the sense wire. Electrons produced by the passage of a particle through some part of the chamber drift under the influence of the drift field to the anode. The time taken to reach the anode depends on the magnitude of the drift field and the distance of the initial ionization

from the sense wire. The output pulse is normally taken from the anode. The two potential wires in the anode plane maintain a more uniform drift field in the chamber[27]. As in the MWPC, the output pulse can also be extracted from the cathode which can be in the form of a printed circuit[28]. The type of gas mixture is a major factor in the D.C. performance. Some commonly used mixtures are, argon + 10% methane (CH_4) or argon + 30% isobutane (C_4H_{10}). Pure ethylene (C_2H_4) has also been used[26]. The importance of the type of gas is mainly due to the characteristic of the drift velocity of electrons in these gases, which is almost independent of the electric field. This chamber forms the first part of the hybrid detector under investigation, so more details will be given in other chapters.

The next section deals with the two main characteristics of interest to us, that is the energy resolution and count rate capability of X-ray detectors.

1.4 ENERGY RESOLUTION AND COUNT RATE

The calculation of the energy resolution (E.R %) and the full width half maximum of the pulse height distribution FWHM (keV) for different detectors are useful parameters, as far as comparisons are concerned. The energy resolution of scintillators, gas type detectors and semiconductors have been calculated[29] using values of the energy required to produce electron hole pairs in semiconductors of 3 eV and the energy to produce ion pairs in gas type detectors of 30 eV and in scintillators of 500 eV[16]. The E.R.% as a function of X-ray energy is given in Fig.1.8 for the three types of detectors. Gas type detectors are better than scintillators in the low energy region, but for high energy particles the detection efficiency of scintillators, due to their high density, is higher than that of gas type detectors.

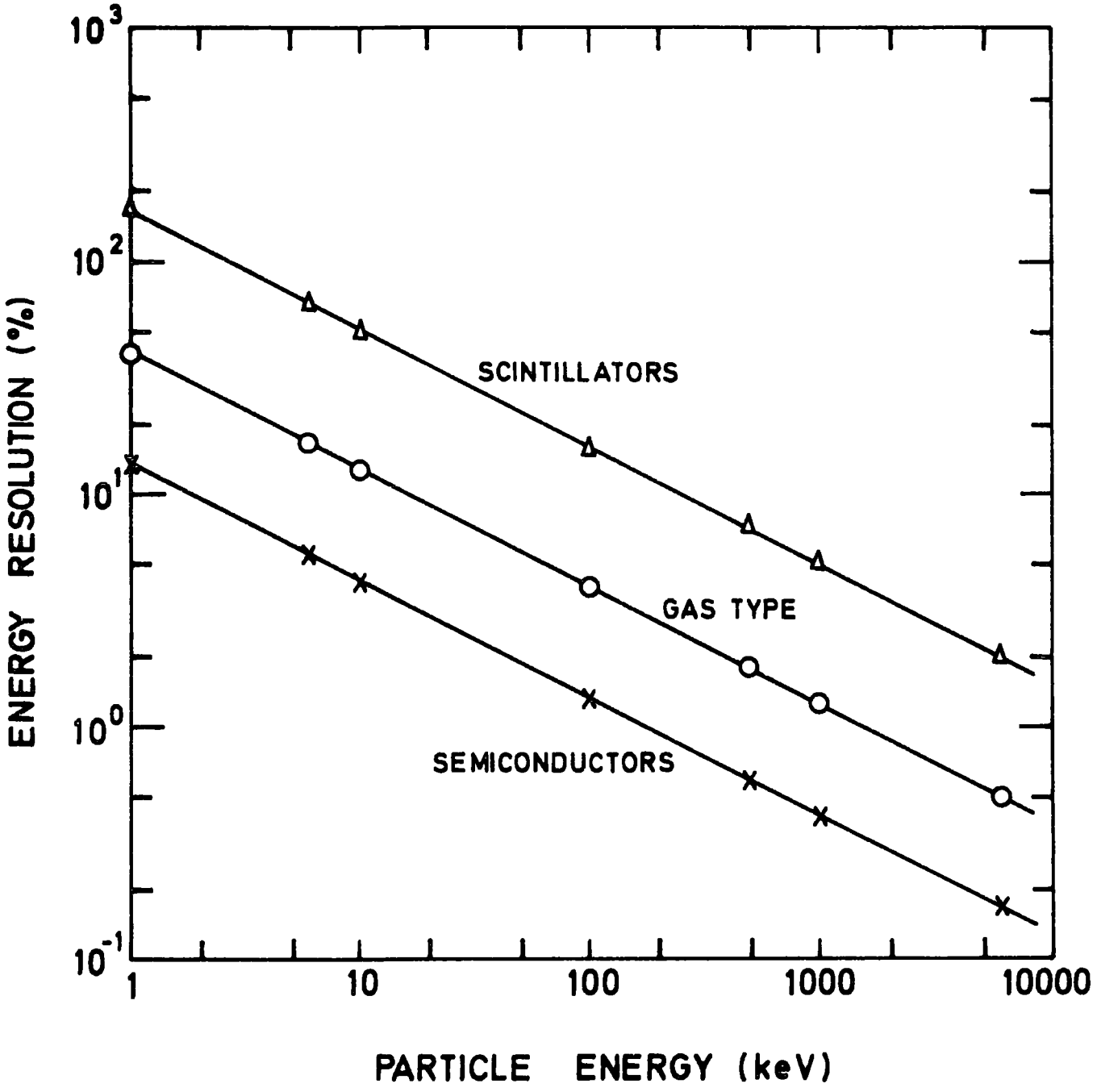

FIG. 1·8 Energy Resolution (%) Variation with Particle Energy for three types of Detector.

Fig.1.9 taken from the work of Aitken[30] provides an interesting comparison of the response of various detectors to the Mn^{55} X-rays from Fe^{55}.

In the region below 10 keV, the noise level in semiconductors is comparable with the signal :

$$(FWHM)_{exp} = \sqrt{(FWHM)^2_{noise} + (FWHM)^2_{\substack{calculated \\ or\ intrinsic}}} \qquad (1.6)$$

Fig.1.10 taken from the work of Goulding[31] shows the variation in energy resolution of a cooled silicon detector as a function of energy for various values of electronic resolution $(FWHM)_{noise}$. The $(FWHM)_{calculated}$ is obtained entirely from the statistical effects of charge production in the detector. Nevertheless, the energy resolution of semiconductor in this low energy region is better than that of gas type detectors, but if the second important factor is added, i.e. the count rate, the gas type detectors will have no rival in the few keV region as far as the energy resolution and high count rate capability are concerned.

For certain scintillators, it is known that high count rates are obtainable, but as was mentioned earlier, the energy resolution is very poor. With a tin loaded plastic scintillator (type NE 140-5% Sn) of size 1.5" diameter x 2", a rate of 20 MHz was obtained[15,32], with the 42 and 100 keV group lines of Gd^{153} well resolved (40%). (The energy resolution of gas type detectors in this region (100 keV) is 4.09%[30]). But using Fe^{55}, the photopeak was only partially resolved from the dark current, this sets the practical energy limit in the 6-10 keV region for that system[32].

As far as the high rate performance of semiconductors is concerned,

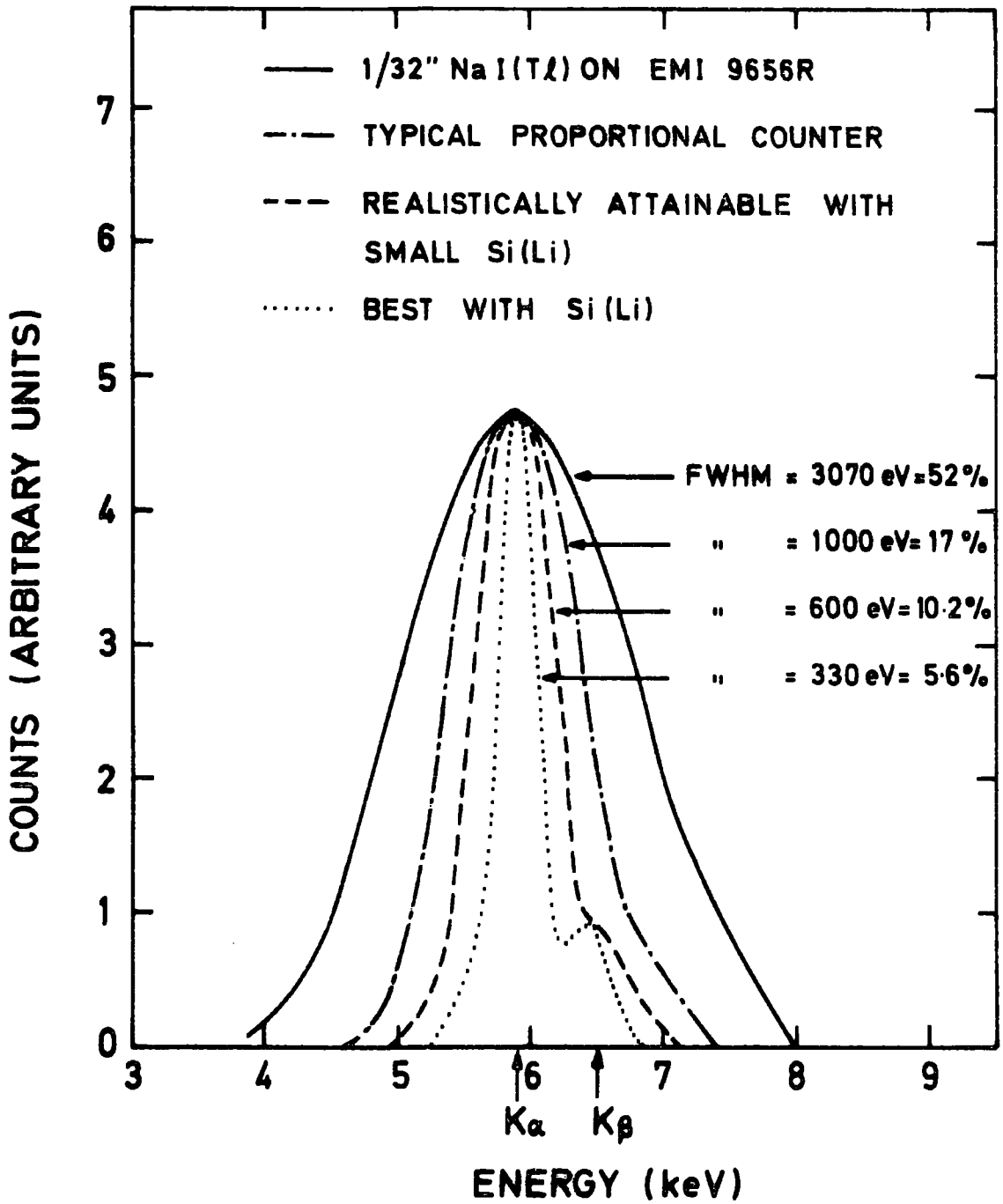

FIG. 1·9 Response of various detectors to the Mn^{55} X-Rays from Fe^{55}. The separation of the two peaks is about 600 eV.

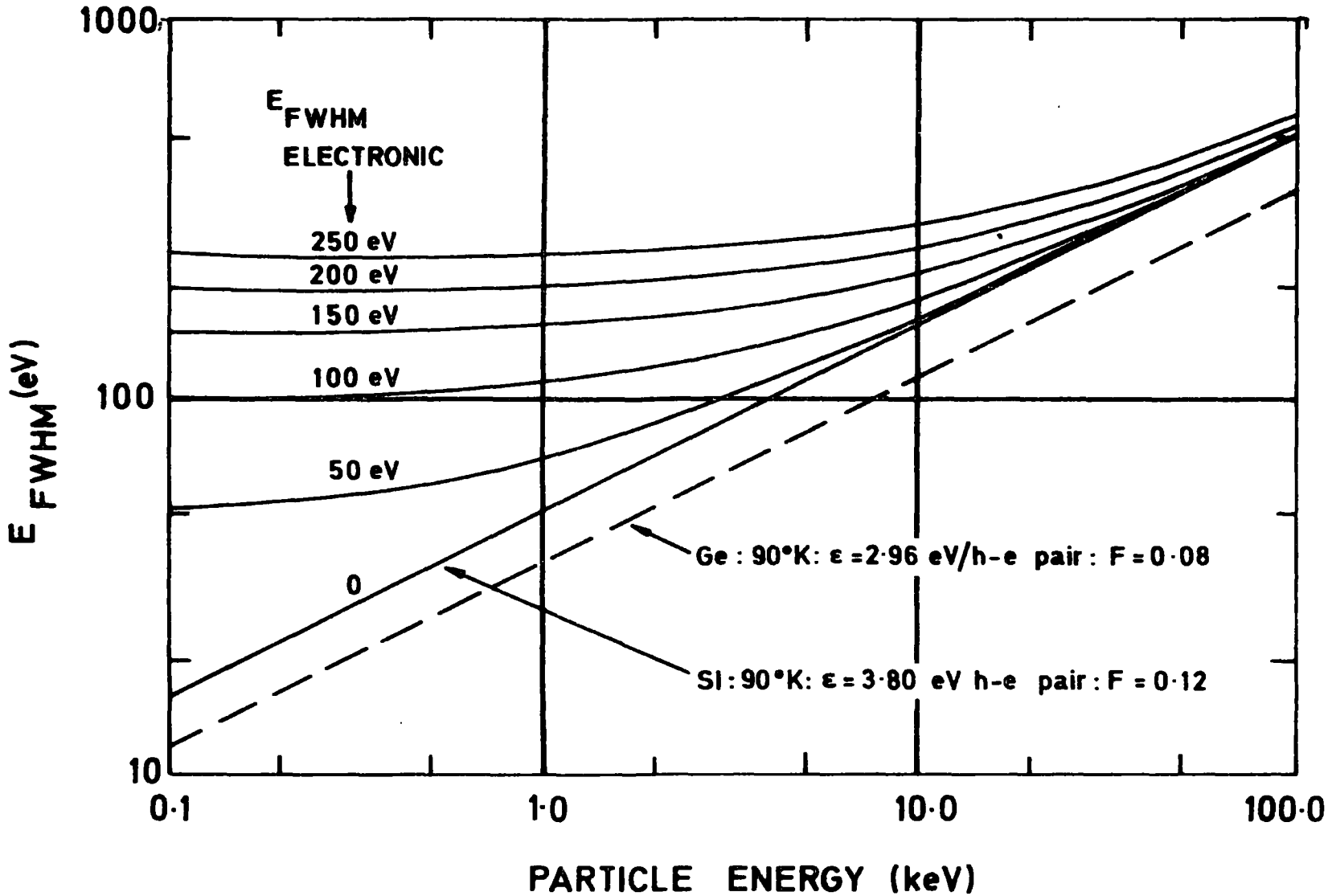

FIG. 1·10 Variation in Energy Resolution of a Cooled Silicon Detector as a function of Energy for various values of Electronic Resolution.

the highest rate reported is 2×10^5 sec^{-1} using a cooled silicon detector[31]. This rate is accompanied by a resolution of 255 eV (4.3%) It was mentioned also that at high rates the resolution can easily degrade much more than that shown in Fig.1.10 if care is not taken to minimize the high rate effect on other parts of the system.

The gas type detectors maintain also certain limitations for the high rate performance, which will be discussed later, but the rate of 10^7 sec^{-1} with reasonable energy resolution should be obtainable.

1.5 PRESENT WORK

This work describes a study of the parameters affecting the performance of the gas scintillation counter, which is necessary in order to understand the present counter and will help to develop it in the future. Some parameters are inter-related and one cannot individually optimize them, but a compromise value has to be reached.

The next chapter is concerned with scintillation counters in general, and as the gas mixture plays a main role, chapter three will deal with the effect of gas mixtures on the performance of the counter. The MWPC or DC forms the first part of the GSC, so the understanding of their performance at high rate (chapter four) and the preliminary results from the MWPC,and the DC,led to the choice of the GSC as a suitable detector for high count rate experiments with moderate energy resolution (chapter six). Chapter five is dedicated to electric field computations in MWPC's and DC's.

Chapter One : References

1. F.S. Goulding, J.M. Joklevic & A.C.Thompson, SSRL. Report No.78/04 Stanford Linear Accelerator Center, May (1978).

2. R. Von Leishout et al, α.β.γ Ray Spectroscopy (ed. K. Siegbahn, North Holland/American Elsevier - Amsterdam, 1974), vol. 1 P 518.

3a. J. H. McCrary et al, Phys. Rev. A2 (1970) 2489.

b. , Phys.Rev. 153 (1967) 307.

c. R.C. Weast (ed.), C.R.C. Handbook of Chemistry and Physics (C.R.C - Press - U.S.A. 1977-1978).

d. C.M. Davisson, α.β.γ Ray Spectroscopy (ed. K. Siegbahn, North Holland /American Elsevier - Amsterdam, 1974), vol.1 P 827.

e. E. L. Grove & A.J. Perkins (eds), Development in Applied Spectroscopy (Plenum Press, London, 1971) vol.9.

4. P. Rice-Evans, Spark, Streamer, Proportional and Drift Chambers (Richelieu Press, London, 1974).

5. E. Rutherford and H. Geiger, Proc. Roy. Soc.A81 (1908) 141.

6. B. B. Rossi and H.H.Staub, Ionization Chambers and Counters (McGraw-Hill, New York, 1949).

7. J. Price, Nuclear Radiation Detection (McGraw-Hill, New York, 1964).

8. B. H. Bransden, J. V. Major & D. Evans, The Fundamental Particles (Van-Nostrand Reinhold Company, London, 1973).

9. J. Lightfoot, Ph.D. Thesis, University of Durham,(1972).

10. J. E. Chaney, Ph.D. Thesis, University of Durham,(1974).

11. G.C.Smith, Ph.D. Thesis - University of Durham (1973).

12. J. Fischer & S. Shibata, Brookenhaven Report BNL-14899 (1970).

13. B. Rossi, Bull.Amer. Phys. Soc., Ser II 2 No.1 (1957) 53.

14. E. C. Anderson et al, Nucleonics 14 no.1 (1956) 53.

15. Z. H. Cho, I.S. Ahn & C.M. Tsai, IEEE Trans.on Nucl.Sci., NS-21 (1974) 218.

16. J. H. Neiler and P.R.Bell, α.β.γ Ray Spectroscopy (ed. K. Siegbahn, North Holland/American Elsevier, Amsterdam, 1974) Vol.1 P 271.

17. G. Charpak et al, Nucl. Instr. and Meth., 62 (1968) 262.
--- , 65 (1968) 217.

18. G. Charpak, Ann. Rev. Nucl. Sci., 20 (1970) 195.

19. G.A.Erskine, Nucl. Instr. and Meth. 105 (1972) 565.

20. S. N. Kaplan et al, LBL-Report 778 (1972).

21. B. Sitar, R.J.Stubbs and J.M.Breare, Nucl. Instr. and Meth. 134 (1976) 267.

22. S. Al-Dargazelli, Durham University, Internal Report. N1-76-24 (1976).

23. G. Charpak, Wire Chambers : A Review and Forecast, Comments on Nuclear and Particle Physics (1976).

24. T. Bressani et al, Track Localization by means of a drift chamber, Proc.Int.Sem.on filmless Spark & Streamer Chambers. Dubna (1969). (JINR.Dubna 1969) p.275.

25. G. Charpak, D. Rahm and H. Steiner. Nucl. Instr. and Meth. 80 (1970) 13.

26. A. H. Walenta, J. Heintze & B. Scharlein, Nucl. Instr. and Meth. 92 (1971) 373.

27. R. Browell, Ph.D. Thesis, Durham University (1975).

28. A.R.Hedge, J.M.Breare, M. Comyn, A. Humrich and U. Meyer - Berkhout Nucl.Instr. & Meth. 156 (1978) 203.

29. S. Al-Dargazelli, Durham University, Internal Report, NI-77-11(1977).

30. D. W. Aitken, IEEE Trans on Nucl. Sci.15 (1968) 10.

31. F. S. Goulding and D. A. Landis, IEEE Trans. on Nucl.Sci. NS-25 (1978) 896.

32. Z. H. Cho, C. M. Tsai and L. A. Eriksson, IEEE Trans. on Nucl. Sci. NS-22 (1975) 72.

CHAPTER TWO

SCINTILLATION COUNTERS

In this chapter a review is given of solid scintillation counters and photomultipliers with special reference to the RCA 8575 tube which is used in this work. This is followed by a discussion of gaseous scintillators and gas scintillation counters.

2.1 THE SCINTILLATION PROCESS AND LIGHT COLLECTION

Scintillators can be divided into three main categories : Inorganics, organics and gaseous scintillators. The mechanism of the scintillator process differs with different types. Considering first the inorganic substances, the passage of an ionizing particle may provide electrons in the crystal of sufficient energy to be raised to the conduction band. This is equivalent to ionization in free atoms or molecules, or photoionization when the incident particles are photons.

$$X + h\nu \longrightarrow X^{*} + e^{-} + k.E. \quad \text{(Atomic photoionization)}$$

If the energy is not enough to raise an electron to the conduction band, it remains bound electrostatically to the hole in the valence band (excitation).

$$X + h\nu \longrightarrow X^{*} \quad \text{(Atomic excitation)}$$

De-excitation (return to the ground level) can take place with the emission of radiation (luminescence). If an allowed transition is permitted between the excited state and the ground state, the radiation emission (fluorescence) occurs in about 10^{-8} sec or less. This is the same order

as the life time of an atomic state for an allowed transition. The radiation emission decays with an approximately exponential dependence. If the excited state is not connected to the ground state through an allowed transition (metastable state), the return to the ground state can occur by means of the electrons receiving enough energy to reach a non-metastable state. Hence the emission of radiation (phosphorescence) is delayed and occurs in a time which may be as short as a microsecond or as long as an hour. The characteristic decay time for NaI(Tℓ) is approximately 2.5×10^{-7} sec[1]. Apart from the usual radiative transitions, non-radiative de-excitation can also occur from thermally excited states. By this mean much of the energy of the exciting particle is lost as far as light emission is concerned.

For the organic compounds, the scintillation process is primarily a molecular phenomenon which is different from the process in inorganic solids whose luminescence is associated with the energy band structure of ionic crystals. Here the luminescence arises from the de-excitation of a molecule from an excited state.

$$XY + h\nu \longrightarrow XY^{*} \qquad \text{(molecular excitation)}$$

$$XY + h\nu \longrightarrow XY^{+} + e^{-} + k.E. \qquad \text{(molecular photoionization)}$$

In addition to various electronic states, the molecules will possess states of different vibrational energy which appear in the absorption spectrum as bands due to transitions from various vibrational levels of the ground state to the excited electronic states. The luminescence emission from organic materials usually occurs in 10^{-8} sec which is much faster than from inorganic materials, because the emission is nearly all prompt and there is very little phosphorescence. A decay time of few

nanoseconds is obtainable[1] in some organic phosphors.

The radiation emitted in gaseous scintillators is that coming from the gaseous atoms or molecules which are ionized or excited due to inelastic collisions with the passing particles. Each excited atom or ion returns to its ground state with the emission of one or more photons within about 10^{-9} sec[2], giving rise to a fast light pulse. The primary energy deposited in metastable states can be transferred by thermal collision to nearby resonance levels and can thus be emitted as resonance radiation. These radiations are primarily in the ultra violet region (generally beyond the range of sensitivity of ordinary photomultiplier tubes) and the efficiency of conversion (or intrinsic efficiency) from light photons to photoelectrons is low. Therefore the use of wavelength shifters is necessary in order to match the photocathode response curve (i.e. to obtain maximum signal from the photomultiplier).

The main characteristics that the wavelength shifter should have are a fast decay time, to match the fast decay time of the gaseous scintillators ; a high quantum efficiency, to provide maximum light output ; and a thickness which is adequate to absorb completely the ultra violet radiation. The wavelength shifters are usually organic solids deposited by vacuum evaporation onto the face of the photomultiplier with thickness of 20-30 $\mu g/cm^3$.

Sayres and Wu[3] showed the importance of using wavelength shifters because they obtained an increase in the output light pulse height by a factor of 17.5 in a glass window photomultiplier type Du Mont 6292 and 1.65 in a quartz window photomultiplier tube type K 1306. The wavelength shifter they used was 75 $\mu g/cm^3$ quaterphenyl ($C_6H_5-C_6H_4-C_6H_4-C_6H_5$). From this it can be deduced that most of the emission occurs in the ultra violet region to which the glass windows are opaque.

In some early work, Policarpo et al[4] used, p-quaterphenyl with an Ar + 5% Xe mixture. They also obtained a large increase in the light output. The relative efficiencies of various wavelength shifters have been studied by Policarpo's group[5] for a xenon gas scintillation counter. They measured the mean light pulse amplitude as a function of the thickness of the wavelength shifter and in view of the results, p-quaterphenyl, with 2.5 mg/cm^2 thickness, was used.

It is possible to use a gas as a wavelength shifter, Eggler and Huddleston[6] used a small mixture of nitrogen gas in argon, and also in helium to increase the light output. The maximum pulse height was obtained with 10% nitrogen in argon and 0.1% nitrogen in helium.

The use of reflectors surrounding a scintillator may also increase the number of photons which fall on the photocathode. Many types of reflector have been used, such as metals, evaporated metal films and pigments. Aluminium is one of the most satisfactory reflectors for most purposes. It has a high reflectance, particularly in the UV region and is very resistant to corrosion. Evaporated aluminium gives better reflection than an aluminium foil. The reflection is about 90% from the visible down to about 2537°A as shown in Fig.2.1[1,7]. Reflectance of evaporated aluminium decreases due to oxidation of the surface, hence a special coating is needed. Between 1200°A and 3600° A, aluminium reflection is greater than that of any other metal, but above 3600° A it is exceeded by that of silver. However, silver has a very pronounced minimum in its reflection curve at 3150°A - see Fig.2.1[7]. The reflection coefficient for ultra violet light from pigments covers a range from almost zero up to more than 90%. The two most commonly used reflectors are magnesium oxide (MgO) and magnesium carbonate ($MgCO_3$). Magnesium oxide (shown in Fig.2.1)[1] provides higher reflectivity than magnesium carbonate. Reflectivity depends on the thickness of the coating.

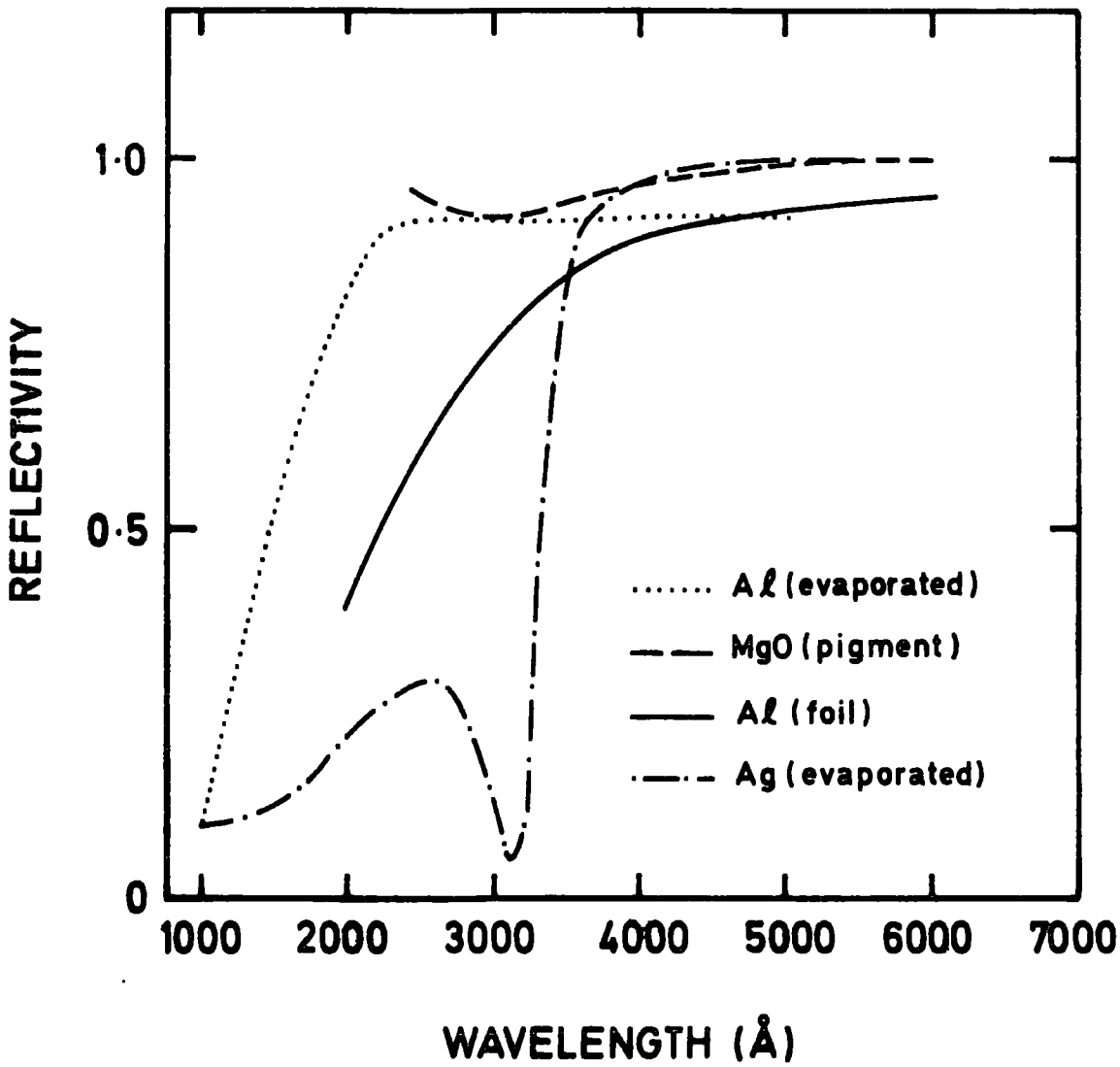

FIG. 2·1 Reflectivity of surfaces.

2.2 SUMMARY OF MAIN CHARACTERISTICS OF SCINTILLATORS

The characteristics of a scintillator, such as density, chemical composition, decay time and light output, determine its area of application. The main characteristics are the following :

1. The light output intensity is usually considered to be a nearly linear function of the energy deposited by the incident particles. In the case of NaI, for example, where the linearity is very good, this provides a direct method of measuring particles energies. Even in these cases, however, a distinct non-linearity was observed in the scintillation response of NaI(Tℓ) to low energy gamma rays (below several hundred keV)[8]. The scintillation response of anthracene to gamma rays was also found to be linear only above 100 keV[9].

2. High density scintillators provide highly efficient detection of gamma rays. For example, one of the heaviest materials is cadmium tungstate ($CdWO_4$) with a density of 7.9 g/cc[10]. Most of the organic and plastic scintillators have densities only a little above 1 g/cc.

3. The fast response to ionizing radiation makes the technique useful in high count rate experiments. However, the decay time for inorganic compounds is temperature dependent[11]. The influence of the temperature dependence on the decay time of NaI(Tℓ) was studied[12] in the range of 0° C to 24° C, the decay time changed from 380 nsec at 0° C to 240 nsec at 24° C, i.e. at an approximate rate of 5 nsec/ $^{\circ}$C. This temperature dependence is attributed to the competition between radiative and non-radiative transitions, the latter being caused by thermal excitation. Many inorganic substances which are not luminescent at room temperature becomes so at reduced temperature. Organic crystals may also be temperature dependent, the decay time of anthracene was observed[13] to decrease with decreasing temperature from 38 nsec at 40° C to 12 nsec at -180° C.

For an Argon + 8% nitrogen mixture, Grün and Schopper[14] studies the effect of temperature on the light output. They observed a constant increase in light intensity with increase in temperature. Hence the factor of temperature can be used to change the decay time of a scintillator, which may be an important consideration at high count rates.

2.3 PHOTOMULTIPLIERS

The photomultiplier forms an important part in a scintillation counter. It converts the light pulses from the scintillator into electric pulses. The current multiplication within the tube can be as high as a million or more. The essential parts of each tube are the photocathode for releasing the photoelectrons, the dynodes for producing the electron multiplication and the anode for collecting the current pulse. To ensure the passage of electrons from the photocathode to each of the dynodes in succession and finally to the anode for collection, each of these elements is placed at successively higher potentials.

2.3.1 Windows

Transmission is a function of wavelength and of window thickness. This is shown in Fig.2.2[7] for different window materials. Tubes with windows of fused quartz can be used at wavelength down to 1800° A, while for pyrex, it is around 3000° A. Very pure synthetic fused silica has been made in a variety of grades, such as surpasil, where the weak absorption band at 2400° A of fused quartz has been eliminated.

2.3.2 Photoemissive Materials and Photocathodes

Photoemission of electrons occurs when the energy of the incident radiation (hc/λ) is higher than the work function of the surface (ϕ). The threshold wavelength of a surface (λo) is that when the photoelectrons are emitted with zero energy and is given by

$$\lambda o = \frac{12390}{\phi} \quad \begin{matrix} (^{o}A) \\ (eV) \end{matrix} \qquad (2.1)$$

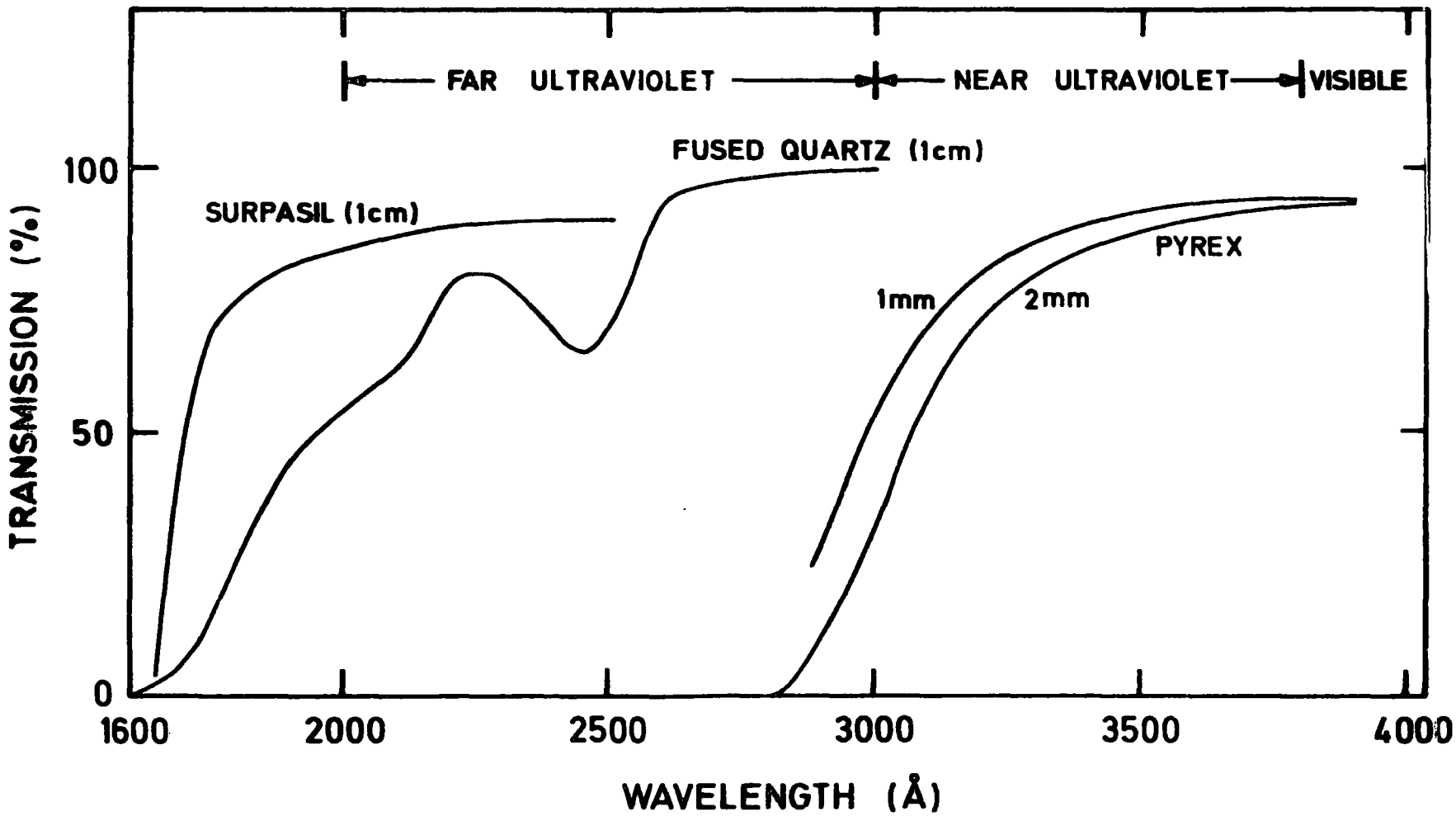

FIG. 2·2 Transmission of windows.

Materials with low work function provide good photoemissive surfaces. Metals work functions are usually between 4 and 5 eV. However, alkali metals have low work function in the range of 1.8 to 2.4 eV. The low work function of alkali metals is due to the single electron in their outer orbits. Table 2.1[15] gives the work function of alkali metals and their atomic numbers. Caesium has the lowest work function, because its outer electron is more easily detached than that of other alkali metals, as it is farther from the nucleus.

TABLE 2.1[15]

Work Function for Some Metals

	Metal	Z	ϕ (eV)
Alkali Metals	Li	3	2.9
	Na	11	2.75
	K	19	2.3
	Rb	37	2.16
	Cs	55	2.14
	Ag	47	4.26
	Mg	12	3.66
	Sb	51	4.7
	Bi	83	4.22

The cathode of a photomultiplier tube normally consists of a semitransparent layer of the photoemissive material which is deposited on the inside surface of the end face of the tube. The factors determining cathode spectral response are the transmittance of the window and its thickness, the absorption spectrum of the cathode and its thickness and

the quantum efficiency of the cathode. The limit of the short wavelength response is determined mainly by the window material and the response at long wavelengths is determined by the photocathode material.

The optimum quantum efficiency is not obtained from pure alkali metal photocathodes. It has been found that mixtures of metals of low work functions give a higher yield.

The various types of photocathodes differ according to their base material and thickness of the layers. Photocathodes deposited on a metal surface may have different characteristics from a similar cathode deposited as a semitransparent layer on the inside of the tube envelope. Table 2.2 gives the typical sensitivity values for some types of photocathodes with their wavelength thresholds.

TABLE 2.2[16]

Types of Photocathodes

Photocathode material	Spectral response number	Long wavelength threshold (Å)	Typical sensitivity (μA/ℓm)
Ag-O-Cs	s-1	12000	20
Cs_3Sb	s-11	6700	50
Bi-Ag-O-Cs	s-10	7800	35
$Na_2K\ S_b[Cs]$	s-20	8500	150

Table 2.3 shows the effect of more than one alkali on the typical sensitivity to 2870° K tungsten light[17].

TABLE 2.3

Multi-alkali Photocathodes

Photocathode	μA/ℓm
Sb-Na	1
Sb-K	5
Sb-Cs	40
Sb-K-Na	50
Sb-K-Na-Cs	180

2.3.3 Dynodes

The secondary emission process is similar to that of photoemission except that an electron conveys the energy to the emitting surface, hence similar materials are usually used as photoemitters and secondary emitters. Caesium antimonide is a good secondary emitter and is often used as a coating for dynodes to produce a high gain. Another type of dynode may be formed by oxidising copper containing about 2% of beryllium. The secondary emission coefficient of the copper-beryllium material is increased by the presence of caesium vapour during the photocathode manufacture.

The performance of the photomultiplier is controlled by the dynodes geometry, i.e. venetian blind, focused, box-and-grid and circular cage.

For example the venetian blind usually gives higher gain and focused tubes tend to have a smaller spread of signal transit time than focused types.

The anode is usually a wire grid to keep the stray capacitance, associated with this electrode, low.

2.3.4 Gain

The electron gain of a photomultiplier (G) should ideally be given by :

$$G = (\delta)^n \tag{2.2}$$

where δ is the average secondary emission coefficient and n is the number of dynodes. However, this expression takes no account of the fact that the cathode-first dynode ($K-D_1$) collection efficiency (f) will inevitably be less than 100%, as will the transfer efficiency of electrons between dynodes (g) although g is almost 100%. A more realistic expression is therefore :

$$G = f\,(g\delta)^n \tag{2.3}$$

δ usually has a value between 3 and 6, and the value of f may be about 0.9[16].

The secondary emission factor (δ) is a function of the voltage applied per dynode stage (V_s). The relation between δ and V_s is different for different dynode materials, for example, the empirical relation for δ in the case of Cs Sb dynodes is[18] :

$$\delta = 0.2\,(V_s)^{0.7} \tag{2.4}$$

while for caesiated Ag Mg O dynodes

$$\delta = 0.025\,V_s \tag{2.5}$$

The overall voltage (V) is approximately proportional to V_s, so substituting eq. 2.4 in eq. 2.3

$$G = \text{Const. } V^{0.7n}$$

$$dG = \text{Const. } 0.7n \; V^{0.7n-1} \; dV \tag{2.6}$$

The fractional change in gain (dG/G) is given by

$$\frac{dG}{G} = 0.7 \; n \; \frac{dV}{V} \tag{2.7}$$

eq. 2.6 and 2.7 show the dependence of the gain on the applied voltage and also indicate the importance of the stability of the power supply and its effect on the gain fluctuation.

2.3.5 Photomultiplier Circuit

The photomultiplier dynode potentials are obtained by means of a resistor chain across a high voltage source. The photomultiplier tube can be run either with the cathode grounded and the anode at a high positive potential (using a coupling capacitor for the output signal), or with the cathode at a high negative potential and the anode near earth potential. Conducting material close to the tube envelope may disturb the potential distribution inside it. Hence any material in contact with the envelope should be at cathode potential. A mu-metal shield properly connected performs the dual function of an electrostatic shield and a magnetic shield. This is particularly important with the cathode at a high negative voltage.

With a grounded cathode, the ripple from the power supply is injected through the anode load resistor and coupling capacitor into the measuring circuit. This will affect the gain stability as shown in eq.2.6, so it is more convenient to use the grounded anode method to operate the

photomultiplier, taking particular care to avoid field distortions round the photocathode. The overall gain of the photomultiplier tube is a very sensitive function of the applied voltage, eq. 2.6, hence it is necessary to use a well stabilized high voltage supply for quantitative scintillation spectrometry.

The output of a photomultiplier is an electric charge and usually this charge is allowed to flow through the load resistor R_L while the voltage across it is measured. The electrons flowing into the anode give a negative output signal. The exponential decay of light following the passage of ionizing particle gives rise to a corresponding exponential current at the photomultiplier. The photoelectron current I is therefore given by

$$I = I_o \exp\left(-\frac{t}{\tau}\right) \tag{2.8}$$

where τ is the decay time. The anode of a photomultiplier is almost an ideal current generator. The appropriate equivalent circuit for the output of the photomultiplier is a current generator in parallel with an output resistance R_L and capacitance C_L. The magnitude of C_L depends on the type of tube used and the circuit design. From Kirchoff's Laws

$$I = \frac{V_o}{R_L} + C_L \frac{dV_o}{dt} \tag{2.9}$$

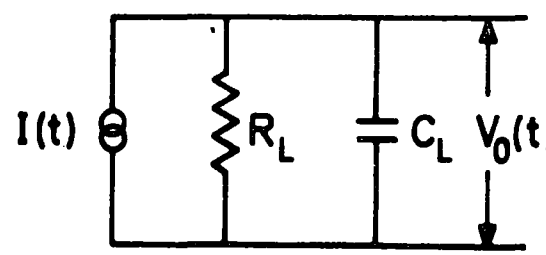

Substituting 2.9 in 2.8 and solving for V_o[19]

$$V_o = \frac{I_o \tau R_L}{\tau - R_L C_L} \left[\left(\exp\left(-\frac{t}{\tau}\right) \right) - \left(\exp\left(-\frac{t}{R_L C_L} \right) \right) \right] \tag{2.10}$$

hence, when $R_L C_L$ is very much greater than τ

$$V_o = \frac{I_o \tau}{C_L} \exp\left(-\frac{t}{R_L C_L} \right) \tag{2.11}$$

The output has a rise time of τ and a fall time of $R_L C_L$. A typical value for R_L is 470 k Ω and for C_L is 100 pF. These values make $R_L C_L$ equals to 47 μsec which is much greater than τ. When τ is much greater than $R_L C_L$

$$V_a = I_o R_L \exp\left(-\frac{t}{\tau} \right) \tag{2.12}$$

V_a in this case is a reproduction of the input current I, and the rise time is then determined by the value of $R_L C_L$ (100 Ω x 10 pF = 1 nsec). However, the fall time is controlled trailing edge by the scintillator decay time constant. Hence the capacitance with the anode load resistance determines the nature of the output signal.

As was shown earlier, the "grounded cathode" mode of running the photomultiplier needs a coupling capacitor to isolate the signal output from the positive high voltage supplied to the anode. This capacitance coupling distorts the output signal, by causing the base line, or reference level of the output signal, to shift with rate and pulse amplitude[20]. This form of signal distortion can be avoided by using the "grounded anode" mode, where the anode can be directly coupled to an external circuit, and this is another reason for using this configuration.

2.4 THE PERFORMANCE OF PHOTOMULTIPLIERS AT HIGH RATES

It has been observed[21-24] that the operation of photomultiplier tubes at high rates gives rise to a shift in their gain. A test of this phenomenon has been carried out[25] in order to modify the photomultiplier dynode potential divider (the shift is attributed to it) and to stabilize the gain up to count rates of 10^7 - 10^8 sec^{-1}.

A brief description of the photomultiplier tube used is given and this is followed by details of the tests.

2.4.1 RCA 8575 Photomultiplier Tube

An RCA 8575 photomultiplier tube was used throughout the work. Its characteristics are as follows : It is a 2" diameter, 12-stage end window linear focussed tube[26], with a pyrex window. The photocathode type is a bi-alkali (C_s-K-S_b) which has low red sensitivity and low dark current at room temperature. The spectral response of the tube is shown in Fig 2.3[26]; in the same figure the spectral response of the RCA 31000 M is also given for comparison. RCA 31000 M is very popular in gas scintillation counters for its wide range of spectral response. At 10-per-cent quantum efficiency, the spectral response of the RCA 8575 covers the approximate range from 2600 to 6000°A , which is close to the band emission of the gas mixture used in this work, i.e. the nitrogen bands between 3000° A and 4200°A produced due to quenching of the argon band between 1500°A and 3000°A. More details are given concerning the gas mixture in the following chapter. Table 2.4 summarizes the tube characteristics.

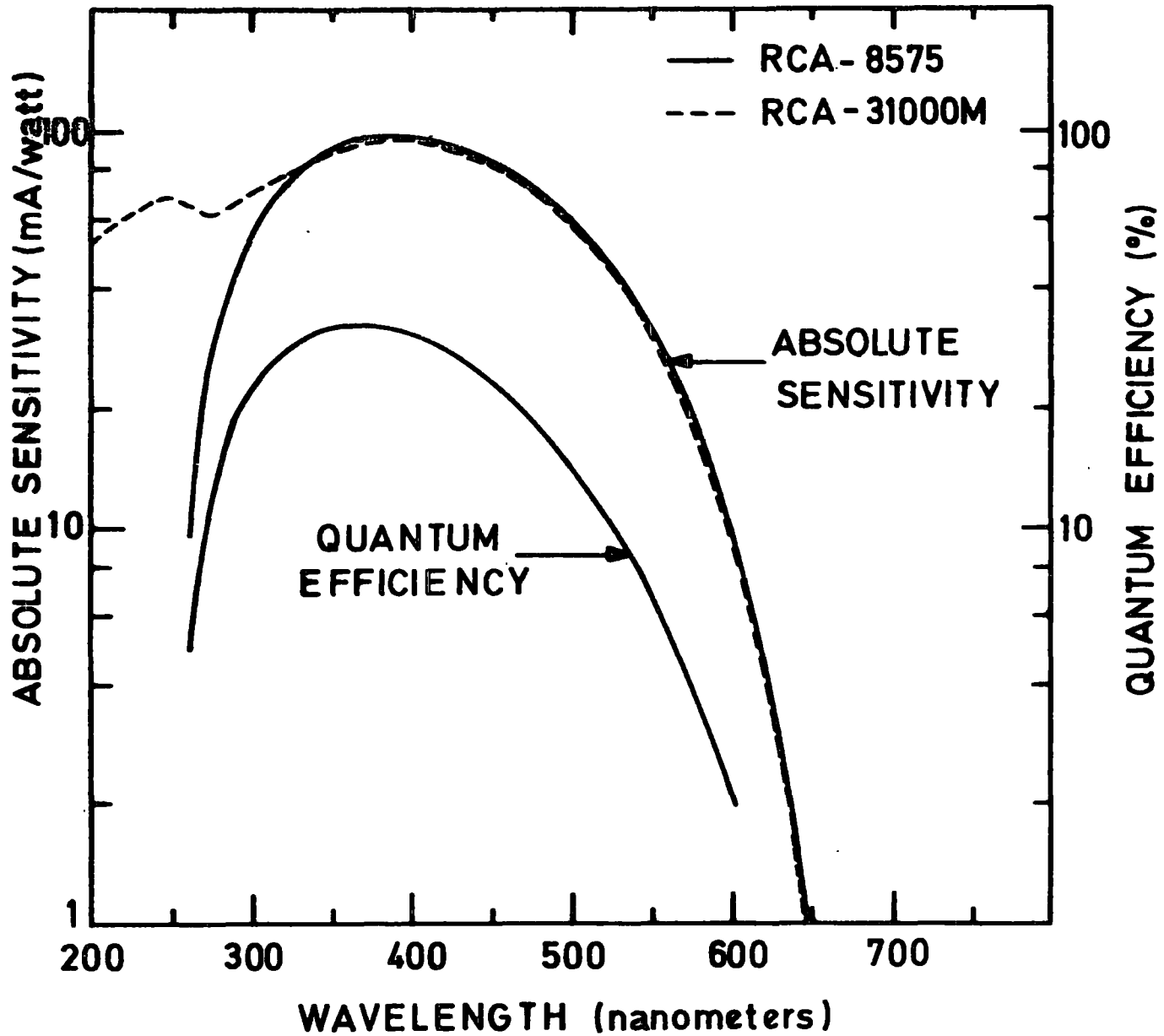

FIG. 2·3 Photocathode spectral response.

TABLE 2.4[26]

Other Relevant Data on the RCA 8575 Photomultiplier Tube

Typical gain at typical voltage*	1.44×10^7
Typical absolute sensitivity (λ peak)	82.8 mA/watt
Typical sensitivity	80 μA/ℓm
Anode-pulse current capability	
linear	0.15 amp
saturated	0.5 amp
Rise Time	2.5 nsec (3.5 at 1500 V)
Electron transit time**	31 nsec (44 at 1500 V)
Maximum rated average anode current	200 μ amp

* The typical operating voltage is that used to measure the tube's characteristics (2000 V).

** At maximum rated supply voltage (3000 V), the photocathode is fully illuminated.

2.4.2 Passive Network Dynode Connections

The manufacturer's recommended dynode connections are shown in Fig 2.4[26]. The test was carried out using a constant light source to simulate a high count rate, and a pulsating light source. The constant light source was a yellow indicator lamp which could be adjusted to produce different average anode currents to simulate various count rates to which the photomultiplier may be exposed. The pulsing source was a yellow light emitting diode (LED) driven by means of a TTL NAND Gate and a pulse generator, type HP-8004A of 1.5 nanoseconds rise time[25].

The variables measured were the pulse amplitudes using a Tektronix 7704 oscilloscope with 7A16 amplifier, and the average anode current, using D.C. microammeters. Fig 2.5 shows the linear relation between the anode current and the pulsing rate at different photomultiplier voltages. Fig. 2.6 shows the amplitude of the photomultiplier pulses (across 50 ohms) as a function of the pulsing rate for different photomultiplier voltages. The pulse height (i.e. the photomultiplier gain) was found to increase with the pulsing rate. The shift in gain is more obvious at high photomultiplier voltages (i.e. high anode currents).

The measurements of the interdynode voltages at different pulsing rates showed an increase in most of the interdynode voltages at high rates, but with a considerable drop in voltage between the last dynode and anode. This effect was observed by Gupta and Nath[22] and it can be explained as follows : At high counting rates, the number of electrons participating in the multiplication process in the last two stages of a high gain photomultiplier becomes extremely large. It is probable then that a substantial part of the electronic current may flow from the resistor chain to compensate. This diversion current causes a drop in the potential difference between the last few resistors. As the total applied voltage to the chain

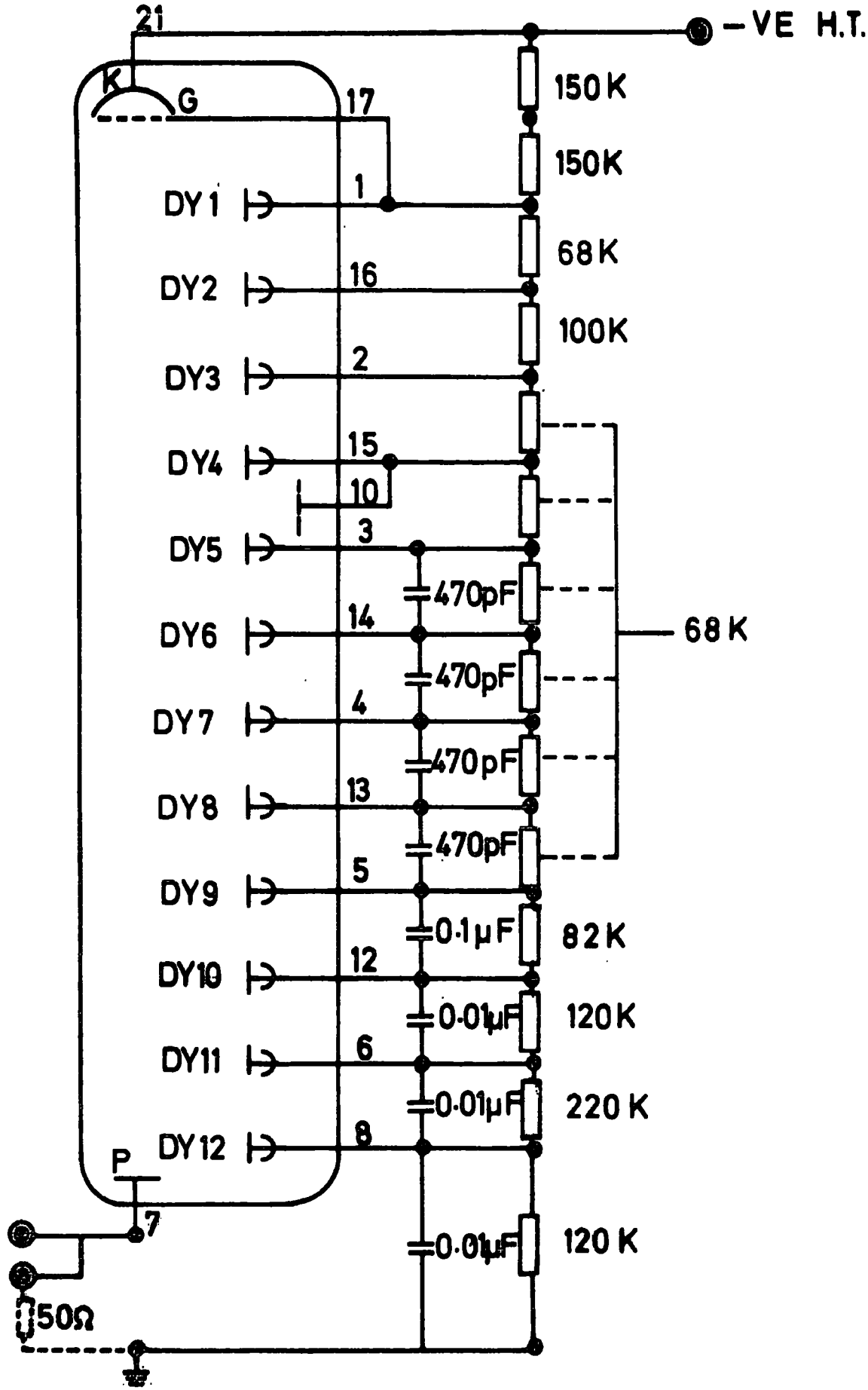

FIG. 2·4 The dynode connections of RCA-8575.

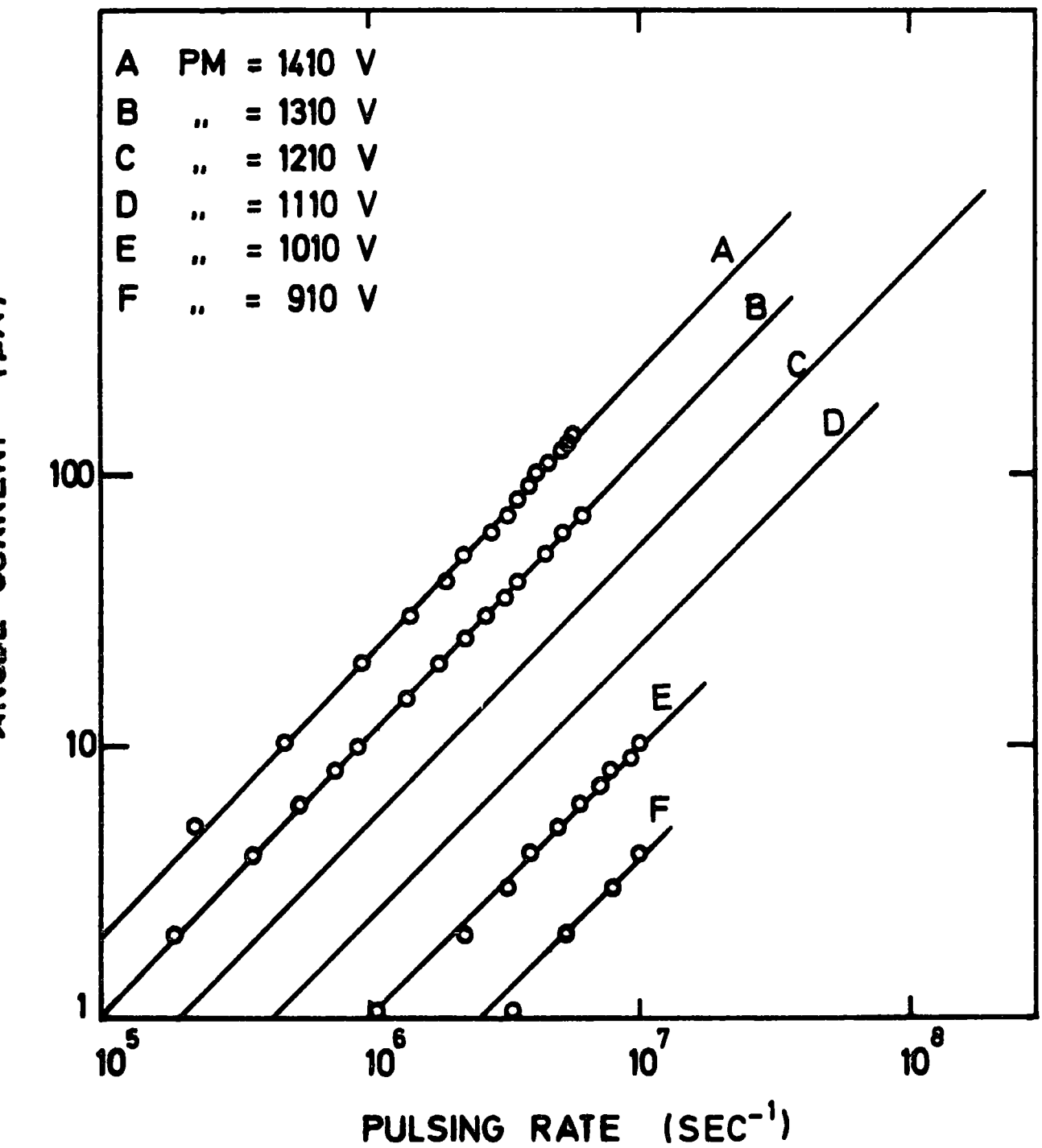

FIG. 2·5 Anode currents in Passive network.

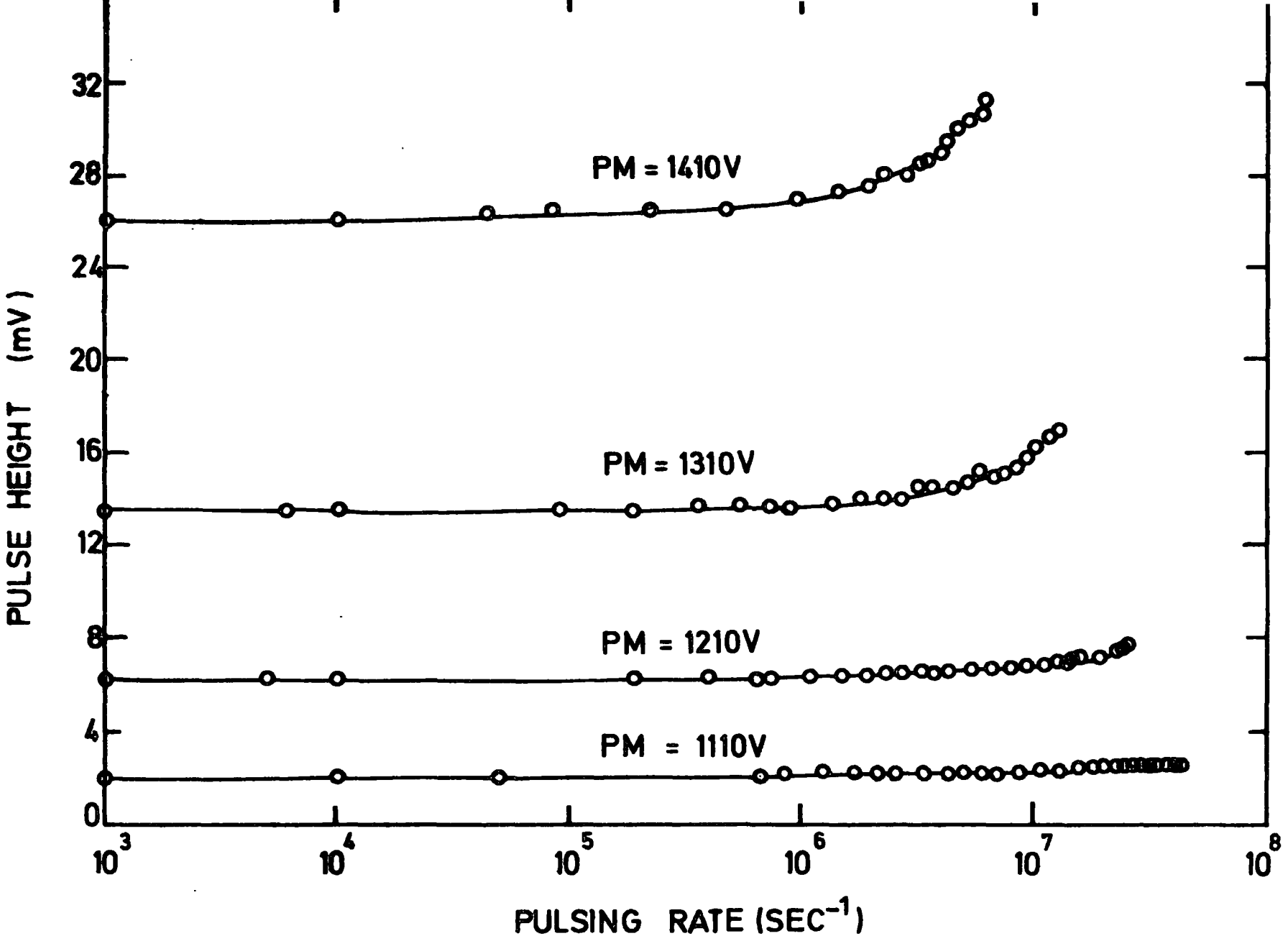

FIG. 2·6 Pulse heights in passive network.

is constant, the decrease in voltage across the last resistors will cause an increase in voltage in the first resistors. This increase will affect the gain of the photomultiplier, as in Eq. 2.7 in such a way that the gain therefore increases with increase in the anode current.

The change in potential can be minimized by decoupling the dynodes to ground with large capacitor. The minimum values of the decoupling capacitors are determined by the maximum charge pulse, or alternatively the peak anode current (i_a) and the duration of the largest pulse (t), since the gain must remain virtually the same at the end of the pulse as at the beginning of it. For the last stage the fluctuation in voltage (dV) will be slightly less than $\frac{i_a t}{C}$, where C is the decoupling capacitance so the fractional change in gain (dG/G), using Eq.2.7 will be :

$$\frac{dG}{G} \approx \frac{0.7\, n\, i_a t}{CV} \tag{2.13}$$

Therefore, if a linearity of L% is required for dG/G, the capacitance is determined by the requirement[16]

$$C > \frac{70\, n\, i_a\, t}{V\, L} \tag{2.14}$$

The currents at the other dynodes will be smaller so the decoupling capacitors can be reduced correspondingly. At continuous high rates, however, the capacitors smoothing effect decreases, and the photomultiplier gain increases with the large current from the potential divider.

2.4.3 Active Network Dynode Connections

From the above results, it was obvious that a new potential divider network was needed for the high count rate experiments. Several

designs have previously been used[22,24,27] for high rate systems. A recent design by Kerns[28] was suitable for the RCA 8575 (as well as any other tubes). According to this design, the last seven resistors in the existing chain were replaced by emitter followers. Fig 2.7 shows the application of Kerns design to the RCA 8575 tube. The emitter follower provides a high input impedance and low output impedance, the voltage gain is almost unity. The current gain property (β) ($\beta \sim 100$) of the emitter follower enables the dynodes to contribute large currents to the anode current while drawing small currents (smaller by the factor β) from the potential divider chain.

When a particular interstage voltage is too high for one transistor, two in series were used as in the D11-D12 stage. Diodes IN918 were connected between emitters and bases of the transistors to prevent the accidental over voltage of emitter base junctions in the reverse direction. The values of the decoupling capacitors were similar to those used in the passive potential divider. The values of the resistors from R1 to R6 were calculated from the manufacturer's recommended voltages to be provided between dynodes. The values of resistors from R7 onwards depend entirely on the emitter current of T1. R_o was set at a value which gives rise to an emitter current equal to half the total chain current. The effect of base currents was taken into account when calculating R8 onwards.

Repeating, with the new circuit, the tests done with the passive network, led to the results shown in Fig 2.8 and Fig 2.9. Fig 2.8 shows the variation of the anode current with pulsing rate and Fig 2.9 shows the variation of the pulse height with pulsing rate. Both figures give results for several photomultipliers voltages. The second figure shows that there is no appreciable change in gain up to anode currents, which

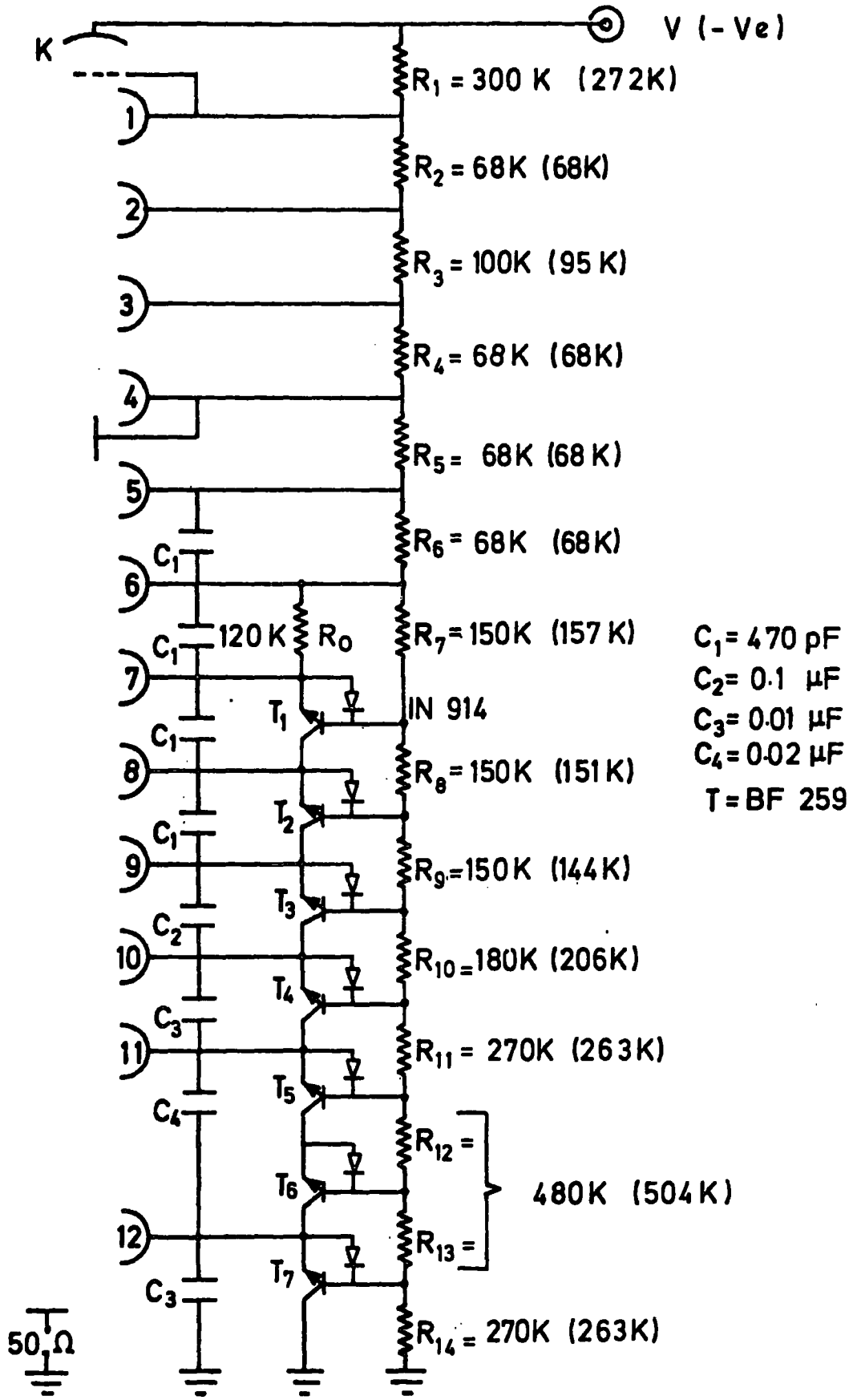
K
V (-Ve)
R1 = 300 K (272K)
R2 = 68K (68K)
R3 = 100K (95 K)
R4 = 68 K (68K)
R5 = 68K (68 K)
R6 = 68K (68K)
R7 = 150K (157 K)
R8 = 150K (151 K)
R9 = 150K (144K)
R10 = 180K (206K)
R11 = 270K (263K)
R12 =
R13 =
480K (504K)
R14 = 270K (263K)
120 K
Ro
IN 914
C1
C2
C3
C4
T1
T2
T3
T4
T5
T6
T7
1
2
3
4
5
6
7
8
9
10
11
12
50 Ω
C1 = 470 pF
C2 = 0.1 µF
C3 = 0.01 µF
C4 = 0.02 µF
T = BF 259

FIG.2.7

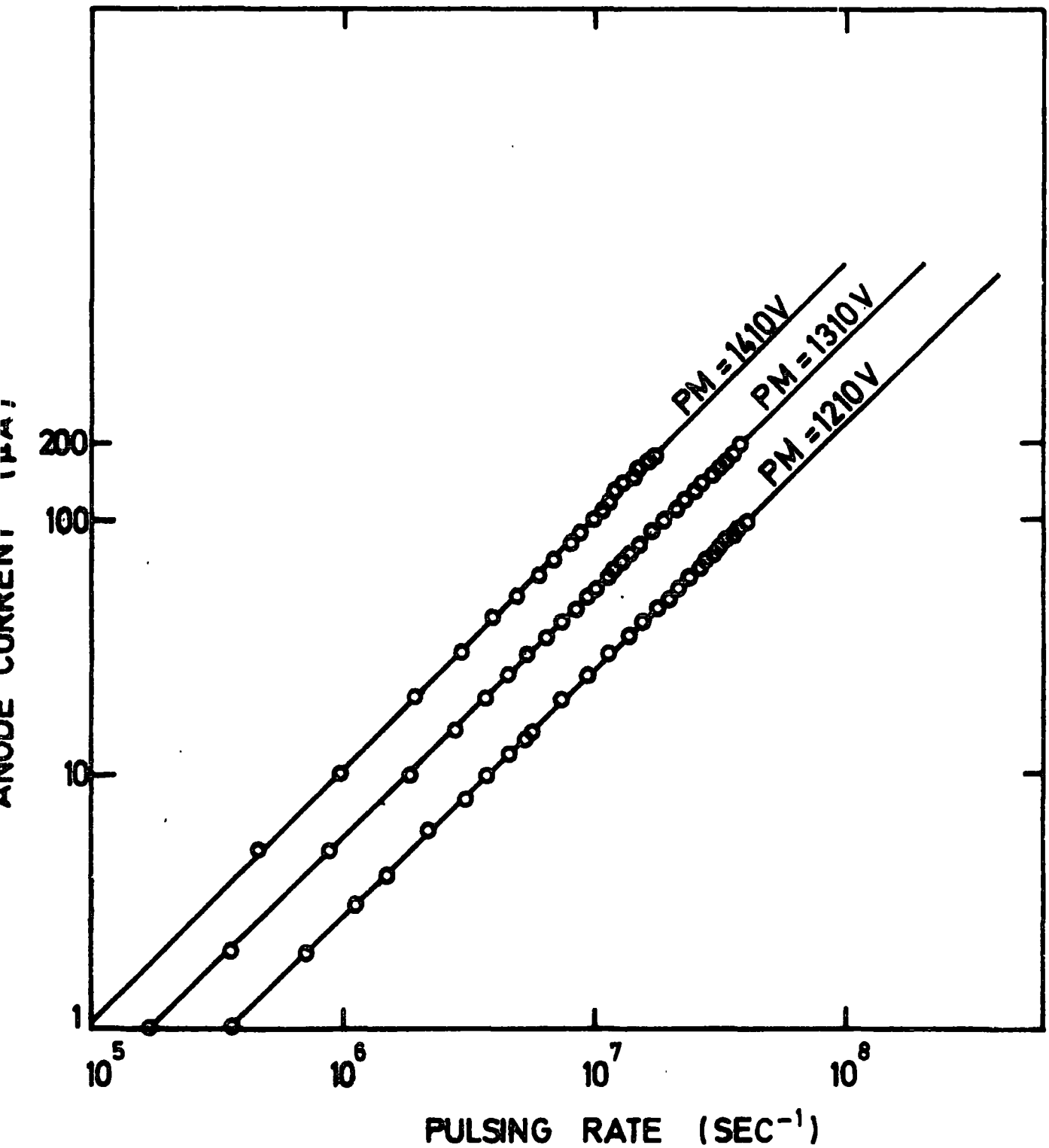

FIG. 2·8 Anode currents in active network.

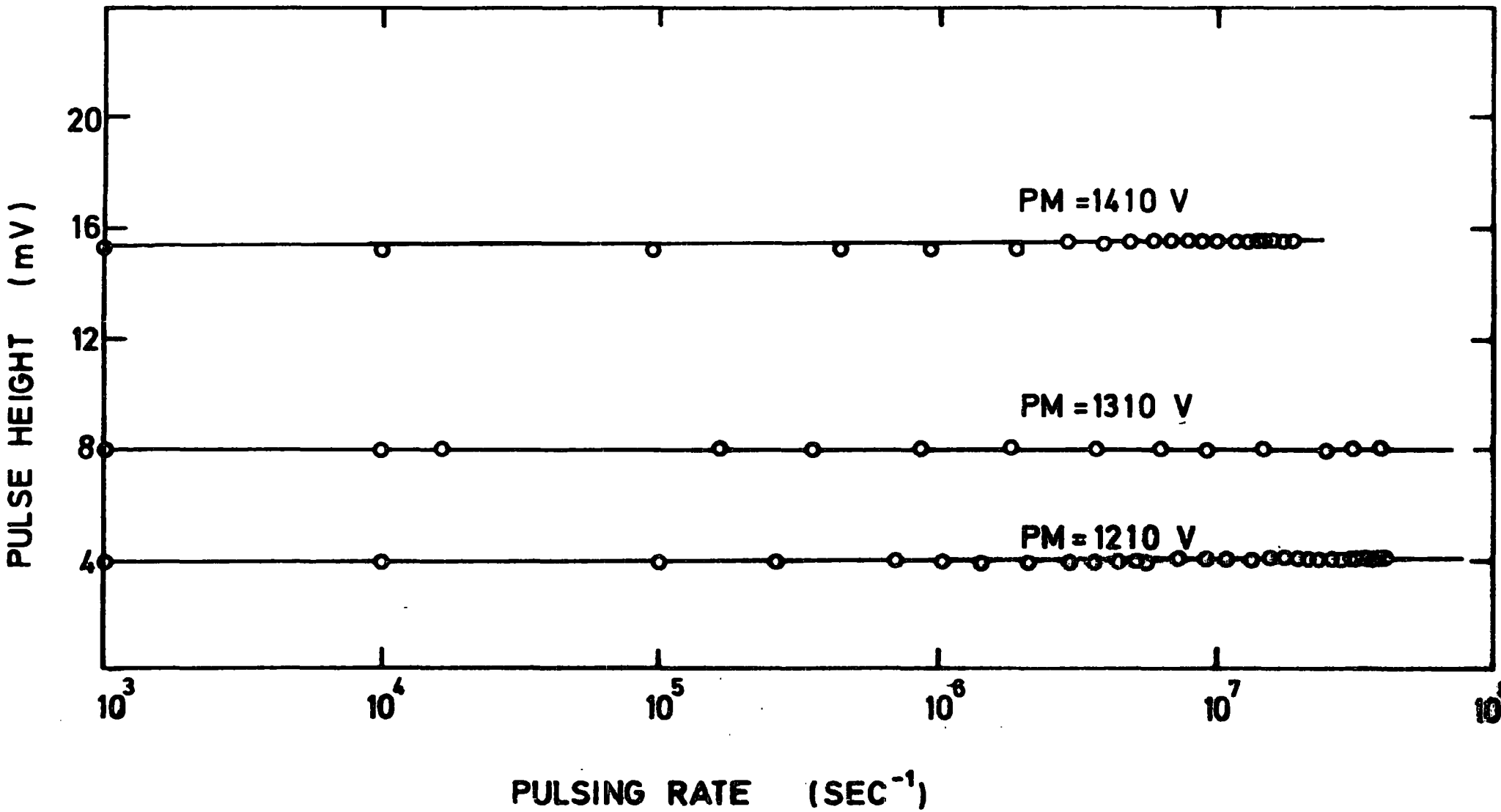

FIG. 2·9 Pulse heights in active network.

are very near to the maximum permissible anode current of the tube. The changes in the interdynode voltages were found to be less than one percent.

As it will be seen later, the effect of the new potential divider network is very significant on the performance of the detector used in conjunction with this photomultiplier.

2.5 GAS SCINTILLATION COUNTERS

2.5.1 Gas Scintillators

The first study of the ultraviolet emission for rare gases, due to the passage of α-particles, was made in 1949 by Audubert and Lormeau[29]. They used several gases at different pressures (Ar, Ne, N2, Air and O_2, the range of pressures was 1-300 mm Hg). They attributed the emission of the ultraviolet radiation to the "deactivation of the activated atoms by α-particles".

Grün & Schopper[30] (1951) developed a gas scintillation counter (GSC) using an argon-nitrogen mixture. The experimental arrangement of this counter is shown in Fig 2.10. Muelhause[31] (1953) independently developed a GSC utilizing both the visible and the UV component of the luminescence. He improved the efficiency of the counter by using a wave-length shifter (trans-stilbene) to detect the UV components.

Eggler and Huddleston[32,6] (1957), to whom the first use of GSC is incorrectly attributed, built a satisfactory counter. The counter was an aluminium hemisphere, 2 inches in diameter, the α-source was inside the detector which was argon at a pressure of 5 atmospheres, at one end of the cylinder there was a pyrex window and a photomultiplier. The inside of the window was coated with a wavelength shifter (a thin layer of butadeine in polystrene). In the counter used by Northrop and Gursky[33] (1958) the face of the photomultiplier tube was coated with

30 μg cm^{-2} of diphenylstilbene by vacuum evaporation.

Pure noble gases have been used[2,3] as well as binary noble gases mixtures[3,33]. The two most important factors relating to gas scintillators, which were studied, were the gas purity and the wavelength shifters. It was observed that a small concentration of impurity decreased the light output[34] and consequently gas purification systems were used by some workers[3,34]. Also as an alternative method, Boicourt and Brolley[35] provided a continuous flow of fresh gas through the counter to achieve the necessary gas purity. Several types of wavelength shifters were used[3,6], as mentioned earlier.

Liquified noble gases were used[34,36,37] in that period as well as noble elements in the solid phase[35], where it was found[34] that liquid and solid xenon produced pulse heights of 0.4 and 1.0 respectively, relative to the pulse height for α-particles on NaI(Tℓ) while the gas produced a relative pulse height of 0.3.

Gas scintillators were used, in the nineteen fifties, mainly as detectors for strongly ionizing particles, such as α-particles and fission fragments. Subsequently the main development of gas scintillation chambers has been the application of electric fields inside the scintillators. This led to the appearance of the gas scintillation counters which had much wider applications.

2.5.2 Gas Scintillation Counters

The application of an electric field inside gas scintillators was attempted by early workers[29a,30a] without success. No effect of electric field on intensity or multiplication factor was observed. However, Wiegand and Segrè[38] in 1953 showed that the light output of an argon counter increased with the application of an electric field. Colli[39] measured the multiplication of the electron pulses, from his

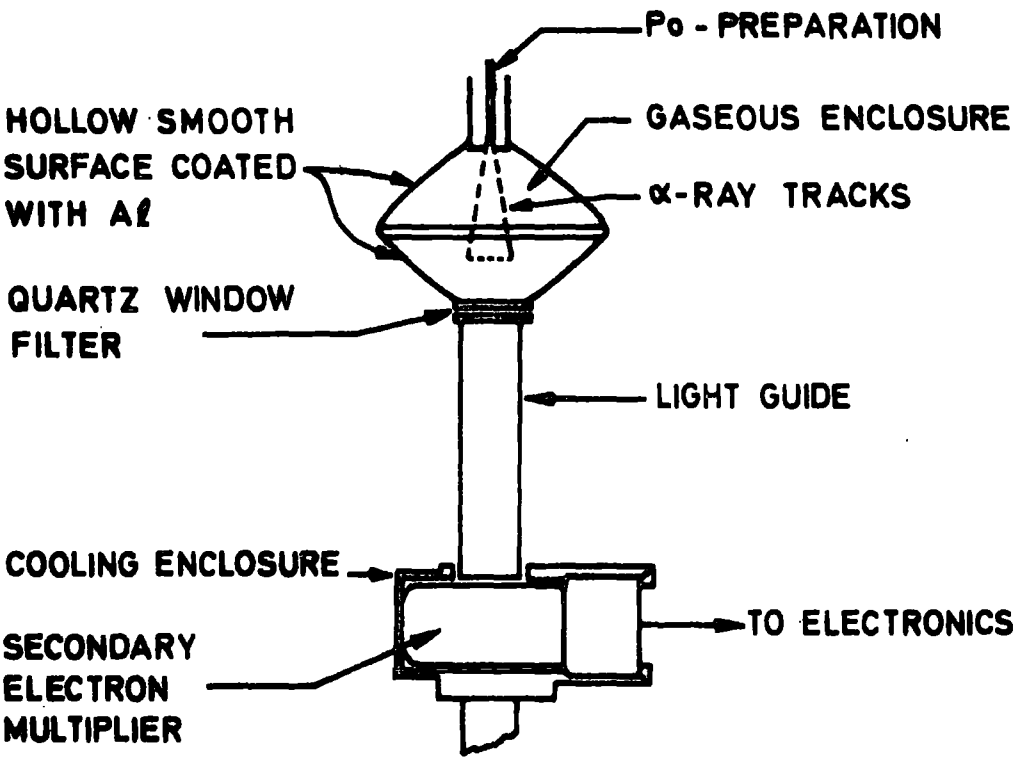

FIG. 2·10 Experimental arrangement for the first GSC by Grün and Schopper.

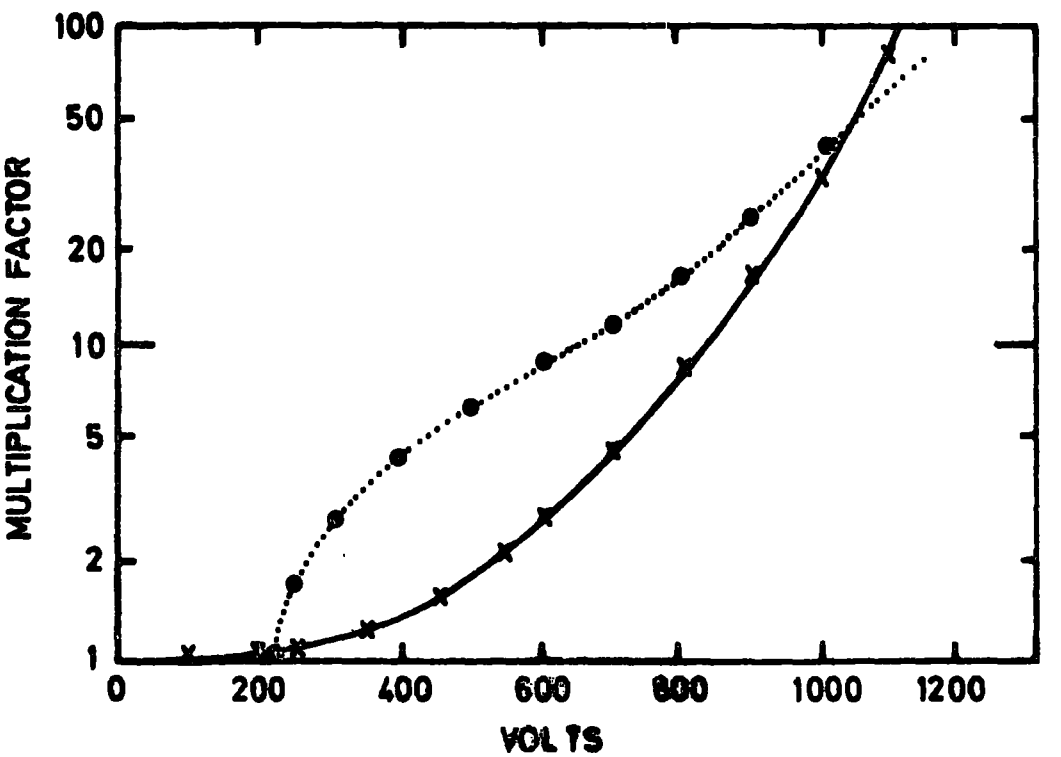

FIG. 2·11 Multiplication for electron pulses (solid-line) and for light pulses (dotted-line). Colli 1954.

counter, and also the light pulses from a photomultiplier, due to the same α-particles in argon. The increase of the multiplication factors (both, electrons and light) with the applied electric field is shown in Fig 2.11. The rise time of the light pulse was observed to decrease with increase of the gas pressure.

Charpak and Renard[40] (1956) used a proportional counter 25 cm long and 5 cm diameter with a photomultiplier at one side facing a thin aluminium window (0.02 mm). A positive electric field was applied to the central wire of the counter - see Fig 2.12a. The electric and light pulses were observed simultaneously from 90% Ar + 10% propane or 90% Kr + 10% propane at pressures between 30 and 75 cm Hg. The low energy X-ray line sources were used. A rise time of 2×10^{-7} sec was obtained with a 30% energy resolution for 5.9 keV X-rays. They showed that the light pulse amplitude was proportional to the X-ray energy. It was explained that the pulses were not due to ionized atoms, because the photomultiplier is not sensitive to the far ultraviolet light emitted by the ionized atoms of krypton, and the propane absorbs the major part of the excitation energy of the ionized atoms, hence the light emission was due to excited states of lower energies.

Koch[41] (1958) studied the influence of electric fields on scintillation pulses using Xenon at 74 cm Hg excited by 4.7 MeV α-particles. Fig 2.12b, shows the experimental arrangement used by her. The fast pure scintillation pulse of xenon was found to be followed by a secondary slower pulse whose amplitude increased with increase in the applied electric field. Since the scintillation pulses were observed at an applied field which is insufficient to produce electron multiplication, i.e. secondary ionization in the gas ; these pulses were attributed, as shown previously by Charpak and Renard[40], to excitation of the gas by electrons

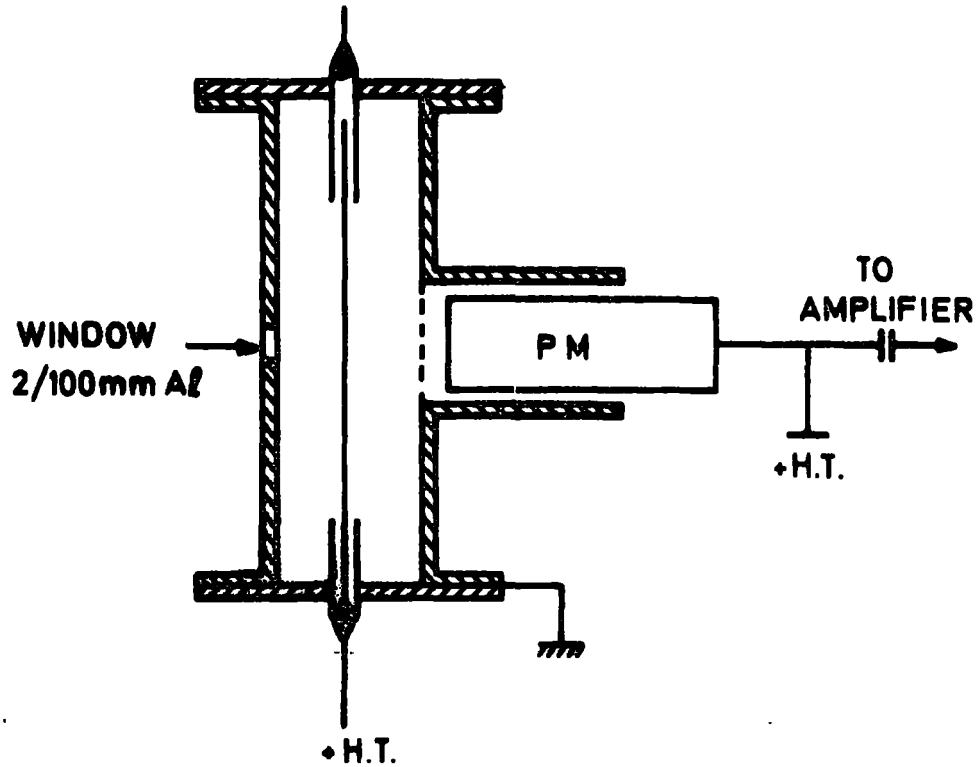

FIG.2·12a.GSC Used by Charpack and Renard.

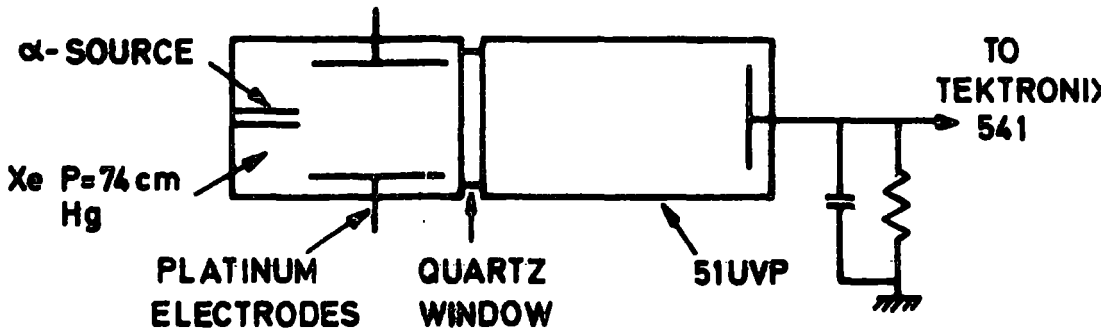

FIG.2·12b.GSC Used by Koch.

accelerated in the field. This was confirmed by Conde and Policarpo[42] (1960) using a cylindrical chamber. In their system, the electric field was applied between the central anode wire and the concentric cylindrical cathode. The gas used was argon with some nitrogen impurity and excitation was provided by an α-source.

Tavendale[43] (1961) observed a decrease in particle scintillation pulse-height in the presence of an electric field and this was attributed to a loss of recombination luminescence by ion collection. Szymanski[44] and coworkers (1963) investigated theoretically and experimentally the infleuence of electric field on the scintillations from rare gases and rare gases mixtures. A series of papers published by Teyssier et al[45] (1962-1967) was also concerned with the influence of electric field on scintillations from rare gases and rare gases mixtures. They used only α-sources to excite the gas scintillators. They assumed that gamma and X-rays, which gave a very small signal in Sayres and Wu's[3] experiment, would still only give a small signal even when a field was applied. They observed an increase in the pulse height with decreasing pressure in a xenon filled chamber[45e], a better energy resolution also obtained from this chamber compared to that from the argon filled chamber. The effect of adding nitrogen to argon on the light output was observed to reach a maximum at 6% nitrogen[45f].

A review of the work on gas scintillation counters up to 1974 has been given by Thiess and Miley[46].

2.6 CONSTRUCTION OF GAS SCINTILLATION COUNTERS

2.6.1 Introduction

The gas scintillation counter has undergone a series of major developments in its basic construction. It started as a gas scintillator in contact with a photomultiplier[29] as in Fig 2.10, then an electric field was applied in the gaseous region to increase the light output[30] - see Fig 2.12. The recent development in the GSC is the use of MWPC[47] or DC[48] in conjunction with a photomultiplier to form a gas scintillation proportional counter (GSPC) or a gas scintillation drift counter (GSDC).

As this work is concerned with the development of GSC's as high count rate detectors, a study of MWPC's was first carried out and then this was extended to GSPC's and GSDC's. The details of construction of MWPC's are given in Chapter four. The details of construction of GSPC's and GSDC's are given below. The reason for this is that in the following chapter, (a study of gas mixtures), some of the results were obtained using the GSDC. Hence it will be useful to look at the details of construction at this stage, firstly to compare them with the early chambers discussed in a previous section and secondly to enable results of the following chapter on gases, to be understood fully.

2.6.2 General Descriptions

The only restriction on the dimensions of both chambers was that they should be compatible with the RCA 8575 photomultiplier. The depth of the chamber was easily changed by inserting frames of the required thicknesses to increase the gas volume or to change electrodes separation values. Small size chambers do not suffer from serious problems due to wire displacement. This problem is only significant with larger chambers where special wire support systems are needed[49].

A screening box was made for the chambers to eliminate light and electrical pick-up. The box was made of 3 mm thickness aluminium plate and its size was 36 x 40 x 25 cm^3. The inside of the box was painted black and the edges of the box were covered with a wide black insulating tape. BNC sockets were fixed in one side of the box, where the chamber connections to the inside of the box and connections to the rest of the electronics were made from the outside without removing the lid. This produced minimum light exposure of the photomultiplier. The lid was provided with gaskets around the edges from the inside as well as black insulating tape from the outside. The box was well earthed and was connected from inside to the earthed electrodes of the chamber. Gas inlet and outlet were also made through the box - see Fig.2.13.

2.6.3 Gas Flow System

The argon-methane mixture was available commercially and its flow rate through the chambers was measured with G.E.C. Elliot Rotameter flowmeters which were calibrated for that gas mixture.

The other gas mixture used was argon and nitrogen which was required withvarious proportions of nitrogen. It was therefore mixed in the laboratory using flowmeters ; the main problem being the difficulty in controlling the small percentage of nitrogen required. A rotameter scale of 100-1000 cc/min, calibrated for the argon-methane mixture was converted into an argon scale by calibrating it against four argon flowmeters of range 10-100 cc/min connected in parallel. The nitrogen was flowing through a 10-100 cc/min argon scale, the factor of correction was obtained from the curve provided by the manufacturer. Another rotameter of range 4-40 cc/min was used for nitrogen, no correction was necessary for this scale. In general the gas flow rates were approximately 100 cc/min and pressures were only slightly above atmospheric pressure.

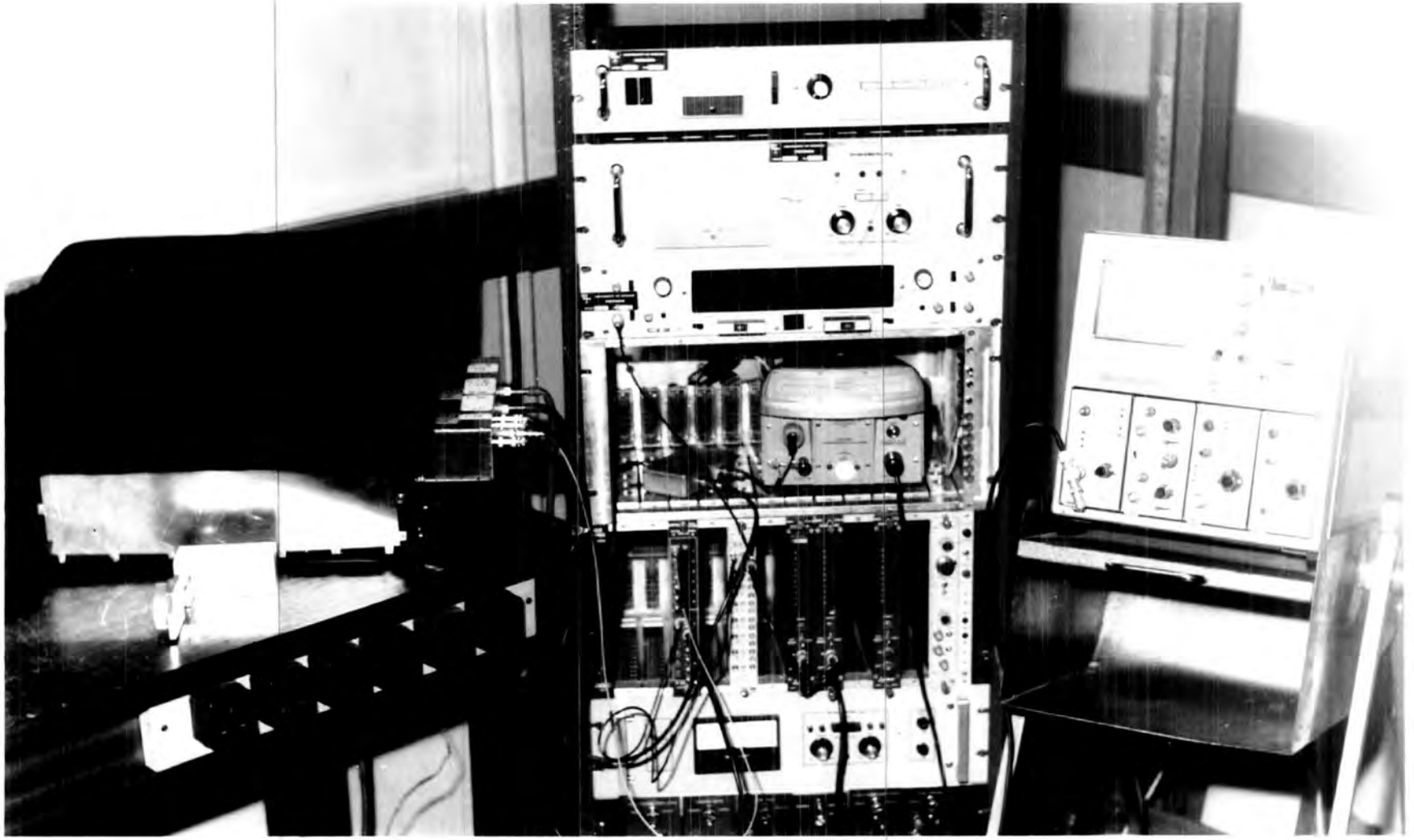

2.6.4 Gas Scintillation Proportional Counter

The GSPC was built from perspex frames covered on the inside with aluminized mylar sheets for better reflection. Fig 2.14a shows the arrangement of the frames. A multi-section chamber facilitates the replacement of broken wires but at the same time increases the probability of gas leak due to the requirement of many rubber gaskets between the frames. An O-ring shaped mylar sheet with an inner diameter less than the photomultiplier tube diameter was used to attach the photomultiplier to the frames using 3 M "Twinstick". Printed circuit boards were used for wire connections and araldite was used to fix the board on the edge of the perspex frames. Mylar windows were fixed using "Twinstick" which could be removed fairly easily for replacement purposes.

The wires were located by eye to the middle of the copper strips on the connecting board. The sense wires were 200 μm diameter nickel wires separated by 8 mm from each other. Large diameter anode wires were used to minimize the charge multiplication. The two cathode planes were made of parallel copper beryllium wires of 1 mm spacing and 125 μm diameter. The distance between the sense wire plane and the cathode planes was 6 mm on both sides. The distance between the first cathode plane (the upper one) and the grounded aluminized mylar window was 3 mm. The thickness of the window was 50 μm. A mesh of 96% transparency was made from 20 μm diameter copper wires with 1 mm separation in the x and y direction. The mesh was placed between the photomultiplier tube and the lower cathode plane, nearer to the tube. This grounded mesh provided an extra protection for the tube as well as a coupling for the lower cathode. Fig 2.14b shows the wires arrangement in the chamber and Table 2.5 summarizes the geometrical characteristics of the counter.

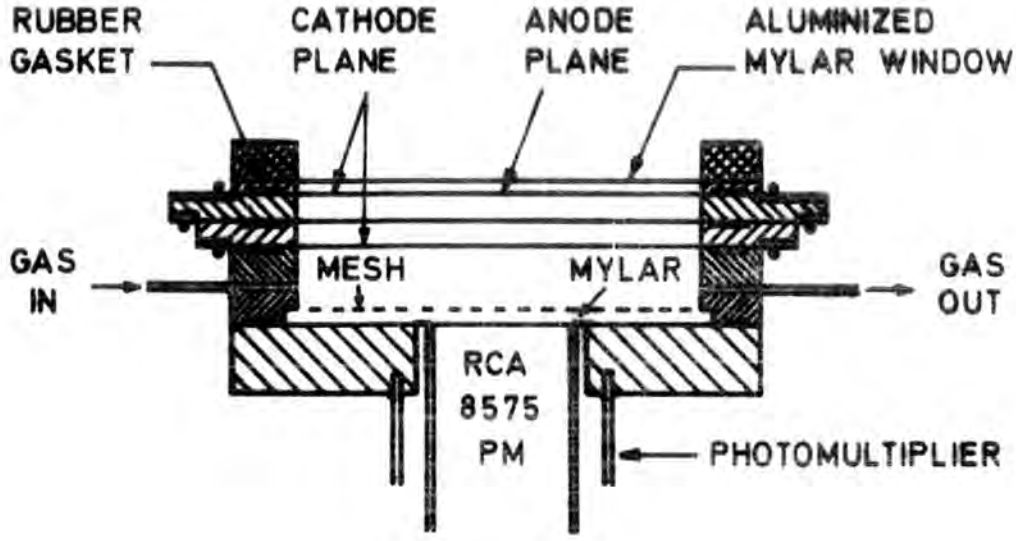

FIG.2·14a. GSPC General view.

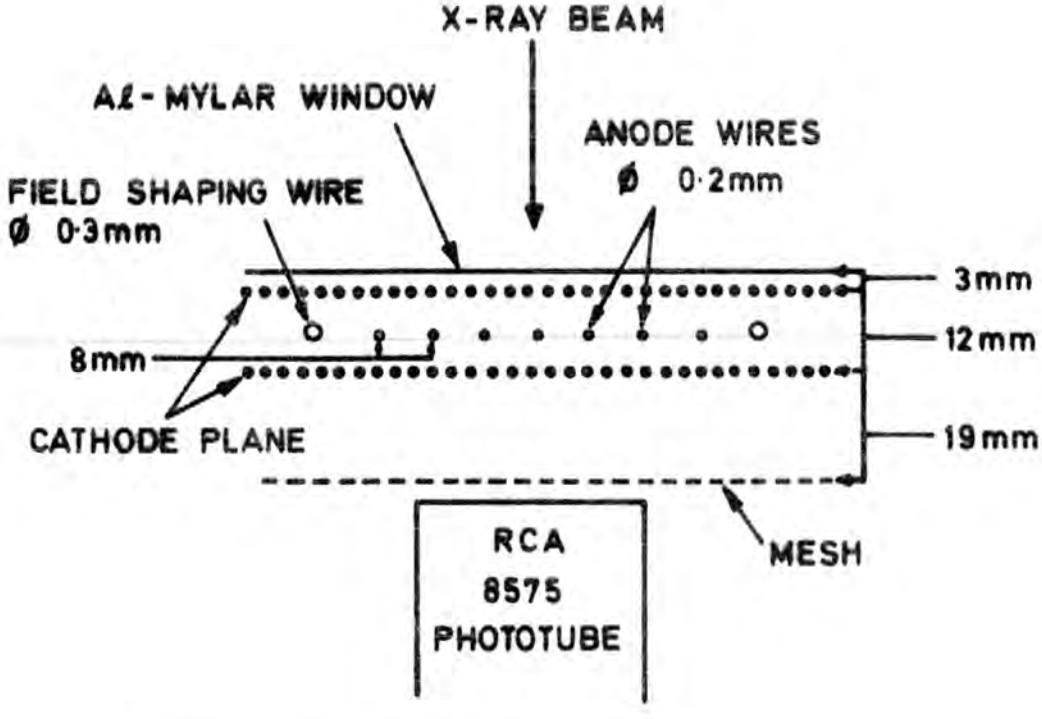

FIG.2·14b. GSPC Wire arrangement.

2.6.5 Gas Scintillation Drift Counter

The gas scintillation drift counter (GSDC) was built from perspex frames covered, as in the GSPC, from inside with aluminized mylar. The frame arrangement is shown in Fig 2.15a. A single frame for the sense wire and two cathodes, Fig 2.15b, permits good alignment of wires as well as a better gas tight system due to the use of fewer gaskets. Three holes were drilled on both sides of the frame for the sense wire and the two potential wires to go through. A travelling microscope was used for sense wire alignment with the corresponding two cathode wires above and below it. After connecting the three wires to the printed circuit boards at both sides, the three holes were filled with araldite to form a gas tight seal. A slot was cut in one side of the frame to be used as a side window for the source. 10 μm aluminized mylar was used to cover the slot. The top window, on a separate frame, was of 20 μm aluminized mylar. In certain tests, when an α-source was used, the top window was replaced by a thick earthed plate of aluminium (2 mm thickness) with a slot cut at the centre, the side facing the photomultiplier tube was covered with aluminized mylar, the collimated radioactive α-source was placed inside the slot so that the beam direction was normal to the cathode plane, Fig 2.15c.

The cathodes were 125 μm diameter copper wires separated by 2 mm from each other and by 4.5 mm from the anode plane. The sense wire in the anode plane was a 200 μm diameter nickel wire and the potential wires, of 125 μm diameter, were separated from the sense wire by 34 mm (in the same plane). A mesh, similar to the one used for the GSPC was made for this chamber. Fig 2.15c & d, show the wires arrangement and the potential divider network of the cathode plane. Table 2.5 summarizes the characteristics of the GSDC. Figs 2.16, 2.17 & 2.18 show a central frame, the chamber with the top window opened and the chamber assembled respectively.

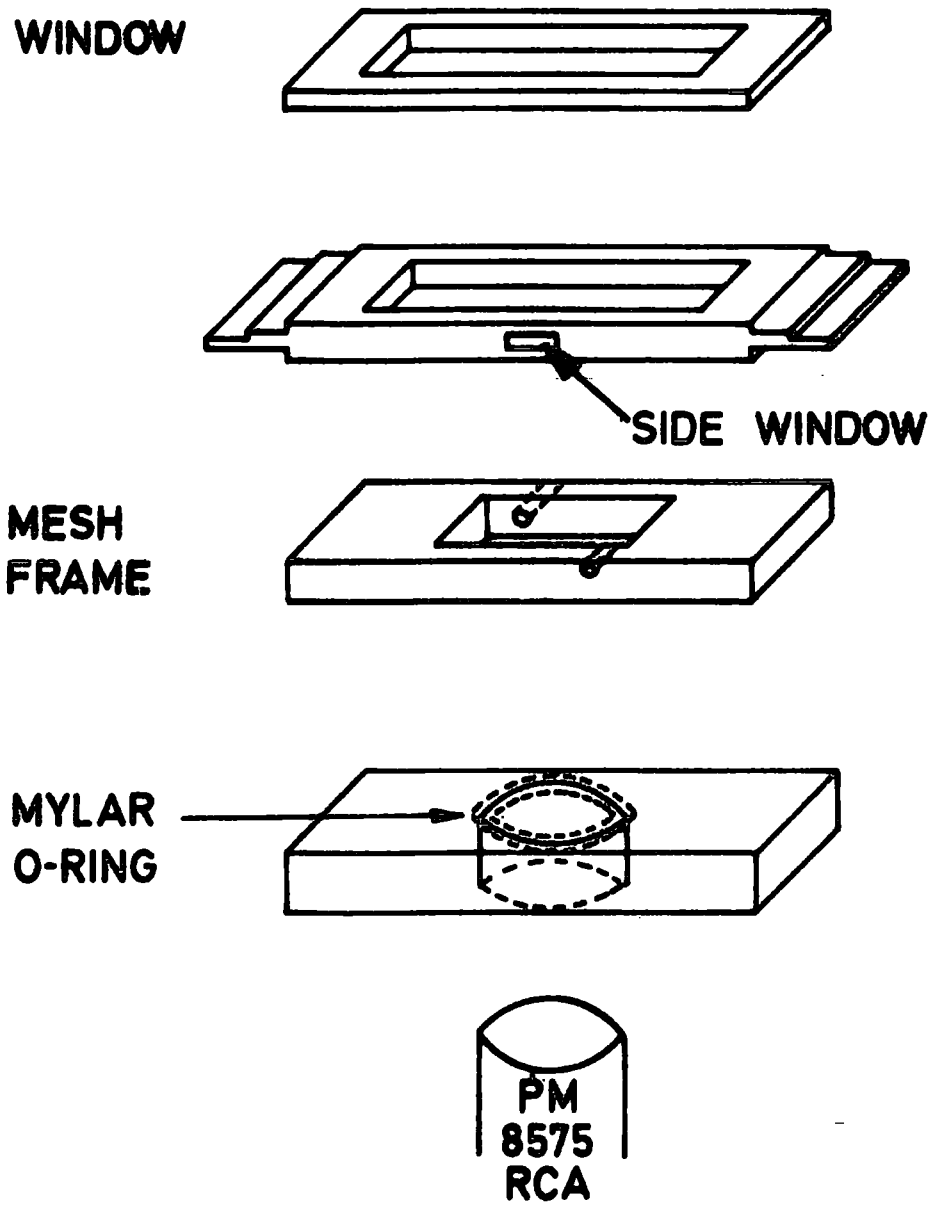

FIG. 2·15 a. GSDC Frame arrangement.

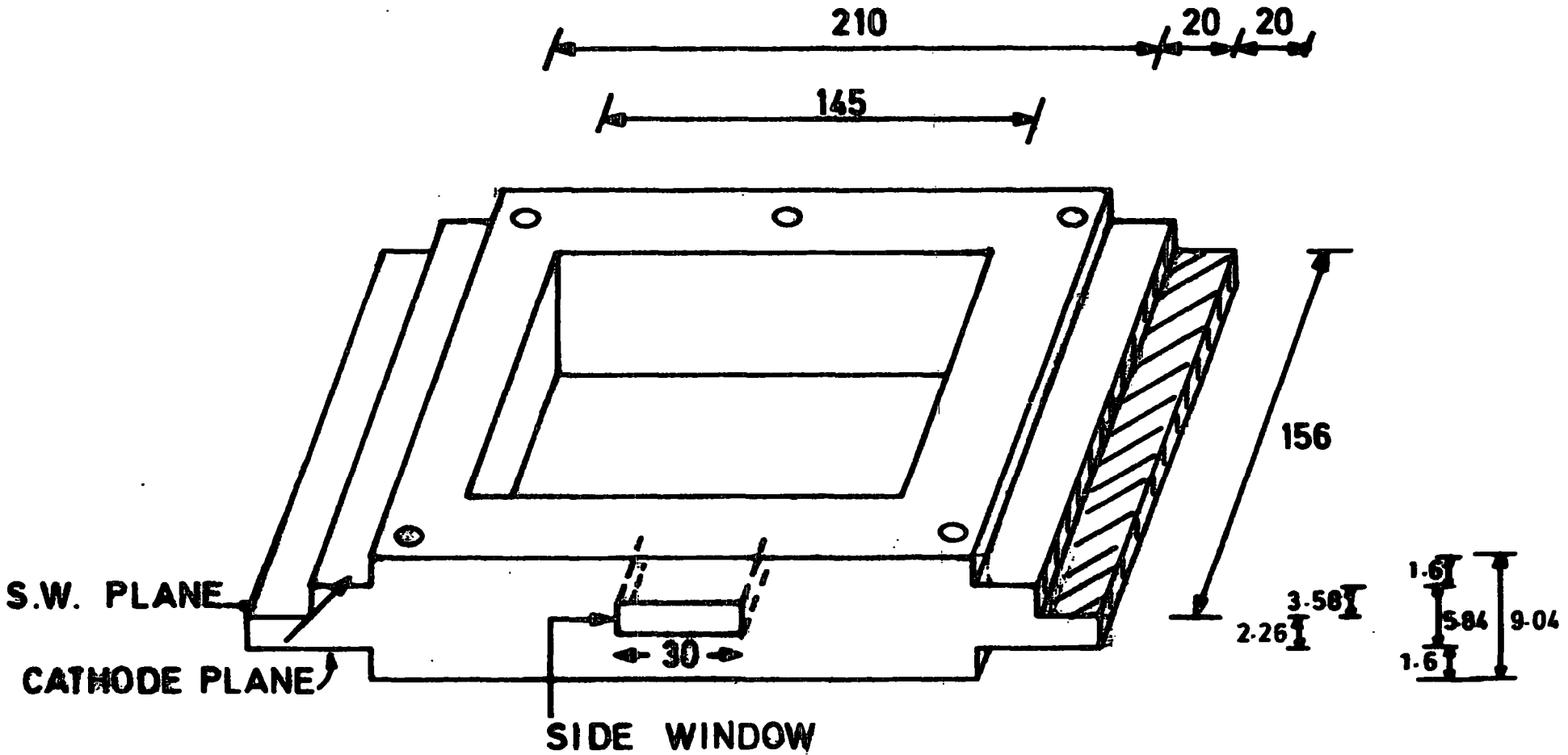

FIG. 2·15 b. THE SCHEMATIC DIAGRAM OF THE CENTRAL FRAME.

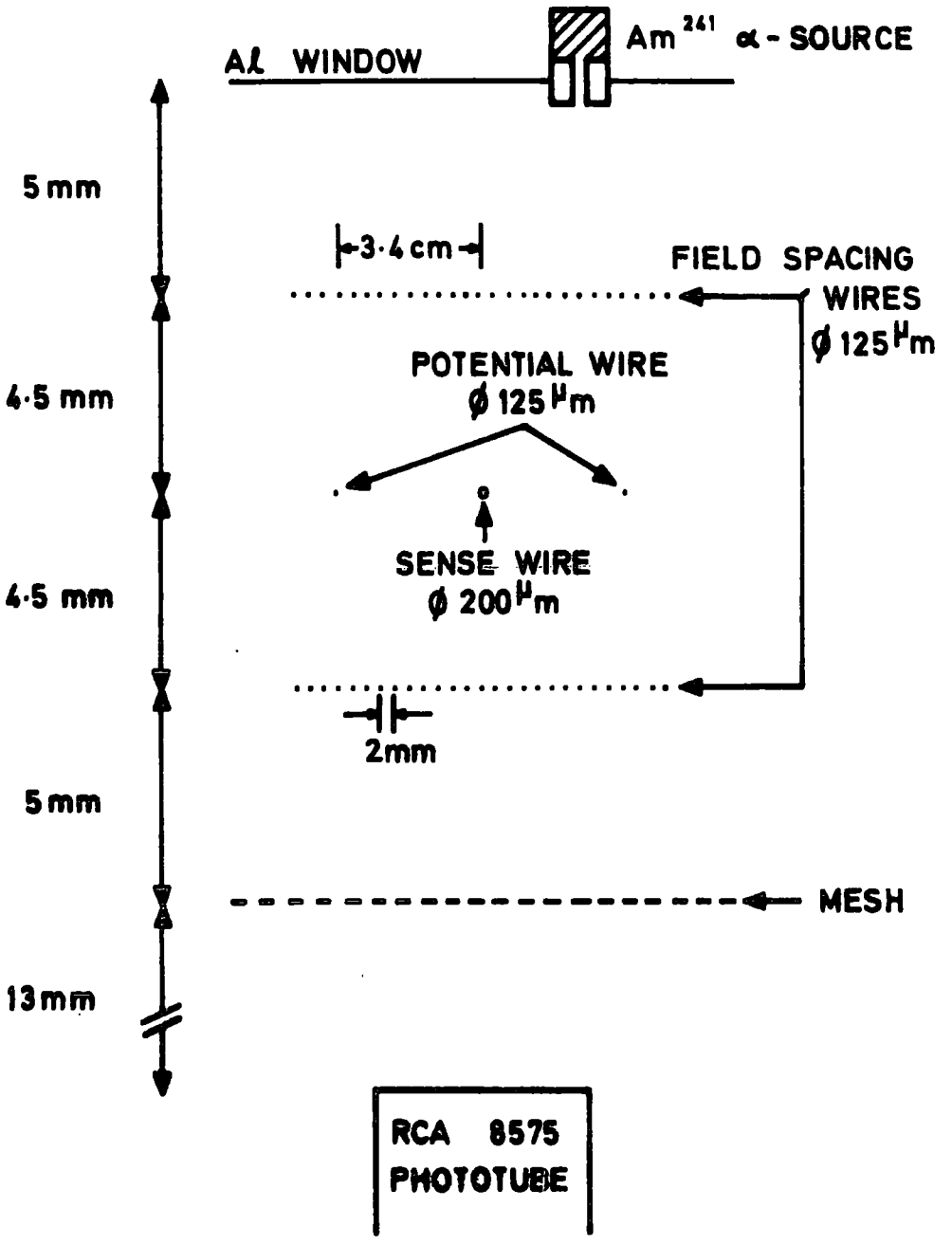

FIG. 2·15c. GSDC Wire arrangement.

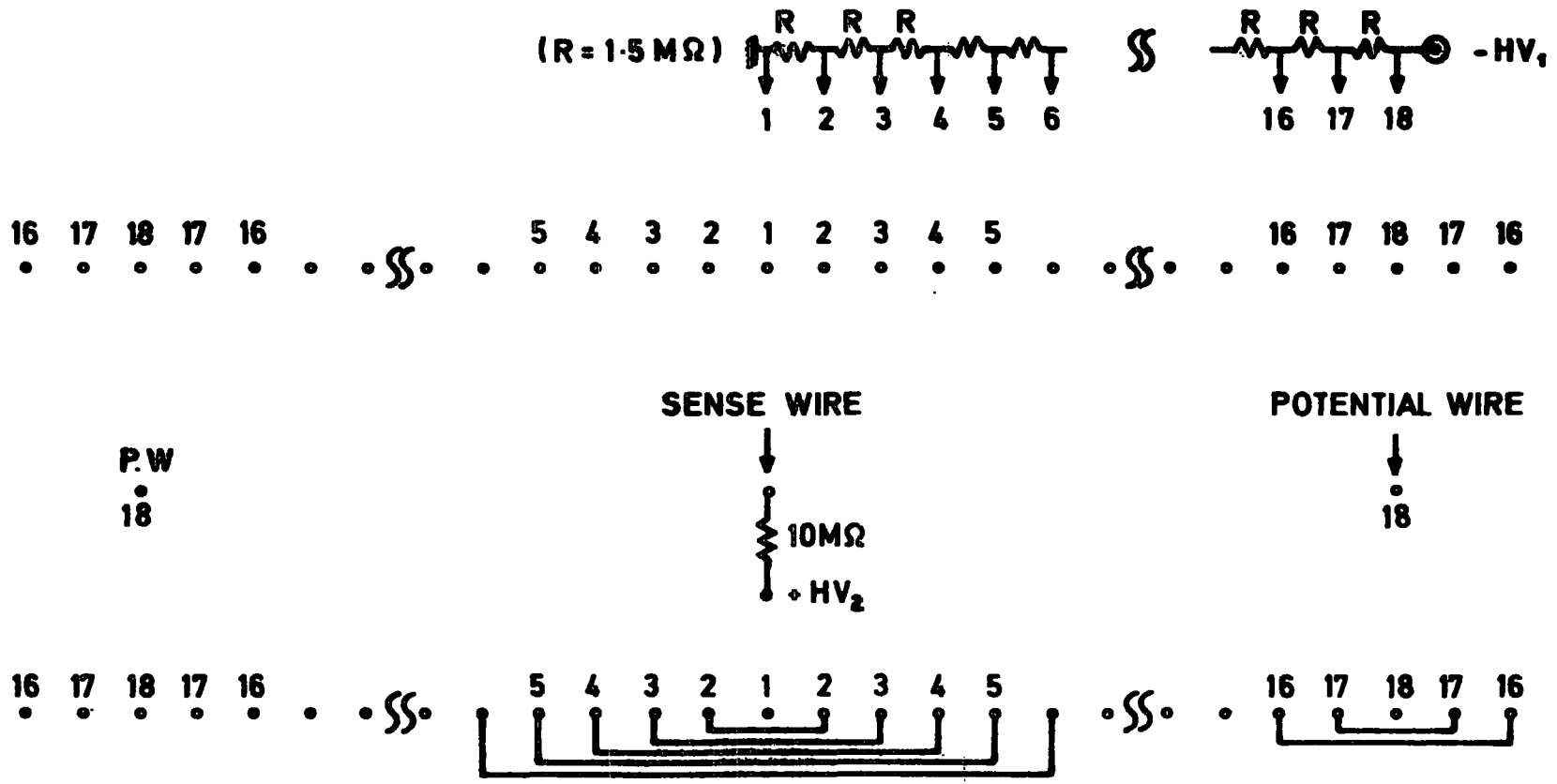

FIG. 2·15d. Resistor network and voltage distributor in drift chamber.

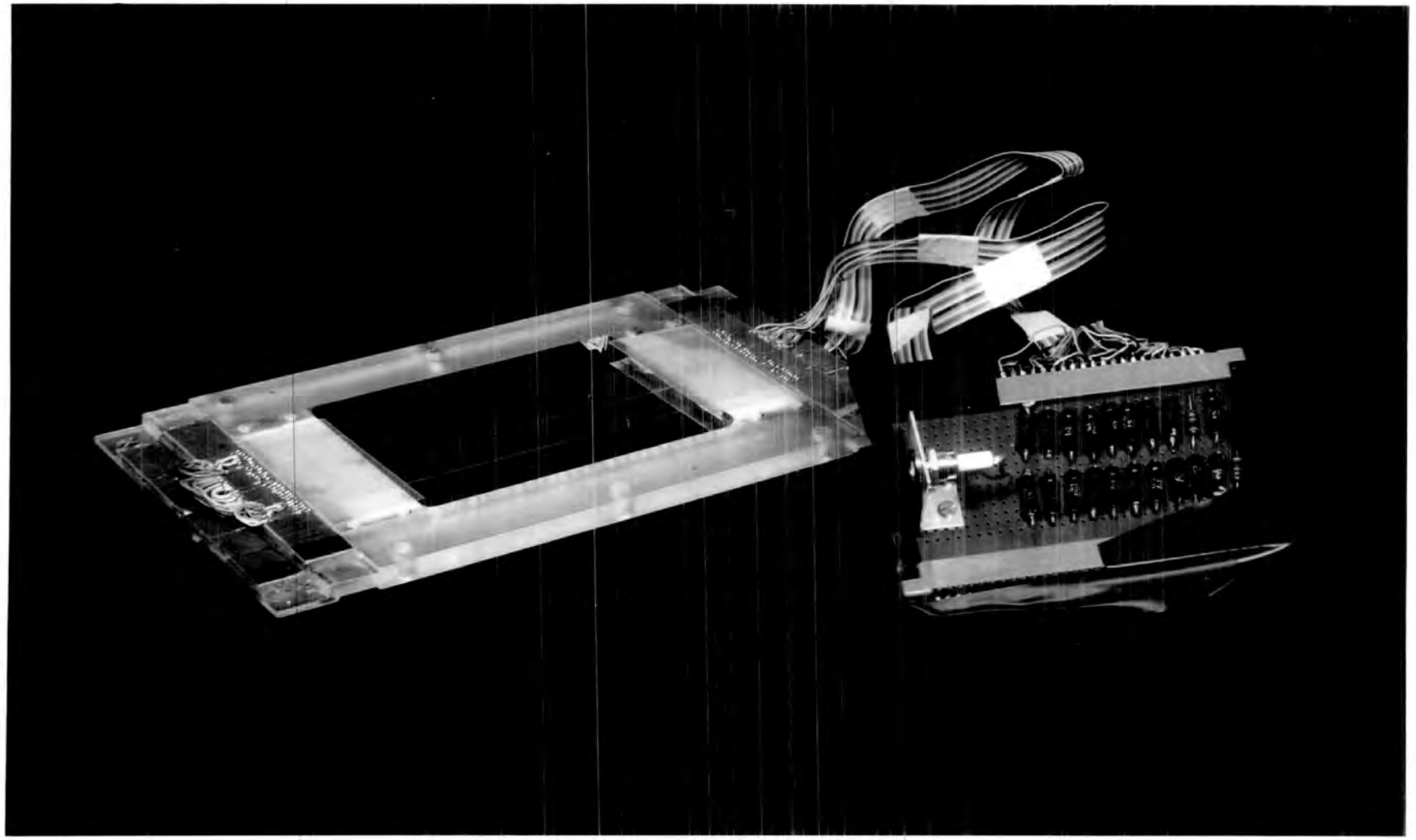

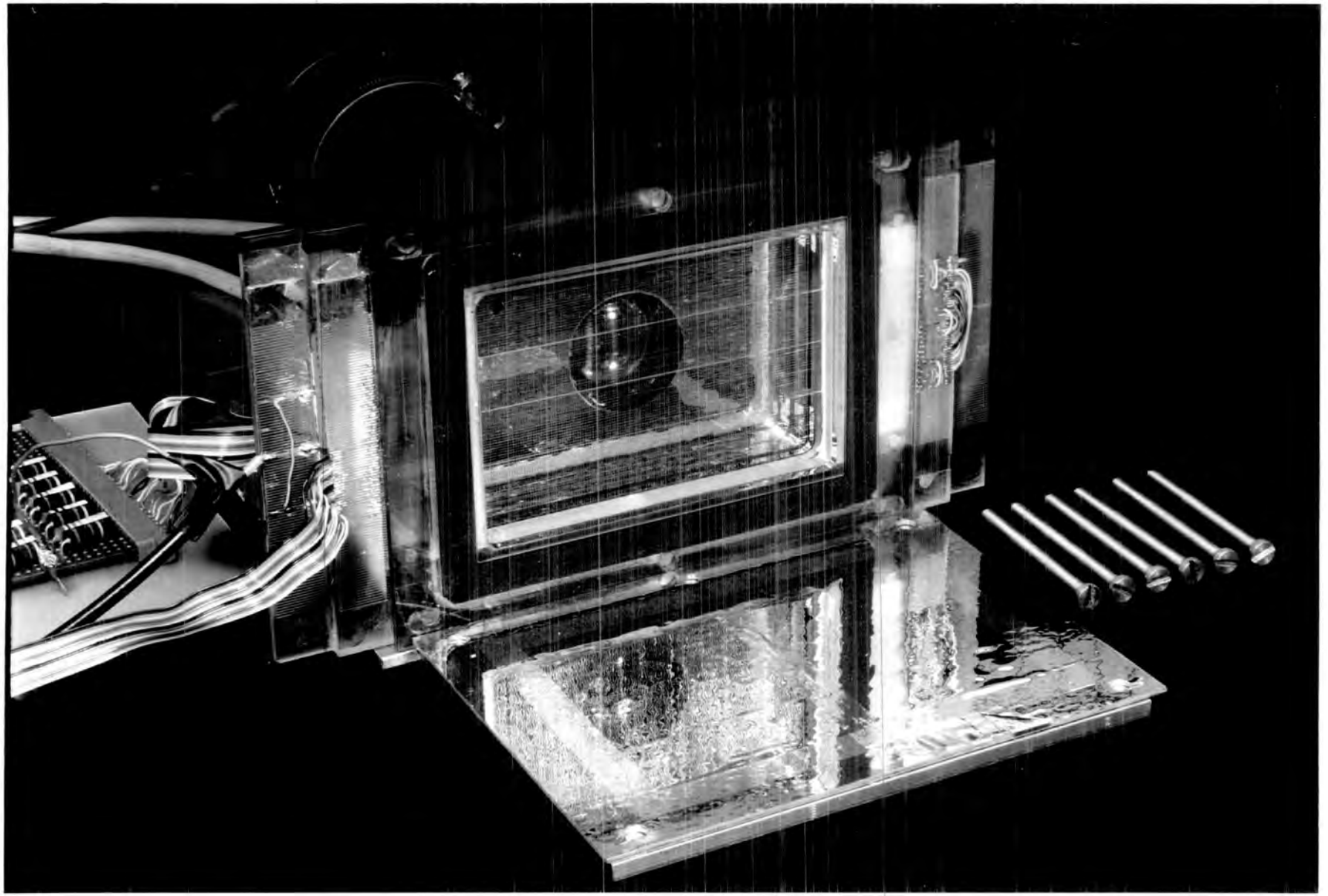

TABLE 2.5

The Geometrical Characteristics of GSDC and GSPC

	GSPC	GSDC	MATERIAL
The Cathode Plane			
Wire diameter	125 μm	125 μm	Copper
Wire spacing	1 mm	2 mm	
The Anode Plane			
S.W. diameter	200 μm	200 μm	Nickel
P.W. diameter (field shaping wires)	300 μm	125 μm	Copper
S.W. spacing	6 mm		
S.W.-P.W. spacing		34 mm	
Anode - Cathode separation	6 mm	4.5 mm	
The Mesh Plane			
Wire diameter	20 μm	20 μm	Copper
Transparency	96 %	96 %	
Windows			
Top	50 μm	20 μm	Aluminized mylar
Side	-	10 μm	" "
Active Area	5 x 5 cm^2	7 x 14.5 cm^2	

Chapter Two - References

1. S. Flügge (Ed), Encyclopedia of Physics (Springer-Verlag, Berlin, 1958), Vol. XLV.

2. R.A. Nobles, Rev.Sci. Instr. 27 (1956) 280.

3. A. Sayres & C.S.Wu, Rev.Sci.Instr. 28 (1957) 758.

W. Benett, V.Hughes and C.S.Wu, Progress Report: Nuclear Physics Lab, Columbia Univ. p 19 (1956).

4. A.J.P.L. Pollicarpo, C.A.N. Conde & M.A.F. Alves, Nucl.Inst. and Meth. 58 (1968) 151.

5. M.Alice et al, IEEE Trans on Nucl.Sci, NS-22 (1975) 109.

6. C. Eggler & C.M. Huddlestone, IRE Trans. Nucl.Sci. NS-3 (1956) 36.

7. L.R.Koller, Ultraviolet Radiation (John Wiley & Sons Inc. New York, 1965).

8. D. Engelkemeier, Rev.Sci. Instr. 27 (1956) 589.

R.L.Heath, IRE Trans. Nucl.Sci. NS-9 (1962) 294.

9. J.H. Hopkins, Rev. Sci. Instr. 22 (1951) 29.

10. G.A.Morton, Nuclear Electronics, Vol.I, Proceedings of the International Symposium on Nuclear Electronics, Paris, (1958) IAEA.

11. W. Van Sciver, Nucleonics 14 No.4 (1956) 50.

12. E. J. Schneid, E. A. Kamykowski & F.R. Swanson, IEEE Trans-on Nucl. Sci. NS-24 (1977) 168.

13. G. G. Kelly and M. Goodrich, Phys. Rev. 77 (1950) 138.

14. A.E. Grün and E. Schapper, 2. Naturfarschg. 9a (1954) 134.

15. CRC Handbook of Chemistry and Physics 58th Edition, (CRC Press, Inc. Ohio, 1977-1978).

16. J. B. Dance, Photoelectronic devices (Illiffe Books Ltd., London, 1969).

17. A.H.Sommer, Rev. Sci. Inst. 26 (1955) 725.

18. J. Sharpe & E.E.Thompson, Proc. Geneva Conf. on Peaceful Uses of Atomic Energy ; EMI Electronics Ltd. Rpt. CP.154(1958).

19. A. J. Parsons, E.M.I. Document R/P064 (1977).

20. A. G. Wright, E.M.I. Document R/P065 (1977).

21. R. D. Corner & M.K. Husain, Nucl. Inst. & Meth 6 (1960) 337.

22. A. K. Gupta & N. Nath, Nucl. Inst. & Meth 53 (1967) 352.

23. R. B. Galloway & D. G. Vass, Nucl. Inst. & Meth. 49 (1967) 55.

24. C. Weitkamp et al, Nucl. Inst. & Meth 61 (1968) 122.

25. S. Al Dargazelli, T. R. Ariyaratne & B.C. Nandi, Durham University, Internal Report. N1-78-2 (1978).

26. R.C.A 8575 Data Manual.

27. A. Fenster et al, Rev. Sci. Inst. 44 (1973) 698-94.

28. C. R. Kerns, IEEE Trans on Nucl. Sci. NS-24(1977) 353.

29. R. A. Audubert and S. Lormeau, C. R. Acad. Sci. 228 (1949) 318.
S. Lormeau, C. R. Acad. Sci. 230 (1950) 956.

30.a A.E.Grun and E.Schopper, Z. Naturforschg. 6a (1951)698.

b A.E.Grun, Z. Naturforschg. 9a (1954) 55.

c ~~A.E.Grun & E. Schopper, Z. Naturforschg. 9a (1954) 134~~.

d A.E.Grun, Z. Naturforschg, 9a (1954) 1017.

31. C.O.Muehlhause, Report BNL-242 (T-38) (1953)
" , Nucleonics, 14 (1956) 38.

32. C. Eggler & C.M.Huddleston, Phys. Rev. 95 (1954) 600.
" , Nucleonics, 14 (1956) 34.

33. J. A. Northrop and J.C.Gursky, Nucl. Inst. 3 (1958) 207.

34. J. A. Northrop and R. Nobles, Nucleonics, 14 (1956) 36.

35. G.P. Boicourt and J.E.Brolley, Jr., Rev.Sci.Inst. 25 (1954) 1218.

36. J.E.Simmons & R.B.Perkins, Rev.Sci.Inst. 32 (1961) 1173.

37. J.R.Kane, R.T. Siegel and A. Suzuki, Rev. Sci. Inst. 34 (1963) 817.

38. E. Segre and C. Wiegand, UCRL 2152 (1953).

39. L. Colli, Phys. Rev. 95 (1954) 892.

40. G. Charpak and C.A.Renard, J.Phys. Radium 17 (1956) 585.

41. L.Koch, Nucl. Electronics Proc. Symp. Paris (Vienna IAEA) Vol. 1 (1958) 151.

L. Koch and R. Lesneur, J. Phys. Radium 19 (1958) 103.

L. Koch, J. Phys. Radium 21 (1960) 169.

" , Acta Electronic 5 (1961) 103.

42. C. A. N. Conde and A.J.P.L.Policarpo, Diploma Report, University of Manchester (1960).

43. A.J.Tavendale, Rev. Sci. Inst. 32 (1961) 1398.

" , Proc.Phys.Soc. 79 (1962) 652.

44. A. Szyinanski and J.A. Herman, J. Chim. Phys. 60 (1963) 379.

45.a J.L. Teyssier et al, Rev. Sci. Instr. 10 (1962) 1128.

b " , C.R.Acad. Sci. Paris 257 (1963) 2458.

c " , J. de Physique, 24 (1963) 55.

d " , Electronique Nucleaire, European Nuclear Agency (1964) p 43.

e J.L. Teyssier et al, Nucl. Inst. & Meth 30 (1964) 331.

f " , C.R.Acad. Sci, Paris 260 (1965) 1614.

g " , Nucl. Instr. & Meth. 33 (1965) 359.

h " , C.R. Acad. Sci.Paris, 262 (1966) 417.

i " , J. de Physique, 28 (1967) 427.

46. P.E. Thiess and G.H. Miley, IEEE Trans. on Nucl. Sci. NS-21 (1974) 125.

47. C.A.N. Conde and A.J.P.L. Policarpo, Nucl. Inst. & Meth. 53 (1967) 7.

48. G. Charpak, Majewski & Sauli, Nucl.Inst.& Meth. 126 (1975) 381.

49. G.C.Smith, Ph.D Thesis, Durham University, 1973.

CHAPTER THREE

EXCITATION, IONIZATION AND DRIFT

3.1 INTRODUCTION

The pulse formation principles are the same in MWPC's, DC's and GSC's and can be divided into three main parts:

(i) The passage of an ionizing particle through the gas causing initial excitation and ionization due to inelastic collisions.

(ii) The drift of the liberated electrons under the influence of the applied field towards the positive electrode.

(iii) The multiplication process near the positive electrode due to the high field around it.

This chapter is concerned with the first two parts. The third is discussed in Chapter 4. Each of the first two parts deals with the process in pure gases and in gas mixtures and the phenomena which accompany each process. The experimental measurements of the drift velocity, using a GSC, are given for different argon-nitrogen mixtures.

3.2 EXCITATION AND IONIZATION

3.2.1 Initial Processes

The particles passing through the gas lose energy by collisions with the gas molecules. The slowing down of the incident particles gives rise to excitation and ionization of the gas molecules. The ejected electrons, usually referred to as δ rays, can have enough energy to produce further ionization and therefore secondary ion pairs (n_s) are produced. The primary ionization and the total ionization, which is the sum of the two contributions, have been measured for most gases[1]. It was found that the number of primary ion pairs produced per cm (n_p) is a linear

function of the average atomic number of the gas, with the exception of xenon. The total number of ion pairs produced per cm (n_T) can be expressed as follows

$$n_T = \frac{\Delta E}{W_i} \quad \frac{(\text{keV/cm})}{(\text{keV})} \tag{3.1}$$

where ΔE is the total energy loss in the gas volume and W_i is the effective average energy to produce an ion pair ; ΔE is usually obtained from the Bethe and Bloch[2] relation for the average differential energy loss per unit length (dE/dx).

Table 3.1 gives some properties of pure gases and gas mixtures commonly used. Energy loss and ion pairs per unit length are given at atmospheric pressure for minimum ionizing particles[1]. The values of n_T and n_p were calculated making use of the following general formula

$$n = n_A a_1 + n_B a_2 + \ldots \tag{3.2}$$

where a_1 and a_2 are the percentages of gas A and gas B. The last column in Table 3.1 gives the number of secondaries produced for each primary, where $n_s = n_T - n_p$. The reciprocal of n_p gives the average distance between primary interactions under normal conditions, for example, for pure argon it is 340 μm whereas for xenon it is 227 μm, which makes xenon superior in producing secondaries for each primary.

TABLE 3.1

Gas	Z	I_o (eV)	W_i (eV)	ΔE (keV)	n_p $\left(\frac{\text{ion pairs}}{\text{cm}}\right)$	n_T $\left(\frac{\text{ion pairs}}{\text{cm}}\right)$	$\frac{n_s}{n_p}$
N_2	14	15.5	35	1.96	10	56	4.6
Ar	18	15.8	26	2.44	29.4	94	2.2
Kr	36	14.0	24	4.6	22	192	7.7
Xe	54	12.1	22	6.76	44	307	6.0
CO_2	22	13.7	33	3.01	34	91	1.7
CH_4	10	13.1	28	1.48	16	53	2.3
Gas mixtures using eq. 3.2							
90% Ar + 10% CH_4					28.1	89.8	2.2
90% Ar + 10% N_2					27.5	90.1	2.3
48% Ar + 48% N_2 + 4% CO_2 (3)					20.3	75.6	2.7
99% Xe + 1% N_2 (4)					43.7	304.5	6

Comparing the energy required to produce an ion pair in any gas (W_i) with the ionization potential (I_o) in Table 3.1, it is obvious that only about half of W_i is required to produce an ion and most of the rest of W_i is spent in exciting atoms, ions or molecules. These usually return to the ground state through a radiative process.

3.2.2 The Gas Mixture

The choice of the gas mixture in a chamber is determined mainly by the type of information required from that chamber. In one part of the work, position localization of the incident particle was needed; this required a mixture in which the drift velocity of electrons was approximately independent of the drift field. In other parts of the work, a high light emission was required.

The gases used in counters are usually rare gases or their mixtures. The main reasons for this are first because they are inert to most other elements and compounds so they do not form negative ions by electron attachment. This is due to their outer most shell being fully occupied. They all have valence shells which are closed octets designated $ns^2\ np^6$, except for helium which has a duet ($1\ s^2$). The second reason is the high light output which makes them very useful as gas scintillators. Table 3.2 gives some of the characteristics of rare gases. It is evident that the ionization (and excitation) energies[5] decrease on going down the table because the outer shells are farther away from the nucleus.

TABLE 3.2

Gas	Z	Lowest excited energy levels "metastable" (eV)		Resonance Potential (eV)	Ionization Potential (eV)		Ionization cross section $cm^2 x10^{-17}$	Light output
					1st electron	2nd electron		
He	2	19.81	20.61	21.13	24.59	54.4	3.1	110
Ne	10	16.61	16.71	16.84	21.56	41.07	6.8	80
Ar	18	11.55	11.75	11.83	15.76	27.62	36	95
Kr	36	9.77	10.52	9.99	14.0	24.56	51	200
Xe	54	8.315	-	8.44	12.13	21.21	75	350
Rn	86	6.77	-	6.94	10.75	21.4	-	-
N	7	2.38	-	10.3	14.54	29.60	-	-

The lowest excitation potential[5] are listed as metastable due to their long life times (greater than 10^{-6} sec) compared to those of an excited state for which the return to the ground state, by the emission of a photon in a time of about 10^{-8} sec, occurs without violating any of the selection rules (resonance). The consequences of metastables are the following : ionization can occur by collision with an electron which does not have enough energy to ionize an atom in its ground state ; also in the case of a gas mixture, the metastable atoms of one gas may ionize the atoms of the other gas by the Penning effect. For example, metastable neon (16.6 eV) can ionize argon (ionization potential 15.76 eV). In other collision processes metastables can transfer their energy to emission levels of the second gas which are very close energetically. In this manner an increase in the light emission can occur. Both the ionization cross-section[5] and the light output[6] increase with increasing Z as the ionization and excitation energies decrease. The light output listed in the last column of Table 3.2 was obtained from the number of photoelectrons ejected, due to α-ray bombardment. The resonance radiation of all the inert gas elements occur in the far ultraviolet region[7]. The discussion on the light emission from rare gases and their mixtures will be limited in the coming section to argon only, because it is the gas used throughout the work. Argon provides reasonable light output and ionization probability as well as being readily available commercially at a low cost of about £30. a bottle.

3.2.3 Light Emission from Argon and Argon Mixtures

The light emission of pure argon and argon mixtures were investigated by Strickler and Arakawa[8]. Alpha particle bombardment was used to excite the argon. The general features of the emission spectrum of argon at a pressure 80 cm Hg were observed to have a broad continuum which extends from the short wavelength limit of the quartz window 1100 Å up to about 2800 Å. This continuum is pressure dependent. It was distinguished by

(a) a rapid increase in the intensity of the emission between 2000 and 2800 Å as the pressure increased,

(b) the intensity of light between 1700 and 2000 Å remaining fairly constant from 20 to 80 cm Hg total pressure,,

(c) the intensity between 1700 and 2000 Å beginning to increase with pressure above 80 cm Hg.

The addition of a second gas to argon affects the ionization current and the light emission. This can be explained as follows. Two of the excited states of argon are at approximately 11.5 and 14.5 eV[8] (see Fig 3.1[9]). A second gas whose ionization potential is lower than 11.5 eV causes a large increase in the total ionization. Gases whose ionization potentials were between 11.5 and 14.5 eV produce a lesser but significant increase in ionization, e.g. I_o for methane is 13.1 eV, as given in Table 3.1, However, gases whose ionization potentials were higher than 14.5 eV, as in the case of nitrogen (I_o = 15.5 eV), produce no change in ionization. On the other hand, N_2 exciation levels are near the Ar-11.7 eV level, so light emission occurs. Hence the transfer of energy between argon atoms and the second gas atoms increases the observed ionization current or light emission according to the second gas energy levels.

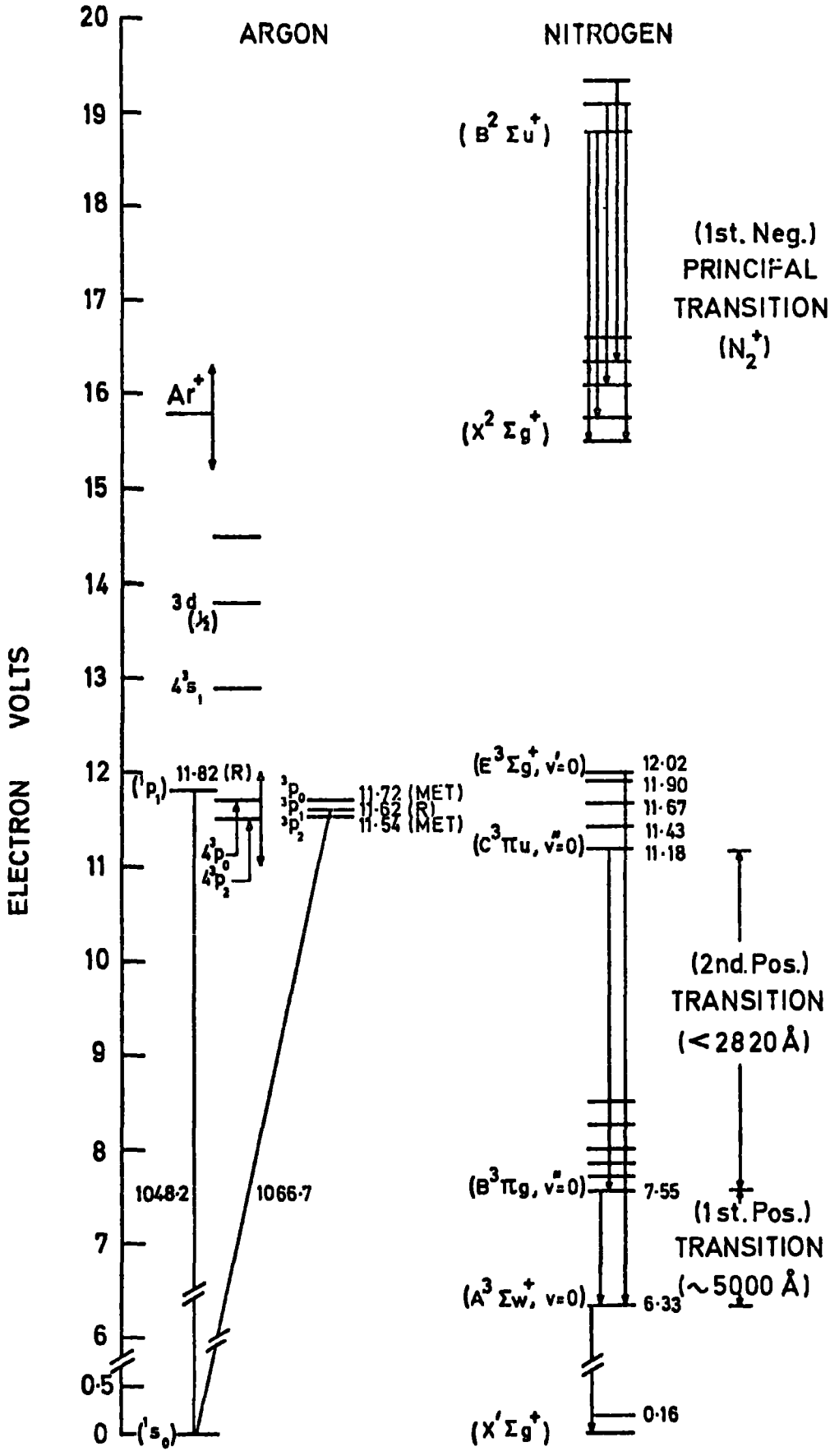

FIG. 3·1 Some energy levels in the argon atom and in the nitrogen molecule.

The effect of adding a second gas on the argon continuum is illustrated in Figs 3.2 and 3.3, and can be accounted for by the same argument. The intensity of the argon continuum has been plotted for several different concentrations of the second gas which is either methane or nitrogen. In the case of methane, shown in Fig 3.2, there is a rapid decrease in intensity of the continuum by more than a factor of 10 with the addition of only 1% of methane. In the case of nitrogen, its presence quenches the argon continuum and gives rise to the emission of new lines in the spectrum. Fig 3.3a shows the quenching of the argon continuum by nitrogen, at low percentages of nitrogen. Fig 3.3b shows the spectrum from 1600 Å to 4300 Å for a mixture of argon with 0.1% N_2. The new lines appearing in this case were attributed[10] to the second positive group of nitrogen, shown in Fig 3.1[9], and the lines originate from energy levels between 11 and 12.5 eV. Fig 3.4[8] shows the changes in the intensity of the 2200 Å argon band and that of 3380 and 2360 Å nitrogen bands as the percentage of nitrogen increases. While the intensity of the 2200 Å argon band falls off, the intensity of the 3380 Å line in N_2 increases as N_2 is added, up to a concentration of about 3% N_2. With further increase in the concentration of N_2, the intensity of the second positive group (3380 Å) begins to decrease. The lines at 2240, 2360, 2490 and 2600 Å first appear at about 3% N_2 and gradually increase in intensity with increasing N_2 concentration until they reach a maximum intensity in pure nitrogen as shown in Fig 3.3c. The reasons for the effect of nitrogen percentages on the light emission is given in the next section with the discussion of energy transfer.

To summarize the effect of adding a second gas to argon, it is evident that the addition of methane increases the ionization current, as well as quenching the argon continuum. The addition of small quantities

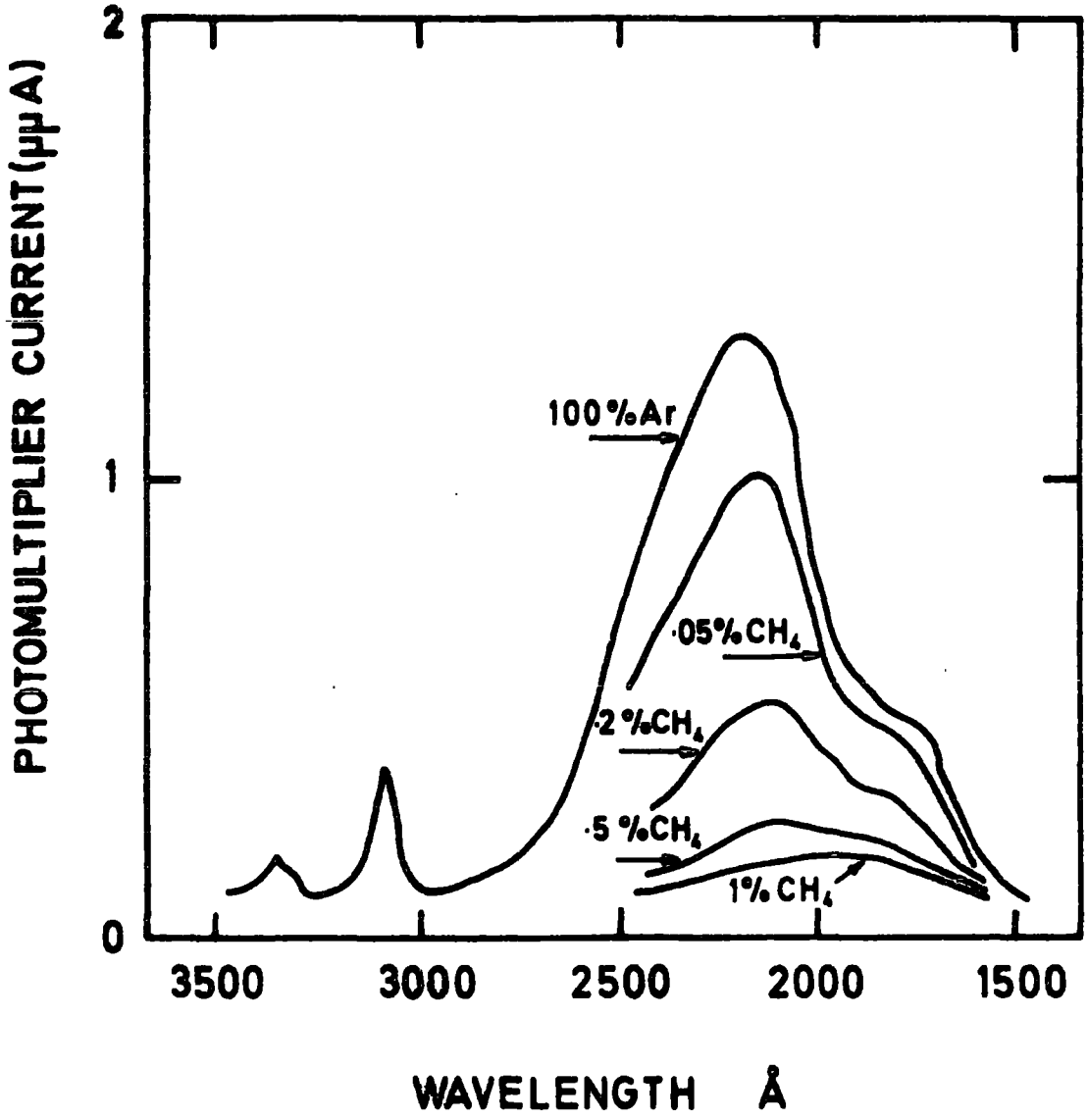

FIG. 3·2 Quenching of argon continuum by CH_4

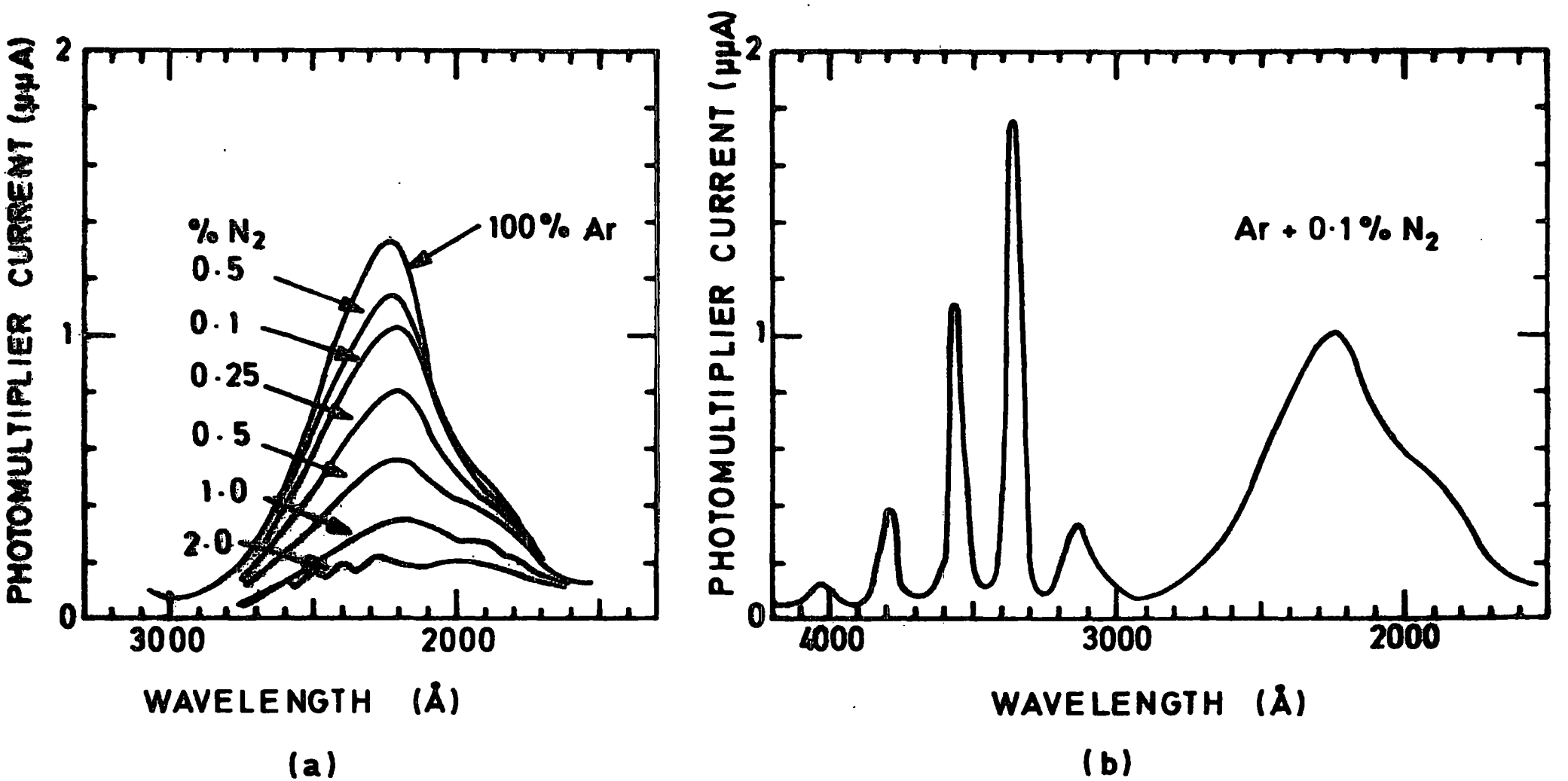

FIG. 3·3 Quenching of argon continuum by N_2.

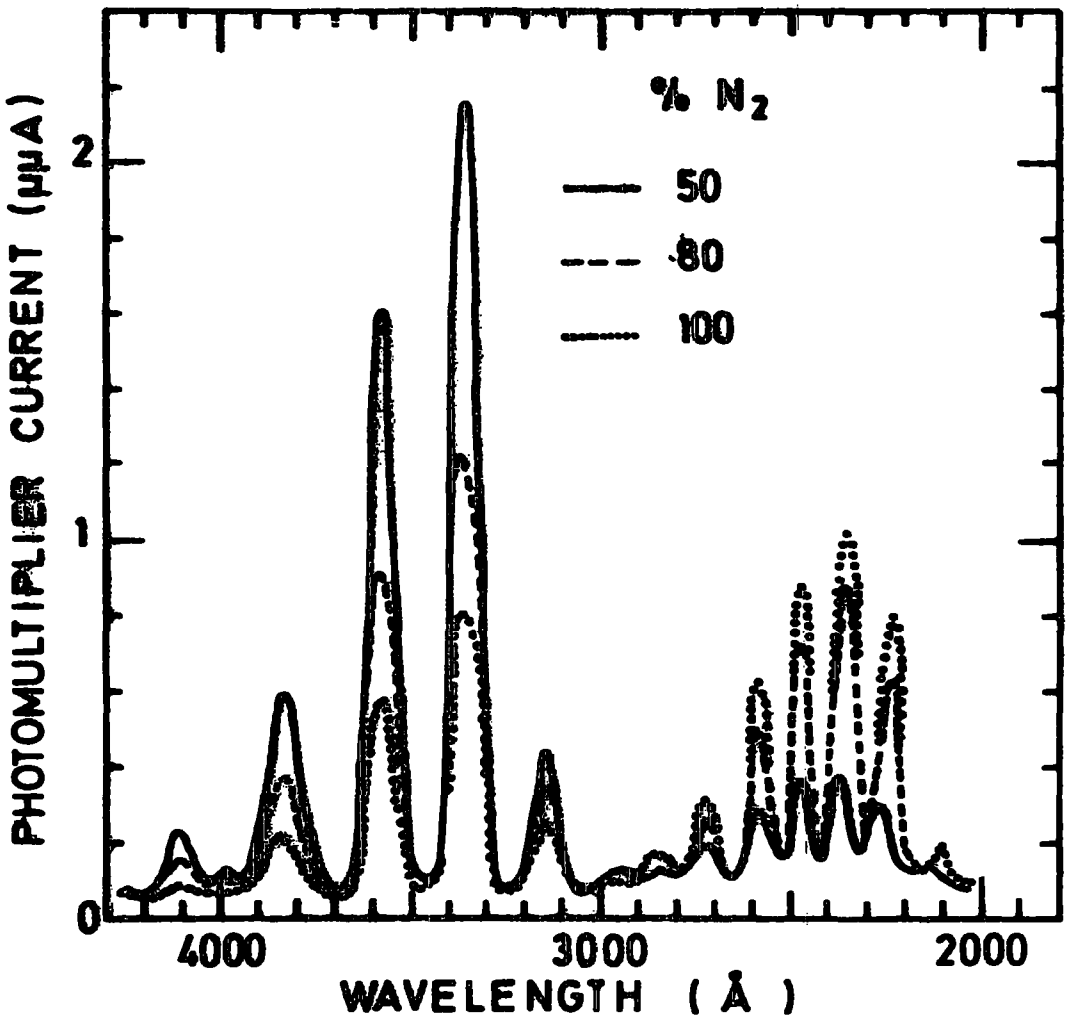
% N2
50
80
100
PHOTOMULTIPLIER CURRENT (μμA)
2
1
0
4000
3000
2000
WAVELENGTH (Å)

FIG. 3·3c

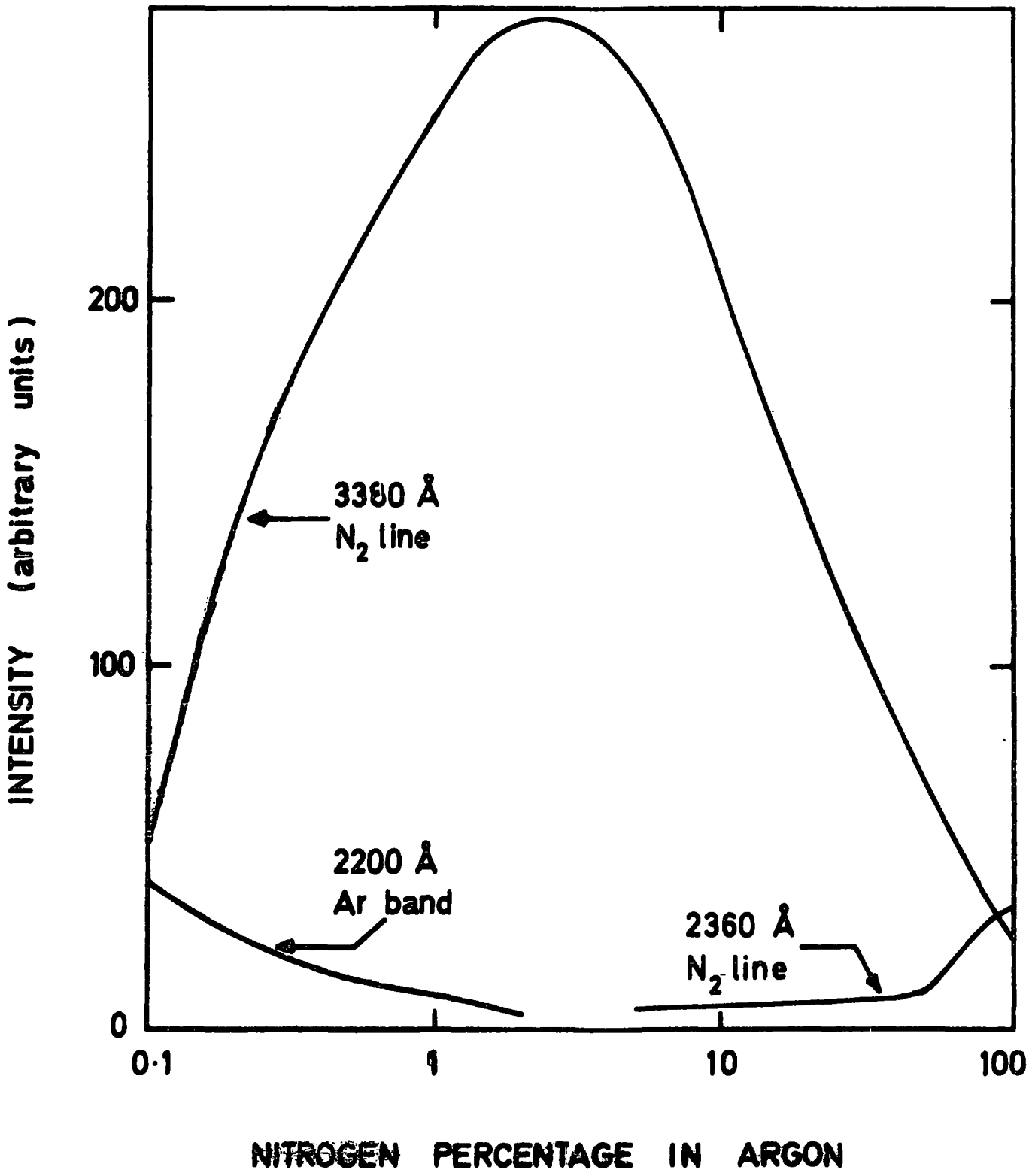

FIG. 3·4 Light intensity as a function of nitrogen concentration in argon.

of nitrogen to argon, quenches the argon band in the region between 1500-3000 Å and produces the emission of a band spectrum between 3000 Å and 4200 Å, which is very close to the maximum sensitive region of the photomultiplier (RCA 8575) used in this work (see section 2.4).

3.3 THE DRIFT PROCESS

3.3.1 In Pure Gases

Electrons and ions produced in the initial process will rapidly lose their energy by means of elastic and inelastic collisions with the gas molecules and then will move randomly and maintain the agitational energy. According to the Maxwell formula, the average energy of agitation is $\frac{3}{2}$ kT, which is equivalent to 0.03 eV at room temperature and corresponds to a velocity of approximately 10^7 cm/sec for thermal electrons.

When an electric field (E) is applied, electrons and ions, in addition to their random movement, will be drifted in a direction parallel to the electric field and at the same time their agitation energy (ε) will increase above the thermal value $\frac{3}{2}$ kT by the energy factor k_1.

$$k_1 \left(\frac{3kT}{2} \right) = \frac{1}{2} \quad mu^2 = \varepsilon \tag{3.3}$$

where u is the root mean square velocity of agitation. The value of k_1 is very near to unity for ions while for electrons it is usually considerably larger. For example at E/p = 1 volt/cm/torr, it is 285 for argon[11]. The value of k_1 for molecular gases is much lower than that for noble gases, for example, k_1 for nitrogen at E/p = 1 volt/cm/torr is 21.5. This is due to the high occurrence of inelastic collisions at lower electron velocities[11].

The number of collisions occurring between electrons and atoms is governed by the number of atoms/cm^3, which is directly proportional

to the pressure (p). Therefore, the processes associated with electron drift depend not only on the electric field E but also on the gas pressure. In fact it can be shown that the drift velocity itself depends on E/p which is referred to as the reduced electric field. The computed curves, shown in Fig 3.5[12] using an approximate formula, represent the effect of E/p on the distribution of electron energy between various processes for Ar, Ne, N_2 and Ne + 1% Ar. In these figures, the fraction of electron energy (acquired from the electric field) lost due to elastic collisions(Eℓ), excitation of electronic levels leading to light emission and metastable states (EE), ionization(I), increase of kinetic energy of electrons (S), excitation of vibrational levels (EV) are given as a function of E/p. The effect of adding another gas on this distribution may be quite large (see Fig 3.5d). The effect is described later in this section.

The agitation energy of the electron depends on the equilibrium between the gain of energy and momentum of the electrons from the electric field and the energy and momentum that they lose in collision with the gas molecules. Townsend[13] derived a relation between the applied field (E) and the drift velocity (ω) by using momentum conservation laws and by taking into consideration the distribution of free paths about the mean, i.e. the variation of the mean free path with the velocity of agitation, and the velocity distribution. This introduced a numerical factor C, which was calculated by Townsend, rendering the relation between ω and E to be

$$\omega = C \frac{e}{m} \frac{\lambda}{u} \frac{E}{p} \tag{3.4}$$

where C = 0.815 and λ is the mean free path per torr. Similarly, using the energy conservation principle

$$\left(k_1 \frac{3kT}{2}\right)\left(\frac{up}{\lambda}\right) \eta = e E \omega \tag{3.5}$$

where η is the average fractional energy loss per collision. Substituting

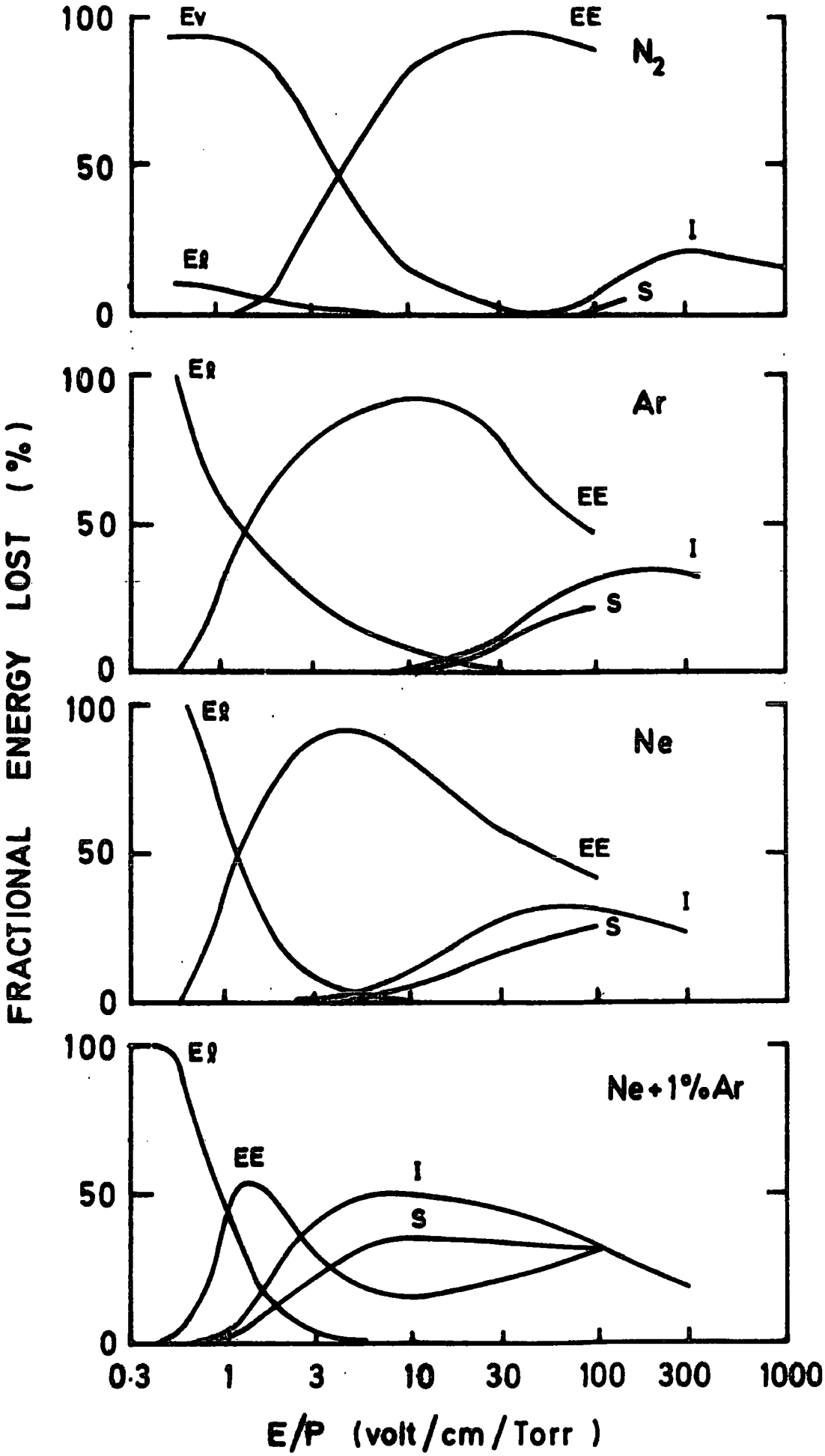

FIG. 3·5 Electron energy distribution.

the value of E from eq. 3.4 in eq. 3.5 gives

$$\omega^2 = 0.407 \quad \eta \, u^2 \tag{3.6}$$

The quantities λ and η are particularly useful in connection with the problem of determining the behaviour of electrons and ions in a mixture of gases from data relative to their behaviour in the pure components.

3.3.2 <u>In Gas Mixtures</u>

An approximate method for calculating the drift velocity of electrons in a mixture of gases was developed by English and Hanna[14], knowing the characteristics of the constituents and using Townsend's equation 3.4, 5, 6. The method is applicable to any mixture. Argon-nitrogen mixtures will be used because of their relevance to this thesis. The subscrips A, N and M denote respectively argon, nitrogen and the mixture.

If λ, η and F are the electron mean free path per torr, the average fractional energy loss by an electron per collision and the fraction of nitrogen in the mixture respectively, then [14]

$$\frac{1}{\lambda_M} = \frac{1-F}{\lambda_A} + \frac{F}{\lambda_N} \tag{3.7}$$

and

$$\frac{\eta_M}{\lambda_M} = \frac{(1-F)\ \eta_A}{\lambda_A} + \frac{F\eta_N}{\lambda_N} \tag{3.8}$$

Re-writing and substituting numerical values in eq. 3.4 and eq. 3.6

$$\frac{E}{p} = 4.44 \times 10^{-16}\ u^2 \quad (\eta_M)^{\frac{1}{2}} \quad (\lambda_M)^{-1} \tag{3.9}$$

$$\omega = 0.637 \quad u\ (\eta_M)^{\frac{1}{2}} \tag{3.10}$$

The distribution of electron energies is often taken to be Maxwellian. Large departures from this type of distribution are associated with a collision cross-section which varies rapidly with electron energy. Crompton and Sutton[15] derived relations for λ and η using the Druyvesteyn energy distribution of electrons. In this type of distribution diffusion, as well as elastic impacts and constant free paths were considered[16].

$$\lambda = 7.38 \times 10^{-9} \frac{\omega(k_1)^{\frac{1}{2}}}{E/p} \tag{3.11}$$

$$\eta = 2.21 \times 10^{-14} \frac{\omega^2}{k_1} \tag{3.12}$$

where k_1 is the measured value of the Townsend energy factor which was shown earlier as the ratio between the mean electron energy to the mean energy of translation of molecules ($\frac{1}{2} m u^2 / \frac{3}{2} kT$) (eq. 3.3).

The above equations with the following procedure were applied to the gas mixtures used in this work, i.e. the argon-nitrogen mixtures. The measured drift velocity values of pure argon[17] and of pure nitrogen[18] as a function of E/p , have been used with the values of k_1 for argon[13] and k_1 for nitrogen[13] in eq. 3.11 and 3.12 to calculate λ_A, η_A, λ_N and η_N. Then using eq. 3.7 and eq. 3.8, λ_M and η_M were calculated for different nitrogen concentration (F). Substituting in eq. 3.9 and 3.10, the values of the drift velocity as a function of E/p has been calculated for different nitrogen concentrations of nitrogen.

Figs 3.6 and 3.7 show the variation of ε with E/p and nitrogen concentration respectively and Figs 3.8 and 3.9 show the variation of λ_M and η_M respectively with the variation of nitrogen percentage. The variations of λ and η with nitrogen concentration are similar except that λ_M decreases with increasing field while η_M increases with increasing field.

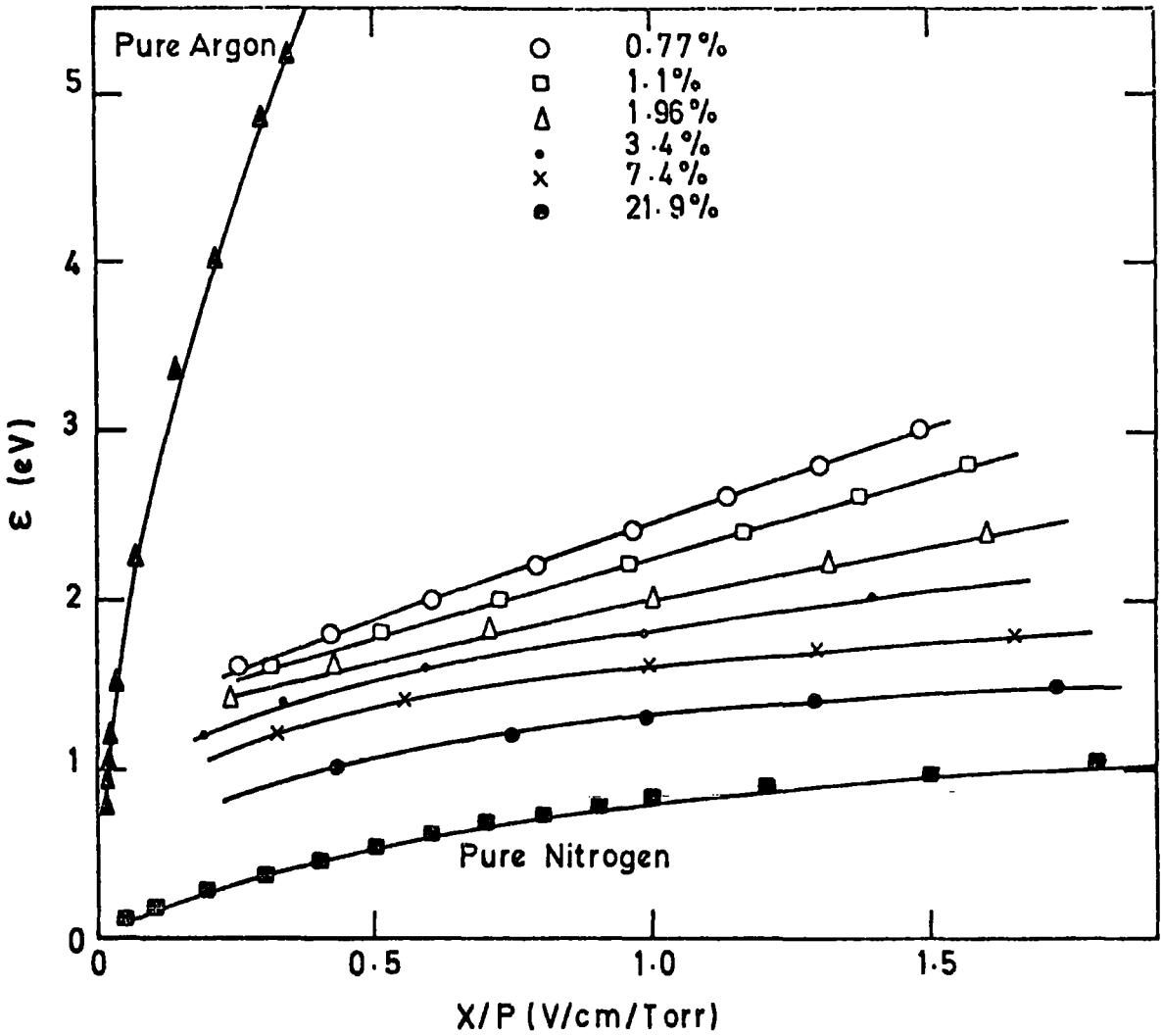
Pure Argon
0·77%
1·1%
1·96%
3·4%
7·4%
21·9%
Pure Nitrogen
ε (eV)
X/P (V/cm/Torr)
0
0·5
1·0
1·5
1
2
3
4
5

FIG. 3·6

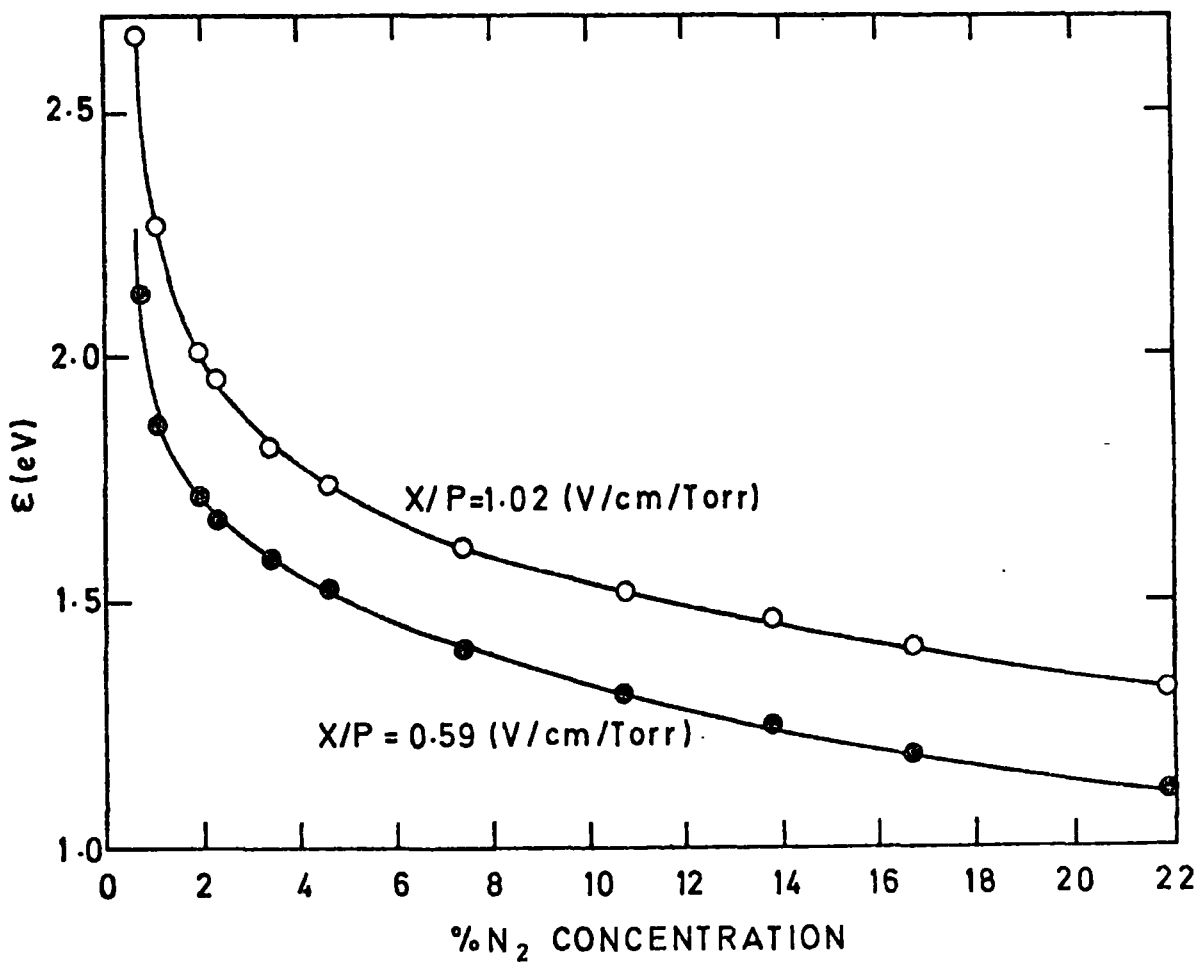
X/P=1·02 (V/cm/Torr)
X/P = 0·59 (V/cm/Torr)
ε (eV)
%N2 CONCENTRATION
1·0
1·5
2·0
2·5
0
2
4
6
8
10
12
14
16
18
20
22

FIG. 3·7

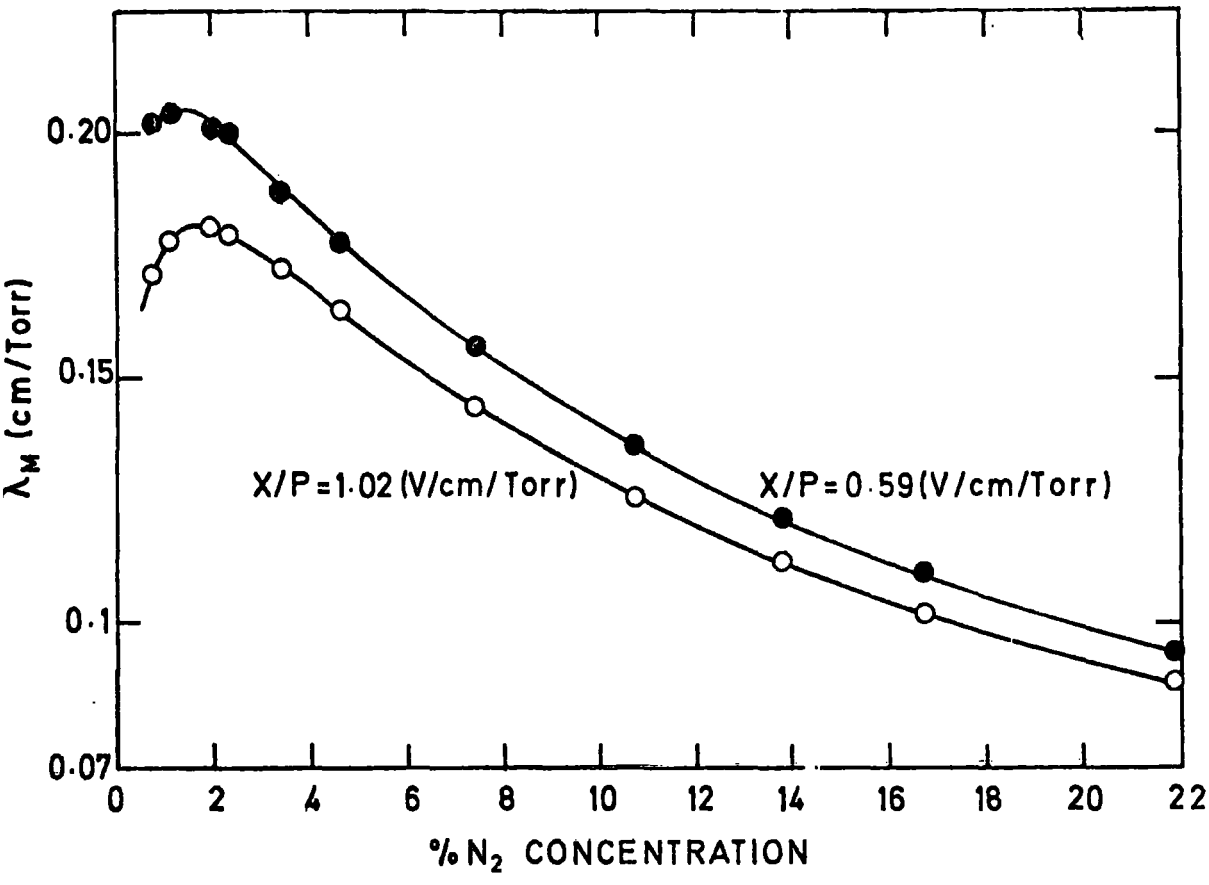
0.20
0.15
0.1
0.07
λ_M (cm/Torr)
X/P = 1.02 (V/cm/Torr)
X/P = 0.59 (V/cm/Torr)
0
2
4
6
8
10
12
14
16
18
20
22
% N_2 CONCENTRATION

FIG. 3·8

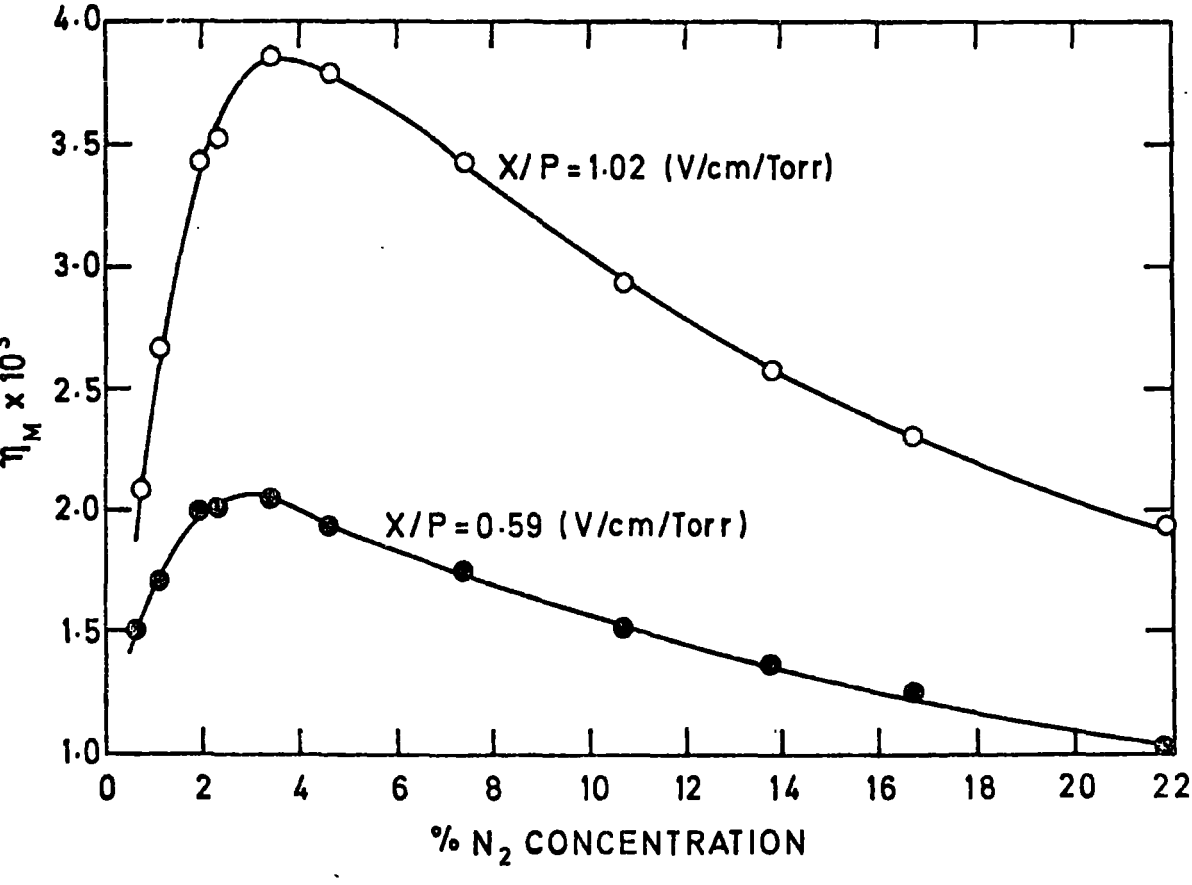
4.0
3.5
3.0
2.5
2.0
1.5
1.0
$\eta_M \times 10^3$
X/P = 1.02 (V/cm/Torr)
X/P = 0.59 (V/cm/Torr)
0
2
4
6
8
10
12
14
16
18
20
22
% N_2 CONCENTRATION

FIG. 3·9

The variation of ε and ω with nitrogen concentration, Figs 3.6, 3.7 and 3.10, is related to the variation of the momentum transfer cross-section (Q). The addition of small amounts of N_2 causes the value of ε to decrease rapidly, then this decrease slows down at higher percentages. The increase of ω with small additions of nitrogen is a result of the high agitational energy of pure argon which rapidly falls with the addition of small amounts of nitrogen as shown in Figs 3.6 and 3.7. The momentum transfer cross-section or the diffusion cross-section, which is a measure of the average forward momentum lost by the electrons in collision with molecules, is shown in Fig.3.11 for pure argon[19] and pure nitrogen[20] as a function of the mean agitational energy of electrons (ε). From the two curves in Fig 3.11, it is evident that small additions of nitrogen, up to 1%, would not modify the dominating Ramsauer rising edge in pure argon, which is the interesting region for our work ($\sim$ 1 eV), hence with the decrease of ε, Q_M ($\alpha \frac{1}{\lambda_M}$) will decrease leading to an increase in λ_M as shown in Fig. 3.8. From eq. 3.4 $\omega \alpha \lambda/\sqrt{\varepsilon}$, hence ω will increase due to the increase of λ and decrease of ε. But with the increase of nitrogen percentage the nitrogen momentum transfer cross-section begins to dominate and the total Q for the mixture (Q_M) starts to increase with decrease in ε leading to a decrease in λ and hence a decrease in ω. It should be noted here, that the maximum light emission obtained in argon-nitrogen mixtures of $\sim$ 2% N_2 (as shown earlier in Fig.3.4) can be referred to the above argument.

To summarize the previous discussion, for argon nitrogen mixtures, no inelastic collisions occur with argon atoms unless the electrons have an energy larger than the first excitation potential of 11.55 eV. In nitrogen, inelastic collisions occur at much smaller energies because of the vibrational levels of the molecules beginning at about 1 eV. As shown

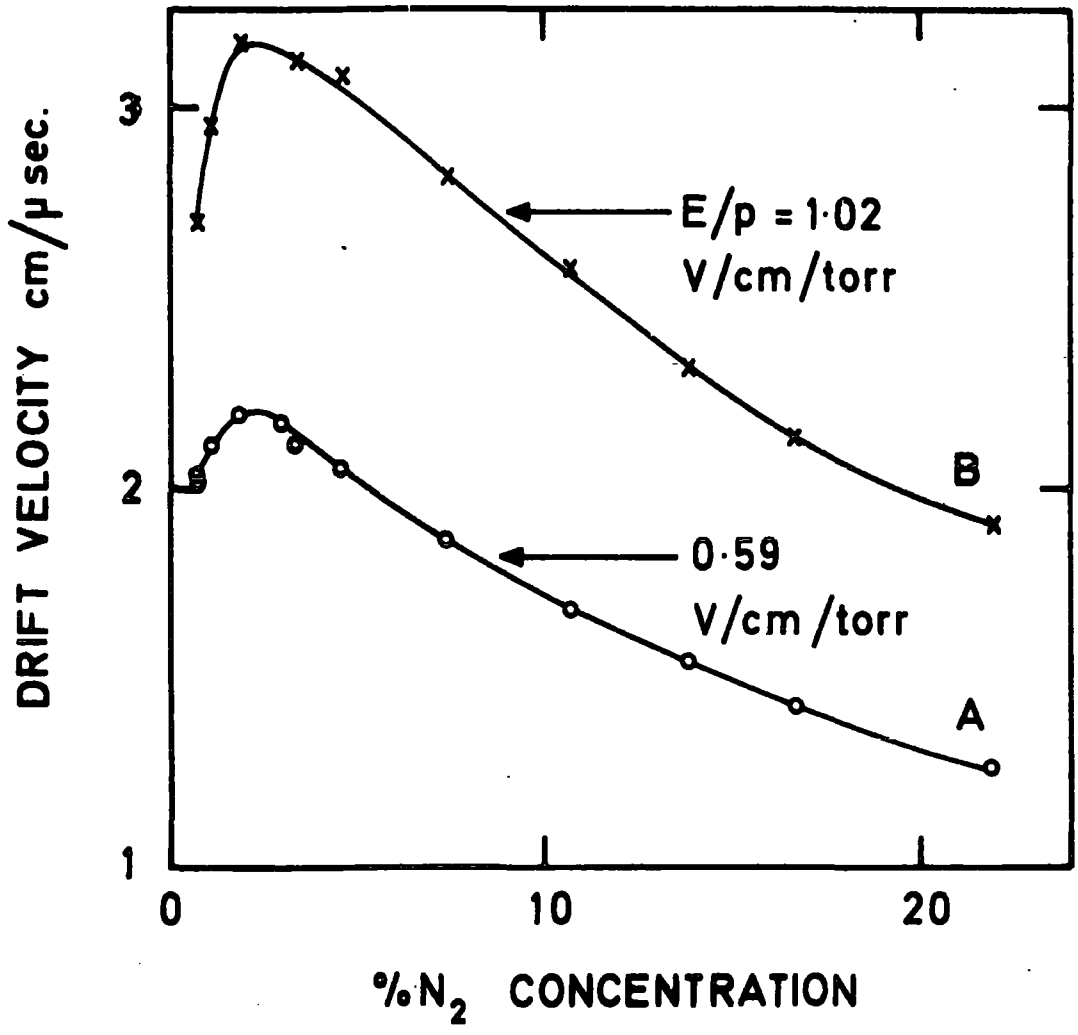

FIG. 3·10 Drift velocity vs nitrogen concentration.

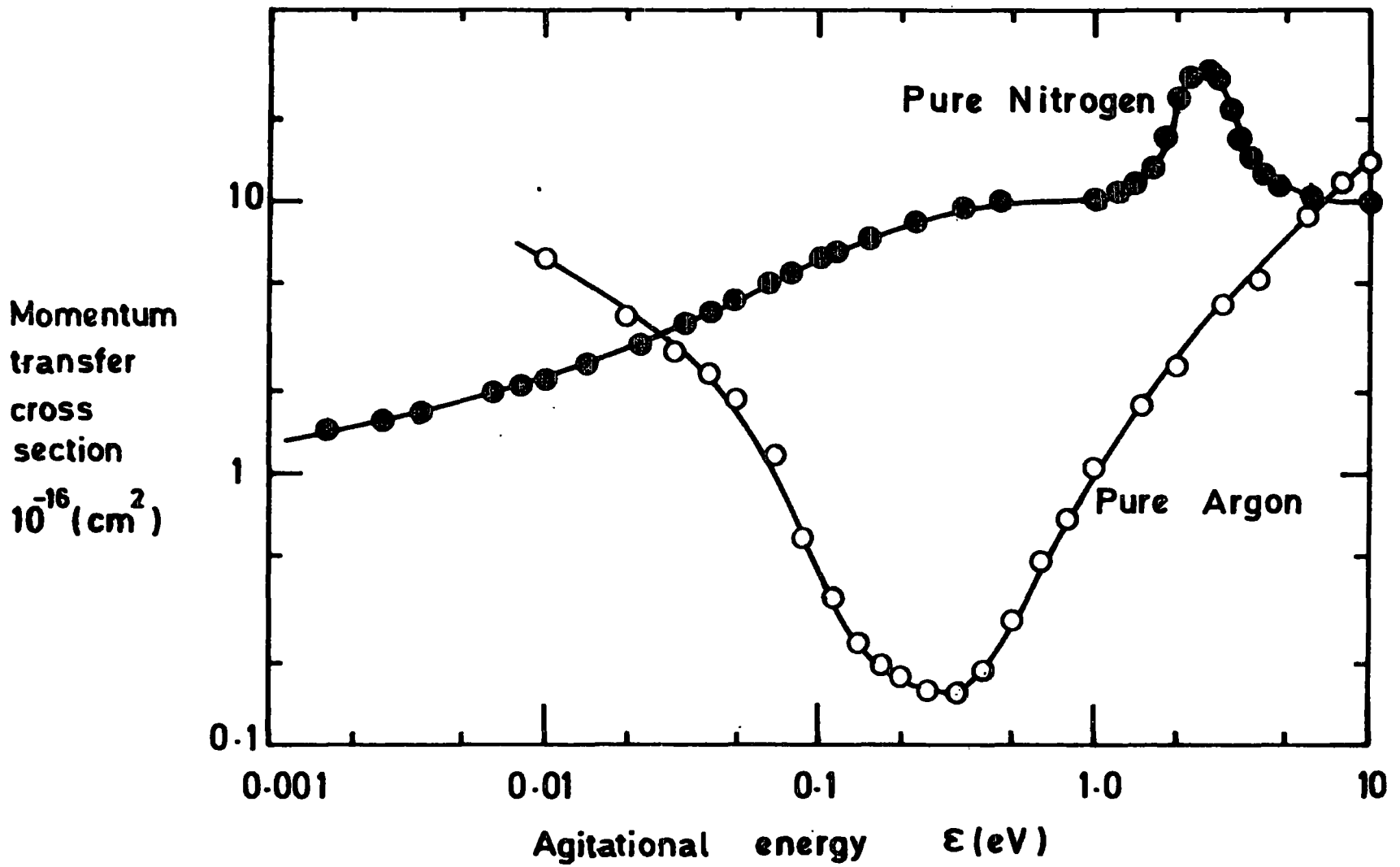
Pure Nitrogen
Pure Argon
Momentum transfer cross section 10^{-16} (cm^2)
10
1
0·1
0·001
0·01
0·1
1·0
10
Agitational energy ε (eV)

FIG. 3·11

in Fig. 3.6, in Ar-N_2 mixtures, the average electron energy reduces from 10 eV to 1 eV at E/p = 1, and this is the reason for the change of distribution of processes shown in Fig.3.5 in gas mixtures. The change has only been compiled for the case of neon with a small amount of argon as the second gas and this is given in Fig. 3.5b. It is seen that at E/p=2, the ionization is virtually non-existent in pure neon or pure argon, but accounts for 30% of the energy loss in a mixture containing only 1% of argon.

3.3.3 Processes Accompanying Drift

A. Diffusion

The drift process is accompanied by diffusion of particles (ions or electrons) from points of high concentration to those of low concentration. While the liberated particles drift in a direction parallel to the applied field, they diffuse outward. The origin of this motion is a purely thermal one[21]. The velocity of diffusion in one direction is given by

$$v = -\frac{D}{N}\frac{dN}{dx} \tag{3.13}$$

where D is the diffusion coefficient in cm^2/sec, N is the concentration of particles. The negative sign indicates that the motion occurs in the direction of decreasing concentrations[21]. The relation between D and the mobility μ (= ω/E) was first derived by Townsend and can be written as

$$\frac{D}{\mu} = \frac{kT}{e} \tag{3.14}$$

Data on drift velocities and μ as a function of E/p show that ω increases with increasing E/p and the ratio ω/E or μ decreases with increasing E/p[19]. The variation of D with E/p can be obtained from values of

D/μ [19] and known values of μ. It is evident that D increases with increasing E/p, but the rate of increase is much lower than that for ω. For example, in nitrogen at 239 K, for the range from 0.33 to 3.3 volt/cm/torr, D increases by 29% while ω increases by 76%.

The diffusion coefficient D is a function of temperature (T). Experimental values of D for various binary mixtures of rare gases[5] show an increase of D with increasing T. Hence the cooling effect due to the addition of molecular gases to noble gases decreases diffusion considerably.

The root mean square of the dispersion of electrons in one dimension is given by

$$\sigma = \sqrt{2Dt} \tag{3.15}$$

hence, any parameter which causes an increase in the drift time t will consequently cause an increase in the dispersion[22].

In chambers where diffusion is an undesirable feature, the value of D, or σ, must be made as small as possible. In order to decrease σ one should decrease the temperature and increase E in the drift region[23], as these two parameters are not independent of each other, a compromise usually has to be made.

B. Attachment and Recombination

The other two factors which should be mentioned in this section are the attachment coefficient α and the recombination coefficient β. The first is the probability for electrons to attach themselves to a gas molecule. Practically, α is zero for H_2, H_e, Ar, N and CO_2 if these gases are sufficiently pure[24]. The most common impurities are O_2 and H_2O.

The second factor β, is the probability of recombination of electrons or negative ions with positive ions. In general, the value of β for recombination between negative ions and positive ions is 10^4 times

that between electrons and positive ions[25]. The recombination coefficient varies with the gas, its temperature and pressure, and with the ions present. It increases with increasing pressure, and it decreases with increasing temperature[25]. Some authors[26] attributed the drop in the pulse height, in proportional counters at high rate, to the recombination of the primary ions rather than to space change effects.

3.4 DRIFT VELOCITY MEASUREMENTS IN $Ar-N_2$ MIXTURES

It was shown earlier that argon-nitrogen mixture is a suitable medium for producing light pulses by α or X-ray bombardment. The drift velocity measurements to be described, were to choose a suitable percentage of nitrogen in the argon-nitrogen mixture to be used in a gas scintillation counter, as well as to study the effect of other parameters such as drift distance.

The principle of these drift velocity measurements depends on the fact that, at low applied voltage, the gas scintillation counter produces two trigger signals. The first signal is caused by the primary scintillations of the incident particle and the electrons drifting towards the sense wire produce the secondary scintillation signal. The time difference between the two signals recorded by the photomultiplier gives the drift time and hence the drift velocity of electrons in the gas mixture.

3.4.1 Experimental Arrangement

The counter used in the following tests is the gas scintillation drift counter described in Chapter 2. Fig 3.12 shows the electronic set-up.

The output signal from the photomultiplier, an RCA 8575, was divided into two pulses and converted separately into fast NIM signals by a preamplifier-trigger[27] (P.T.). The primary scintillation signal was used to start the time-to-amplitude converter (TAC). To stop the TAC by the secondary scintillation signal, one of the photomultiplier outputs was

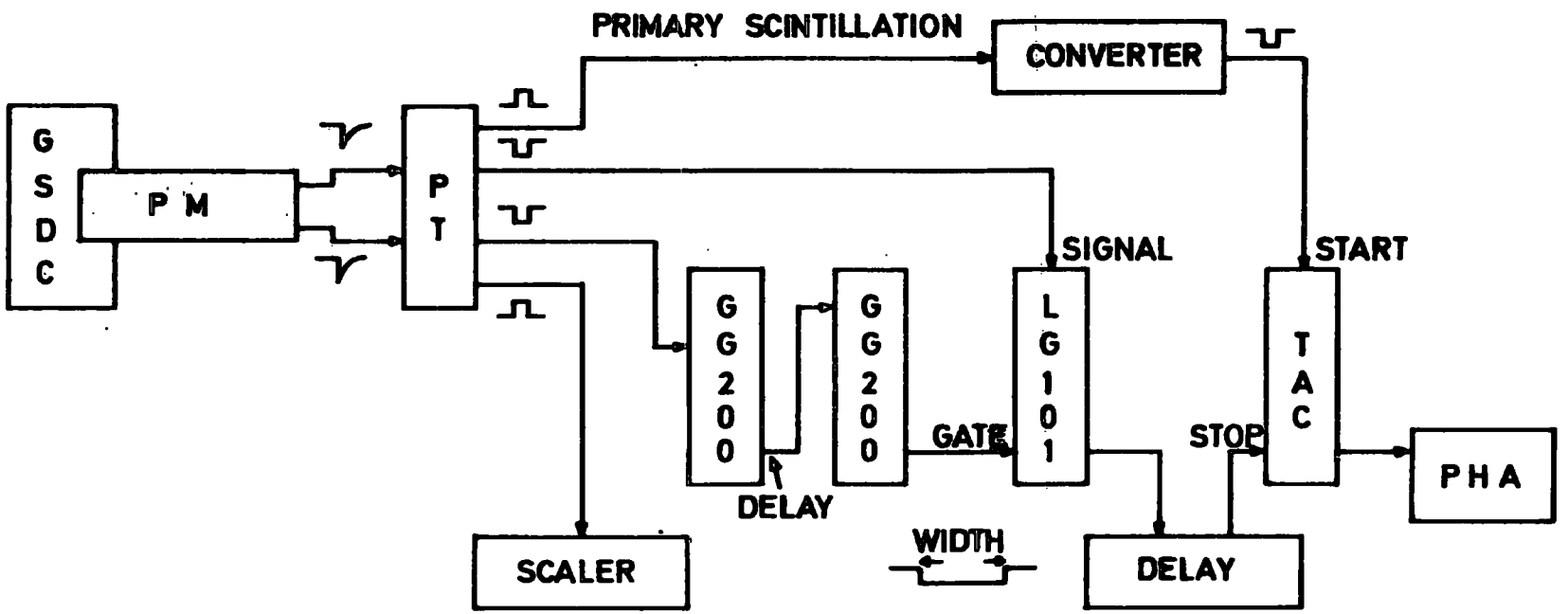

FIG. 3·12 Drift velocity measurements. Electronic set-up.

fed into a linear gate and another output was used to open the gate for a certain duration, covering the time of arrival of the secondary scintillation signal. The width of the gate and the delay were checked regularly to ensure that the gate window (width) always contained the secondary pulse. In order to shift the drift time distribution to convenient channels on the pulse height analyser (PHA), an extra delay was introduced to the stop signal.

The drift time was measured as a channel number, which was converted into nanoseconds by a calibration curve, shown in Fig 3.13. This calibration was obtained by feeding in pulses, separated by known delays, to the TAC using a pulse generator. The TAC-PHA system was linear throughout the operating range with a slope of 10 ns/channel. The channel number corresponding to zero drift time was obtained by irradiating the region around the sense wire with α-particles and noting the lowest channel to be filled. This number was then subtracted from each reading of drift velocity.

The primary scintillation pulses were observed to have a much faster rise time than the secondary pulses. To decrease the time walk due to this difference both pulses were discriminated at a very low level (200 μv). The fast NIM standard signal was generated by the discriminator. Another factor affecting the time walk was the amplitude of the pulse from the photomultiplier. It was observed to drop with increasing nitrogen concentration, the photomultiplier voltage was therefore adjusted to bring the amplitude back to the same level, which reduced the time walk due to this drop.

In the next section, parameters under investigation, namely the drift field, the drift distance and nitrogen concentration are discussed.

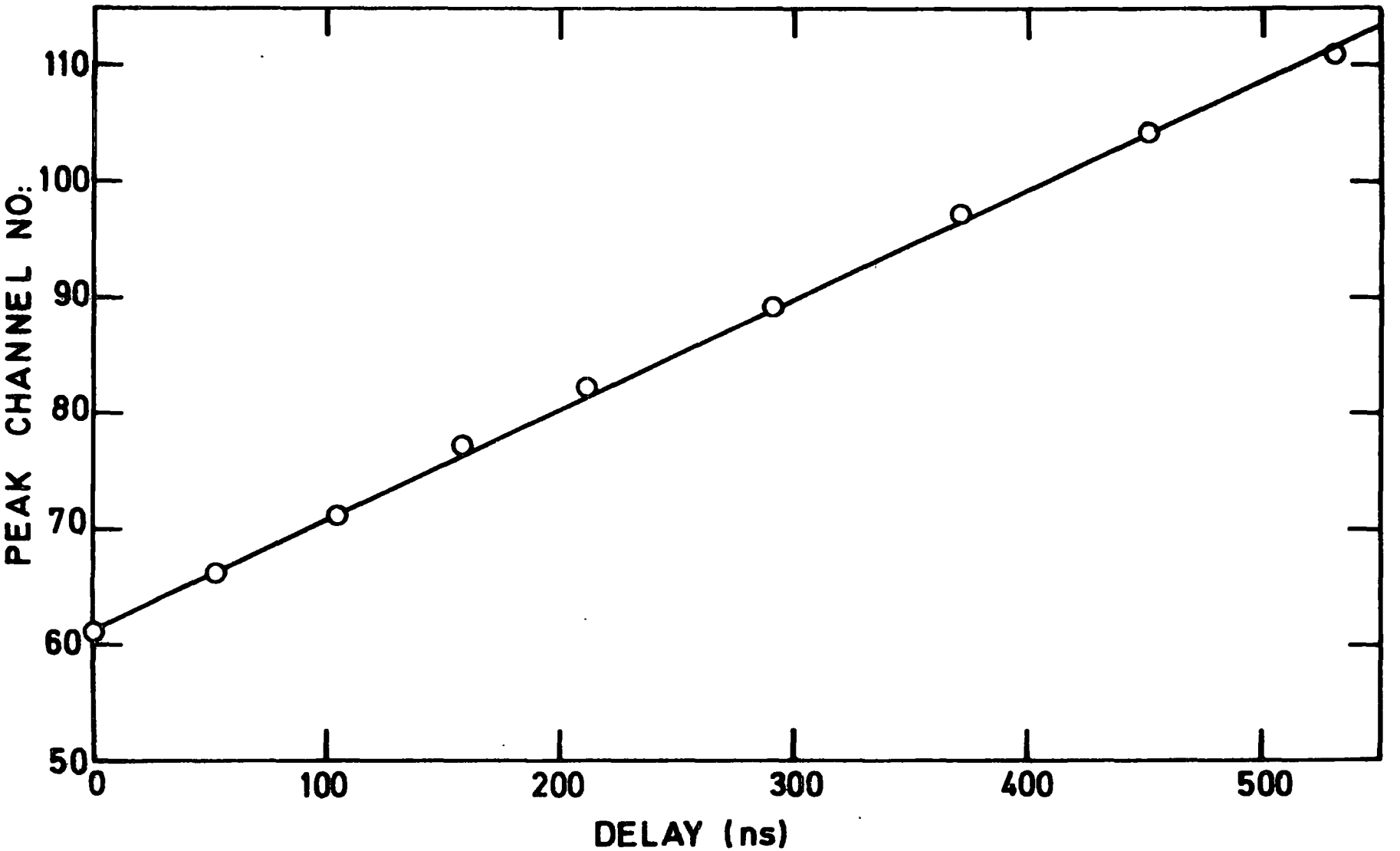

FIG. 3·13 PHA Calibration curve

3.4.2 Drift Field

(i) The effect of the sense wire potential on the drift time.

An α-source(Am^{241}), which had a collimator of 0.5 mm diameter and 10 mm thickness, was placed at a drift distance (d) of 1.8 cm from the sense wire. The drift field set by the cathode planes was kept at a fixed value and the drift times of the electrons were measured at different sense wire voltages. These measurements were repeated for different drift fields and different nitrogen concentrations.

A considerable dependence of the drift time on the sense wire potential was observed and this is shown in Fig 3.14. It is caused by the drift velocity of electrons in argon-nitrogen mixtures not attaining saturation, at least within the working range of the drift field. The drift time is therefore affected by the high sense wire field.

To minimize the effect of the sense wire potential on the drift time, the chamber was operated with the lowest possible sense wire potential which was found to be 550 volts. Furthermore a correction factor for the drift time was used to reduce this effect. It was obtained as follows : The relation between the sense wire potential and the drift time is linear on a log-linear scale, as shown in Fig 3.14, where it is observed that the gradients of the plots for different concentrations of nitrogen and different drift fields are nearly the same. Hence, the drift time correction factor (DTC) was obtainable from the ratio of the drift time at zero sense wire potential, obtained by extrapolation, to that at the potential of 550 volts, (see Table 3.3). The correction factor was calculated for different drift fields and different concentrations of nitrogen and the mean value of the factor was used to correct all the subsequent measured drift times for d = 1.8 cm. An error of less than 2% was involved due to the assumption that the correction factor is the same for all the measured drift times.

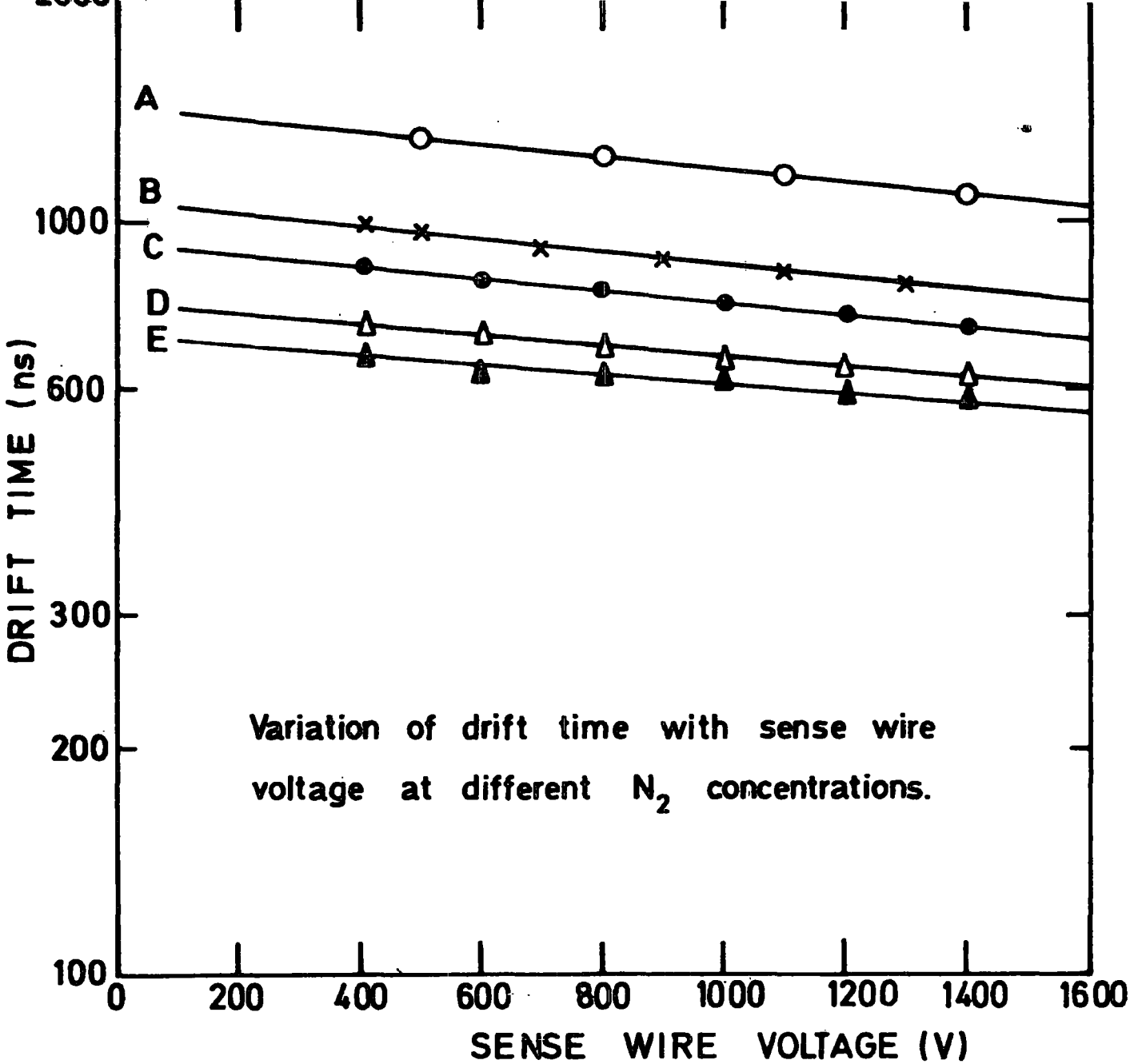
A
B
C
D
E
1000
600
300
200
100
DRIFT TIME (ns)
0
200
400
600
800
1000
1200
1400
1600
SENSE WIRE VOLTAGE (V)
Variation of drift time with sense wire voltage at different N_2 concentrations.

FIG. 3·14

TABLE 3.3

Drift Distance = 1.8 cm

Curve (Fig 3.13)	Drift Field V/cm	E/p V/cm/torr	N_2 %	DTC
A	447	0.59	13.7	1.1
B	447	0.59	4.6	1.09
C	989	1.3	13.7	1.11
D	776	1.02	4.6	1.10
E	989	1.3	4.6	1.08

(DTC) average = 1.1

A similar procedure was used to correct the drift time for d = 1 and 2.5 cm. The correction factor for d = 2.5 cm was less than that for d = 1.8 cm and the latter was less than that for d = 1 cm. The correction factor varies with d because the fraction of the drift space which is influenced by the non-uniform field around the sense wire decreases as d increases and the correction factor decreases accordingly.

(ii) Effect of drift voltage on the drift time.

The effect of the drift field on the drift time is shown in Fig 3.15 for two values of nitrogen concentration. A' and B'are the corrected drift time values for the corresponding A and B values. At high nitrogen concentration, the drift time decreases with increase of the drift field due to the increase in drift velocity, however at low concentration the drift time shows an apparent maximum. This can be attributed to the decreasing effect of the sense wire voltage, as the drift voltage increases, on the electron drift motion.

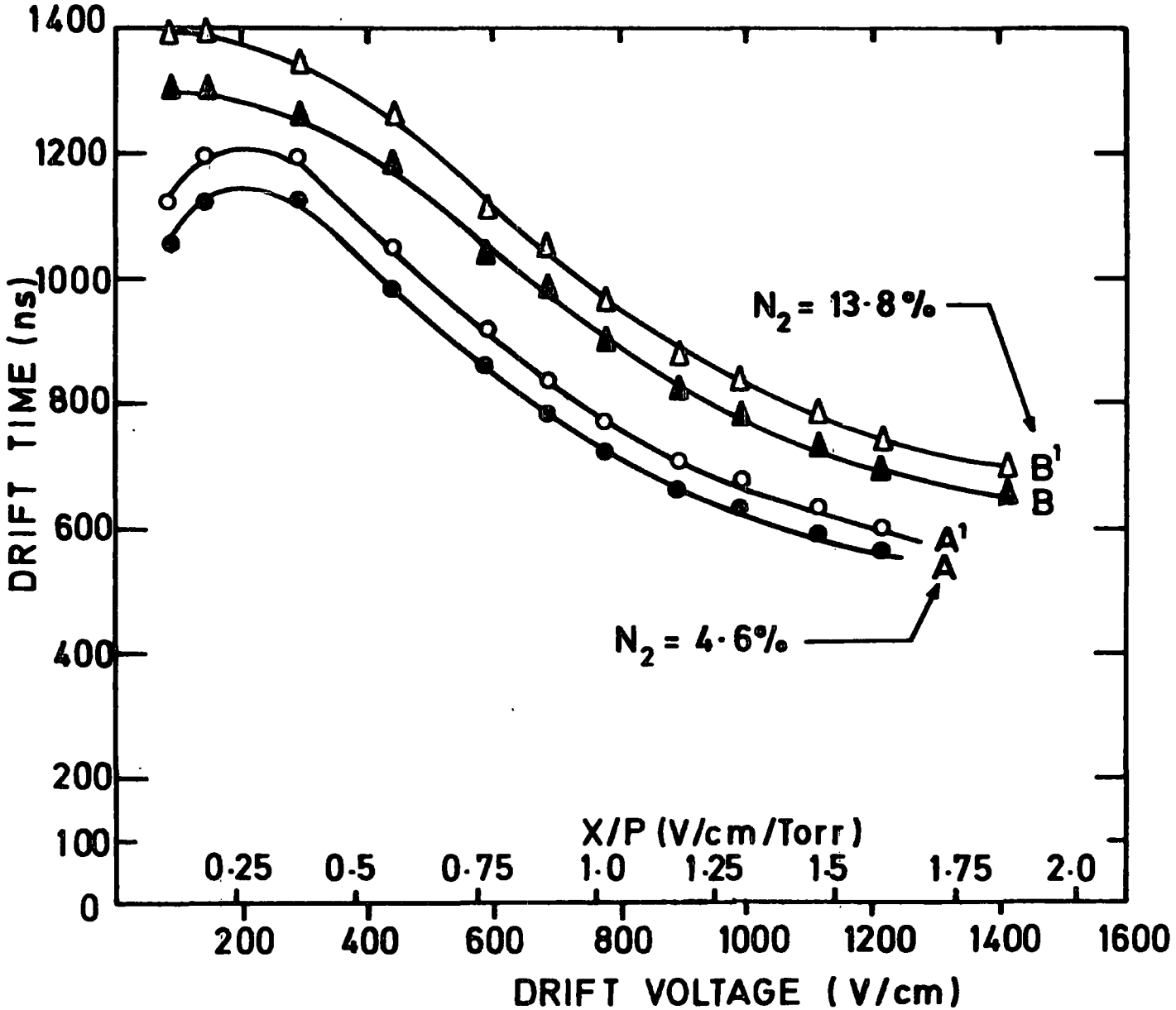

FIG. 3·15 Variation of drift time with drift voltage

(iii) Measured and calculated drift velocity variation with the field.

The variation of the drift velocity with the field for Ar, N_2, CH_4, Ar + 10% CH_4 and Ar + 10% N_2 measured by several workers is shown in Fig 3.16[28]. The saturation in drift velocity occurring in Ar + 10%CH_4 mixture makes it suitable for particle locating experiments. In the case of the Ar + 10% N_2 mixture the drift velocity in the mixture is approximately twice the values in either Ar or N_2 at the same field.

The change in the measured drift velocities with the drift field at 10.7% N_2 is shown in Fig 3.17 with the calculated values at the same percentage ; using the procedure mentioned in section 3.3.2 for calculating the drift velocity in a gas mixture. Also the measured and the calculated values of the drift velocity in Ar + 10% N_2 given by Klema and Allen[29] are given by in the same figure for comparison. The calculated and measured curves show the same general shape. The reason given by Klema and Allen[29] for the difference between calculated and measured values was that the values of the drift velocities for pure argon and pure nitrogen taken from Townsend's data[13] to calculate the drift velocity for the mixture may not be correct due to some impurities. The present calculations are nearer to the present results, for example, at 1 volt/cm/torr the difference between the present calculations and results is 26% while at the same field it is 36% in Klema and Allen[29] curves. The reason for this difference in the present results is similar for that given by Klema and Allen, i.e. unreliable data used in the calculation. The drift velocities for pure argon and pure nitrogen were taken from different sources[17,18] but the values of k_1 were taken from Townsend's data[13]. A difference between Klema and Allen's meausred values and the present measured values is expected due to the use of unpurified gas mixture by them. The argon was 99.6% pure

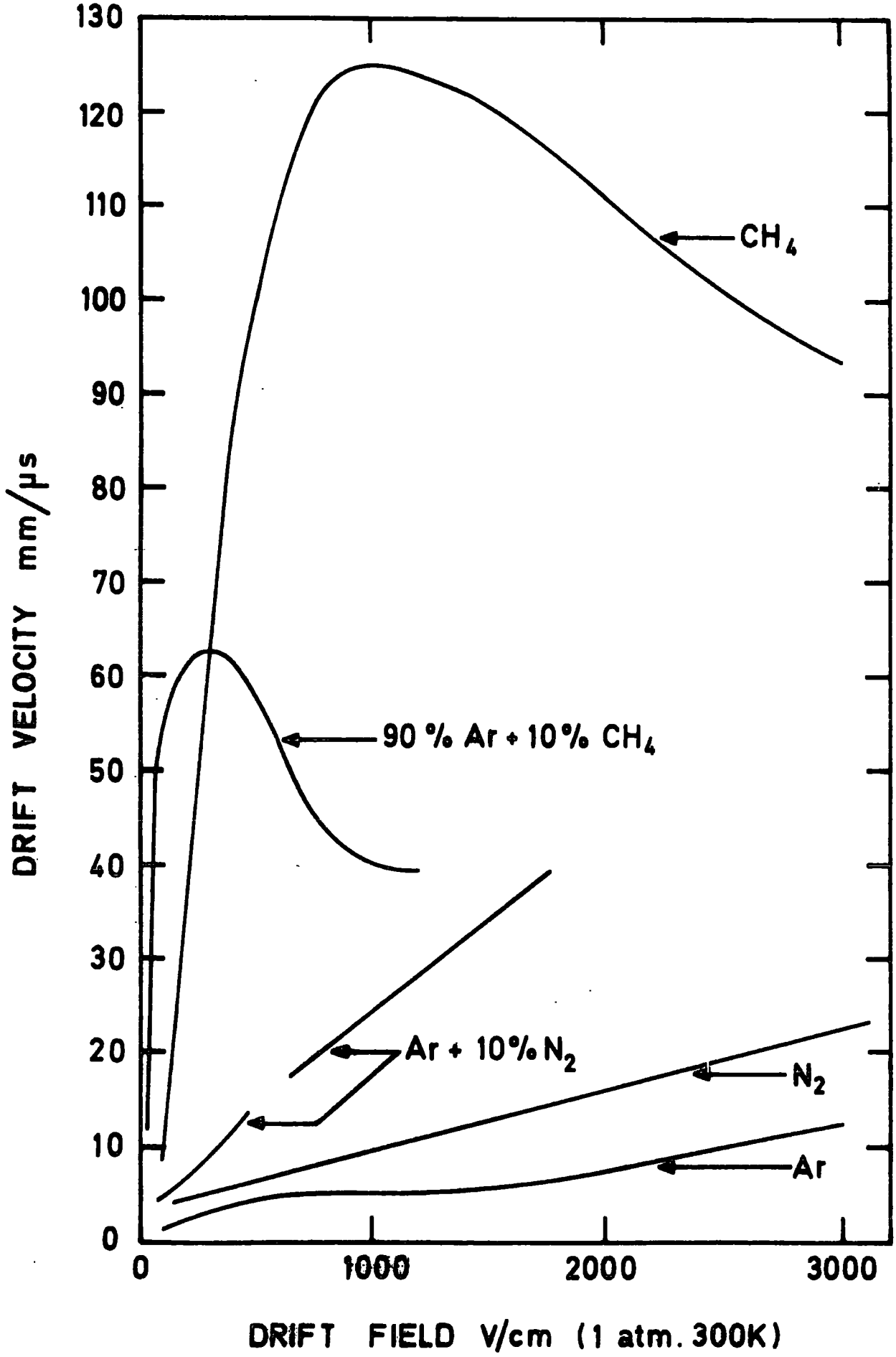

FIG. 3·16 Drift velocities of some gases at 1 atm. 300K.

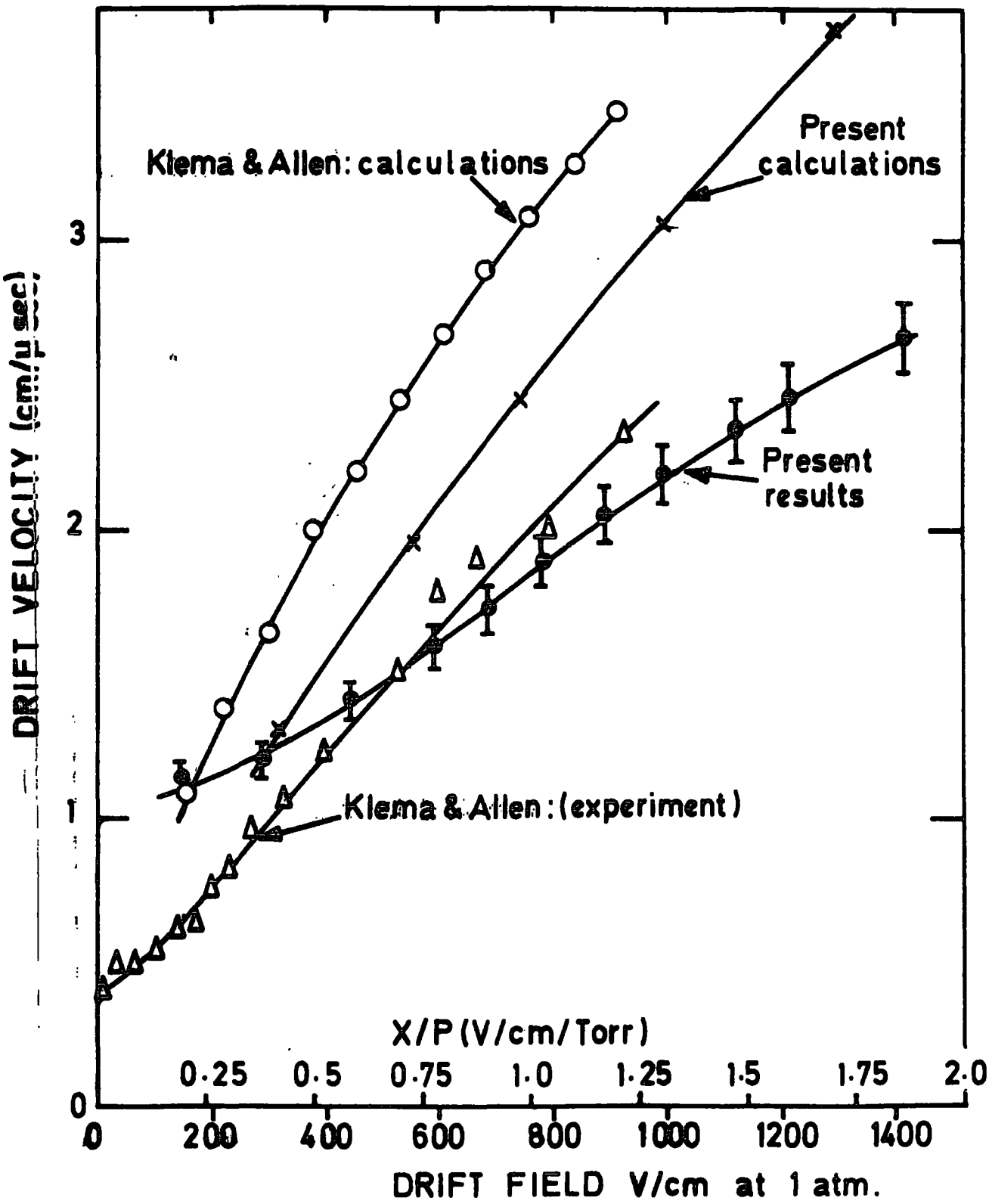

FIG. 3·17 Measured and calculated drift velocities.

while in this work it is 99.99% pure. Also the difference is due to the slight difference in the nitrogen percentage used, in their case 10% and in the present case 10.7%. At low drift field the experimental values become more inaccurate.

3.4.3 Drift Distance

The drift velocity values as a function of the drift field were measured for three different drift distances, 1, 1.8 and 2.5 cm. The corrected drift velocities as a function of the drift field are shown in Fig 3.18. The percentage of nitrogen used in this test was 4.6. For d = 1 cm, the curve is in a good agreement with that for d = 1.8 cm, except at low drift field values, where the 1 cm values are slightly higher than the 1.8 cm values. This rise, which is less than 4%, may be due to the increase of the sense wire region of influence at low drift field. For d = 2.5 cm, the curve is lower than the other two which could be caused by diffusion and also the potential dip around the field wire, which is close by at a distance of 3.6 cm from the sense wire.

3.4.4 Nitrogen Concentration

With a drift distance of 1.8 cm, the corrected drift velocity was measured as a function of the drift field for different nitrogen concentrations. These measurements are shown in Fig 3.19. At low drift field (i.e. less than 0.5 V/cm/torr) the measurements are slightly inaccurate due to the slow rise times of the secondary pulses caused by diffusion.

The change in the measured drift velocities with nitrogen concentraation is shown in Fig 3.20 for E/p = 0.59 and 1.02 V/cm/torr alongside the calculated drift velocities at the same fields shown earlier in Fig 3.10. The changes in ω with concentration percentage of nitrogen, experimental and calculated, show similar shapes with maximum values around 2.5%. The reason for the maximum at low nitrogen percentage was given in section 3.3.2.

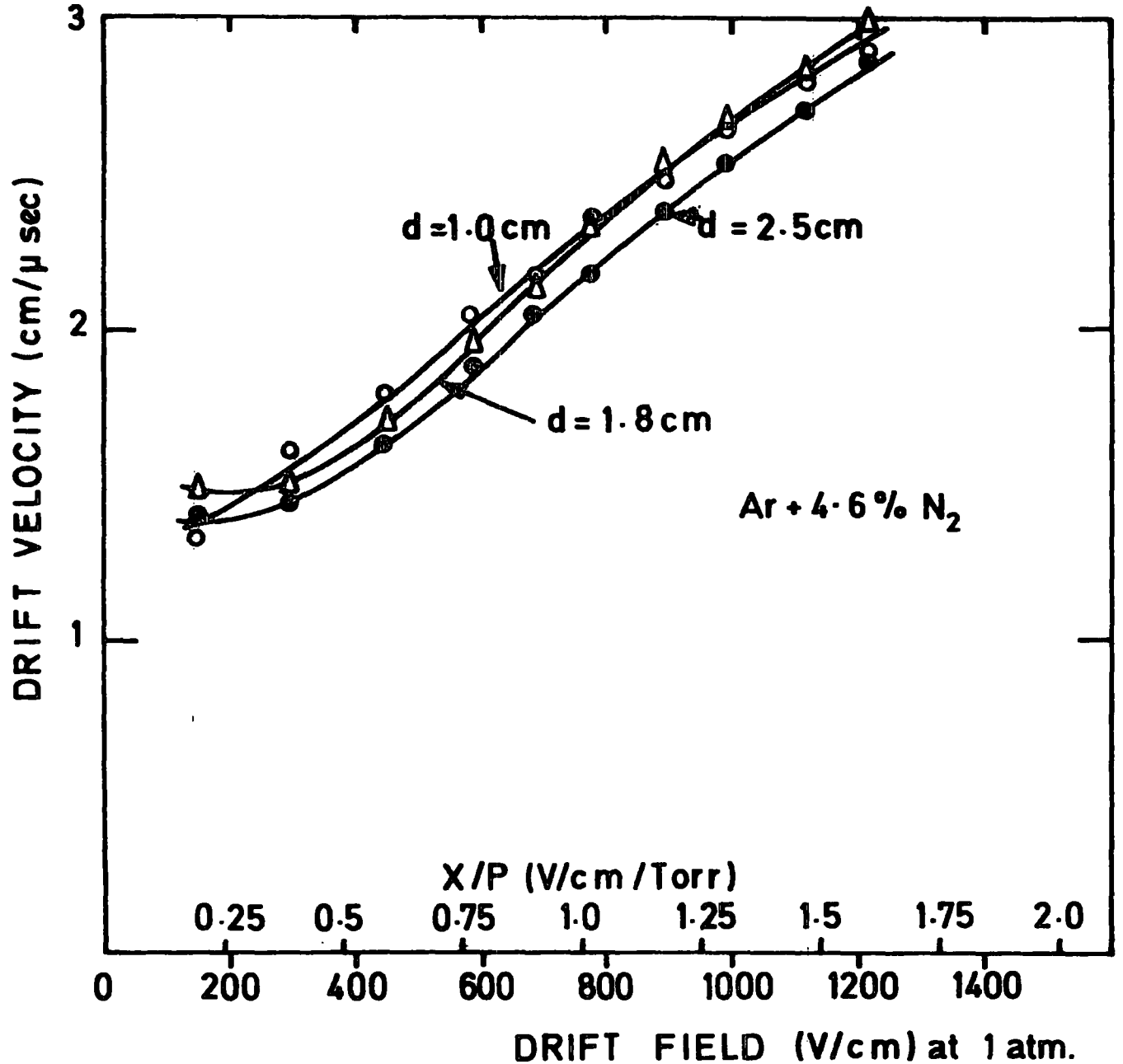
DRIFT VELOCITY (cm/μ sec)
3
2
1
d = 1·0 cm
d = 2·5cm
d = 1·8 cm
Ar + 4·6 % N2
X/P (V/cm/Torr)
0·25
0·5
0·75
1·0
1·25
1·5
1·75
2·0
0
200
400
600
800
1000
1200
1400
DRIFT FIELD (V/cm) at 1 atm.

FIG. 3·18

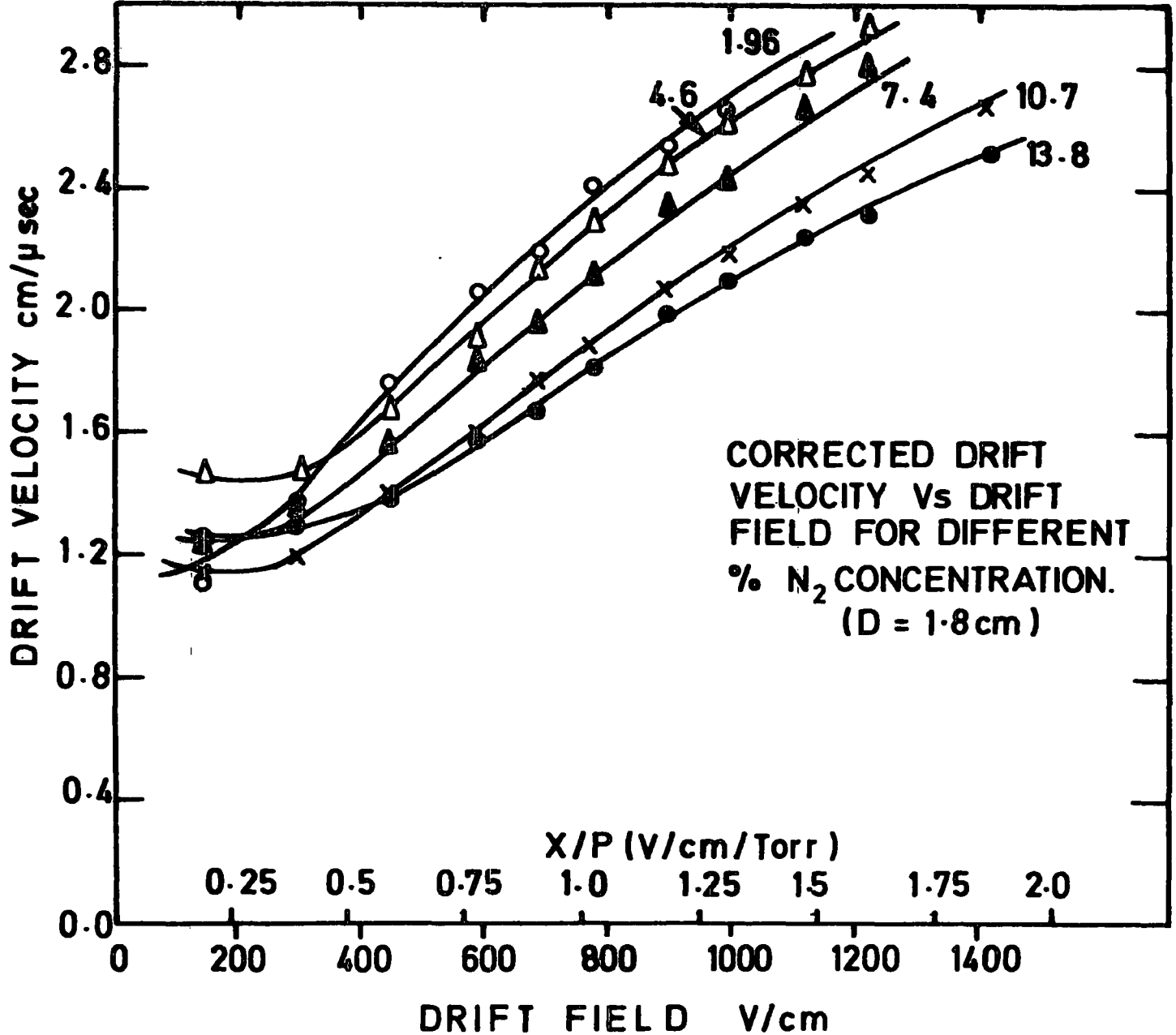
DRIFT VELOCITY cm/μ sec
2.8
2.4
2.0
1.6
1.2
0.8
0.4
0.0
1.96
4.6
7.4
10.7
13.8
CORRECTED DRIFT VELOCITY Vs DRIFT FIELD FOR DIFFERENT % N_2 CONCENTRATION. (D = 1·8 cm)
X/P (V/cm/Torr)
0.25
0.5
0.75
1.0
1.25
1.5
1.75
2.0
0
200
400
600
800
1000
1200
1400
DRIFT FIELD V/cm

FIG. 3·19

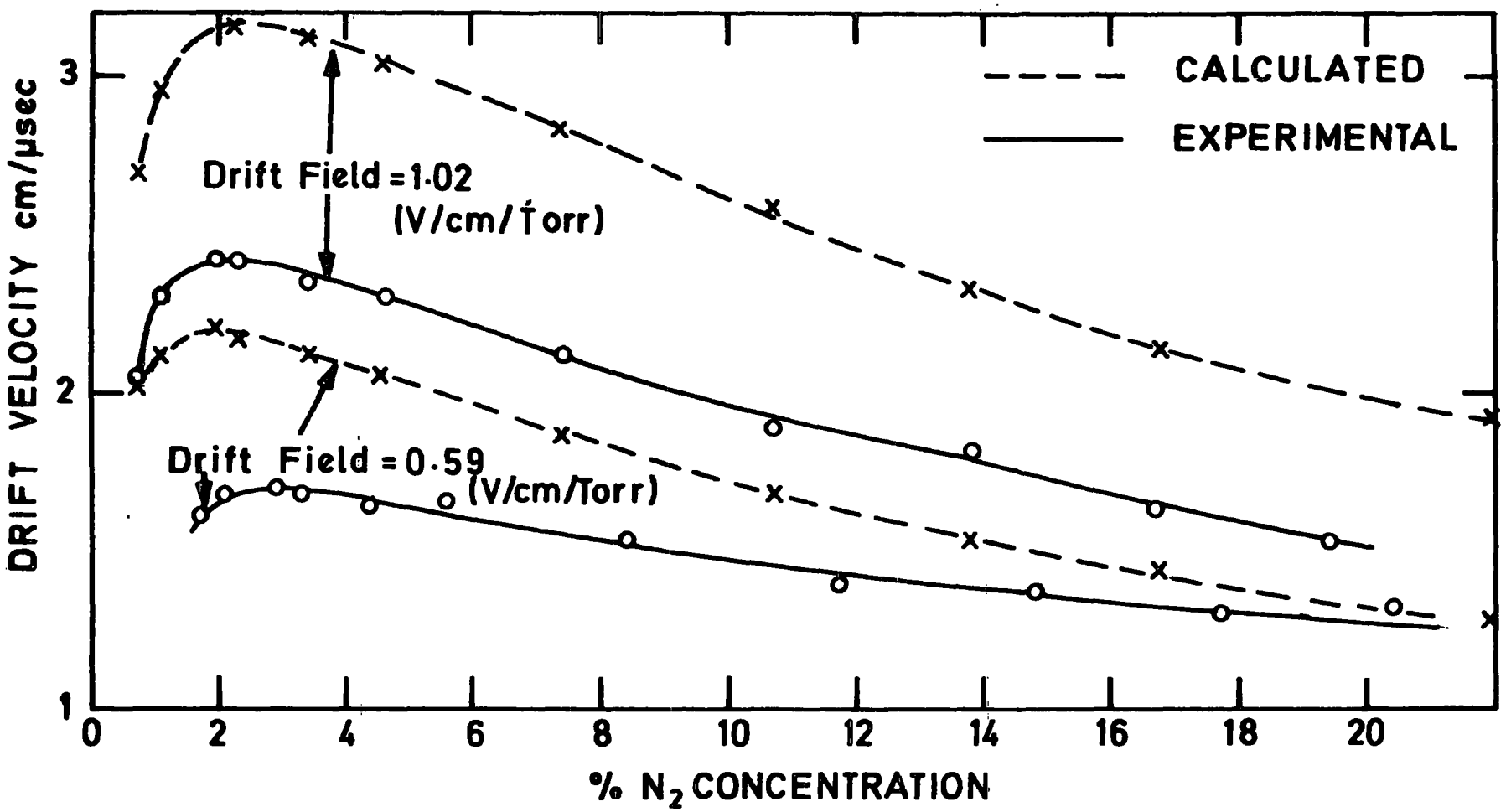

FIG. 3·20 Measured and calculated drift velocity vs. N_2 concentration.

The calculated values are found always to be higher than the measured values and this is due to the calculation method being an approximate one, in this method the distribution of electron agitational energy was assumed to be Maxwellian, and the electrons were in collision equilibrium with the gas molecules so that the mean electron energy is some constant (C) times the energy of agitation of the gas molecules. In Fig 3.17, it is evident that the ratio between the calculated ω and the measured one increases with increasing E/p. This can be attributed to the approximate method used for calculating λ_M in Eq.3.7 which depends only on the percentage of each gas and assumes no interaction, such as the Penning effect, between gas molecules. The pronounced departure from the computed values at high field is due to the big change in the energy distribution processes in gas mixtures at high field (see Fig 3.5d).

3.5 CONCLUSION

The high light emission from argon-nitrogen mixtures, in the region to which the RCA 8575 photomultiplier is sensitive, makes it a proper mixture to be used in GSC's (Chapter 6). The drift velocity saturation in argon-methane mixture is the reason for using this mixture in MWPC's and DC's (Chapter 4).

A comparison between the measured and the calculated values for the drift velocity at different fields and different nitrogen concentrations has been made and the difference can be attributed to the theory being incomplete on one hand and to the inaccuracy of some data for pure gases used to calculate the corresponding data for their mixtures.

The inaccuracy in the present measurements were limited in the region of low field, and this is attributed to the diffusion process which is more pronounced at low drift field and to the effect of the sense wire voltage in this case.

Chapter Three - References

1. F. Sauli, Principles of Operation of MWPC's and DC's, CERN 77-09 (1977).

2. D. Ritson, Techniques of High-Energy Physics (Interscience, New York, 1961).

3. G. Charpak, S. Majewski and F. Sauli, IEEE Trans. on Nucl.Sci. NS-23 (1976) 202.

4. A.J.P.L.Policarpo, M.A.F.Alves and M.J.T. Carvalho, Nucl.Inst. & Meth. 97 (1971) 491.

5. G.A.Cook (Ed), Argon, Helium and the Rare Gases, Vols. I & II, Interscience publishers, New York, (1961).

   For $Ar-N_2$ mixtures

   L.E.Boardman and N.E.Wild, Proc.Roy.Soc.(London) A162 (1937) 511.

   L.Z.Waldman, Z. Physik 124 (1947) 1.

   A.A.Westenberg and R.E.Walker, J.Chem.Phys. 26 (1957) 1753.

6. L.Koch and R.Lesueur, J. de Physique et Radium. 19 (1958) 103.

7. J.H.Holloway, Noble Gas Chemistry, (Methuen,London, 1968).

8. T.D.Strickler and E.T.Arakawa, J.Chem.Phys. 41(1964) 1783.

9. C.H.Chen et al, J.Chem. Phys. 65 (1976) 4068.

   J.B.Birks, Theory and Practice of Scintillation Counting (Pergamon Press, London, 1964).

10. W.R.Bennett, Jr., Ann. Phys. (N.Y) 18 (1962) 367.

11. D.H.Wilkinson, Ionization Chambers and Counters (University Press, Cambridge, 1950).

12. F.M.Penning, Physica 5 (1938) 286.

13. J.Townsend, Electrons in Gases, (Hutchinson's Scientific and Technical Publications, London, 1947).

14. W.N.English and G.C.Hanna, Can. J. Phys. 31 (1953) 768.

15. R.W.Crompton and D.J.Sutton, Proc. Roy. Soc (London) A215 (1952) 467.

16. L.B.Loeb, Basic Processes of Gaseous Electronics (University of California Press, Berkeley & Los Angeles, 1961).

17. L. Colli and V. Facchini, Rev. Sci. Inst. 23 (1952) 39.

18. R.A.Nielsen, Phys. Rev. 50 (1936) 950.
V.L.Frommhold, Z. für Phys. 160 (1960) 554.

19. L.G.H.Huxley and R.W.Crompton, The Diffusion and Drift of Electrons in Gases (John Wiley & Sons, New York, 1974).

20. A.G.Engelhardt, A.V.Phelps and C.G.Risk, Phys. Rev. 135 (1964) A1566.

21. A. von Angel, Ionized Gases (Clarendon Press, Oxford, 1965).

22. H.Reather, Electron Avalanches and Breakdown in Gases, (Butterworths, London, 1964).

23. V.Palladino and B. Sadoulet, Nucl.Inst. & Meth. 128 (1975) 323.

24. B.B.Rossi and H.H.Staub, Ionization Chambers and Counters, (McGraw-Hill, New York, 1949).

25. L.B.Loeb, Encyclopedia of Physics, Ed. S. Flüge, vol. 21 (Springer-Verlag. Berlin, 1956) p 471.

26. K.Mahesh, Nucl.Inst. & Meth. 153 (1978) 465.
133 (1976) 57.
L.Ferguson, Rev. Sci. Inst. 37 (1966) 964.

27. M.Comyn, Ph.D.Thesis, Durham University, 1978.

28. A.Breskin et al, Nucl. Inst. & Meth. 119 (1974) 9.
G.Charpak, Drift Chambers, Proc. ESRO Workshop, Frascati, 1974.
W.H.Fulbright, Encyclopedia of Physics (S.Flüge,Ed.,Vol.45, Springer-Verlag, Berlin 1958).
K.-P.Schelhaas et al, Nucl.Inst. & Meth. 154 (1978) 245.

29. E.D.Klema and J.S.Allen, Phys. Rev. 77 (1950) 661.

CHAPTER FOUR

CHARACTERISTICS AND LIMITATIONS OF MULTIWIRE PROPORTIONAL CHAMBERS

4.1 INTRODUCTION

A general description of multiwire proportional chambers was presented in Chapter One whilst discussing X-ray detectors. In this chapter, details of the tests made to study the general characteristics of MWPC's are described. The study of the characteristics of MWPC's is given with special emphasis on the capability of MWPC's as high count rate detectors. The limitations on high rate detections are given through a study of the factors affecting multiplication, such as the applied field and the chamber parameters, and through the effect of high rate on the performance of the chamber, i.e. dead time, peak shift, and energy resolution.

4.2 THE MULTIPLICATION PROCESS AND SPACE CHARGE LIMITATION

4.2.1 The Effect of the Electric Field on Multiplication

It was shown in Chapter One that the field near the sense wire is very high. Due to this high field, drifted electrons gain an energy higher than the ionization potential and so ionization due to electron collisions begins. The inverse of the mean free path for ionization, α, is called the first Townsend coefficient and represents the number of ion pairs produced per unit length of drift. If n is the number of electrons at a given position, then in a length dx, the increase in the number will be $dn = n\alpha \; dx$ and by integration

$$n = n_0 \exp(\alpha x) \tag{4.1}$$

and

$$M = \exp(\alpha x) \tag{4.2}$$

where M is the multiplication factor (n/n_o). In a non-uniform electric field, i.e. $\alpha = \alpha(x)$ then

$$M = \exp\left[\int_{x_1}^{x_2} \alpha(x)\, dx\right] \tag{4.3}$$

Townsend's empirical relation for low values of α is

$$\frac{\alpha}{P} = A \exp\left[-BP/E\right] \tag{4.4}$$

The coefficients A and B are known for several gases over a range for which formula 4.4 applies[1]. Knowing the dependence of α on the electric filed, the multiplication factor can be computed for any field configuration. In the region of low α, α is assumed to be linearly dependent on the electron energy ε[2]

$$\alpha = k N \varepsilon \tag{4.5}$$

where k is a constant and N is the number of molecules per unit volume. Sauli[2] has listed the values of the constants A and B in eq.4.4 as well as the values of the constant k in eq. 4.5 for some pure gases.

The addition of methane to many gases increases α at high fields. For example in 10% CH_4 + 90% Ar mixture at fields greater than 10^2 kV/cm, α is larger than that for pure argon[3]. For small fields, however, the effect is reversed and the value of α is lower in the mixture. This is due to the cooling effect of the mixture, i.e. larger mean free path for ionization which is caused by the numerous low ~~level~~ vibrational excitation levels. When the field is high enough to start ionizing collisions with

the methane molecules, i.e. for fields greater than 10^2 kV/cm and near the sense wire, the situation is reversed and the ionization is increased, because methane molecules have a lower ionization potential than pure argon.

For one of the MWPC's used in this work, the variations of E and α at any point as a function of χ, where χ is measured from the centre of the sense wire to that point, are shown in Fig 4.1a and 4.1b respectively for three values of the applied voltage V. The field E was calculated with the assumption that the region around the sense wire (up to a distance equal to the cathode-sense wire spacing) approximated to the space inside a cylindrical proportional counter, i.e. using equation 1.3 with $r_1 = 10$ μm and $r_2 = 4$ mm. The experimental variation of α with E determined by Charles[4], for 90% Ar + 10% CH_4, was used to find the corresponding variation of α with χ. From these figures, the rapid increase of E and α shows that the region in which high amplification occurs is of the order of the diameter of the wire. In this small region nearly all the ionization occurs.

4.2.2 The Effect of the Chambers Parameters on Multiplication

The dependence of the multiplication factor M on the parameters of the chambers was derived by Rose & Korff[5].

$$M = \exp \sqrt{2aN} \quad f(r_o) \quad \sqrt{V_o} \left(\sqrt{\frac{V_o}{V_s}} - 1 \right) \tag{4.6}$$

The term $f(r_o)$ involves the capacitance of the system and Erskine[6] has derived the following relation for MWPC's:

$$f(r_o) = \frac{1}{\left(\pi \frac{L}{s} - \ln \frac{2 \pi r_o}{s} \right)^{\frac{1}{2}}} \tag{4.7}$$

In these equations, V_o is the applied voltage, V_s is the threshold voltage

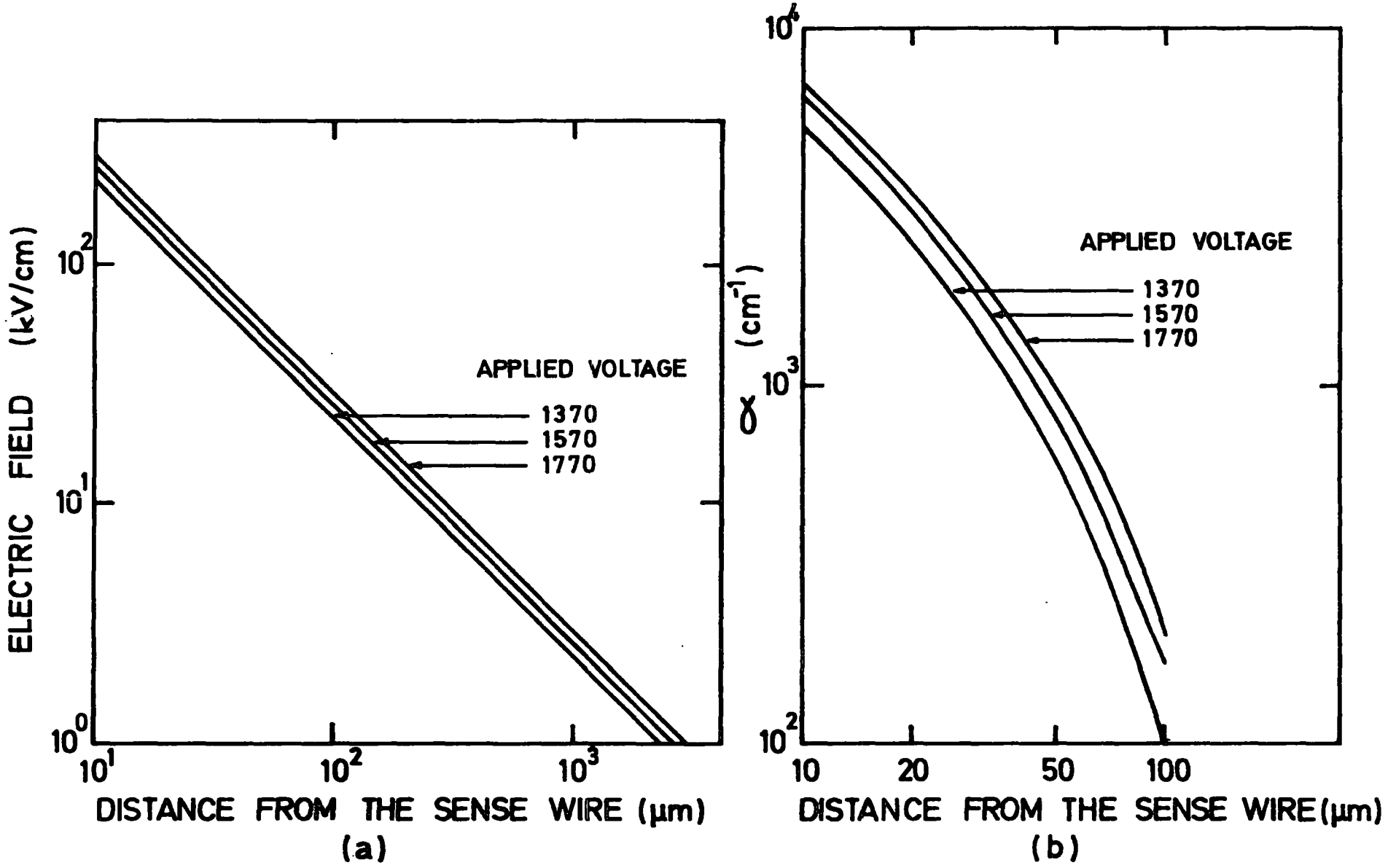

FIG. 4·1 VARIATION OF ELECTRIC FIELD AND α WITH THE DISTANCE FROM THE SENSE WIRE

(the potential at which multiplication starts close to the anode), r_o is the anode-wire radius, N is the number of gas atoms per cm^3, a is the rate of increase of the ionization cross-section with energy, s is the sense wire spacing and L is the anode-cathode spacing.

The Rose and Korff relation 4.6 coincides fairly well with the experimental measurements for low and moderate fields. The dependence of M on the anode wire radius r_o has been measured by Korff[5] and it was found, as predicted in eqn. 4.6, that M increased as the wire diameter decreased. As V_s also depends on r_o, the stability of the amplification factor (dM/M) is related to the wire diameter. The thicker the wire, the higher must be the relative uniformity[7].

A departure from equation 4.6 was observed[5] at high fields for which $M > 10^4$. In this situation the pulse size increased with voltage faster than predicted. This was attributed to the photons formed in the avalanche liberating photoelectrons which also contribute to the multiplication. The pulse size will therefore be larger than predicted by equation 4.6, which assumes the only multiplication process to be via Townsend's first ionization coefficient.

The pulse produced on the sense wire is due to the movement of both electrons and ions, formed in the avalanche. The mobility of electrons is very much higher than that of positive ions, μ_e in argon at 1 atm. is 1.47×10^3 cm^2/volt/sec and μ_+ is 1.7 cm^2/volt/sec[2]. Hence it is only the electrons which, when they are a few microns from the sense wire, give rise to a fast rise time of a few nanoseconds. The slower positive ions, moving back to the cathode wires through the rest of the field form the majority of the pulse which is few microseconds in duration. The output pulse is usually observed using a differentiating circuit, hence only the fast rising part of the pulse is observed in a practical situation.

4.3 CONSTRUCTION OF MWPC's

Many chambers were built in the process of testing and studying the parameters of MWPC's.

All the chambers had rather similar characteristics and were built from one or more perspex frames. The main difference between the chambers was in the cathode planes.

In most of the chambers the anode planes were similar. They consisted of a plane of sense wires, 20 μm in diameter, separated by 4 or 5 mm from each other. The last two wires at each end of the plane were of thicker diameter, 100 μm, in order to keep field non-uniformities small around the sense wires at the ends of the chamber. The sense wire plane was midway between the two cathode planes. The separation between the two cathode planes varied from 8 mm to 12 mm.

The cathode planes were either zig zag delay lines or a series of parallel wires. In the case of a zig zag delay line an outer grounded plane made of a copper mylar plane was also used as part of each cathode (see Fig 4.2a, b). The different characteristics of the delay lines and their outer planes for the different chambers are tabulated in Table 4.1. The zig zag delay lines were made so that one of them was parallel to the direction of the sense wires and the other was orthogonal to them. In the case of the parallel wire cathodes, both cathode planes were orthogonal to the sense wires, (see Fig 4.2 c).

The zig zag delay line was constructed by winding the wire around two lines of teeth at the ends of the cathode plane. The teeth were spaced in such a way that wires of 150 μm diameter were separated by exactly 1 mm from each other (see Fig. 4.3). The outer plane lies on the top of the delay line teeth. Hence the height of the teeth is the separation value between the delay line and its outer plane. It is desirable to maintain

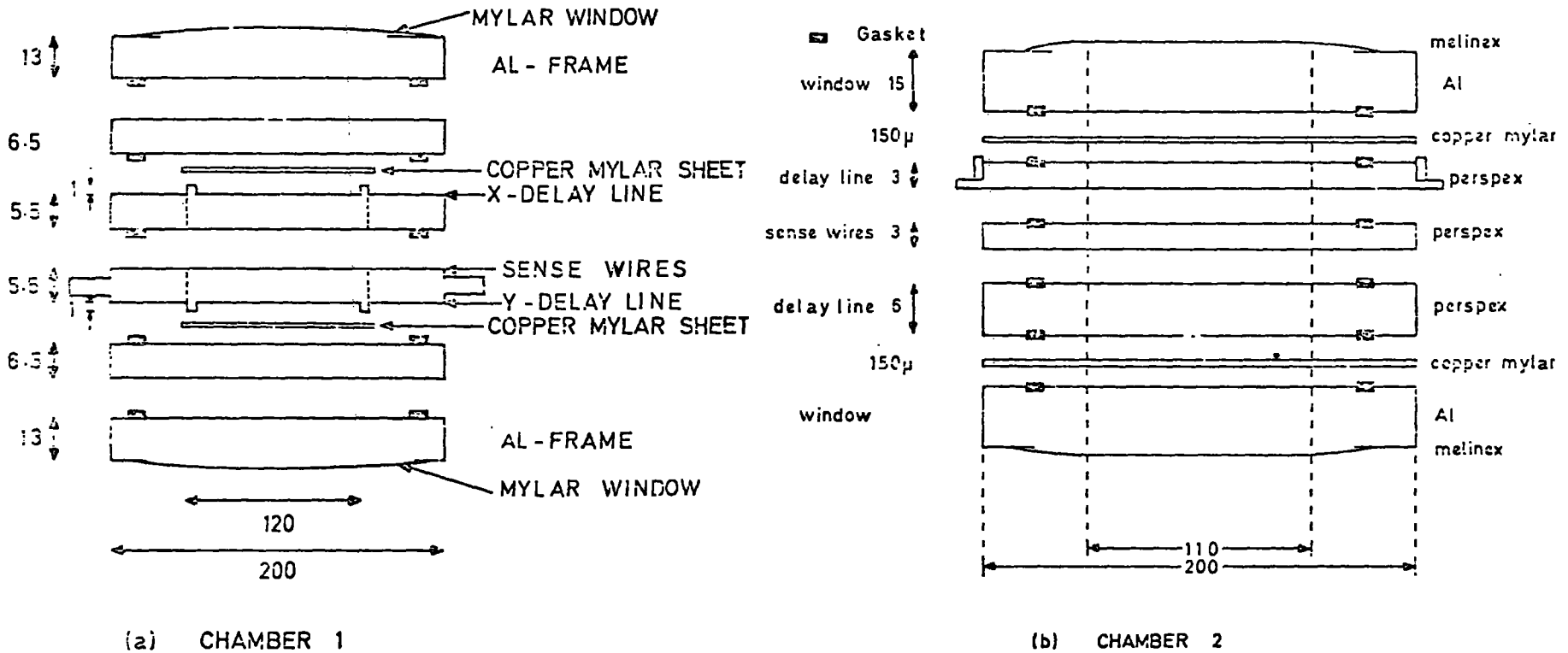

FIG. 4·2 FRAMES ARRANGEMENT (mm)

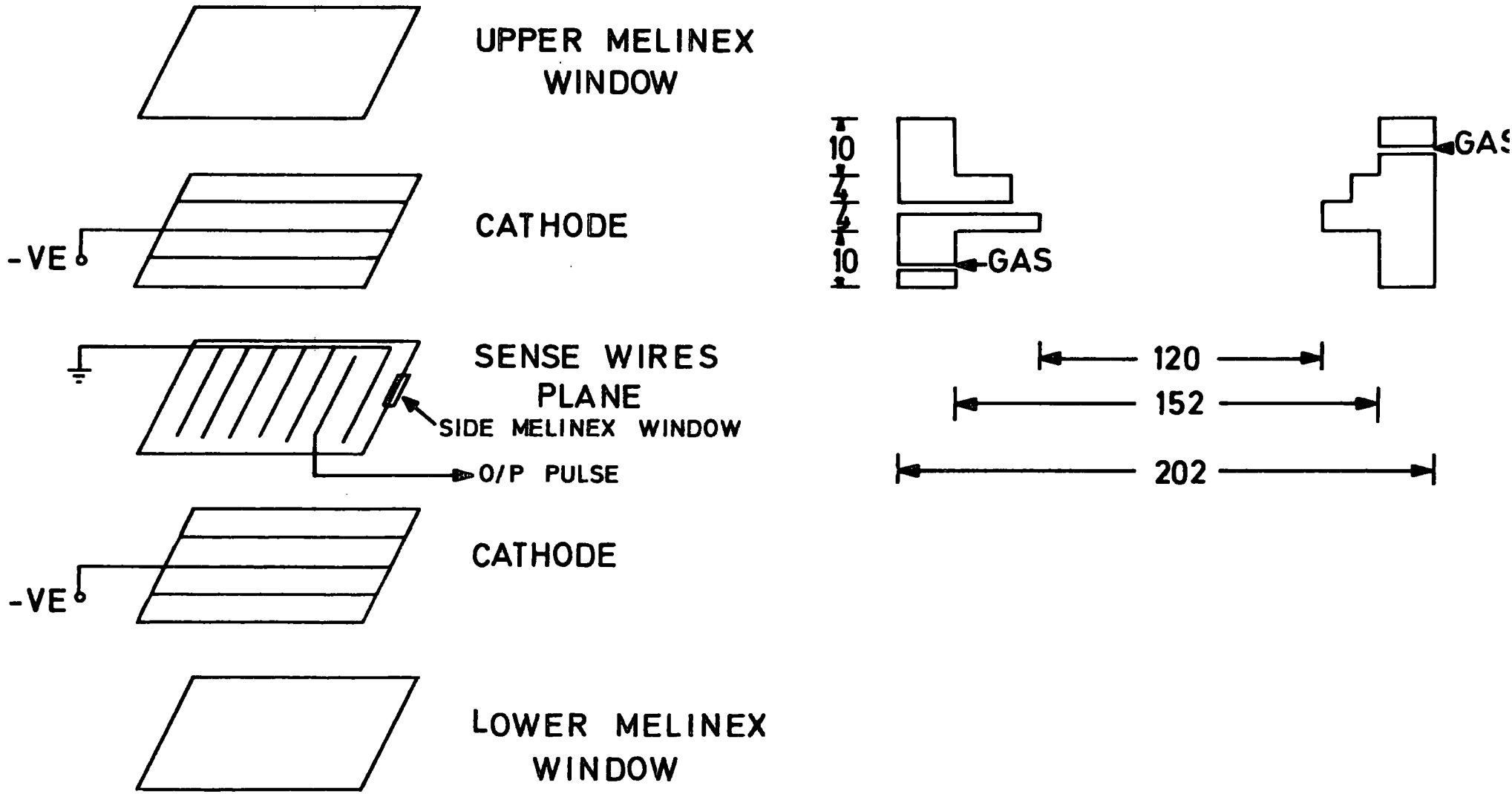

FIG 4·2(c) CHAMBER 3 (mm)

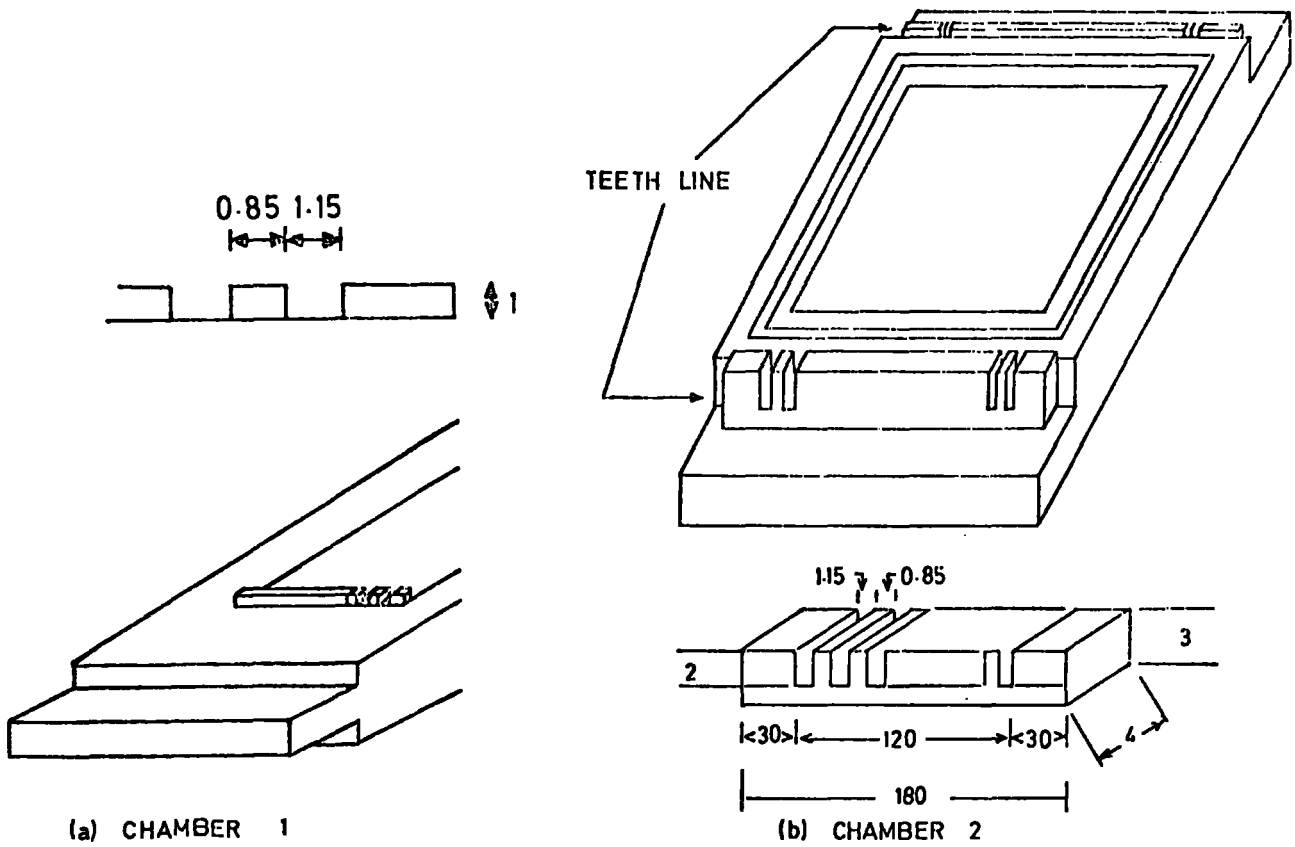

FIG. 4·3 THE DELAY LINE FRAMES. (mm)

this separation value as small as possible to obtain a high capacitance value. This gave rise to difficulties in machine processings and the height of the teeth of less than 1 mm was not attainable. A consequence of this high separation value is that the capacitance between the zig zag cathode and its outer plane is low, and this has an effect on the characteristics of the delay line.

In Chamber 1, just described, the lines of the teeth were inside the active area of the chamber. A better method was achieved with Chamber 2 when the line was put outside the active area and the copper-mylar plate was pressed between the frames rather than lying above the teeth line where it could only be fixed at its four corners (see Fig 4.3.b). The thin copper-mylar sheet (150 μm) placed with the copper layer facing outwards provided not only low separation value but also higher dielectric constant between the delay line and the copper surface which acts as the earth plane - relative dielectric constant for mylar is 3.12[8] in D.C. conditions. The low separation value and the high dielectric constant provided a higher value of C. Fig 4.2a and 4.2.b show the frames arrangements for both chambers.

Chamber 3 was built for the high count rate experiments, using a different readout technique. It was possible to build the chamber from one perspex frame, of 28 mm thickness, which is advantageous for gas-tight requirements. The cathode planes were made of a series of parallel wires, of 100 μm diameter, spaced on a 1 mm pitch (see Fig 4.2c). The readout technique used was to extract the pulse from the sense wire plane rather than the cathode plane as was the case for the previous chambers.

TABLE 4.1

	Chamber 1	Chamber 2	Chamber 3
The anode plane:			
Wire diameter	20 μm	20	20
Wire spacing	5 mm	4	4
Anode-Cathode separation	5.5 mm	6	4
The cathode plane:			
Type	delay line	delay line	parallel wires
Wire diameter	152 μm	152	100
Wire spacing	1 mm	1	1
Total length	14.3 m	23.4	
D.C. resistance	12.1 Ω	24	
Total delay time	45 ns	90 ns	
Cathode-earth gap	1 mm	<150 μm	
C	190 pF	1180	
L	10.66* μH	8 μH	
Z_o*	237 Ω	76.5	
V_p*	$0.22 \times 10^8 \frac{m}{sec}$	$0.11 \times 10^8 \frac{m}{sec}$	

* Calculated

4.4 PERFORMANCE OF MWPC's

4.4.1 Delay Line Readout Techniques

As it was mentioned earlier (Section 1.3.3), there are different techniques for extracting data from MWPC's and the requirements of the particular experiment dictate the most appropriate technique. A number of arrangements for reading out data, without the use of individual amplifiers, has been described by Charpak et al[9]. A notable method is the one which involves the use of delay lines. In this method the position of the avalanche can be localized by the time difference in the arrival of the two pulses at each end of the delay line.

The delay line technique was developed by the Perez-Mendez group[10]. The delay line was capacitively coupled to the anode wire of the chamber. This method suffered from small measurable signals which led to the requirement of high gas gains and low noise amplifiers. A more satisfactory method used direct coupled delay lines where the whole outer plane was made part of a transmission line[11]. A simpler method was developed by Lee et al[12] using a helical delay line connected to the anode plane. In a variation of this method, the helical delay line was connected to the cathode wires. With one delay line per cathode plane, two dimensional readouts were achieved from one chamber. This method proved to be less costly and a spatial resolution better than 400 μm was achieved[13] along the direction of the sense wire. One disadvantage of helical delay lines is that they are difficult to handle and great care is needed when soldering the cathode wires to the delay line.

A planar delay line pioneered by Borkowski and Kopp[14] is simpler in construction and can operate at count rates up to 50 kHz[15]. Some tests using a planar delay line are described in this chapter.

4.4.2 Theory of the Pulse Delay

The transmission of a pulse from one point to another introduces delay, merely by the time taken for the pulse to travel the finite distance between the two points concerned. A pulse travels along an ideal conductor with the velocity of propagation of radiation in free space, of 3×10^8 m/sec, causing a delay of 3.3 nsec/m.

Because a transmission line contains both resistive and reactive elements, it offers an impedance (Z_o) to any signal it carries. This is known as the characteristic impedance and can be written as $\left[(R_1+j\omega L_1)/(G_1+j\omega C_1)\right]^{\frac{1}{2}}$, where R_1, L_1, G_1 and C_1 are the resistance, inductance, conductance and capacitance per unit loop length. Practically R_1 and G_1 are negligible and the characteristic impedance (Z_o) is approximately a pure resistance independent of the line resistance[16]. Z_o can be written as

$$Z_o = (L_1/C_1)^{\frac{1}{2}} \tag{4.8}$$

The unit loop length is defined as the spacing between two adjacent turns of the line[17]. The velocity V of a pulse moving along the line is dependent on $1/(L_1C_1)^{\frac{1}{2}}$, and the delay time per unit length is therefore

$$t = (L_1C_1)^{\frac{1}{2}} \tag{4.9}$$

In Table 4.1 the values of Z_o, V_p and L were calculated from the above relations. The increase in inductance increases both the impedance and the delay. Decreasing the spacing between the delay line and its outer plane increases the capacitance. This increases the delay but reduces the impedance. Since the signal amplitude at the amplifier input terminals is proportional to the characteristic impedance of the line[18], high line

impedance is desirable. In general, the delay line must be sufficiently long with respect to the rate of rise of the signal to achieve the desired resolution - a ratio of delay to rise time of at least 10 is necessary. The rate of rise of the signal is dependent on the counter geometry and the electron drift velocity in the gas. The delay should not be so long as to lead to undesirable ambiguities at high count rates.

The propagated pulse along the delay line suffers from two undesirable features, namely attenuation and dispersion. Attenuation limits the length of the line. Also the decrease in the pulse amplitude, due to attenuation, decreases the signal-to-noise ratio and hence deteriorates the spatial resolution. The attenuation along the total length of the line is given[17] by

$$\text{attenuation} = \exp\left(-\frac{R}{2Z_o}\right) \tag{4.10}$$

where R is the total series resistance including the skin effect. Dispersion, which can be identified from the percentage of change in pulse rise time, leads to loss of timing accuracy.

Because Z_o decreases with frequency for helical delay lines and R increases with frequency due to the skin effect, the high frequencies are attenuated more than the low frequencies[19]. The other delay line parameter which is a function of frequency is the series inductance. The change of inductance with frequency generates dispersion[19].

4.4.3 Tests of Transmission Lines

In a practical transmission line the important characteristics are usually a small attenuation of the signal but at the same time a long delay time. However, a long delay time has its own drawbacks, it limits the rate of operation of the chamber.

The characteristics of the planar delay line were studied and tested by varying different parameters of the line[20]. The variables were the diameter of the wire (D), the separation between the delay line and its outer plane (s), and the thickness of the outer plane (t). These tests were carried out with a separate frame on which a transmission line was wound. The input pulse was generated by a scintillation counter irradiated by Fe^{55}. The input pulse and the delayed pulse, from the other end of the transmission line were observed on a fast Tektronix type 7704 oscilloscope. The attenuation coefficient is defined as the ratio between the amplitudes of the delayed to the original pulse. $A\,\% = \left[A(\text{delayed})/A\,(\text{original})\right] \times 100$. The rate of change in rise time R.T% is calculated from the difference between the rise time of the original and delayed pulse to the rise time of the original pulse.

The effect of the wire diameter (D) on the attenuation coefficient (A%), delay time (T), resistance (R_o) and change in rise time R.T% is given in Table 4.2.

TABLE 4.2

Wire length = 2.98 m		Spacing = 1 mm	
D(μm)	50	100	180
T(ns)	7	6	5
A(%)	30.8	53.1	54.9
R_o (Ω)	160	5	2
R.T%	27.3	20	11.1

In thick wires, due to low R_o values, the attenuation and dispersion (or change in rise time) were less than that in thin wires. This follows because $R_o = \frac{\ell\rho}{A}$, hence $R_o \alpha \frac{1}{D^2}$. The use of fine wires leads to high dispersion and attenuation but more delay.

The separation between the delay line and its outer plane (S) was changed and its effect on C, T, Z_o and A% was observed. Increasing the capacity, by decreasing the separation increased the delay time as in eqn. 4.9, but this caused a decrease in the characteristic impedance Z_o which led to more attenuation.

The thickness of the outer plane (t) had an effect on C. Increasing t led to a decrease in C. This was more obvious at low separation values. This may be due to the change in the distance between the delay line and the centre of the outer plane.

To compromise between the low attenuation and dispersion obtained from thick wires and the long delay from fine wires, a wire of 100 μm diameter was chosen. Thin outer planes, very near to the delay line, for high capacity were used. Fig 4.4 shows input and delayed pulses. Attenuation and dispersion are obvious in the delayed pulses.

4.4.4 Spatial Resolution and Two Dimensional Images

Chambers described in Section 4.3 were used to test the spatial resolution of the MWPC and the two dimensional imaging technique. Fig 4.5 shows the experimental arrangement for this part. Moving a collimated Fe^{55} source above the chamber in the x or y-direction, provided a moving spectrum on the pulse height analyser (PHA) from which the spatial resolution was measured. This was achieved by sending the pulses from each end of the transmission line to the START and STOP inputs of a time-to-amplitude converter (TAC). This TAC then produced an output signal whose amplitude was proportional to the time difference between the START and STOP. This

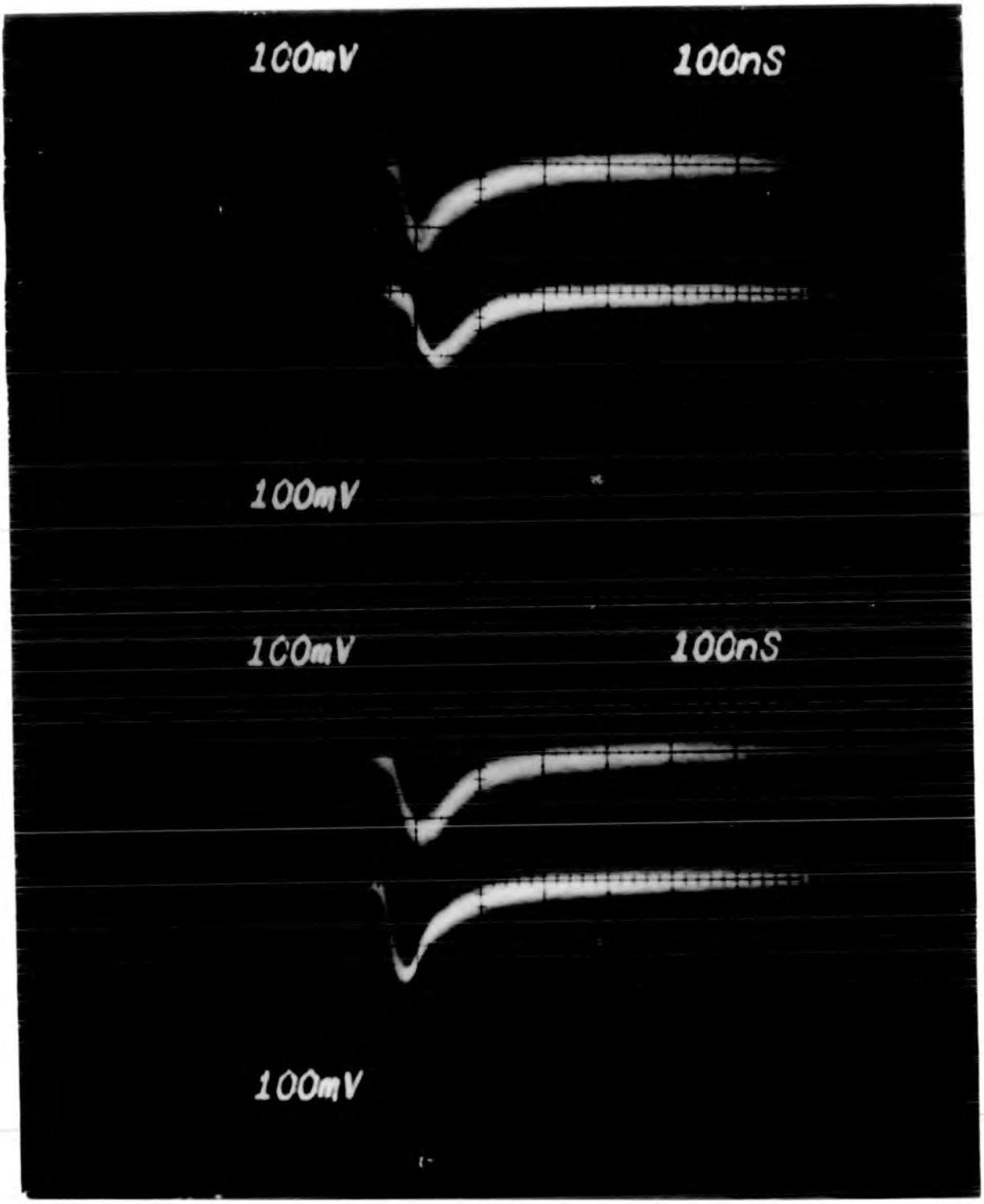
100mV
100nS
100mV
100mV
100nS
100mV

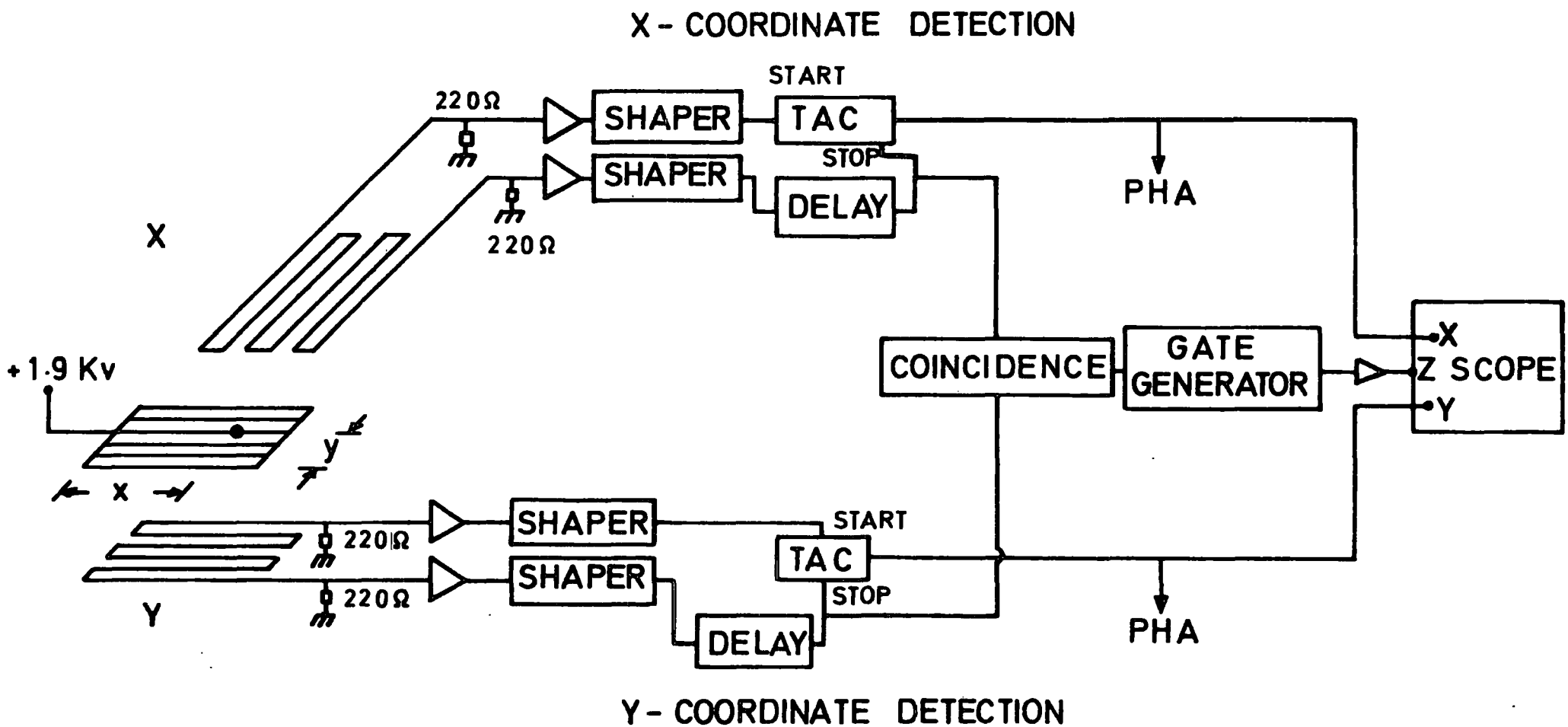

FIG.4·5 CIRCUIT DIAGRAM OF READOUT SYSTEM

operation was performed on the x and y coordinates independently. To ensure that the START signal always came before the STOP, a delay of 127 nanoseconds was added to the STOP.

Fig 4.6 shows the effect on the peak position and the spectra of moving the source from one side of the chamber to the other. The procedure of obtaining this figure was to put the collimated source at position 1, accumulate the data for a few minutes, printout the data then erase it. Next step was to move the source to position 2 and to repeat the previous steps. An accumulation of data for many positions is shown in Fig 4.7. The linear relationship between the peak position and the source position provides the calibration curve to convert the channel number into millimeters as in Fig 4.6. Keeping the gain of the electronics constant, the conversion factor "mm/channel" obtained from Chamber 1 improved from 1 mm/ch.[21] to 0.3 mm/ch. in Chamber 2[22]. The main reason was due to the increase in the capacitance and in the propagation delay of Chamber 2 as shown in Table 4.1. It is also possible to convert the channel number scale into a time scale. The calibration of delay time per channel was done by delaying a pulse using a delay box. Fig. 4.8 shows this calibration.

The spatial resolution was calculated from the (fwhm) of the spectrum taking into account also the length of the sense wire exposed to radiation D[21].

where

$$\text{Spatial Resolution} = \sqrt{(\text{fwhm})^2 - D^2} \qquad (4.11)$$

The best spatial resolution obtained from Chamber 2 was 626 μm in the x-readout. This value includes the contribution of the electronic noise and hence the chamber resolution is much better than the given value (< 500 μm). The spatial resolution along the sense wires (x-readout)

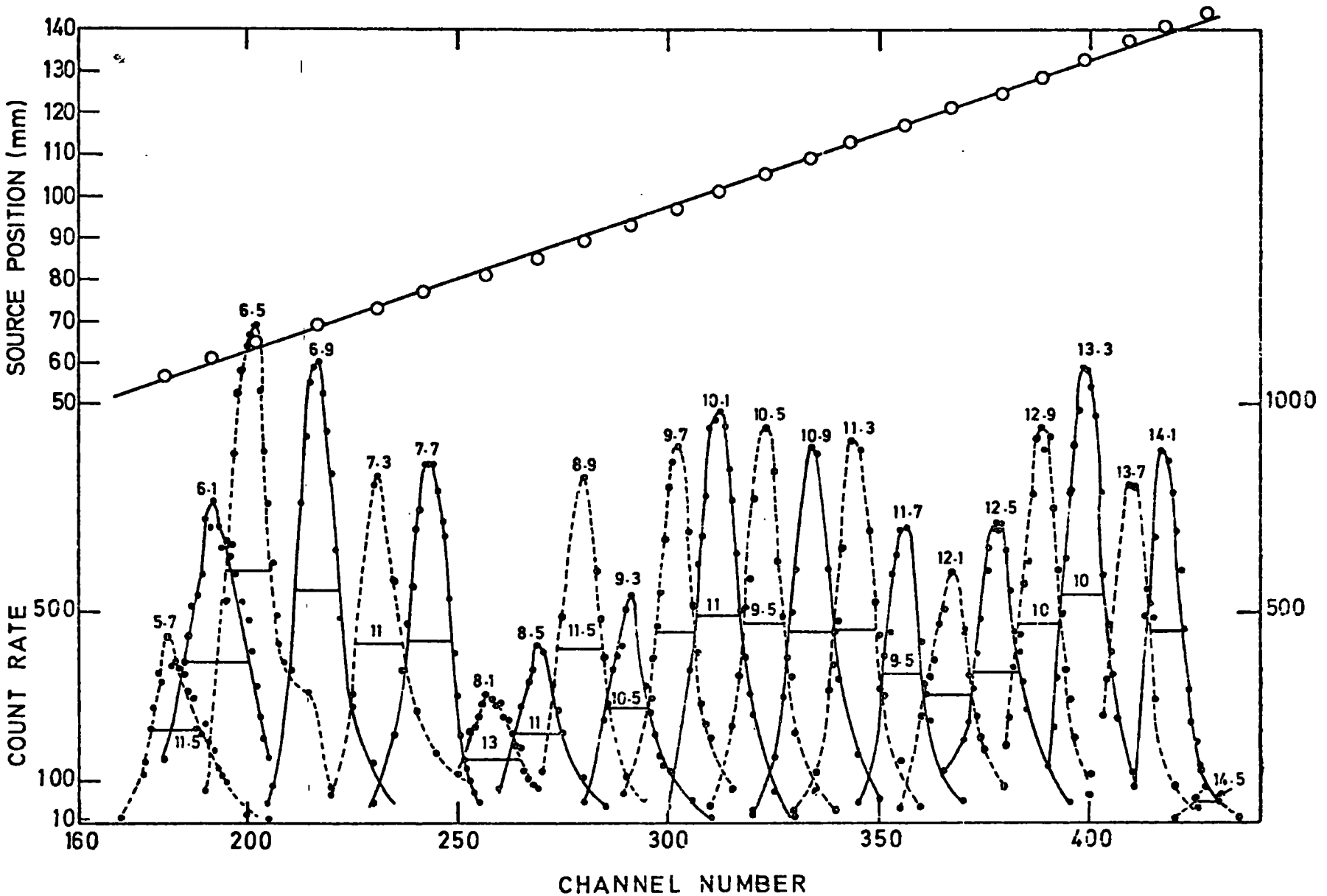

FIG. 4·6 SPECTRA AT DIFFERENT SOURCE POSITIONS AND PHA CALIBRATION.

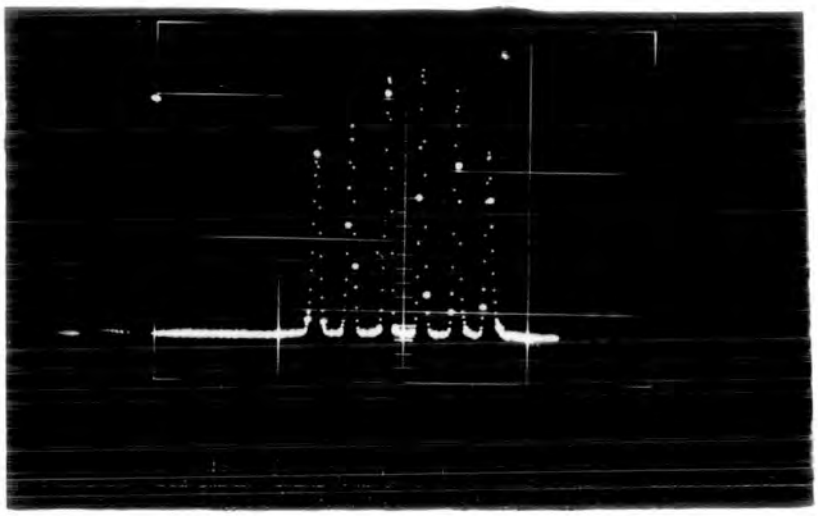

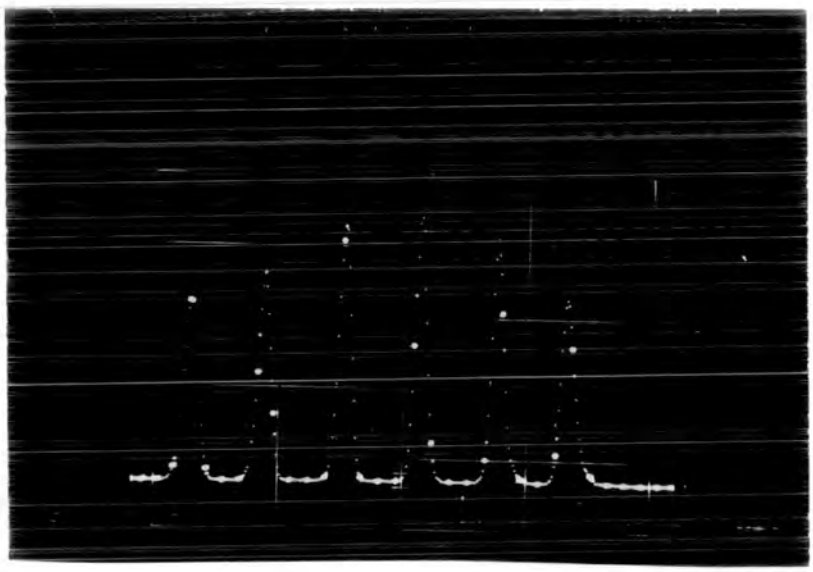

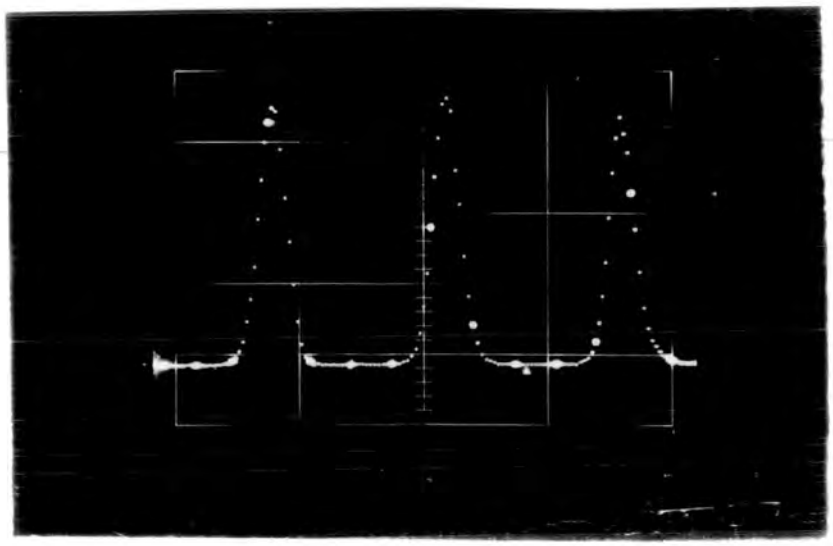

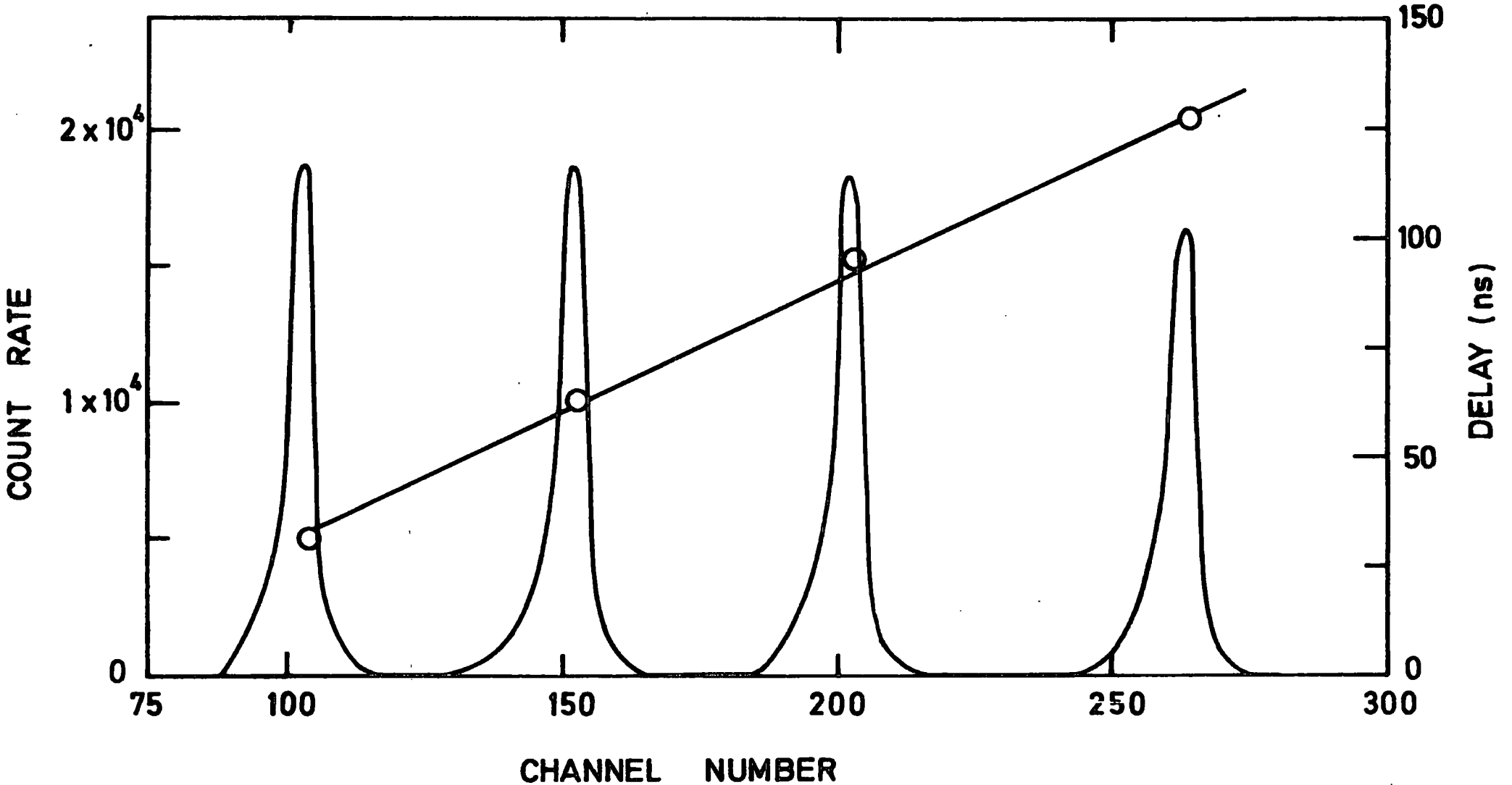

FIG. 4·8 DELAY TIME CALIBRATION.

differed from that in the orthogonal direction (y- readout) for many reasons, such as different C values for the two readouts, and it was difficult to provide identical gain in the four amplifiers.

With good spatial resolution it is possible to obtain two dimensional images from MWPC's. The output from each TAC was fed to the x and y amplifiers of a Philips oscilloscope (PM 3230). The two TAC stop inputs were fed to a coincidence unit to register a genuine event. This event caused an amplifier to unblank the oscilloscope for a period slightly less than the x and y pulse lengths applied to it. A negative pulse voltage of 15 V_{p-p} was required at the Z-input of the scope, and with normal brightness the trace appeared dotted. Objects were put between the source and the chamber. Two dimensional images were observed on the scope. Fig 4.9a shows five pieces of G10 of 500 μm thickness and Fig 5.9b is an image of three spanners. From comparing the size of the actual objects with their images, it was found that the ratio is about 2. This ratio can be varied by changing the distance between the source and the chamber. The two dimensional images obtained show the good spatial resolution of the chamber. The smooth image lines between the sense wires are due to the small delay line spacing (1 mm) in between the sense wires spacing which was 4 mm. The possibility of reading cathode planes and interpolating between wires led to better spatial resolution than obtained from the anode plane.

4.4.5 Energy Resolution

When the chamber was irradiated with x-rays from Fe^{55}, the amplified output pulse was observed on a PHA. The pulse height spectrum indicated two peaks which can be explained as follows. At low energies where the photoelectric effect is predominant, an x-ray produces a photopeak of almost Gaussian shape when all the incident energy has been absorbed, 5.9 keV in the

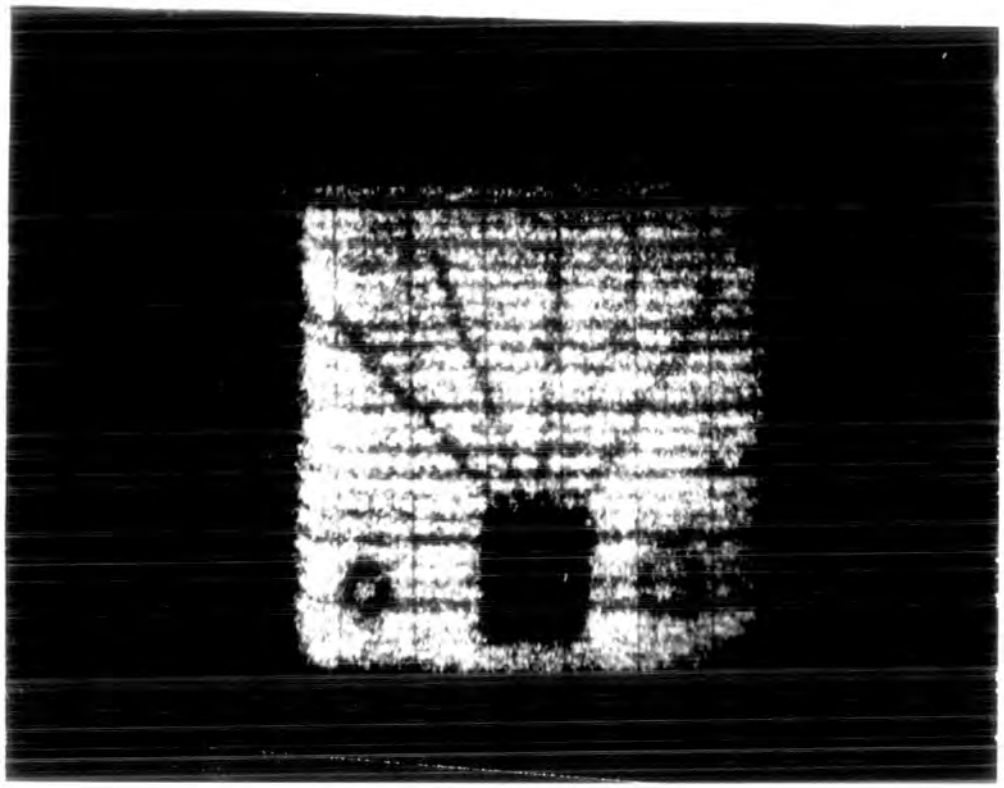

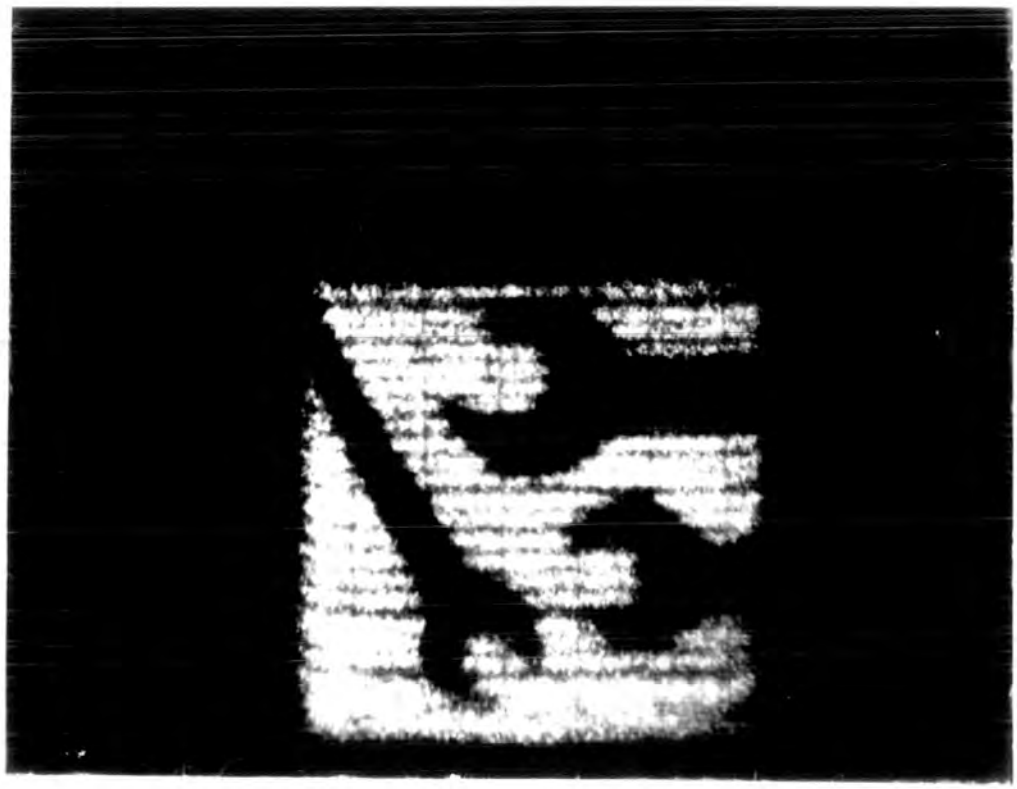

case of Fe^{55}. The second peak, due to the argon K-X-ray escape peak also appears, lying at about 2.9 keV below the full energy peak. This peak is relatively broad due to the escape of K- X-rays of different energies (K_α = 2.95 keV, K_β = 3.19 keV) and to statistics.

In this energy range around 5.9 keV, the calculated energy resolution in a gas filled chamber (using Wi = 30 eV) was found to be 17%[23]. Charpak[24] obtained a 15% energy resolution in an argon-pentane MWPC.

Measurements of the energy resolution using Chamber 2 with Ar+10% CH_4 were obtained from the pulses from all the sense wires, connected together, through a CR network of C = 560 pF and R = 1.5 kΩ [23]. The pulse was amplified and observed on a PHA. The signal-to-noise ratio was measured by decreasing the lower level of the PHA discriminator (LLD) Fig 4.10 shows a spectrum of Fe^{55} with low LLD value. This was done in order to calculate the signal-to-noise ratio which is the ratio between F and A in Fig 4.10. The signal-to-noise ratio was observed to increase with increase of the applied voltage until it saturates as shown in Fig 4.11. This can be explained as due to the increase in the signal with increase of voltage and hence it leads to a better signal-to-noise value until the plateau in the pulse amplitude is reached. The variation of energy resolution with signal-to-noise ratio is shown in Fig 4.12, where the energy resolution improves with higher signal-to-noise values. This is due to the decrease in the contribution of noise to the energy resolution compared to that of the original signal. The best energy resolution obtained with this set-up was 17% when the signal-to-noise ratio was 8.

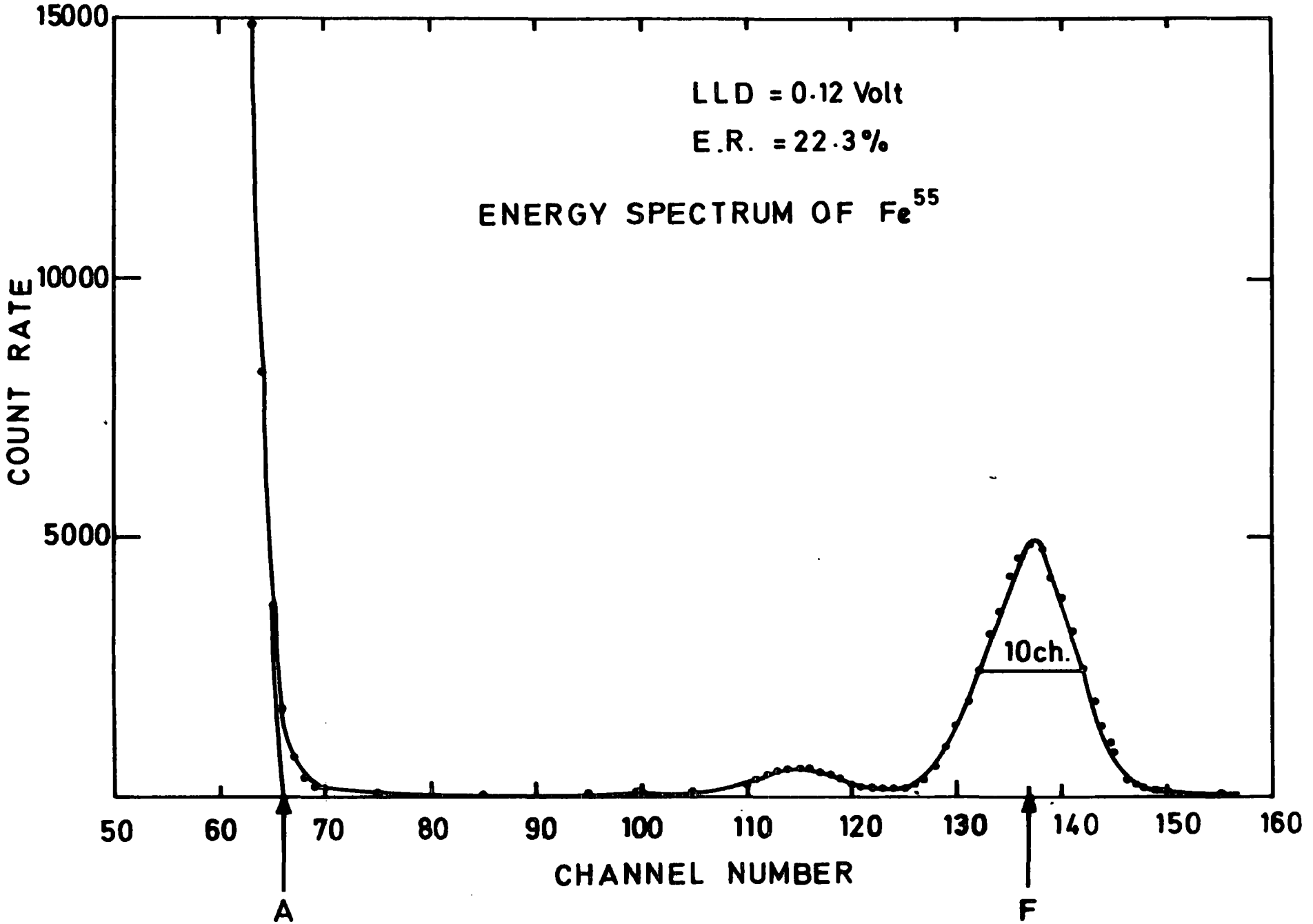
LLD = 0·12 Volt
E.R. = 22·3%
ENERGY SPECTRUM OF Fe55
COUNT RATE
15000
10000
5000
10ch.
50
60
70
80
90
100
110
120
130
140
150
160
CHANNEL NUMBER
A
F

FIG. 4·10

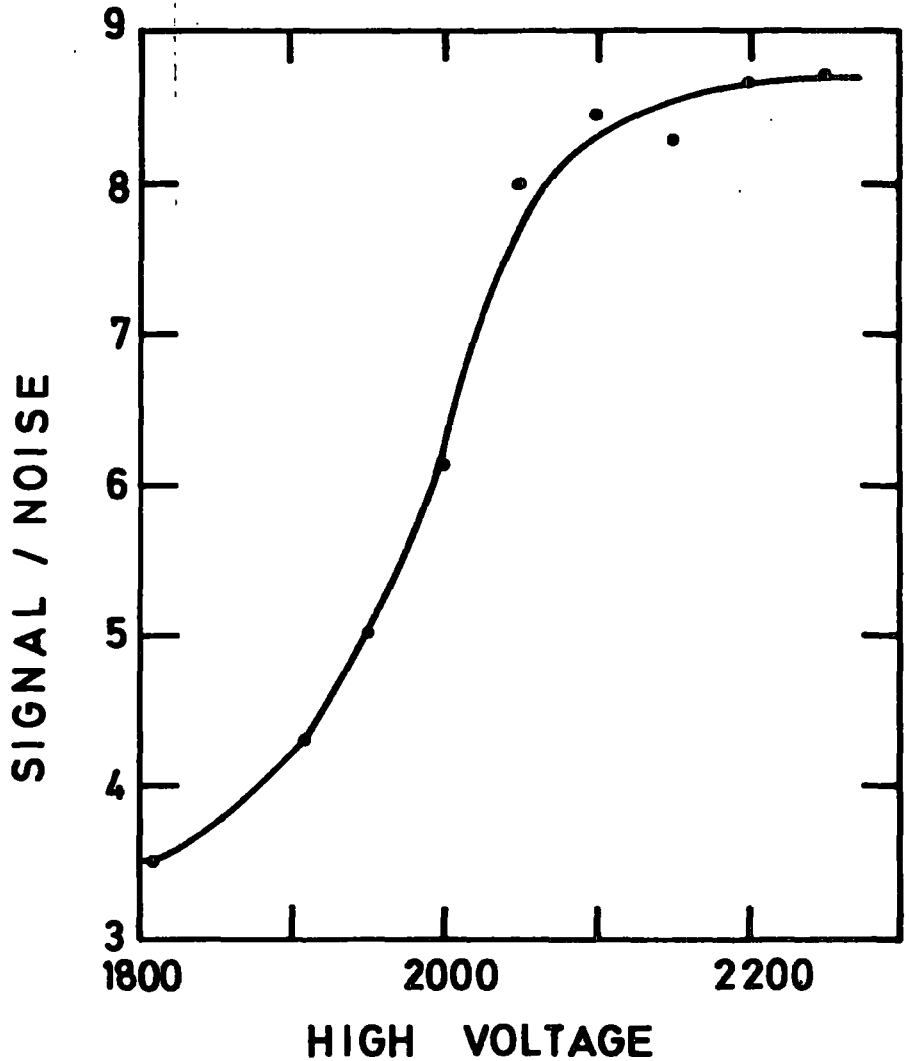

FIG. 4·11 CHANGE OF SIGNAL/NOISE RATIO WITH H.T.

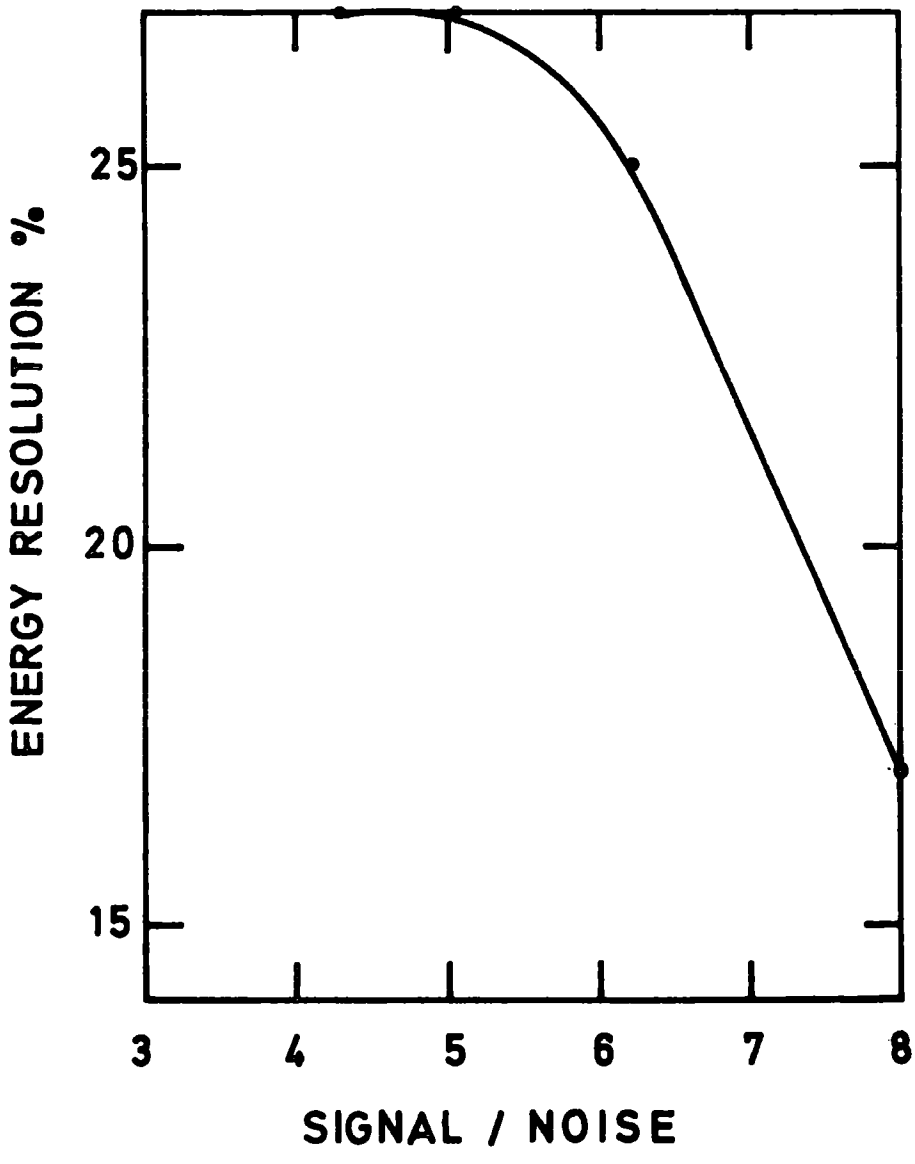

FIG. 4·12 CHANGE OF ENERGY RESOLUTION WITH SIGNAL/NOISE RATIO

4.5 A MWPC FOR HIGH COUNT RATE EXPERIMENTS

4.5.1 Space Charge Limitations and High Rate Effect on Multiplication

At amplifications above 10^4, space charge limitations begin to occur. Due to the avalanche, a high density of positive ions is formed around the sense wire which lowers the effective field around the wire. This phenomenon limits the performance of chambers at high rates.

The decrease of the pulse height, due to the growing space charge around the anode wires at high rates, is an effect which was known in the early days of proportional counters[25]. The effect of the space charge on the performance of proportional chambers was reported by several authors[26], in particular Hendricks[18] developed a quantitative theory for the mean shift of the pulse height and confirmed it experimentally. Makowski and Sadoulet[27] observed the loss of efficiency and decrease of pulse height at high rates in a MWPC. They suggested several solutions to decrease this effect, for example, decreasing the multiplication factor and increasing the ion mobility, such as using helium where $\mu_+ = 10.2\ cm^2/V/sec$ compared to that of argon ($\mu_+ = 1.7\ cm^2/V/sec$)[2]. Spielberg[28] proved that the magnitude of the shift depends on the hardness of the material used for the anode wire and its diameter. He claimed that the space charge is not the major cause of the shift because the space charge should be independent of anode material. He also suggested that some sort of contaminant mechanism, from the quenching gas, may produce another source for the shift. Elimination of the shift, up to a rate of $\sim 2 \times 10^4$ c/sec, was achieved with thicker wire ($\sim$ 125 μm in diameter) of hard material such as tungsten which has hardness (N/m^2) about ten times that of copper and five times that of nickel.

Sipila and Vanho-Honko[29] have studied recently the effect of rate

on the peak shift experimentally and theoretically. A good agreement was obtained between their measured results and the calculated results from Hendrick's space charge model. They contradicted Mahesh's[30] hypothesis which rejects entirely the space-charge model and considers the columnar recombination of primary ions to explain the shift. Pawlowski and Cudny[31] derived the mean space charge in a cylindrical proportional counter and their formula differs slightly from that given by Hendricks[32] by a factor of π . They also attributed the shift at high rates to the influence of space charge.

Hendrick's theoretical predictions[32] show how the mean shift in peak position depends on various parameters of the detector (in particular anode and cathode diameters and gas gain), parameters of the fill gas (pressure, mobility of positive ions), and parameters of the incident radiation (energy, mean count rate, and distribution along the wire). The relative shift of the pulse amplitudes is given by :

$$S = \frac{\ln 2}{8\pi^2 \varepsilon_o} \frac{b^2 p}{\Delta V \mu L} \left\{ 1 + \ln \left[\frac{1}{Kpa \ln\left(\frac{b}{a}\right)} \right] \right\} \frac{M}{V} \bar{R}\, e \frac{E_\lambda}{W} \quad (4.12)$$

where p is the fill gas pressure, μ is the mobility of positive ions, L is the width of the incident beam. ε_o is the permittivity of free space, a is the radius of the central wire, b is the radius of the outer shell, M is the multiplication factor, $\bar{R}$ is the mean counting rate, W is the energy required to create an electron-positive ion pair in the counter fill gas, e is the elementary charge, E_λ is the energy of the incoming photon, V is the voltage between the anode and cathode, ΔV is the potential difference through which an electron has moved in covering the distance between successive ionizing events and K is the critical value of E/p below which ionization does not occur. ΔV and K are usually called[33] Diethorn gas constants.

All the parameters appearing in Eqn. 4.12 were shown experimentally to affect the shift in a similar manner to the theoretical predictions except for the energy of the incident radiation E_λ . This departure was attributed to the fact that the change in the absorption coefficient with photon energy and gas pressure was not considered in the derivation of eqn. 4.12.

From Hendrick's equation 4.12, the parameters which one can alter to decrease the shift are mainly the geometrical parameters and the multiplication factor. A decrease in the ratio b/a, to decrease the shift, will lead to an increase in the operating potential. The effect of geometrical parameters on the energy resolution of the detector is assumed[32] qualitatively to improve the resolution because they decrease the space charge effect.

Drift chambers can be treated approximately as equivalent to cylindrical proportional counters of radius b by treating the zero equipotential which is roughly cylindrical around the sense wire with a radius b as the other electrode[34]. Charpak's derivation[34] of the relation between the mutliplication factor (M) with the average rate ($\bar{R}$) and the effective anode voltage (V_o) is given by

$$M = M_o \exp(-K M_o \bar{R}) \tag{4.13}$$

where

$$M_o = k \exp(V_o) \quad \text{and} \quad K = \frac{ne}{4\pi^2 \varepsilon_o} T$$

n is the total primary ionization and T is the total drift time of positive ions to the cathode (in this approximation to the V = 0 equipotential). The exponential decrease in M with rate coincides with the experimental results[34].

The space charge, resulting from the slowly moving positive ions as they drift from the central wire towards the outer shell, causes a change in the electric field within the detector to a value different from the applied field. This changes the gas amplification factor for any subsequent ionizing event which might occur before the space charge has drifted to the cathode, and ultimately results in a significant change in the position and breadth of the energy peak created by monoenergetic X-rays.

The most significant improvement in performance, from the space charge point of view, was obtained[32] by operating the detector at as low a gas amplification factor as possible. This required that the amplification system consisted of a high gain, low noise preamplifier and a main amplifier to avoid degradation of resolution of the detector due to electronic noise. The amplification factor cannot be adjusted by varying the sense wire potential independently from the drift potential. The method suggested by Charpak[35] for altering the amplification was to adjust the wire diameter in such a way that it works in the proportional amplification region when the proper drift voltage is applied.

4.5.2 Experimental Arrangement

To test the count rate capability of MWPC's and the count rate effect on the energy resolution, a conventional MWPC was built from one perspex frame of 28 mm thickness. The characteristics of this chamber are given in Table 4.1 (Chamber 3) and it is shown also in Fig 4.2c. Upper and lower windows of the chamber were melinex sheet of 50 μm thickness, a side window was also made to allow X-rays into the chamber parallel to the planes of the electrodes and perpendicular to the direction of the sense wires. The two cathode planes were connected together to a negative potential and the sense wires were connected to zero potential. One sense wire at a time was connected to an amplifier and counting system to study the pulse heights.

A block diagram of the circuits used to store the pulses in the PHA is shown in Fig 4.13. The maximum capability of the PHA used for this purpose was only 10 kHz. The input pulse rate into the PHA was reduced by 10 or 100 times as necessary by using decade scalers and a linear gate, which is an AND gate which accepts signals of any shape and not only signals of logic levels. The signal from the chamber was amplified by means of a current amplifier of the type used in the g-2 experiment[36] which was available at that time. The negative output pulse from the amplifier was delayed and then fed into the linear gate. The positive output pulse, from the amplifier, was shaped to NIM standard pulse and was used to open the gate for a specific width controlled by the dual trigger, for every 10 th (using one decade scaler) or 100 th (using two decade scalers) pulse.

4.5.3 Dead Time

The maximum speed of a counter is limited by the dead time of the system after an event. The two-source method provides a means of measuring the dead time (τ) of a counter using the approximate expression[37]

$$\tau = \frac{m_1 + m_2 - m_{12}}{2\, m_1 m_2} \tag{4.14}$$

where m_1 is the count rate of source 1, m_2 is the count rate of source 2 and m_{12} is the count rate of both sources. As the numerator in eqn.4.17 is a small quantity, an accurate measurement of m_1, m_2 and m_{12} would be necessary. To correct a measured count rate (m), the real count rate n will be

$$n = \frac{m}{1 - m\tau} \tag{4.15}$$

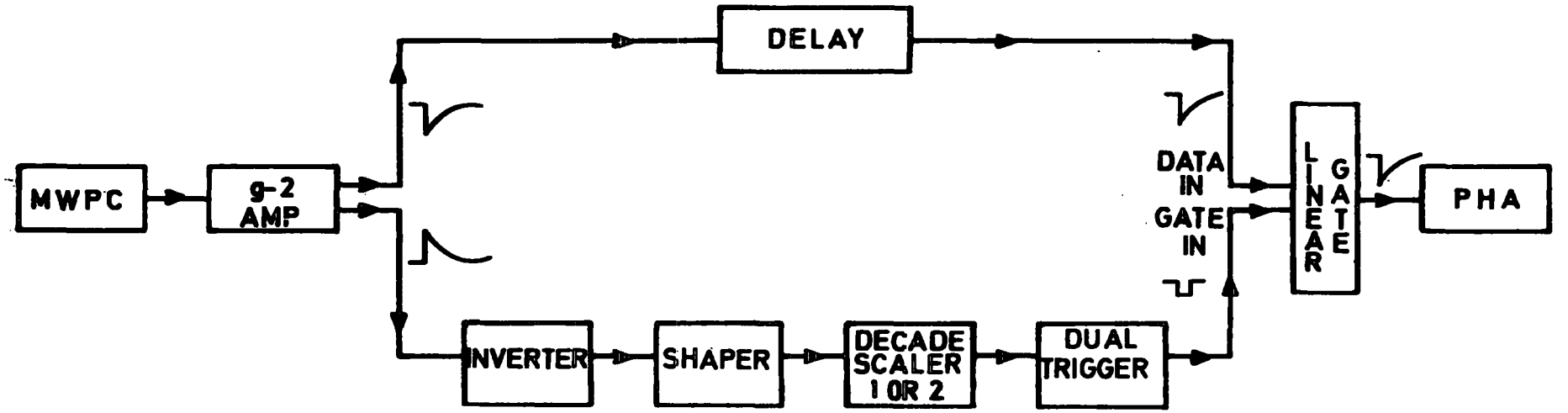

FIG. 4·13 ELECTRONIC ARRANGEMENT FOR HIGH RATE STORING

Two sources, of Fe^{55}, of strength 20 mci and 8 mci were used to measure τ for chamber 3. The dead time of the chamber was found to be 140 ± 30 nsec. This confirms Charpak's conclusion[38] that the total dead time need not exceed a few hundred nanoseconds in MWPC's. From eqn. 4.15, it is obvious that the maximum rate for a chamber should not exceed $1/\tau$, i.e. $m\tau$ should be less than one. Hence with 140 nsec the maximum rate is less than 6 MHz. It is worth mentioning that the dead time in Chamber 2, with delay line cathodes, was found to be 250 nsec[22], i.e. a maximum rate of less than 4 MHz. This confirms Barkomski and Kopp's[15] conclusion that the Chamber 3 type of MWPC can possess higher count rate capabilities than that of Chamber 2 types, because each anode is an independent counter.

4.5.4 High Rate Detection

The performance of the MWPC at high rates was investigated by allowing X-ray into the chamber parallel to the cathode planes and perpendicular to the sense wire plane. To achieve this, the source was placed on the side window. The counting rate of the wire under test was obtained by connecting it to the counting system. The count rates of the first 19 wires are shown in Fig 4.14. The decrease in count rate was found to be exponential as expected : A comparison was made between the count rate obtained by connecting wires together and those obtained by adding the count rates of the individual wires. The additive rates were found to be more than the rates obtained by connecting the wires by about 4%. This is due to the X-ray converting almost exactly in the middle between two sense wires and to the pile-up of pulses in the amplifier at high counting rates. The count rate observed from the first wire near the source was 1.6×10^5 per second, whereas the count rate obtained from the addition of the first 25 wires was 6.9×10^5 per second. This is not the maximum value and the limitation here was the strength of the source.

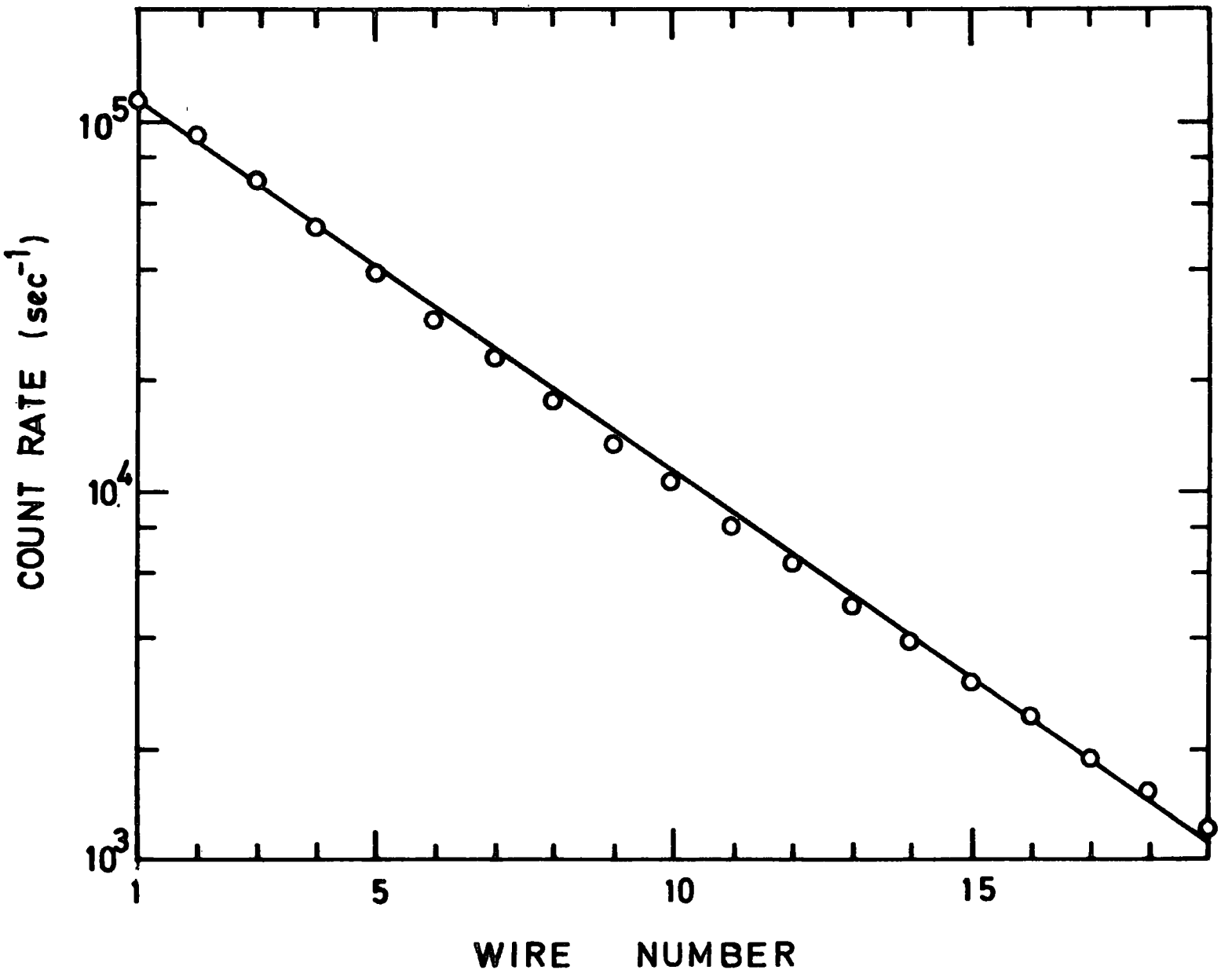

FIG. 4·14 COUNT RATE FOR THE FIRST 19 WIRES

4.5.5 Effect of High Rate on Peak Position and Energy Resolution

The distributions of pulse heights for various rates were obtained by placing the Fe^{55} source near the side window. The rate was changed by varying the distance between the source and the window. The position of the peak of the pulse height distribution was observed on the PHA. The same procedure was repeated with 6.9 keV X-rays from an X-ray generator. Results for both energies are shown in Fig 4.15 as a function of count rate. From this figure the shift percentage S can be defined as

$$S = \frac{x - X}{X} \times 100 \qquad (4.16)$$

where x is the peak position at low rate and X is the peak position at high rate. For an increase of count rate from 10^3 per second to 10^5 per second, the drop in pulse height was 19% for the 5.9 keV source. For the same increase in rate, the drop was much greater, namely 52%, for the 6.9 keV X-ray source. This difference in the drop of pulse height for the two energies was expected. According to Hendrick's[32] calculation, a faster drop in pulse height is expected with the increase in X-ray energy due to a greater space charge effect (see eqn.4.12).

To decrease the peak shift with count rate, the percentage of methane was increased in the chamber. The increase of count rate from 10^2 to 10^5 per second changed the drop in pulse height from 19% with 10% methane to 9% with 76% methane[39]. As the methane was increased, the reduction in pulse height at high count rate became smaller due to a smaller space charge effect. The reason for less space charge is due to the absorption of the ultraviolet light which stops the discharge building up.

Another method used to decrease the peak shift employs a reduction in the cathode potential. The reduction in pulse height at high count rate was found to become smaller as the cathode potential was reduced.

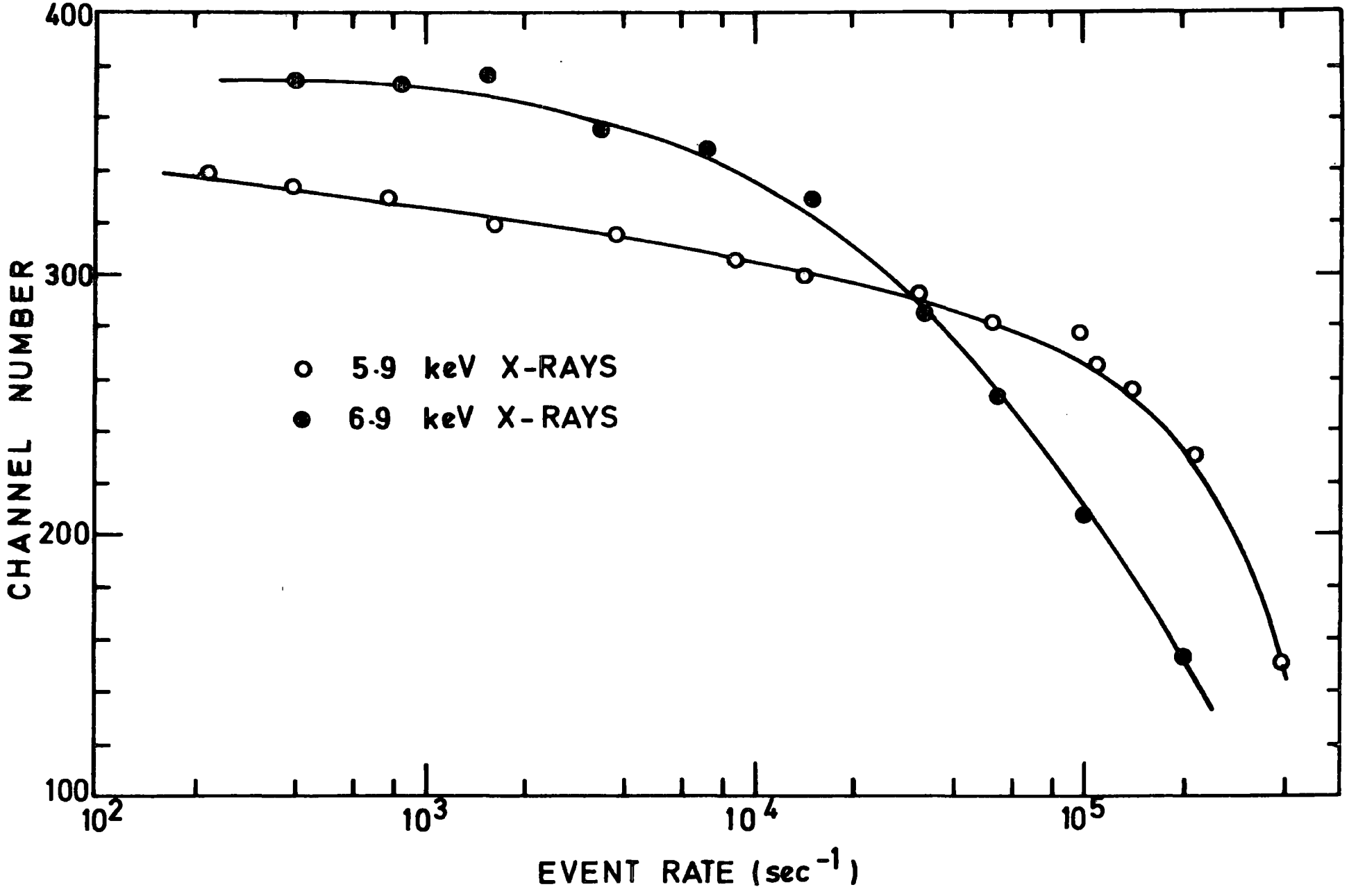

FIG. 4·15 PEAK SHIFT AT HIGH RATES

This reduction was due to the reduction in space charge as the multiplication factor decreased with decreasing applied voltage as shown in Fig 4.1b.

The other phenomenon occurring at high rate is a change in energy resolution. The pulse height distributions for several rates are shown in Fig 4.16. The energy resolution deteriorated with high rates, this is shown in Fig 4.17. For rates higher than 2×10^5 per second, the argon escape peak cannot be resolved from the main peak. The reason for this deterioration is due to the positive space charge produced near the anode wire causing a decrease in the field around it. Both factors, methane percentage and the applied voltage variation, have their effect on the peak shift but decreasing the peak shift leads, as usual, to an adverse effect on the energy resolution.

4.6 CONCLUSIONS

The study of MWPC's with a delay line readout technique has shown that this technique is more limited than the conventional MWPC as far as the high count rate capability is concerned. The basic processes of drift chambers are the same as in MWPC's, since drift chambers were basically developed from MWPC's. The main difference between them is the gas used because in DC's a saturated drift velocity of electrons is needed, i.e. independent of the drift field. Hence the factors limiting high rates apply equally to DC's as well as MWPC's and there was no advantage in going to DC's for high rates.

The common limitation on high rate capability, in both MWPC's and DC's, is the space charge effect. The manifestations of this effect are the peak shift and the deterioration of energy resolution. A method for decreasing this effect was to decrease the multiplication factor to as low a value as possible. Due to this decrease in multiplication it is difficult to extract the data from the chamber, where only small signals are produced.

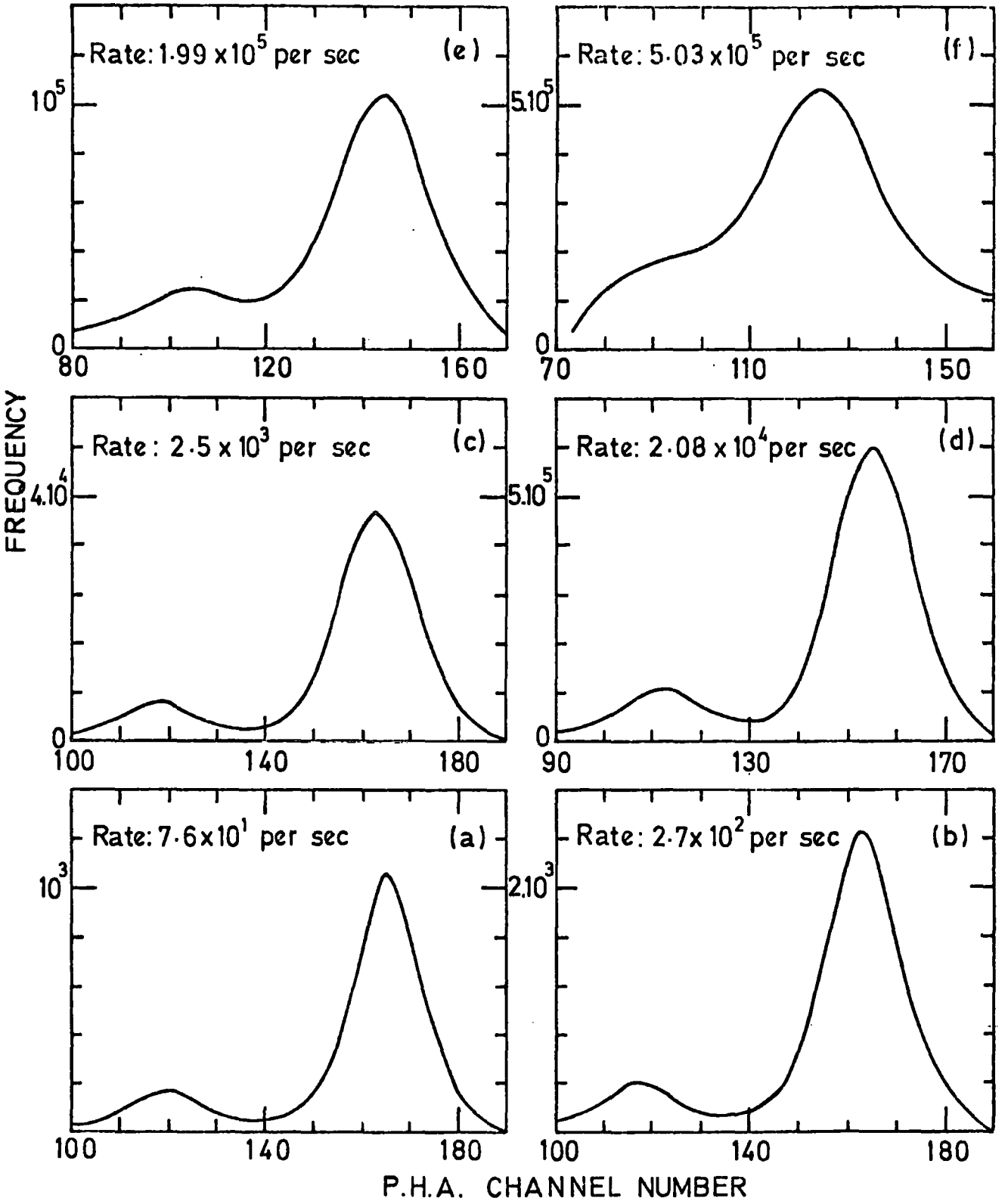

FIG. 4·16 PULSE SPECTRA AT DIFFERENT RATES

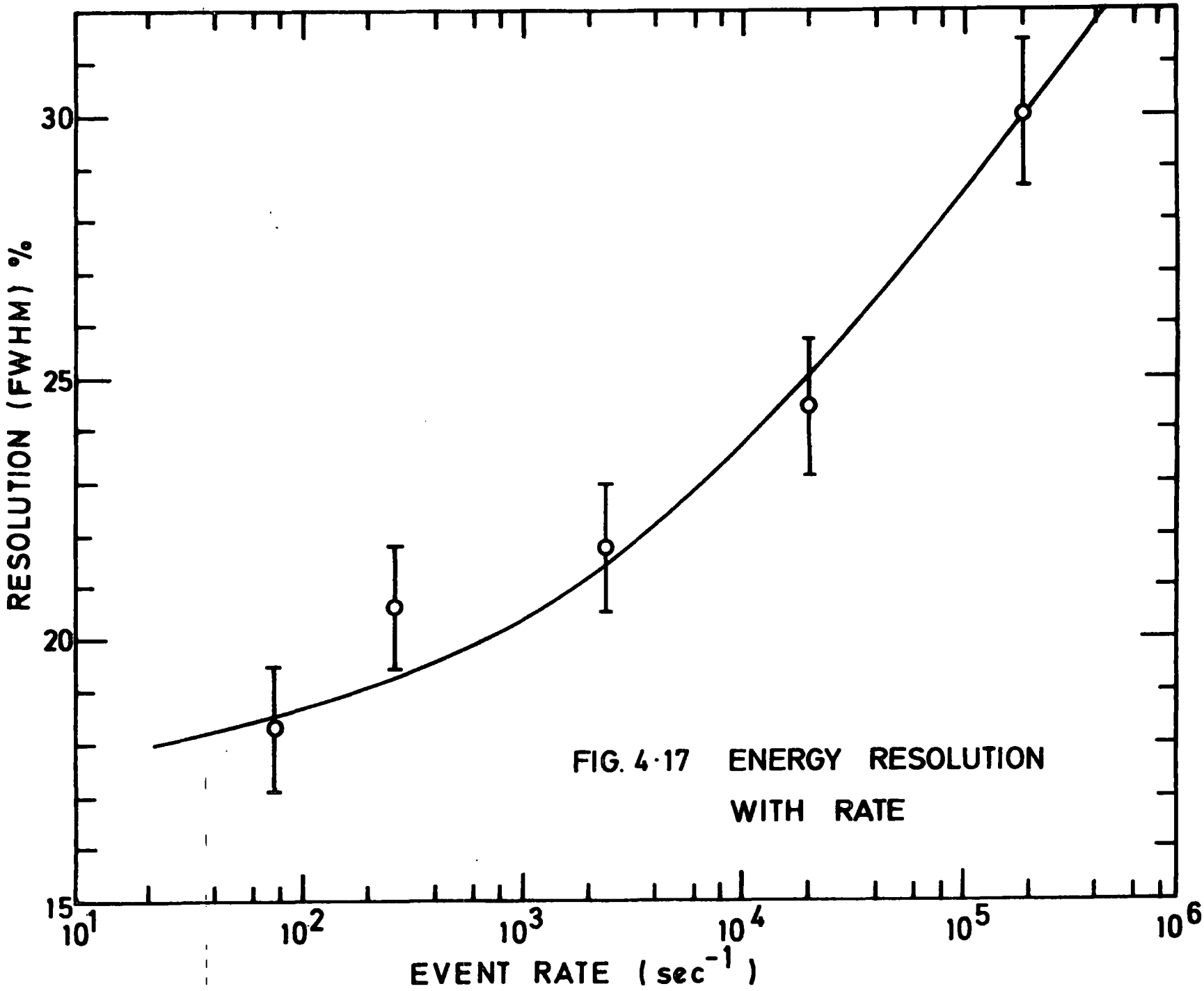

FIG. 4·17 ENERGY RESOLUTION WITH RATE

High gain amplifiers with low noise are needed. An alternative method is to use another readout technique, that is to extract the light output from the chamber rather than the charge output. This can be achieved with using gas scintillation counters in the form of either a gas scintillation proportional chamber or a gas scintillation drift chamber.

Chapter Four - References

1. A.Von.Engel, Ionized Gases, (Clarendon Press, Oxford,1965).
2. F Sauli, Principles of operation of MWPC's and DC's, CERN 77-09 (1977).
3. V Palladino and B Sadoulet, Lawrence Berkeley Laboratory Report, LBL-3013 (1974).
4. M W Charles, J. Phys. E. 5 (1972) 95.
5. S A Korff, Electron and Nuclear Counters, Theory and Use, (D Van Nostrand Comp. New York, 1946).
6. G A Erskine, Nucl. Inst. & Meth 105 (1972) 565.
7. G. Charpak, Ann. Rev. Nucl. Sci. 20 (1970) 195.
8. J B Birks (Ed), Modern Dielectric Materials (Heywood and Company Ltd, London, 1960).
9. G Charpak et al. Nucl. Inst. & Meth. 65 (1968) 217.
10. S N Kaplan, L Kaufman, W Pérez-Mendez and K Valentine, LBL Report 778 (1972).
11. E W Stoub, R A Ristinen and R R Sercely, Nucl. Inst. & Meth. 127 (1975) 329.
12. D M Lee, S E Sobottka and H A Thiessen, Nucl. Inst. & Meth. 120 (1974) 153.
13. B Sitar, R J Stubbs and J M Breare, Nucl. Inst. & Meth. 134 (1976) 267.
14. C J Barkowski and M K Kopp, IEEE Trans. Nucl. Sci. NS-19 (1972)161.
15. C J Barkowski and M K Kopp, Rev. Sci. Inst. 46 (1975) 951.
16. G. P. Harnwell, Principles of Electricity and Electromagnetism, 2nd edition, (McGraw Hill, N.Y. 1949).
17. J G Emming & J R Gilland, IEEE Trans.Nucl.Sci. NS-20 (1973) 145.

18. R Bosshard and R L Chase, IEEE Trans. Nucl. Sci. NS-22 (1975) 2053.

19. D M Lee et al, Nucl. Inst. & Meth. 109 (1973) 421.

LA-5195-MS Informal Report.

20. S Al Dargazelli, Internal Report, Durham University, N1-76-2 (1976).

21. S Al Dargazelli, Internal Report, Durham University, N1-76-24 (1976).

22. S Al Dargazelli, Internal Report, Durham University, N1-77-8 (1977).

23. S Al Dargazelli, Internal Report, Durham University, N1-77-11 (1977).

24. G Charpak et al, Nucl. Inst. & Meth. 62 (1968) 262.

25. D H Wilkinson, Ionization Chambers and Counters (University Press, Cambridge 1950).

26. R S Vogel and L A Ferguson, Rev. Sci. Instrum. 37 (1966) 934.

L A Ferguson, Rev. Sci. Inst. 37 (1966) 964.

P G Burkhalter et al, Rev. Sci. Inst. 37 (1966) 1267.

27. B Sadoulet & B Makowski, CERN/D.Ph. II/PHYS. 73-3 (1973).

28. N Spielberg, Rev. Sci. Inst. 37 (1966) 1268.

N Spielberg, Rev. Sci. Inst. 38 (1967) 291.

N Spielberg and D I Tsarnas, Rev. Sci. Instrum. 46 (1975) 1086.

29. H Sipila and V Vanho-Honko, Nucl. Inst. & Meth. 153 (1978) 461.

30. K Mahesh, Nucl. Inst. & Meth. 133 (1976) 57.

K Mahesh, Nucl. Inst. & Meth. 153 (1978) 465.

31. Z Pawlowski and W Cudny, Nucl. Inst. & Meth. 157 (1978) 287.

32. R W Hendricks, Rev. Sci. Inst. 40 (1969) 1216.

33. W Diethorn, US AEC Rep. NYO-6628 (1956).

34. G Charpak et al, Nucl. Inst. & Meth. 124 (1975) 189.

35. G Charpak et al, Report - Geneva (1974).

36. M Comyn, Ph.D. Thesis, Durham University (1978).

37. R.D.Evans, The Atomic Nucleus (McGraw-Hill N.Y. 1955).

38. G Charpak et al, Nucl. Inst. & Meth. 80 (1970) 13.

39. S Al Dargazelli, T R Ariyaratne, J M Breare, B C Nandi and MV Verells, Nucl. Inst. & Meth. 156 (1978) 63.

CHAPTER FIVE

ELECTRIC FIELD CALCULATIONS IN MWPC's AND DC's

5.1 INTRODUCTION

One of the most important factors which plays a part in the performance of MWPC's and DC's, and hence of GSC's, is the field inside the gas chamber. In this chapter the main factors affecting the field are studied.

Using a numerical relaxation method, a computer program for calculating potentials and fields inside the chamber was developed for both MWPC's and DC's. It was possible to vary all the chamber parameters in the program and the effect of each on the field was studied. Subroutines were used to plot the variation of field inside the chamber and to plot contours of equipotential surfaces. The computer used was the N.U.M.A.C. (Northumbrian Universities Multiple Access Computer) installation which operates on IBM 360 Model 67 computer under control of the M.T.S.[1] (Michigan Terminal System). The language used in this work was FORTRAN.

5.2 THE METHOD

One of the important factors which aids an understanding of the performance of DC's and MWPC's is the shape of the field inside the chambers. This particular topic has been studied in the past by several workers[2]. Computer programs were used to determine the electric field configuration within the chamber.

The computer program used in this work was written by Comyn [3] to calculate potentials in the active volume of drift chambers. The potentials were determined at mesh points of a two dimensional grid, approximately constructed within the chamber volume. The potentials were derived solely

from a knowledge of the chamber wire potentials. The method is based on the solution of Poisson's equation by relaxation. The derivations in Poisson's equation are replaced by finite difference approximations. The region under consideration is divided into a regular mesh of size α - (see Fig 5.1). The optimum mesh size is related to the wire radius by[4]

$$r = \alpha e^{-\frac{\pi}{2}} \tag{5.1}$$

The wires, which are treated as singular points, constitute the boundary conditions. In the program, initial dummy values are set for the non-singular node points. The residuals are given by

$$R(x_o,y_o) = V_1 + V_2 + V_3 + V_4 - 4V_o \tag{5.2}$$

where V_1, V_2, V_3, V_4 and V_o are the potentials for the node points 1, 2, 3, 4 and O (shown in Fig 5.1) respectively. The program systematically reduces the residuals at all non-singular points through the mesh. This is done by varying the non-singular node potentials by one quarter of the residual value. This adjustment of the non-singular node potentials is to reduce all non-singular node residuals to below a set maximum value.

5.3 THE PROGRAM

In the program used the maximum residual value was set at 1.00. The mesh size was set according to eqn. 5.1. From this equation the mesh size for a wire of radius 100 μm is 481 μm and that for radius 20 μm is 96.3 μm. The mesh size used in nearly all the cases was 500 μm which is a good approximation for a wire of radius 100 μm. Hence for a 20 μm wire a good approximation for the mesh size should be 100 μm. When using a mesh size larger than the optimum for a specified wire radius, the radial field

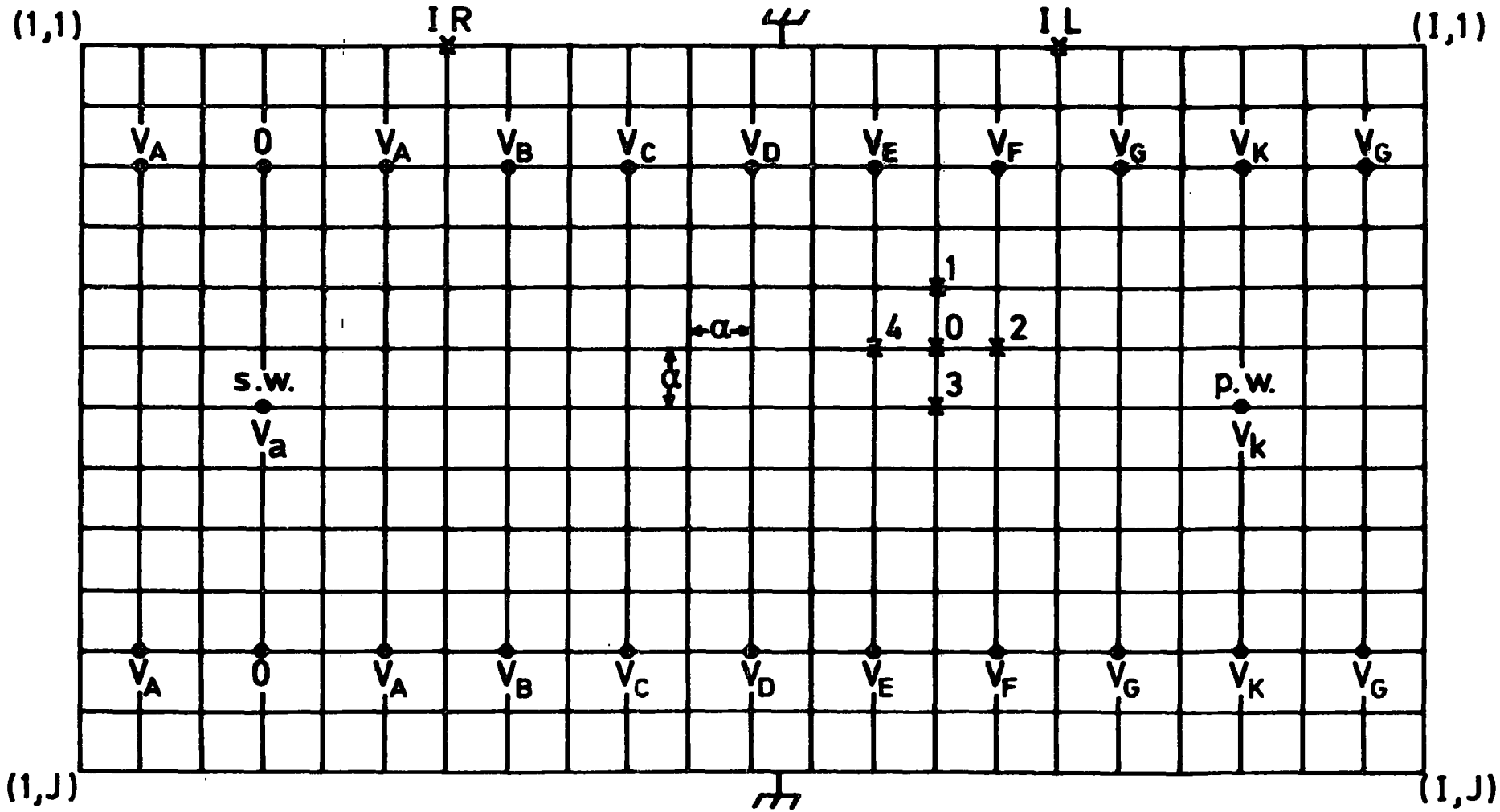

FIG. 5·1 THE ARRAY ARRANGEMENT USED IN THE PROGRAM.

computed around the sense wire is usually higher than the true value. This is illustrated in Fig 5.2 for a MWPC of sense wire spacing S = 3 mm, anode-cathode spacing L = 3 mm and anode voltage V_a = 2000 volts. It is clear that the smaller the mesh size the more accurate the contours. Accuracy, however, is accompanied by a serious disadvantage. The time needed to execute the computer program increases rapidly with increasing array size. Table 5.1 shows the increase of CPU time, needed to execute the program, with decreasing the mesh size α. The number of iterations performed is also given in this Table for the field configurations shown in Fig 5.2. Decreasing the mesh size by a factor of 10 increased the CPU time by factor 10^4. The only way to decrease CPU time significantly is by increasing α.

TABLE 5.1

The Effect of Mesh Size on CPU Time

Mesh Size α (μm)	Array size (I x J)	No. of Iterations	CPU time (sec)
1000	63	943	0.8
500	221	9457	2.6
250	825	118841	88
100	4819	1920325	7895

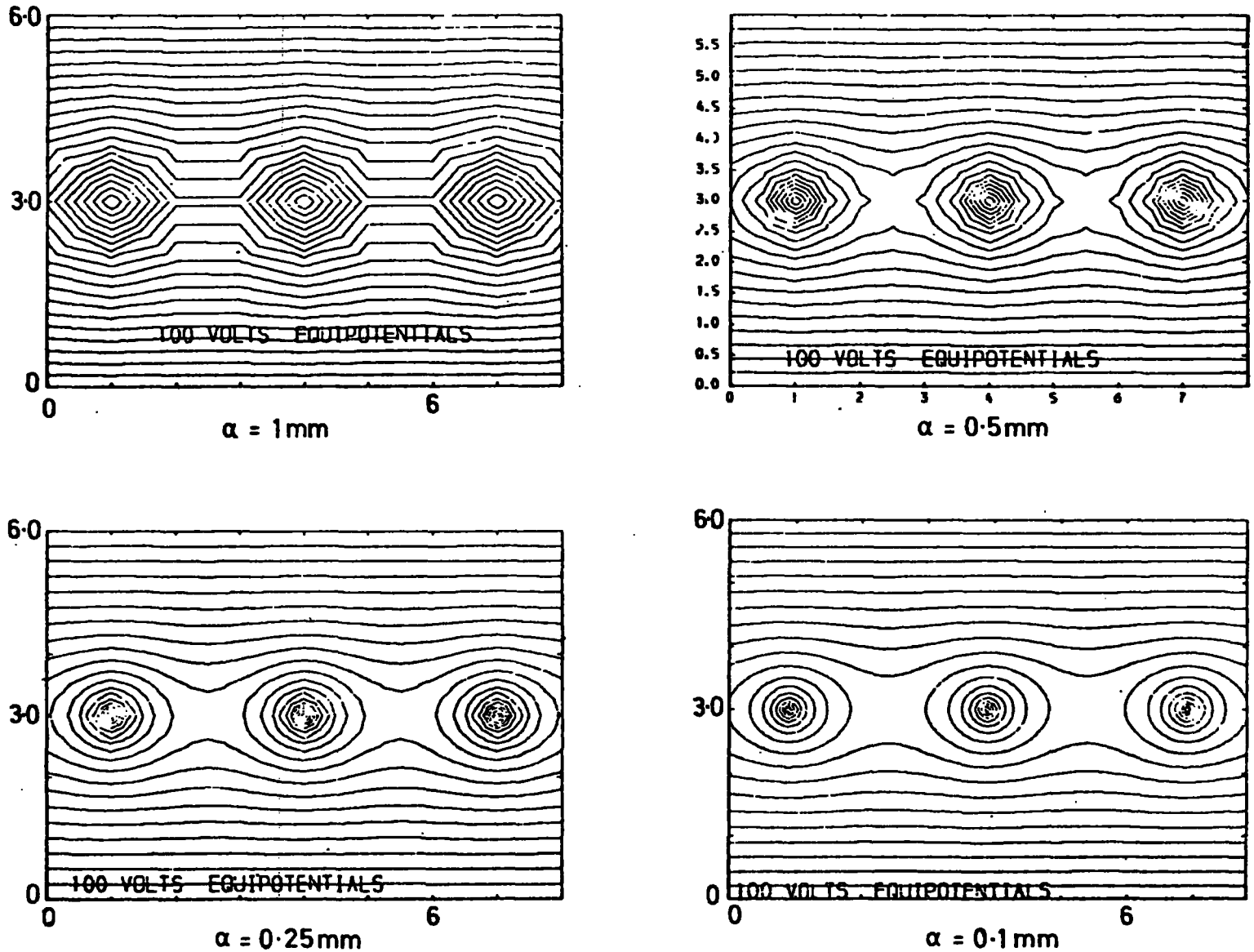

FIG. 5·2 EFFECT OF THE MESH SIZE ON EQUIPOTENTIAL CONTOURS

The program applies to a cell with earth planes at the top and bottom boundaries of the mesh and symmetry at the edges of the mesh (IR & IL) (See Fig 5.1). The program reads the mesh parameters from a file attached to a device. The file contains the chamber array dimensions (I,J) corresponding to the mesh node points. It also contains the following information :- The number of singular points defined (K), i.e. the number of defined wires ; the array column (IR) with identical node potentials to column 1 ; the array column (IL) with identical node potentials to column I ; the number of iterations (ITER) to be performed during the run ; the maximum modules value of a residual (RES) allowed before termination of relaxation ; and the x-y position and potential of each singular point (or wire).

After reading the mesh parameters, the program set dummy residual and potential values for all node points in the array. With potential values of the singular points as boundary values, the residuals were calculated according to eqn. 5.2 and the interactive process repeated, as mentioned earlier, until the residuals were reduced to the value of one at which point the relaxation was complete.

The original program just described was limited to calculations of potentials only. It was extended to calculations of the field also. With the use of some graphic subroutines, the potentials and field values were drawn as functions of distance in different planes inside the chamber. Equipotential contours were also drawn using special graphic contours. The program was used for both MWPC's and DC's with some small alterations to suit each case.

The main limitation in this program is the excessive CPU time needed, especially when the mesh size is small. Also, the solution is not exact if the anode and cathode wire radii are different. Another limitation is that

the edge effect is ignored due to the symmetry assumption around the sense wire and potential wire. This can be cured by removing the symmetry but this leads to another big increase in CPU time. This last point will be discussed in another section.

5.4 FIELDS IN MWPC's

The MWPC configuration shown in Fig 1.6 indicates the three variables changed in the program. They are s the sense wire spacing, L the anode-cathode separation and d the sense wire diameter. The voltage applied to the anode (V) was also changed. Table 5.2 shows the values of the variables used with the corresponding values of the other parameters kept constant.

TABLE 5.2

Variable Parameters in MWPC Field Program

Variables	Other Parameters			
	s	L	α	V
s = 2, 3, 4 mm	-	5	0.5	2
L = 5, 8, 10 mm	3	-	0.5	2
α = 0.1, 0.25, 0.5, 1 mm	3	3	-	2
V = 1, 2, 3 kV	3	5	0.5	-

Fig 5.3a shows the variation of potential inside a MWPC with s = 3 mm, L = 5 mm and V = 2 kV. The six plots are for different distances between the anode and cathode planes. It should be noted that in a plane only 1 mm from the sense wire, the potential has already dropped 30% in the

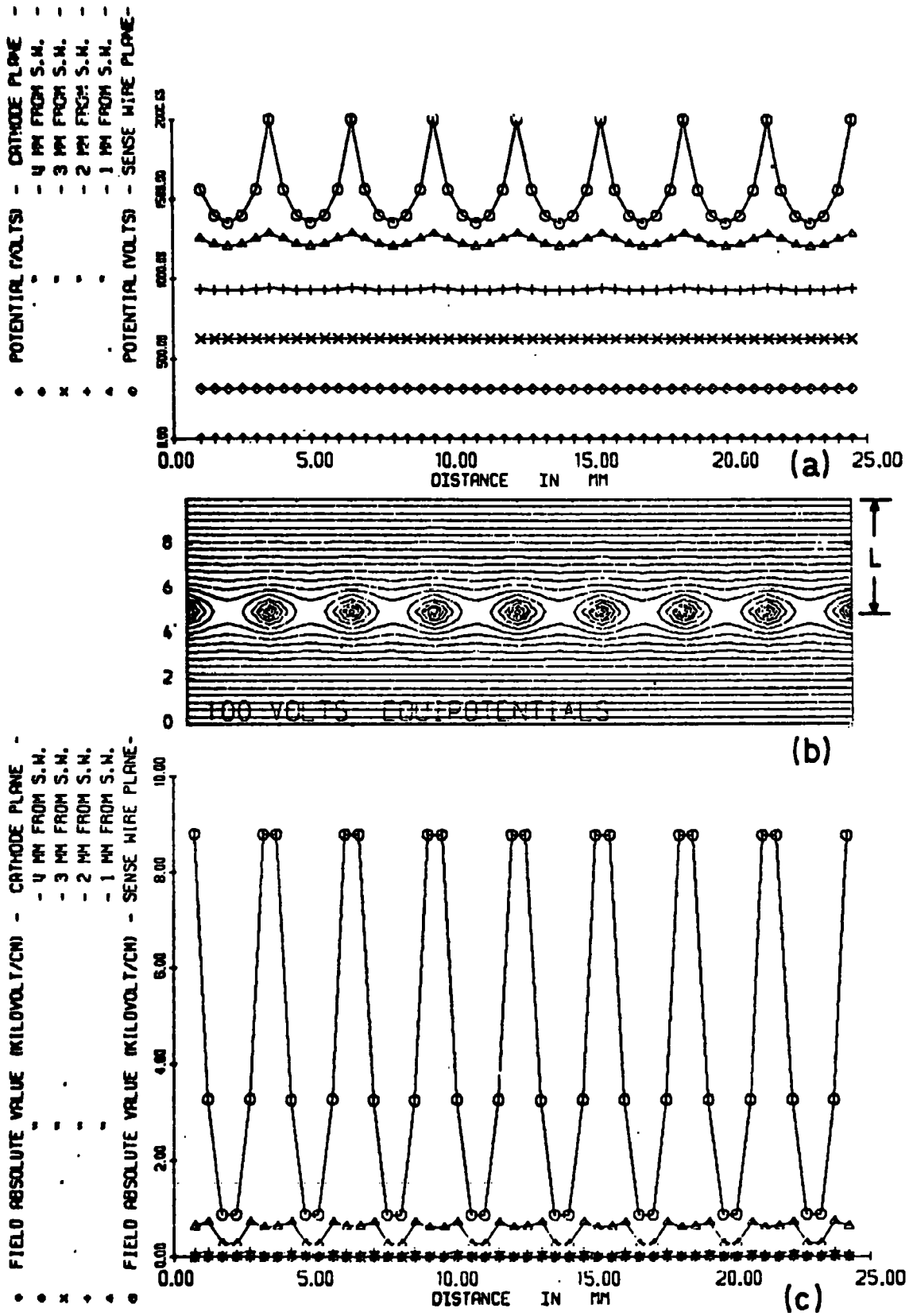

FIG. 5·3 (a) POTENTIAL VARIATION.
(b) EQUIPOTENTIAL CONTOURS.
(c) FIELD VARIATION IN A MWPC.

x-direction and 35% in the y-direction. In the y-direction, i.e. approaching the cathode plane, the potentials are about uniform at only 1 mm away from the sense wire plane, they vary by 6.5% from points adjacent to the sense wire to points midway between them. For the same MWPC, the equipotential contours shown in Fig. 5.3b indicate again the high field around the sense wires and the uniform field away from them. The absolute values of the field in kilovolt/cm are shown in Fig 5.3c, for the same distance intervals of Fig 5.3a. Clearly, fields near the sense wires go higher than that indicated in Fig 5.3c, but due to the limitations of the plotting subroutine the field around the sense wires is limited to the mesh points. It is thus clear from these figures that the region of multiplication can be identified as existing only very close to the sense wires.

As was mentioned earlier, the symmetry assumption in the program eliminates the evidence of the edge effect in the chamber. For a MWPC the symmetry in the x-direction was removed and the edge effect appeared in the equipotential contours as shown in Fig. 5.3d. It was noticed that the edge effect was wider in range at high anode voltages ; the non-uniformity in the field appeared not only around the last wires at the edges but also around the ones before the last. The edge effect is usually avoided by using one, or more, thicker wires at the two ends of the sense wires plane to reduce the high field.

5.4.1 Sense Wire Spacing (s)

Fig 5.4 shows the effect of changing the sense wire spacing on the fields in the sense wire plane only. The corresponding equipotential contours are shown in Fig 5.5. According to eqn. 1.4, the field at the wires depends on the charge stored on it and this itself depends on the wire spacing. It was shown by Charpak et al[5] that the wire capacitance per unit length increases with increase of wire spacing (s). It is clear from Fig 5.4 that if the spacing is decreased then the field around the

Durham University SCIENCE

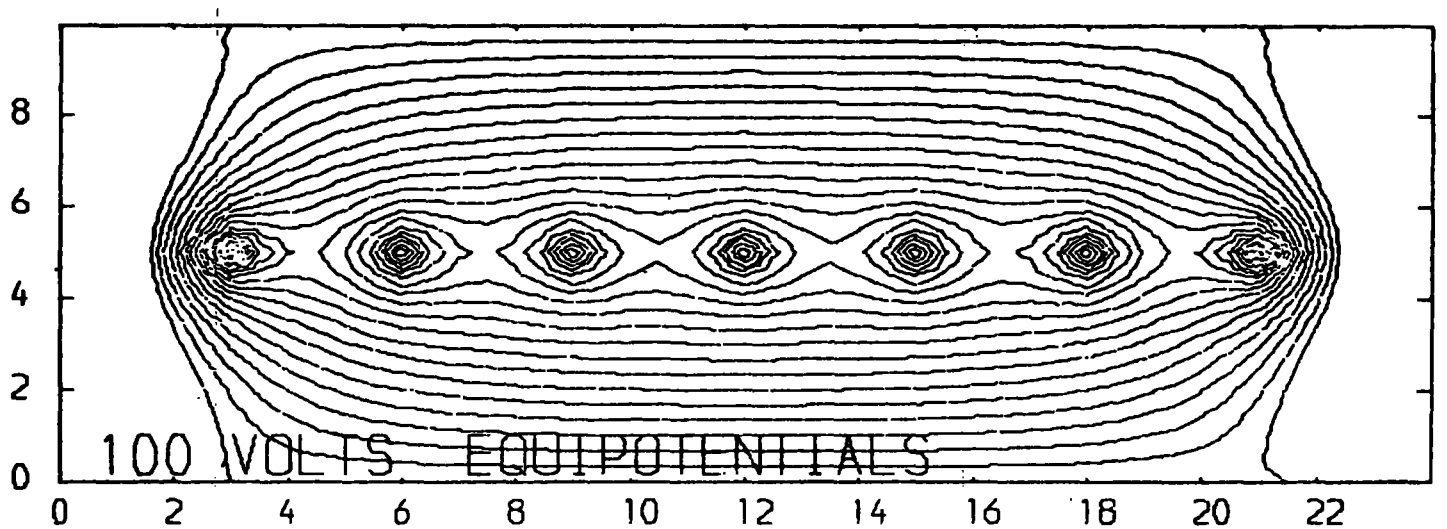

FIG. 5·3 (d) CONTOURS IN A MWPC WITH NO SYMMETRY IN THE COMPUTER PROGRAM TO SHOW EDGE EFFECT.

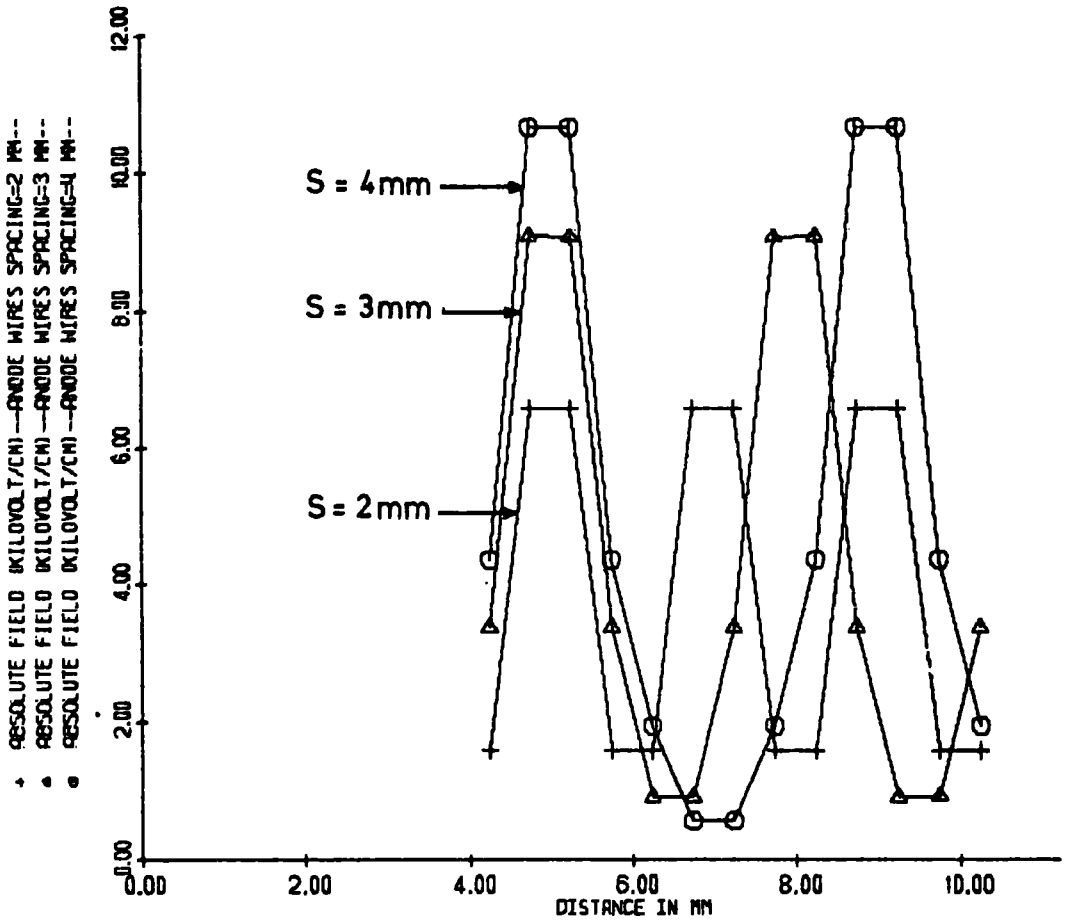

FIG. 5·4 EFFECT OF ANODE WIRE SPACINGS ON THE FIELD IN A MWPC.

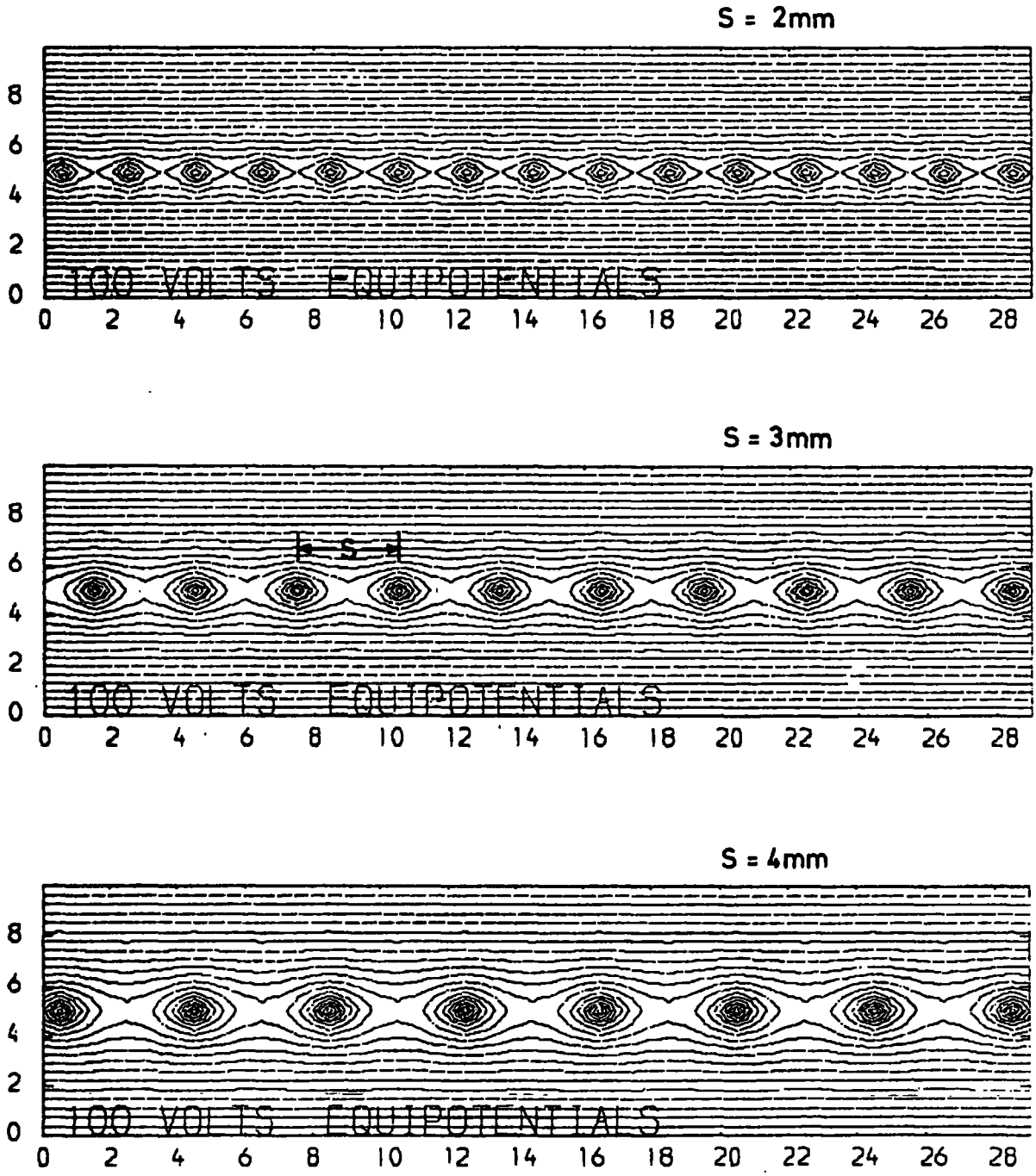

FIG. 5·5 CONTOURS FOR DIFFERENT ANODE WIRE SPACINGS.

sense wire is decreased. Hence, in order to keep the field at the same value, it is necessary to increase the voltage as s decreases. Under these circumstances the risk of breakdown is increased because of the use of higher voltage. Table 5.3 gives the values of the maximum calculated field, at 250 μm from the sense wire, the minimum calculated field, at s/2 from the sense wire, and the percentage drop in fields and potentials for the three values of s.

TABLE 5.3

Spacing (mm)	Max.Field (kV/cm)	Min. Field (kV/cm)	Field Drop %	Potential Drop %
4	10.7	0.57	95	44
3	9.1	0.91	90	33
2	6.6	1.6	76	20

From this Table the drop in the field around the sense wire with decreasing s is clear. The effect of the sense wires on each other can be traced at the middle of the spacing where the minimum field occurs (see Column 3 in Table 5.3). The effect of sense wires on each other decreases with increasing s. This appears in the high percentage drop in fields and potentials at high s values. The typical s value used in MWPCs is 2 mm[6]. In this work the value of s used was in the range of 4-5 mm. It is worth mentioning that chambers with 1 mm spacing have been used and also chambers with 3 wires/mm have been used at high pressures[7], but these are exceptions.

5.4.2 Anode-Cathode Separation (L)

The effect of L on the charge on the wires, and therefore on the capacitance, is opposite to that of the sense wire spacings. In other words decreasing L leads to an increase in C and hence the field around the sense wires is higher at low L values than that at higher L values. This is shown in Fig 5.6 for the fields and 5.7 for the corresponding equipotential contours. The maximum and minimum field values are given in Table 5.4 for different L values. No variation in the percentage drop in field was observed with L, but the percentage drop in potential, given also in Table 5.4, decreased with increasing L. The practical values of L used in this work were in the range of 4-6 mm.

TABLE 5.4 $s = 3_{mm}$ $V_a = 2000$ volts

L mm	Max. Field kV/cm	Min. Field kV/cm	Potential drop %
5	9.1	0.9	33
8	6.01	0.6	22
10	5.01	0.5	18

Similar results were obtained by Steffen & Vannucci[8] and they suggested also the use of smaller gap values, because this requires a lower voltage, gives a higher efficiency and the time distribution exhibits a shorter tail. The higher efficiency was attributed to the change in solid angle, the smaller the gap the larger the solid angle of the apparatus assuming a fixed distance between the front window and the source. The time distribution of pulses from one wire occurs due to the variable distance of the ionization from the wire. This distance could be anywhere from 0 to s/2. When ionization occurs near the wire ion pairs are

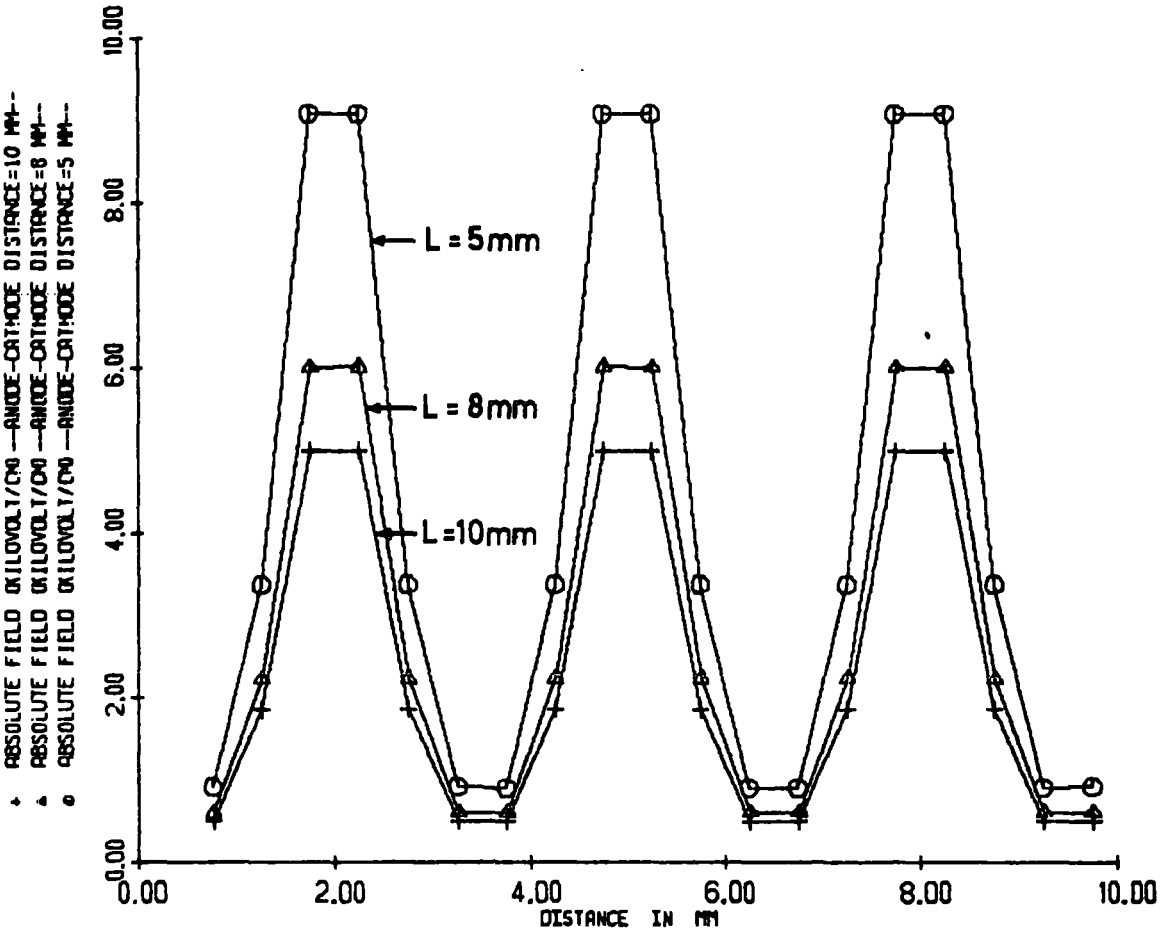

FIG. 5·6 EFFECT OF ANODE-CATHODE SEPARATION ON THE FIELD IN THE SENSE WIRE PLANE.

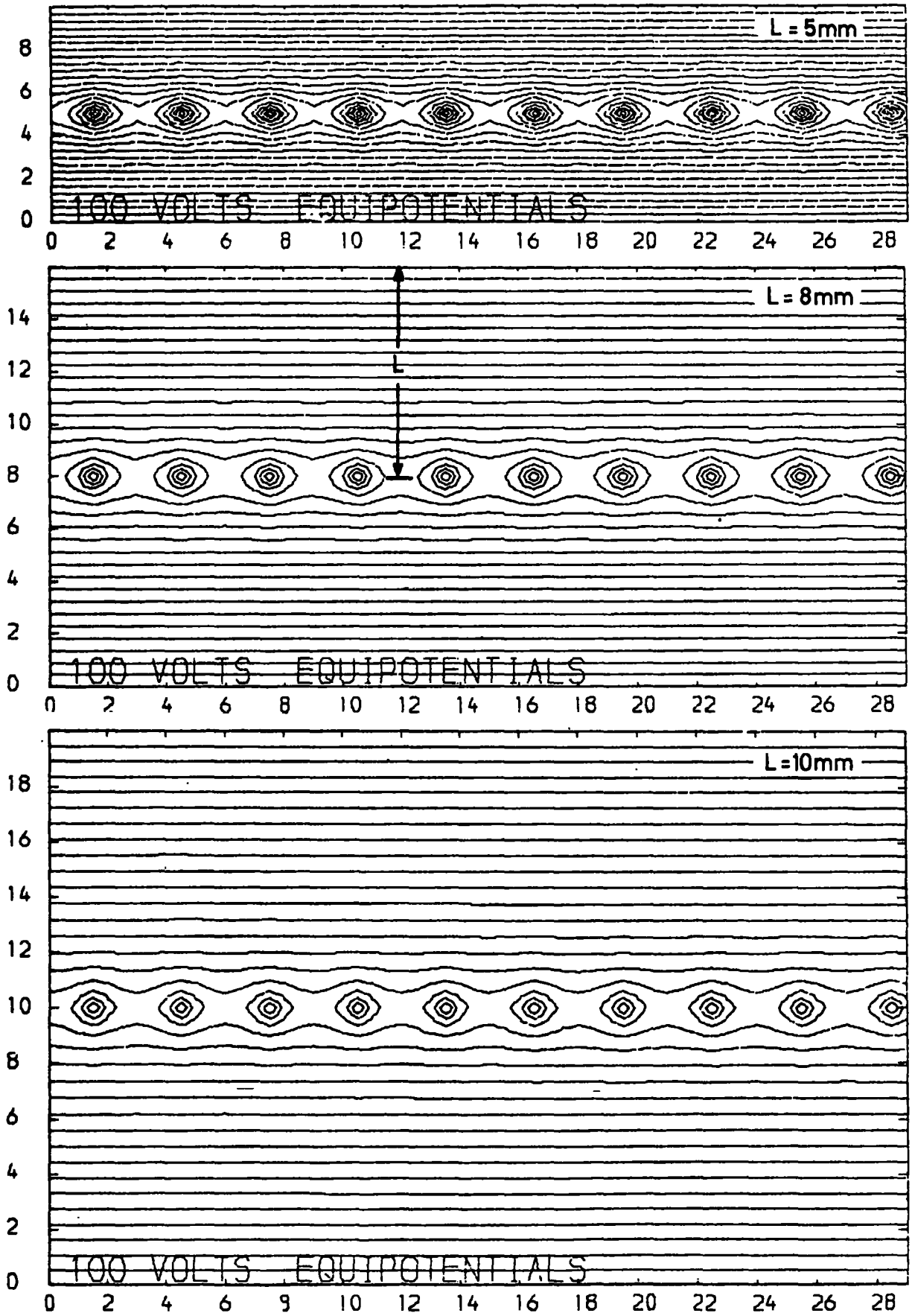

FIG. 5·7 CONTOURS FOR DIFFERENT ANODE-CATHODE SPACINGS IN A MWPC.

rapidly collected and appear in the peak of the time distribution. The tail in the time spectrum is due to pulses in the region between anode and cathode plane. Decreasing the width of this region (L) reduces the tail in the time spectrum and hence improves time resolution obtainable from the chamber.

The value of L in a typical MWPC is 8 mm with s = 2 mm[6]. The choice of L is also dependent on the sense wire spacing (s) in order to obtain high field without the risk of breakdown.

5.5 FIELD IN DRIFT CHAMBERS

As shown in Fig 1.7 the important DC parameters are the drift distance (D) between the sense wire and potential wires, the cathode-earth plane separation (d), the anode-cathode separation (L), the cathode wire spacing (s) ; the anode voltage (V_a) and the cathode voltage (V_k). Table 5.5 gives the values of the variables used with the corresponding values of the other parameters kept constant. The mesh size was 0.5 mm in all the cases.

TABLE 5.5

	D	d	L	S	V_a	V_k
No potential wire	2	3	5	2	2	-2
D = 1,2, 2.6 cm	-	3	5	2	2	-1
d = 1,3, 5 mm	2	-	5	2	2	-1
L = 5,8,10 mm	2	3	-	2	2	-2
s = 1,2,4 mm	2	3	5	-	2	-2
V_a = 0,2,3 kV	2	3	5	1	-	-2
V_k = 0,1,2,3 kV	2	3	5	2	2	-

The typical variation of potentials and fields inside DC's are shown in Fig. 5.8 a and b. The four plots in Fig 5.8a are for different planes between the anode and drift plane, starting on the anode plane itself and moving out in steps of 1.5 mm. The fields for the same steps are drawn in Fig 5.8b. As in MWPC's the potentials,and hence fields, drop very quickly after the peak at the sense wire. In both the x and y directions the field drops 55%, 73% and 81% at distances of 0.5, 1 and 1.5 mm from the sense wire respectively. This fast drop in field very near the sense wire limits the avalanches to a region very close to the sense wires. This can be seen also in the equipotential contours for the same chamber shown in Fig 5.9. The circular equipotential contours around the sense wire show the range of influence of the sense wire. The outer most circular contour is the zero surface which effectively determines the limit of the sense wire influence. This also can be determined from Fig 5.8a when the potential line of the sense wire plane intercepts the x-axis. The uniform drift field between the sense wire and the two potential wires can be distinguished by the approximately straight equipotential lines. Another important region in the chamber is the one between the drift plane and the outer earth plane. The field in this region is highly affected by quite a few factors and hence, due to field penetration, it affects the drift field.

The effect of the potential wires on the sense wire for one half of the chamber is shown in Fig. 5.10 where a comparison can be made between a drift chamber without potential wires and one with potential wires. The latter is usually called adjustable electric field drift chamber (A.F.D.C.). The two potential wires provide more uniform field along a wider range in the chamber. The non-uniformity of the field in a chamber without potential wires covers more than half the drift field while in an A.F.D.C. the non-uniformity is confined to a very narrow region around the potential wires. This can

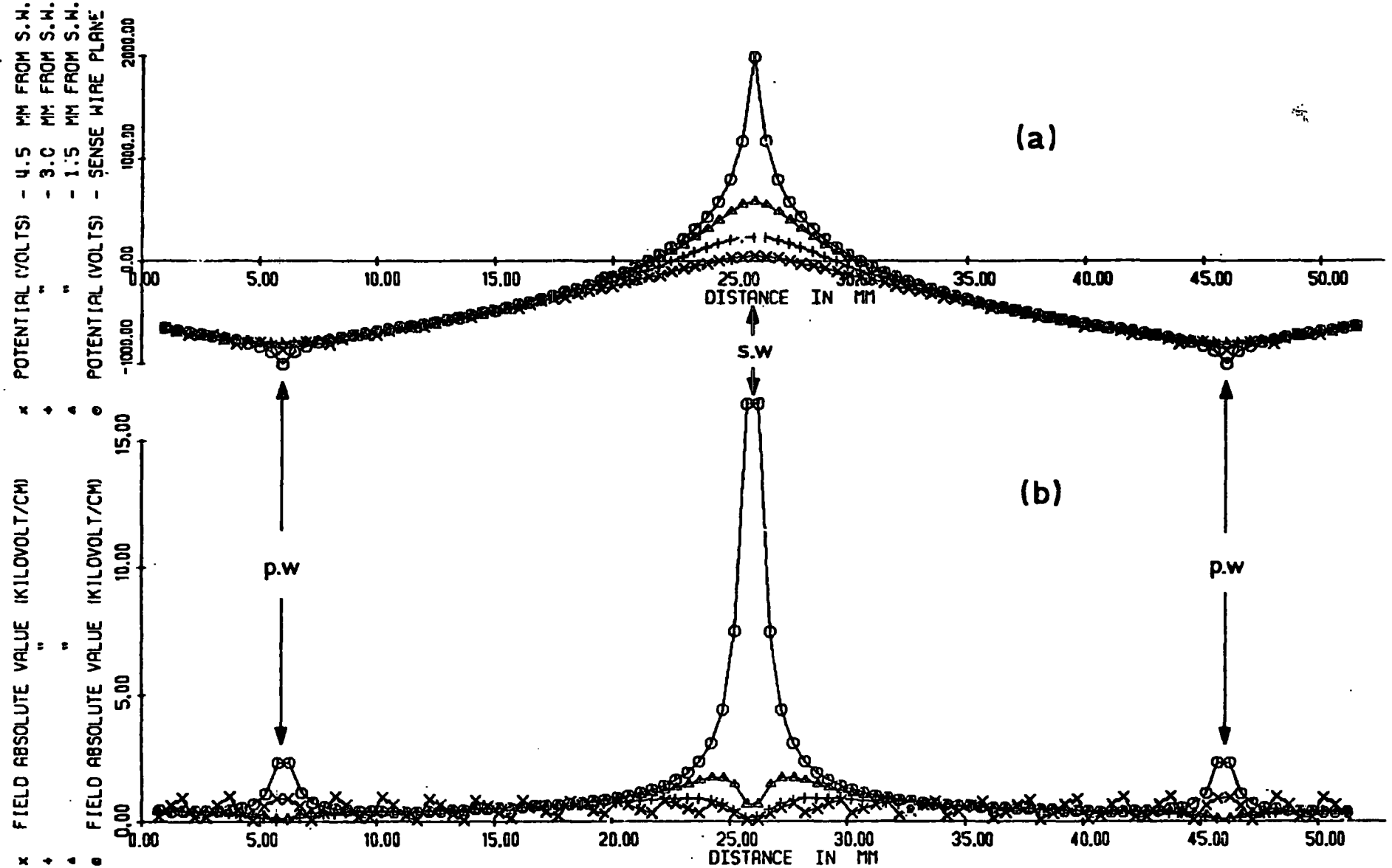

FIG. 5·8 VARIATION OF (a) POTENTIALS AND (b) FIELDS INSIDE A DRIFT CHAMBER.

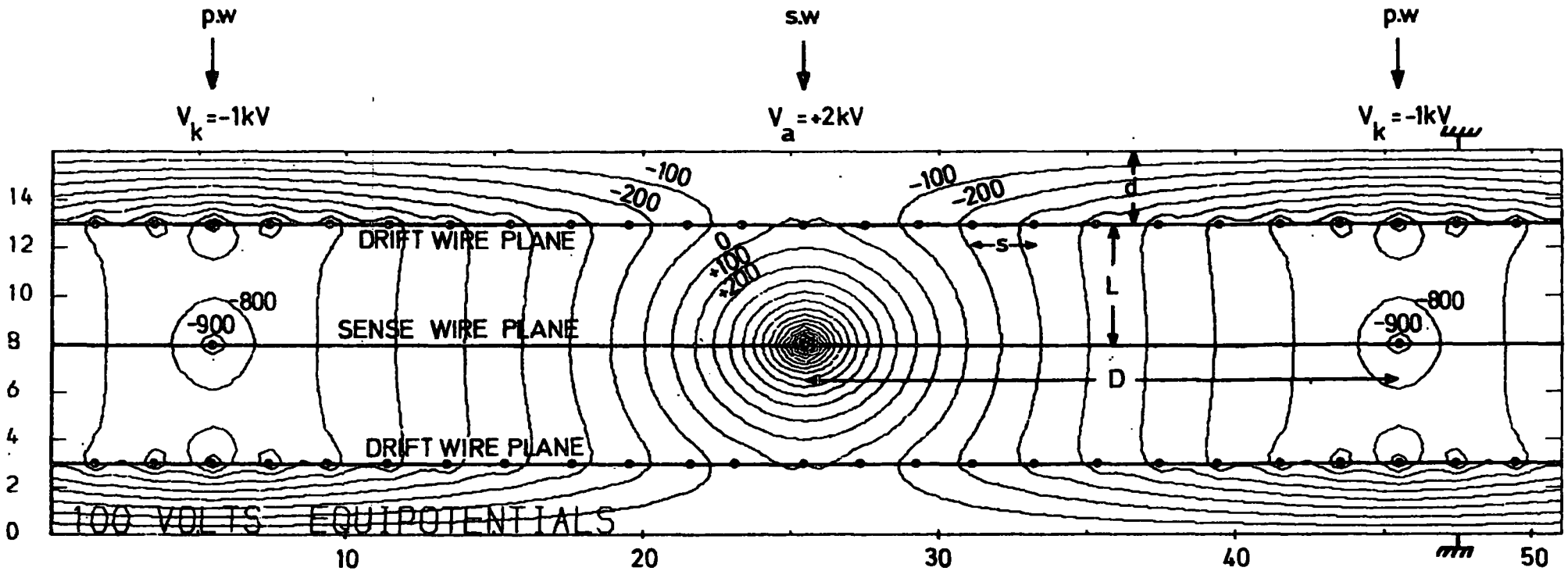

FIG. 5·9 EQUIPOTENTIAL CONTOURS AND PLANES CONFIGURATIONS IN A DRIFT CHAMBER.

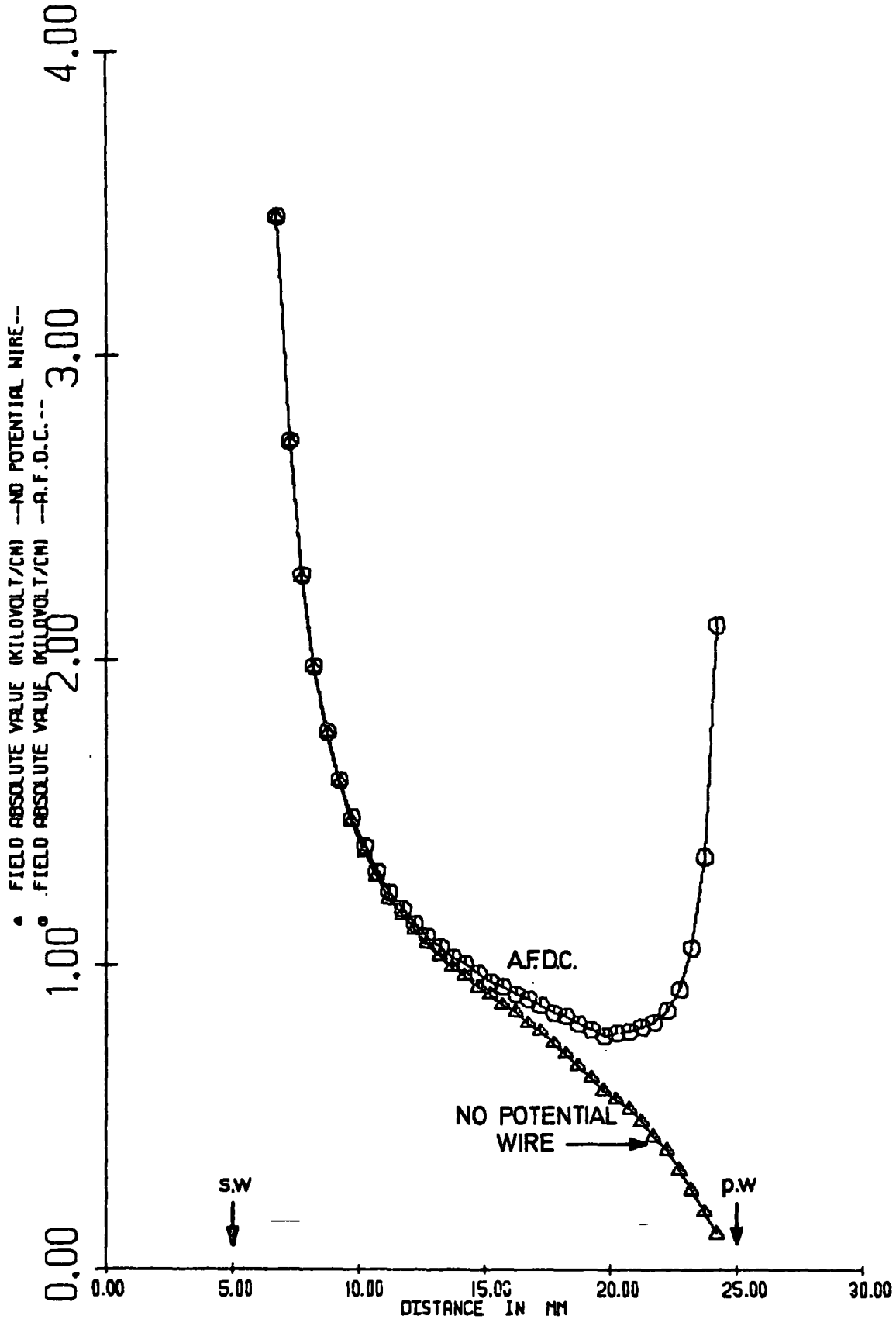

FIG. 5·10 EFFECT OF POTENTIAL WIRE ON THE FIELD IN THE SENSE WIRE PLANE.

be seen also in the contour equipotentials for two similar drift chambers shown in Fig. 5.11-(a) is an AFDC and (b) is a drift chamber without potential wires. A uniform field is necessary to provide constant drift velocity, hence potential wires are essential in drift chambers, even though the lack of them do not appear to affect the amplification.

5.5.1 Drift Distances (D):

The effect of varying D on the fields is shown in Fig.5.12 for the sense wire plane only. The equipotential contours for the three chambers with different D values are shown in Fig 5.13. The last outward contour around the sense wire is the zero equipotential. After this zero equipotential contour the negative potential contours start to occur. The most negative contour is the one near the potential wire. It is desirable to limit the region of influence of the sense wire to a small region for better particle localization. It was found from Fig ~~5.12 and~~ 5.13 that the percentage range of influence of the sense wire potential in the chamber in the x-direction (defined as the ratio of the zero equipotential radius to the chamber half-width) was 34%, 22% and 20% for the values of D = 1, 2 and 2.6 cm respectively. Hence to obtain a smaller range, a higher D value is required. Also high D values produce less fluctuations in the drift wire plane and thus reduce the risk of breakdown. At the same time high D values produce more diffusion and lower fields than low values of D. To obtain a uniform field in the drift region and small range of influence of the sense wire with less diffusion a compromised value of D has to be used. In the last stages of this work the value of D = 2 cm was mainly used.

5.5.2 Drift Wire-Earth Plane Spacing (d):

The variation of fields in drift chambers with three different d values is shown in Fig 5.14. In this figure it is clear that a lower field is obtainable with low d values in 80% of the drift region. Near

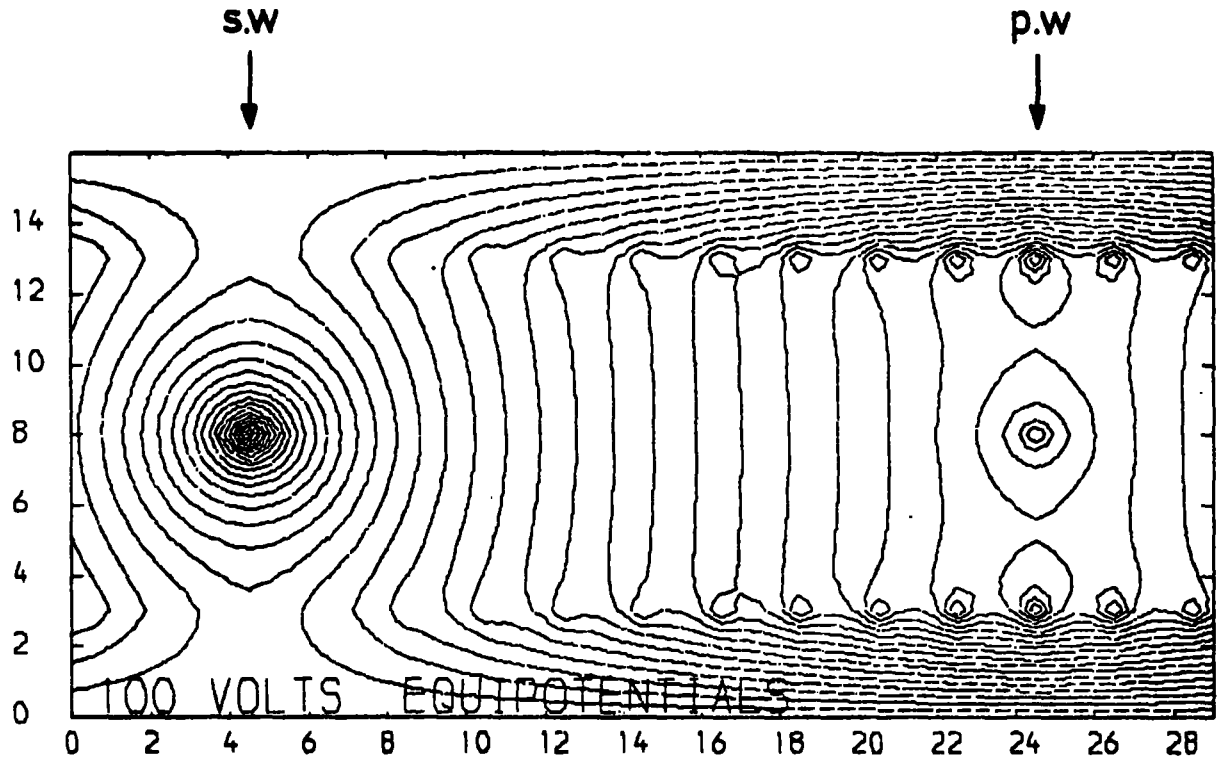

(a)

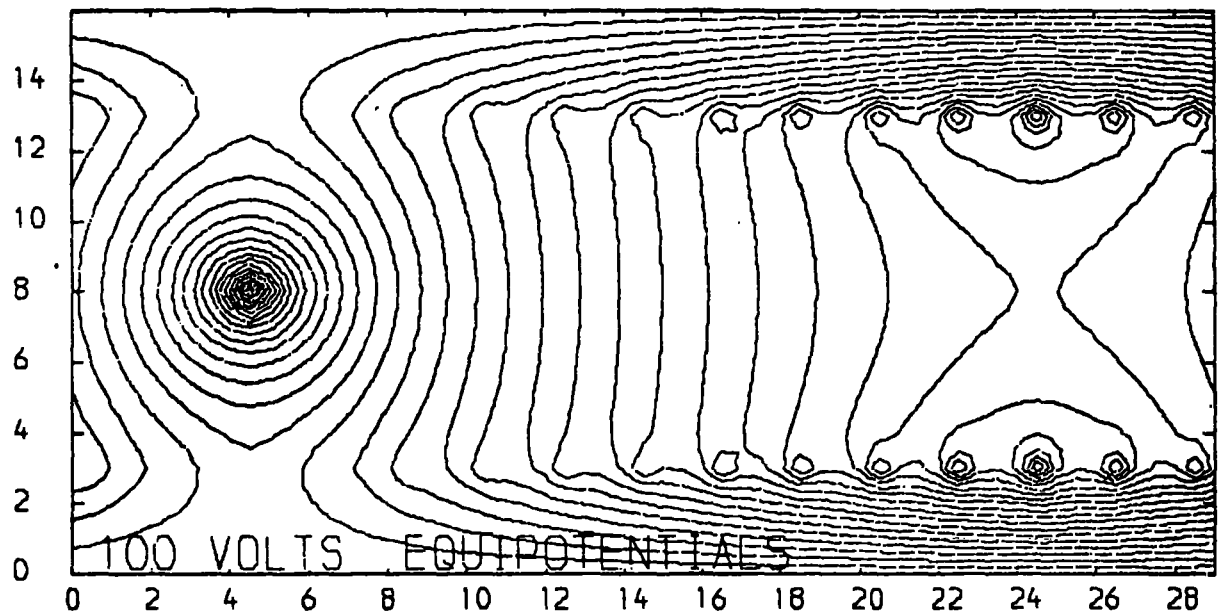

(b)

FIG. 5·11 CONTOURS IN (a) A.F.D.C. AND (b) DRIFT CHAMBER WITHOUT POTENTIAL WIRES.

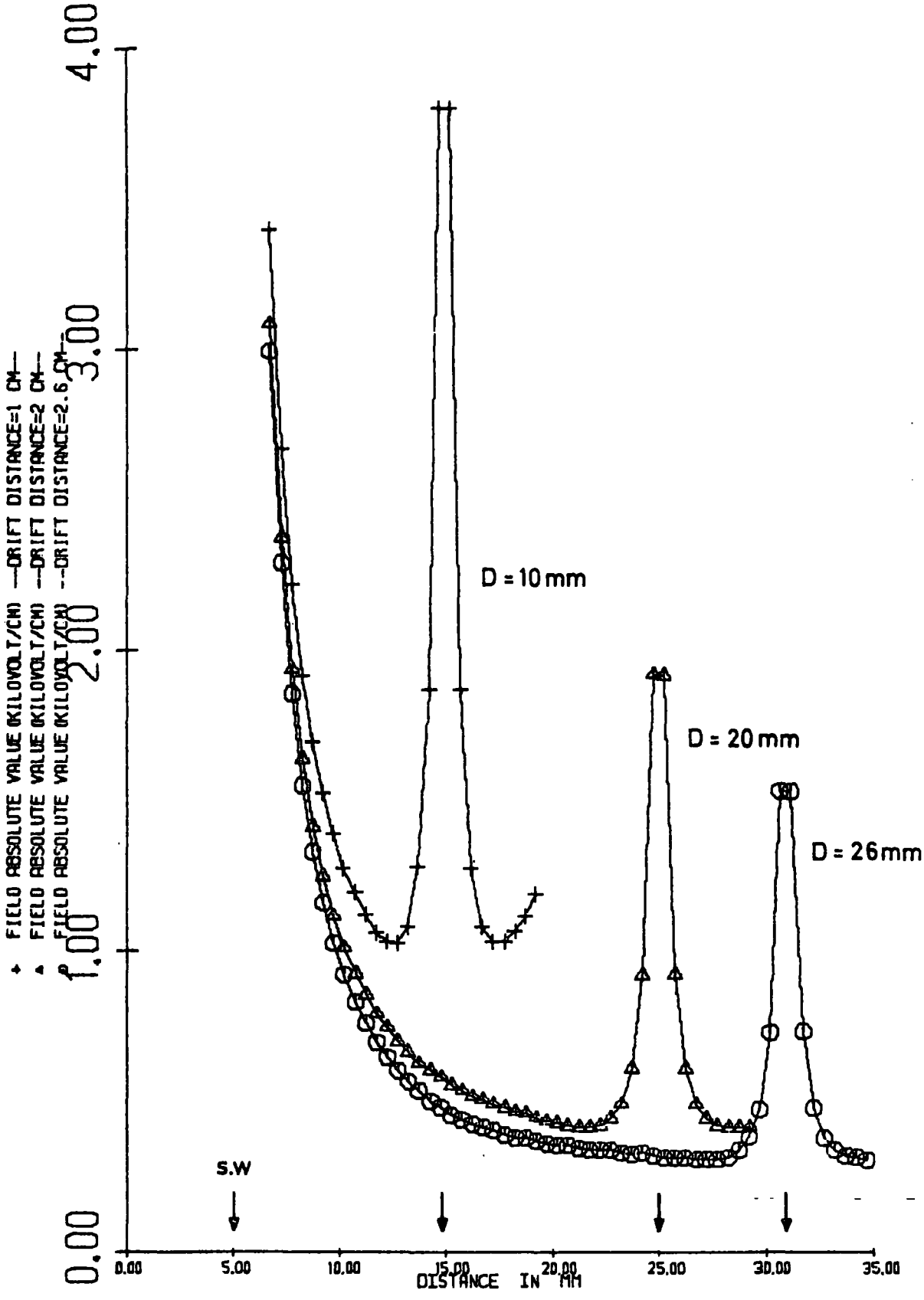

FIG. 5·12 EFFECT OF DRIFT DISTANCE ON FIELDS IN THE SENSE WIRE PLANE.

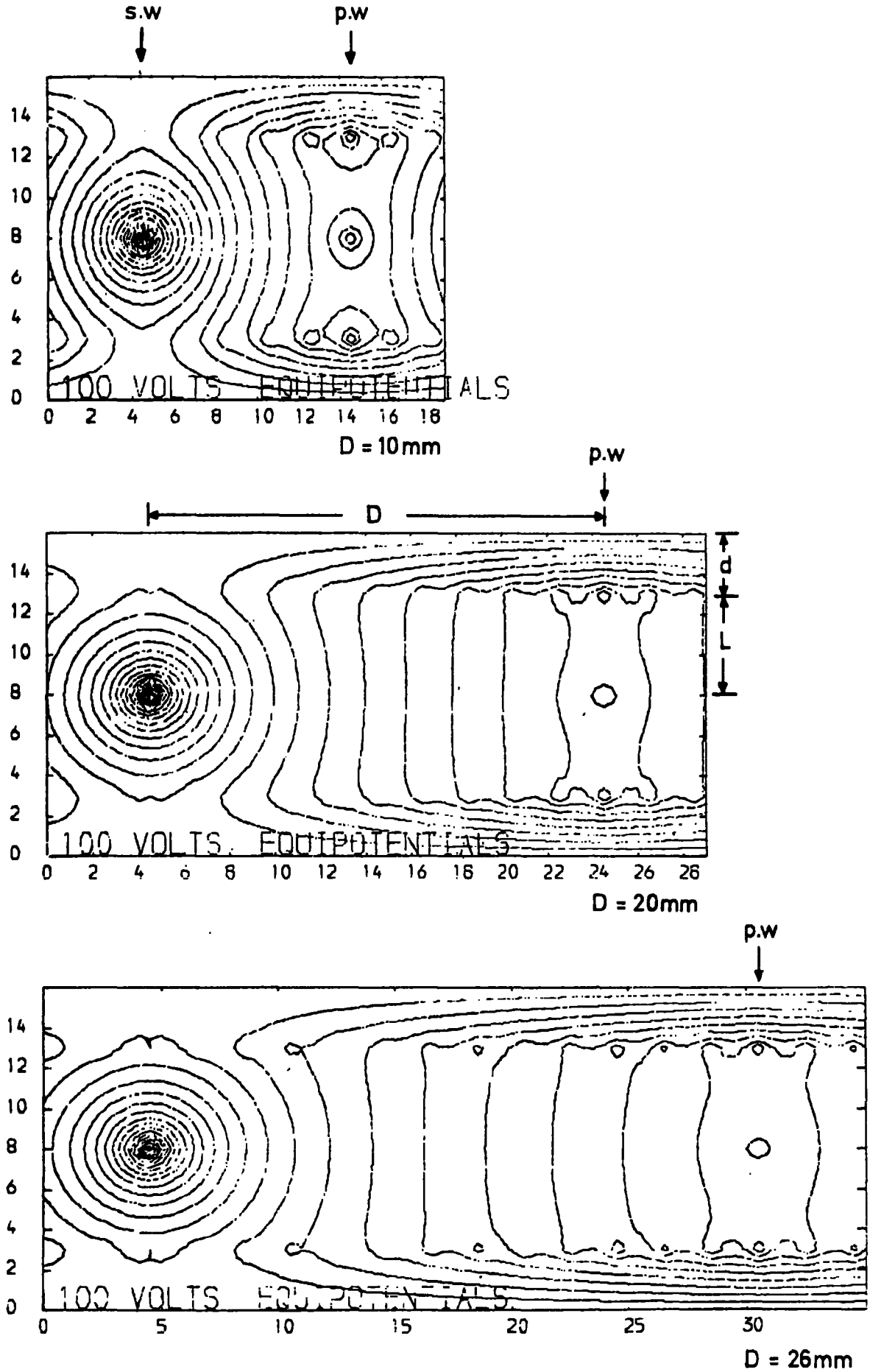

FIG. 5·13 CONTOURS FOR DIFFERENT DRIFT DISTANCES.

the potential wires the situation is reversed and a higher field is obtainable with low values of d. Due to this high field breakdown becomes more probable near this region at low d values due to the high field. These results are similar to those of Wylie[9] who concluded that "non-uniformity becomes greater for larger values of d". It should be noted that Wylie's results were in the sense wire plane only. Examining the field obtained in the drift plane for different d values shows that the fluctuation increases with decreasing d. This is shown in Fig 5.15. where the maximum "average-fluctuation" in field around potential wires are 1.25, 1.59 and 2.95 kV/cm for d = 5, 3 and 1 mm respectively. Due to the high field produced in the drift wire-earth plane region at low d values, field penetration causes an increase in the sense wire region of influence. This can be seen in Fig 5.16 where the radius of the zero equipotential contours are 4.5, 4.6 and 5 mm for d = 5, 3 and 1 mm respectively.

From the above results it is obvious that low values of d are not desirable. The limit on the maximum value of d is set mainly by the solid angle subtended by a source at the front window. This increases with increase of the chamber thickness. In most of this work the value of d was chosen to be 3 mm.

5.5.3 Anode-drift Wire Plane Separation (L):

The effect of changing L on the chamber field is shown in Fig 5.17. From this figure one can see that in the main drift region the field decreases with increasing L until very near the potential wires ($\sim$ 2 mm) where the field increases with increasing L. From the contour equipotentials shown in Fig 5.18, the zero equipotential contour can be seen to become more elongated in the y-direction, when L decreases. At low L values the sense wire region of influence, in the y-direction, extends to 90% of the sense

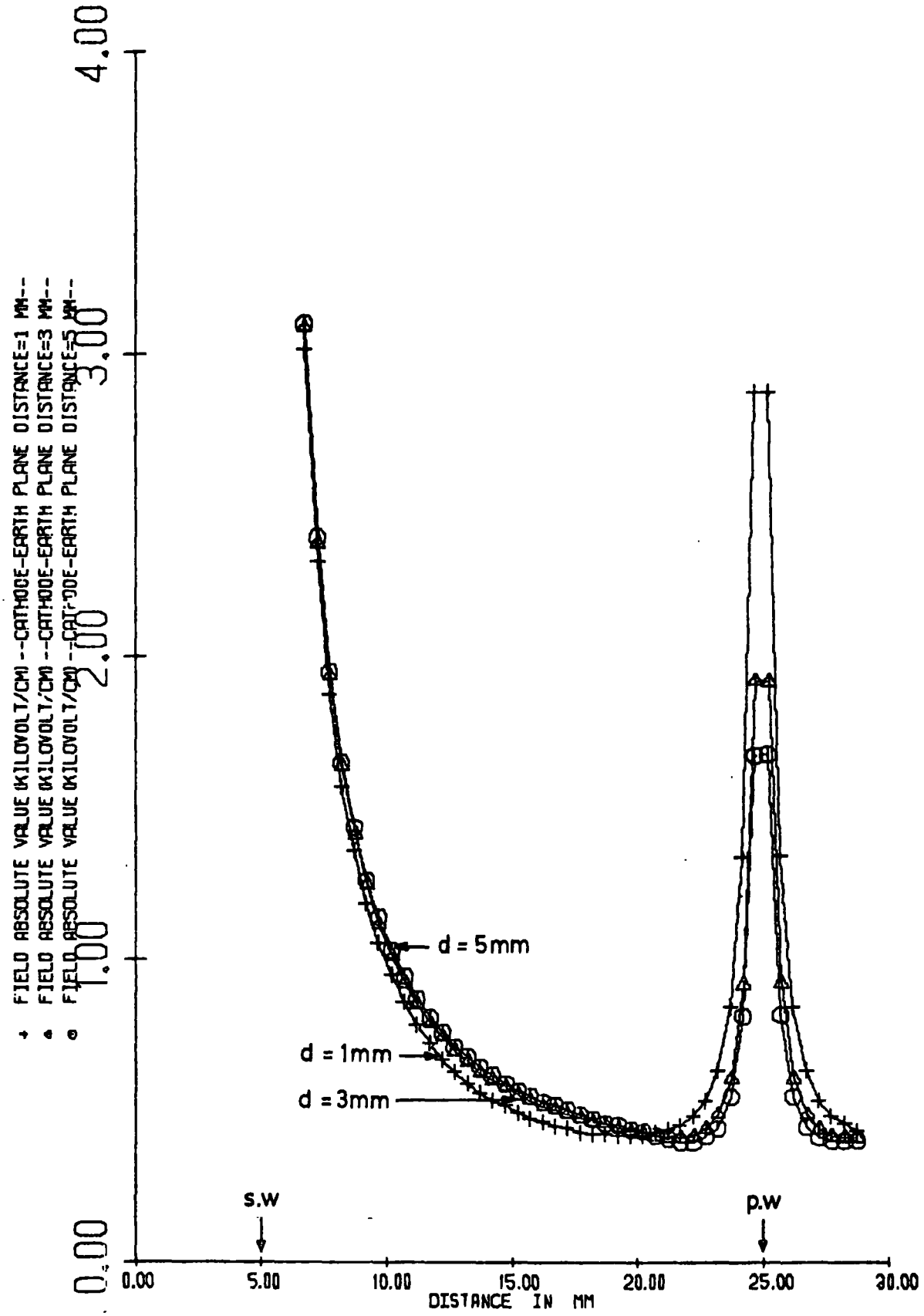

FIG. 5·14 EFFECT OF DRIFT-EARTHPLANE SEPARATION ON THE FIELD IN THE SENSE WIRE PLANE.

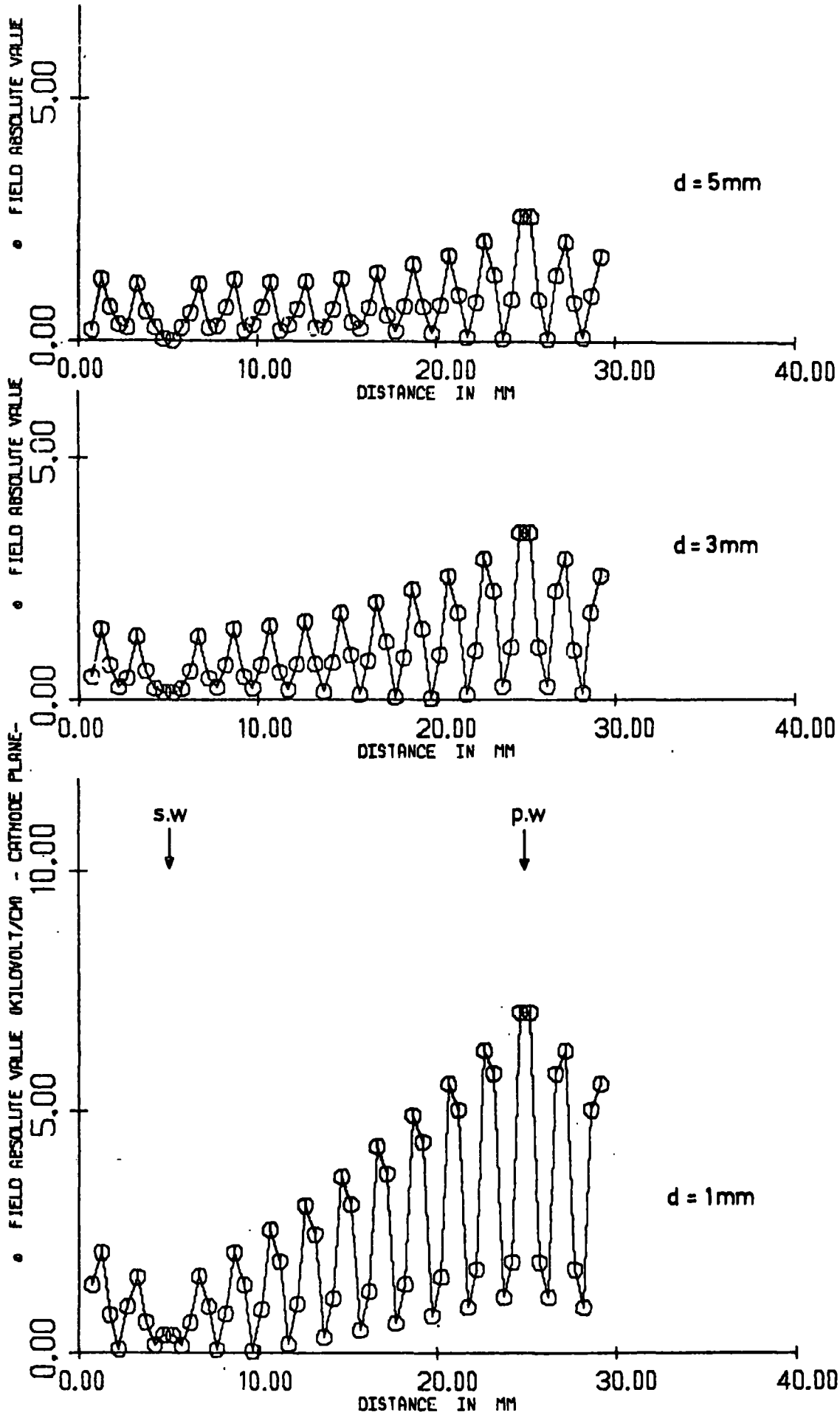

FIG. 5·15 FIELD FLUCTUATIONS IN THE DRIFT WIRE PLANE AT DIFFERENT DRIFT WIRE - EARTHPLANE SEPARATIONS.

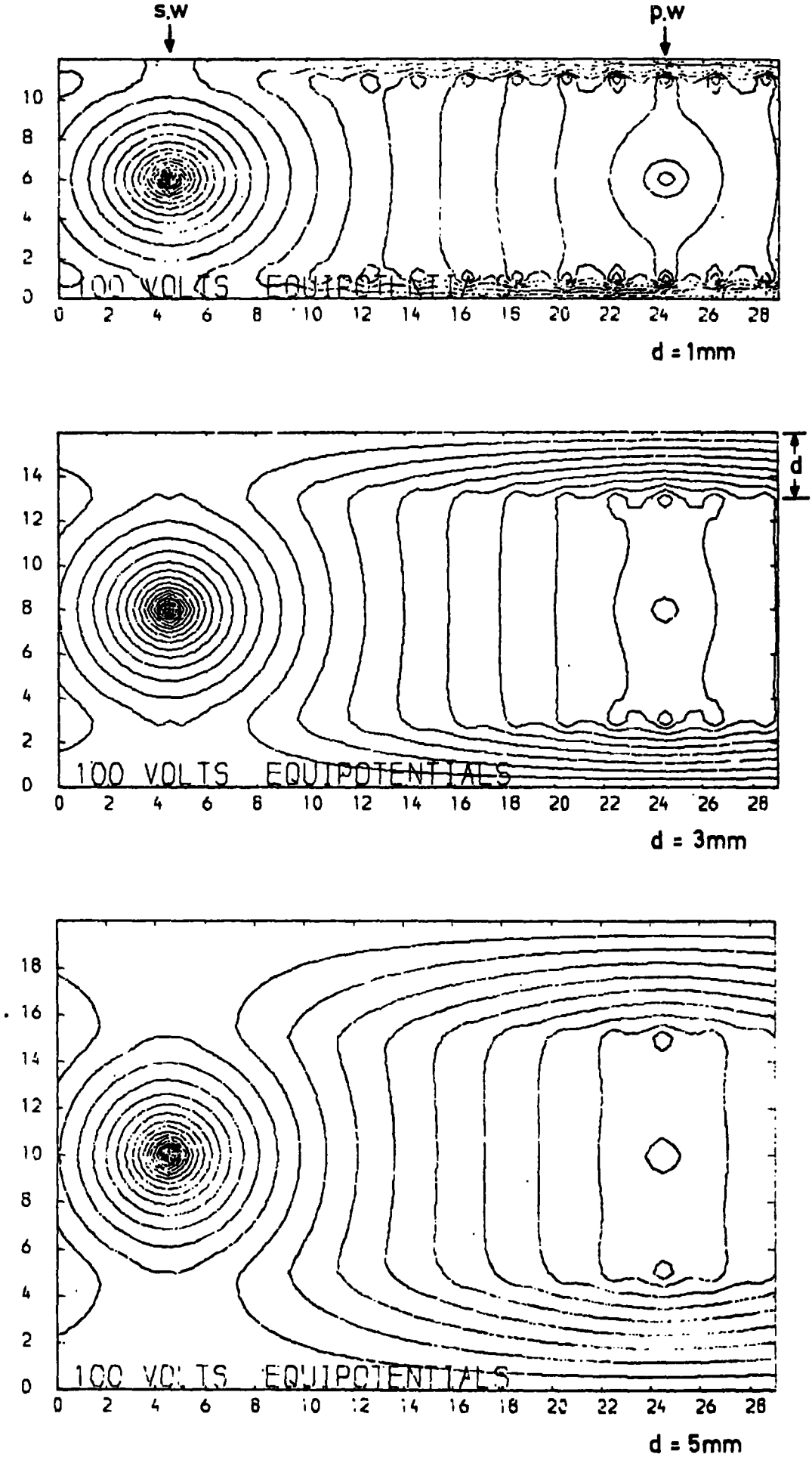

FIG. 5·16 CONTOURS FOR DIFFERENT DRIFT-EARTH PLANE SEPARATION.

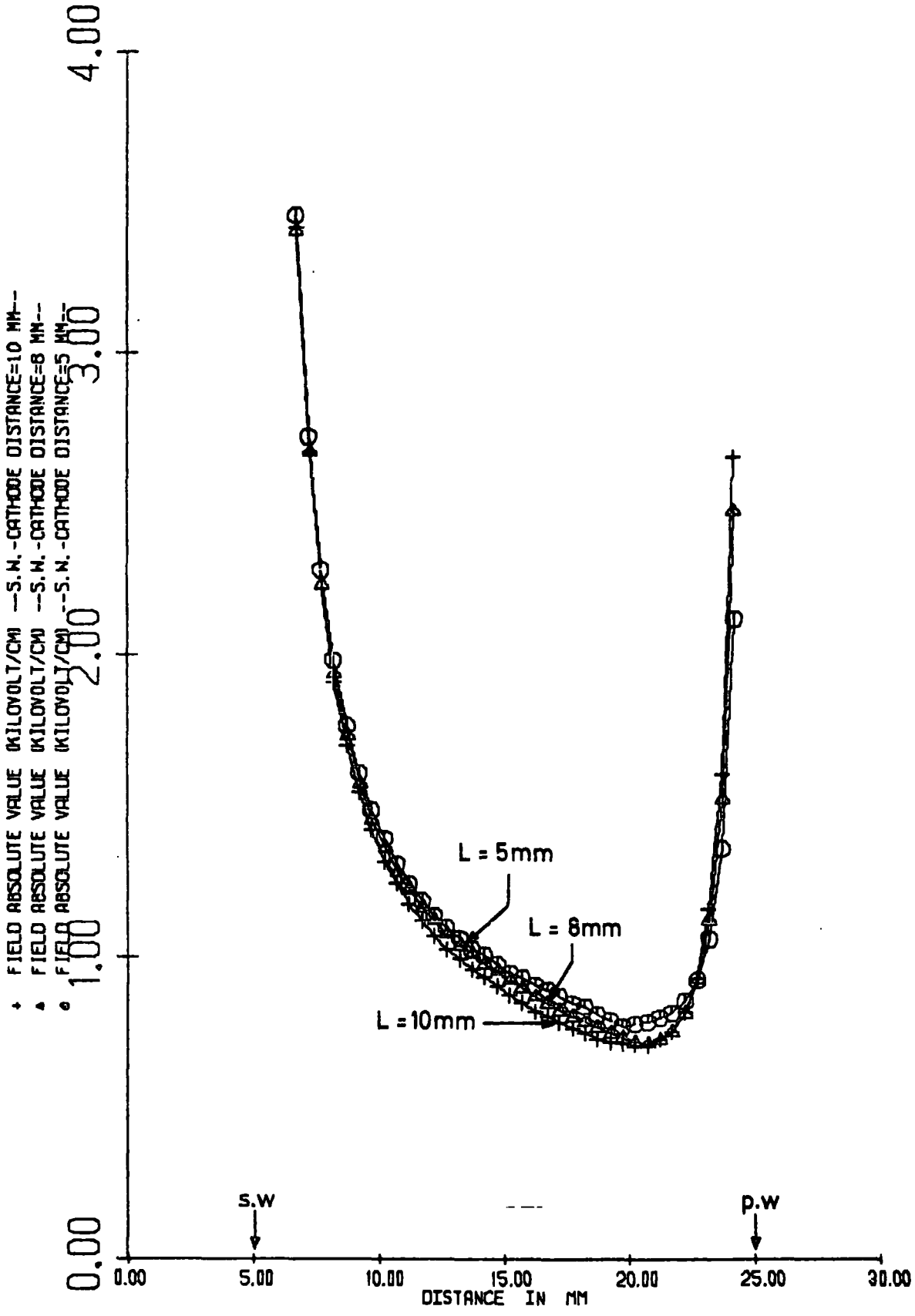

FIG. 5·17 EFFECT OF ANODE DRIFT PLANE SEPARATION ON THE FIELD IN THE SENSE WIRE PLANE.

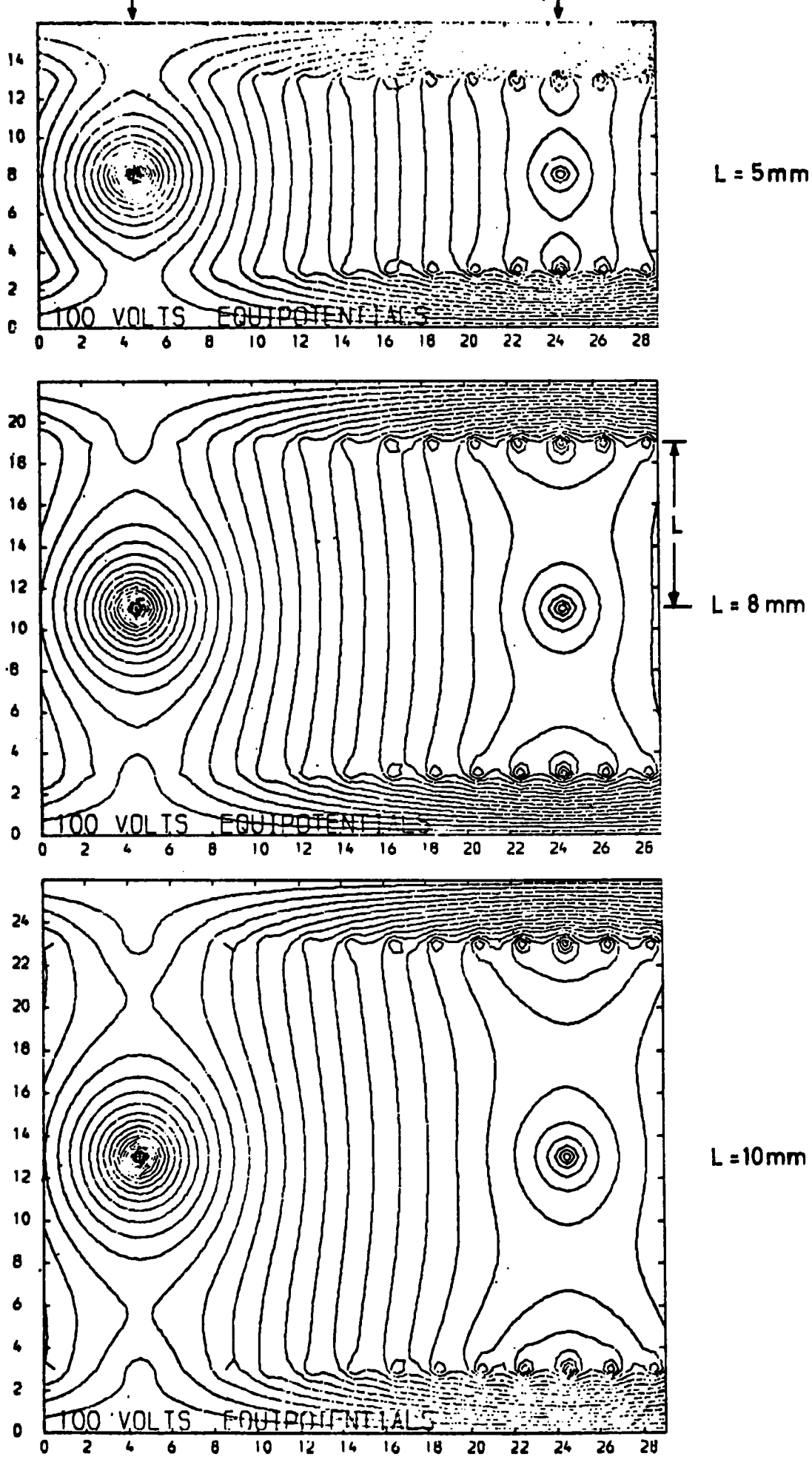

FIG. 5·18 CONTOURS FOR DIFFERENT ANODE DRIFT PLANE SEPARATIONS.

wire-drift wire plane region at L = 5. This extension drops to 44% and 35% at L = 8 and 10 mm respectively. This is due to lower field penetration into the drift region. This is also the reason for the slight decrease in the field fluctuations in the drift plane above the sense wire, observed at high L values. For less field penetration, large L values should be used but according to Steffen and Vannucci[8] the increase in L values caused a decrease in the efficiency of their chamber. This they attributed to the change in the geometrical factor, i.e. the solid angle. In this work the value of L was in the range of 6-9 mm.

5.5.4 Drift Wire Spacing (s):

Fig 5.19 shows the variation of fields, in the sense wire plane, for different values of drift wire spacings (s). In this figure it is clear that lower fields occur at higher spacings in most of the drift region (80%). Near the potential wires, the situation is reversed and higher fields occur with larger drift wire spacings. The other observation was the increase of non-uniformity in the field near the drift plane with increasing s. Fluctuations around the potential wires were 1.19, 3.27 and 4.05 kV/cm for s = 1, 2 and 4 mm respectively. The non-uniformity in the field inside the chamber can be seen in Fig 5.20 for the equipotential contours for the three chambers of s = 1, 2 & 4 mm. From this figure the region of sense wire influence (the zero equipotential) can be seen to increase with increasing s. All the previous mentioned unwanted phenomena namely, lower field, non-uniformity inside the chamber and large sense wire region of influence, are the result of field penetration into the drift region of the chamber. This field penetration is more pronounced at high drift wire spacings and makes the field inside the chamber more sensitive to external components or electrodes[10]. In this work cathode wire spacings were either 2 or 1 mm.

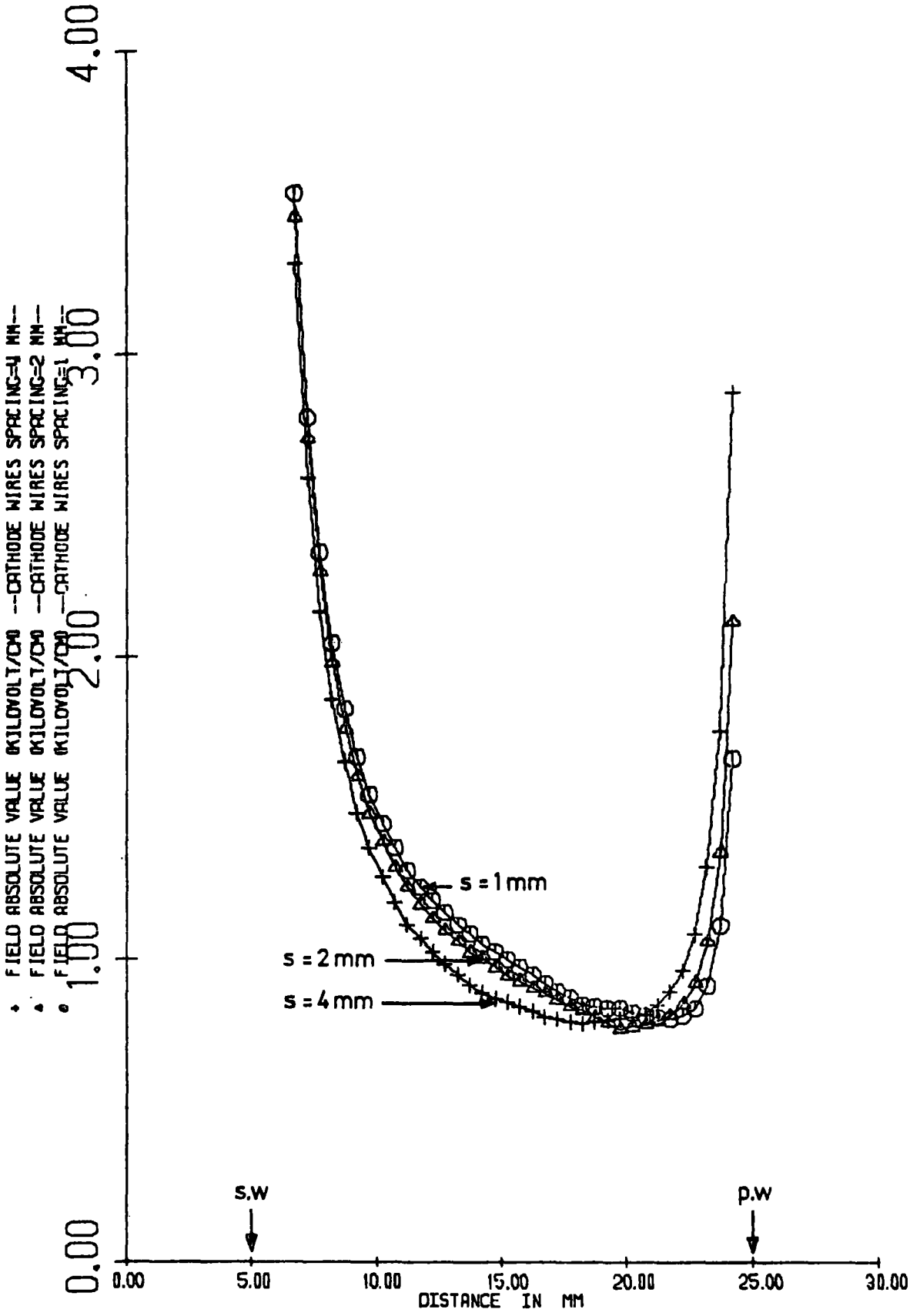

FIG. 5·19 EFFECT OF DRIFT WIRE SPACINGS ON FIELDS IN THE SENSE WIRE PLANE.

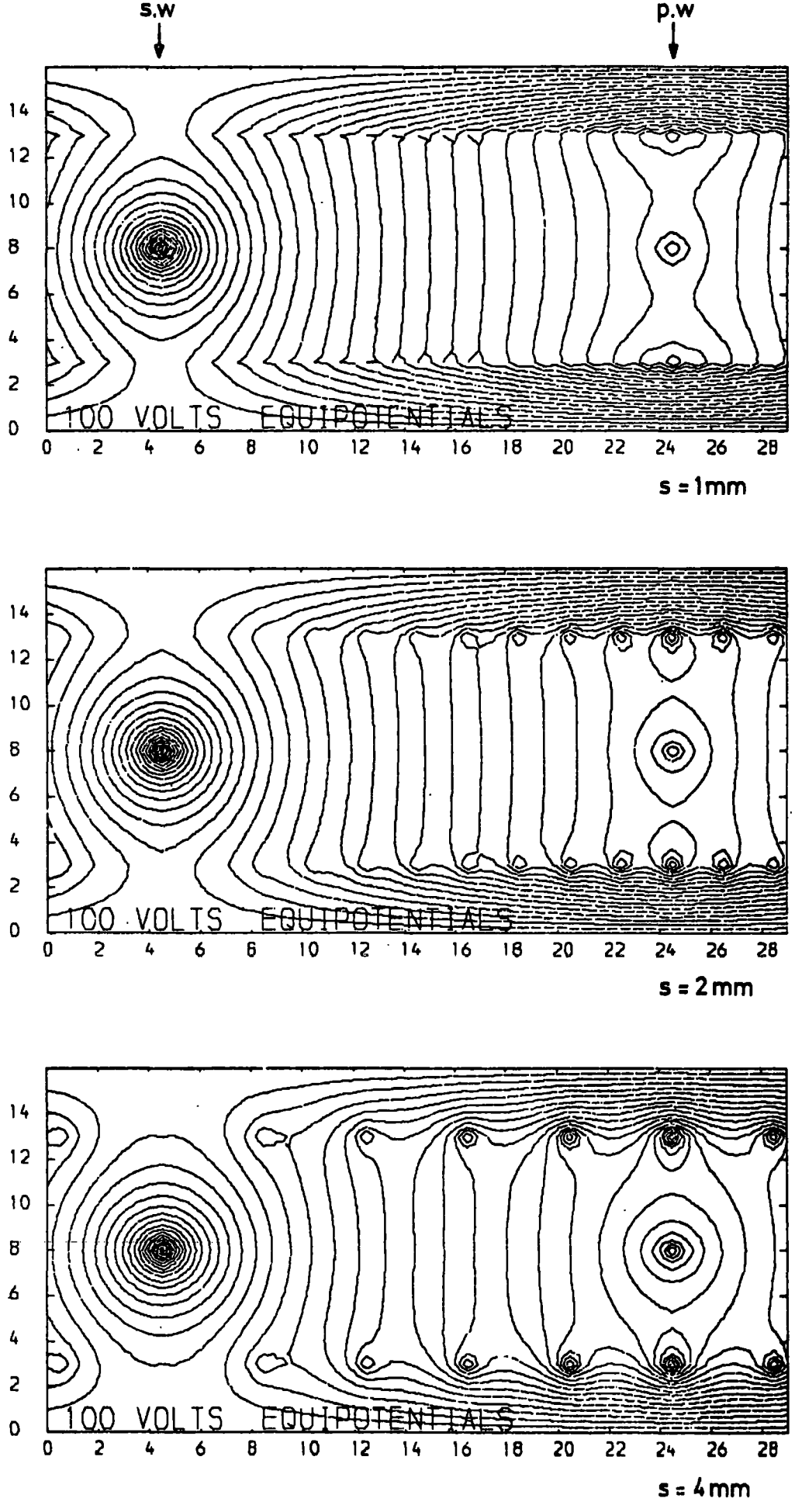

FIG. 5·20 CONTOURS FOR DIFFERENT DRIFT WIRE SPACINGS.

5.5.5 Anode Voltage (V_a):

The increase of field inside the chamber with increasing anode voltage V_a is shown in Fig 5.21 for three values of V_a, 0, 2000 and 3000 volts. Near the potential wires, the field decreases with increase of the anode voltage. Wylie[9] also observed the effect of V_a on the field (in the sense wire plane only) and concluded that no change in field occurred except close to the sense wires. However, in our case the change in the field shown in Fig 5.21 occurs in more than half the drift distance. The region of influence of the sense wire increases, as expected, with increasing V_a and this can be seen in the equipotential contours shown in Fig 5.22. Also in this figure one can see that the fluctuation in field in the drift wire plane is high above the potential wire at $V_a = 0$. This shows the contribution of V_a to the field inside the whole chamber.

5.5.6 Drift Voltage (V_k):

The effect of increasing the drift voltage on the field is shown in Fig 5.23. As expected the field inside the chamber increases with increasing the drift voltage. In the middle of the drift distance the drift field increases from 0.58 to 0.92 and 1.31 kV/cm when the drift voltage increases from 1000 to 2000 and 3000 volts respectively. This less than linear increase is due to the anode voltage effect. At the same time the increase of the drift field leads to a decrease in the region of influence of the sense wire. This range drops from 22% to 16% and then to 12.4% of the total drift distance when V_k increases from 1000 to 2000 and 3000 volts respectively. This can be seen in Fig 5.24 for the equipotential contours. These two favourable phenomena, namely high field useful for high drift velocity and small sense wire range of influence for better particle localisation are accompanied by the following unwanted phenomenon at high fields. Near the potential wires the increase in field with drift voltage is more linear than elsewhere in the chamber.

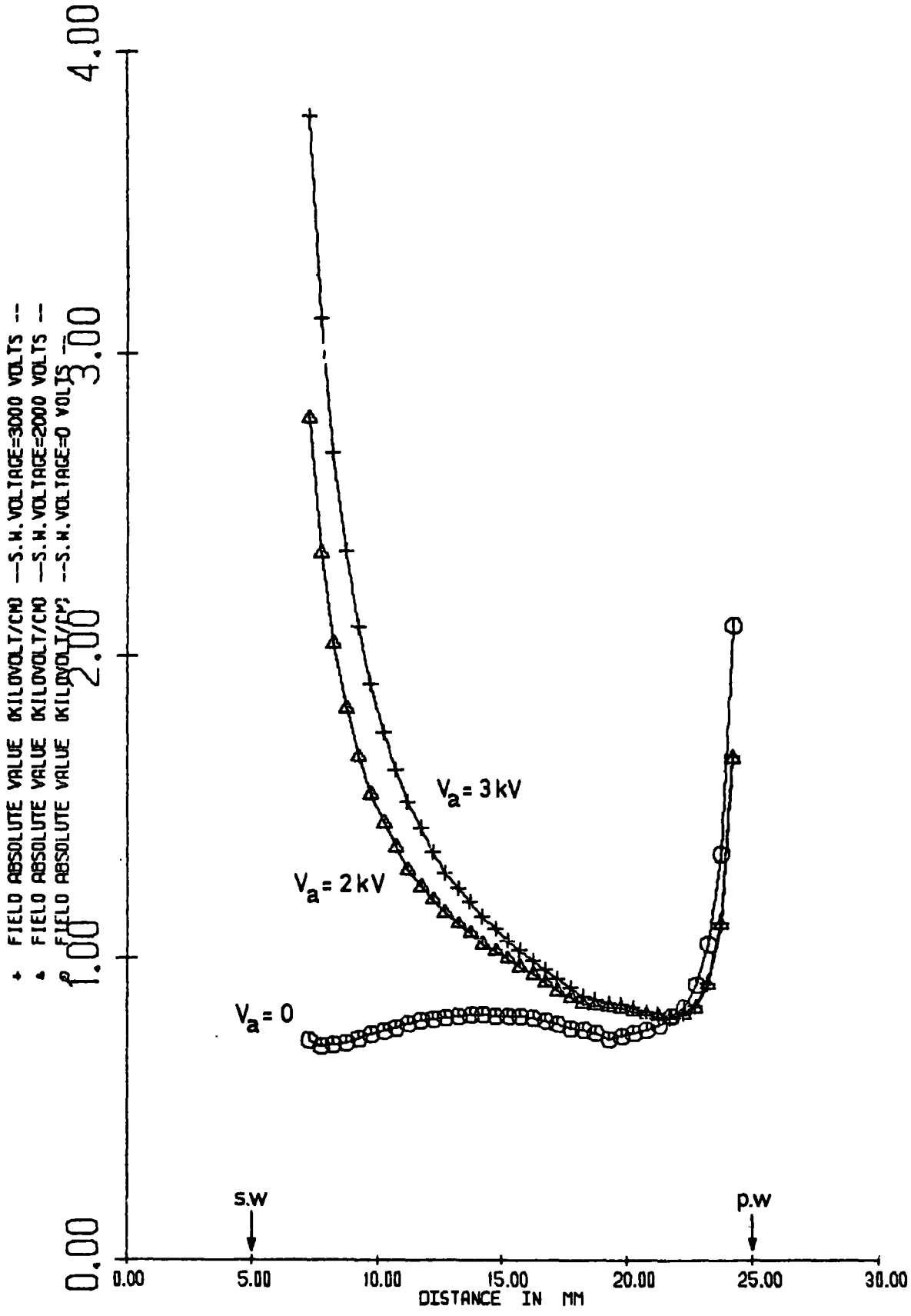

FIG. 5·21 EFFECT OF DIFFERENT ANODE VOLTAGES ON THE FIELD IN THE SENSE WIRE PLANE.

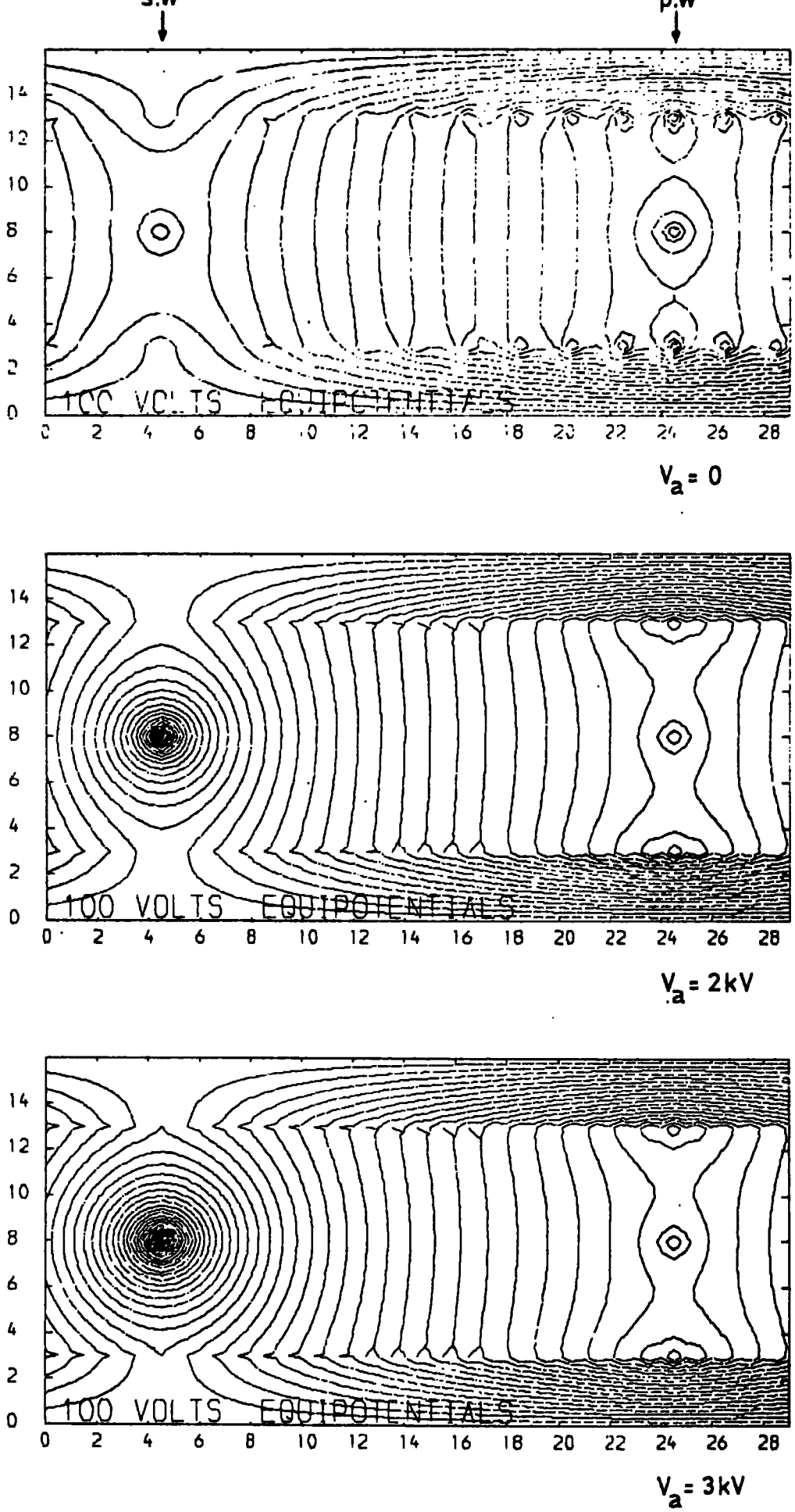

FIG. 5·22 CONTOURS FOR DIFFERENT ANODE VOLTAGES.

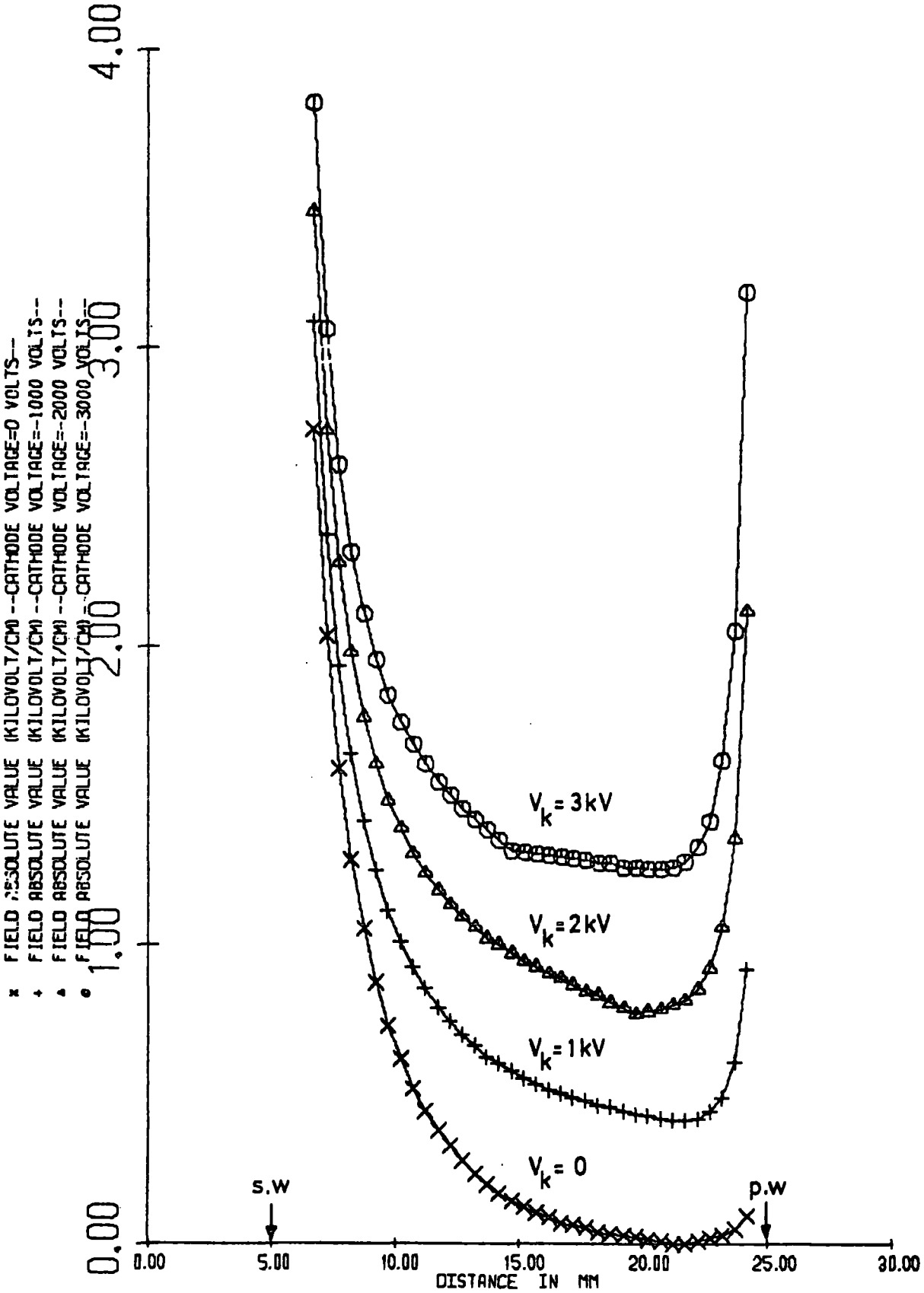

FIG. 5·23 EFFECT OF DRIFT VOLTAGE ON THE FIELD IN THE SENSE WIRE PLANE.

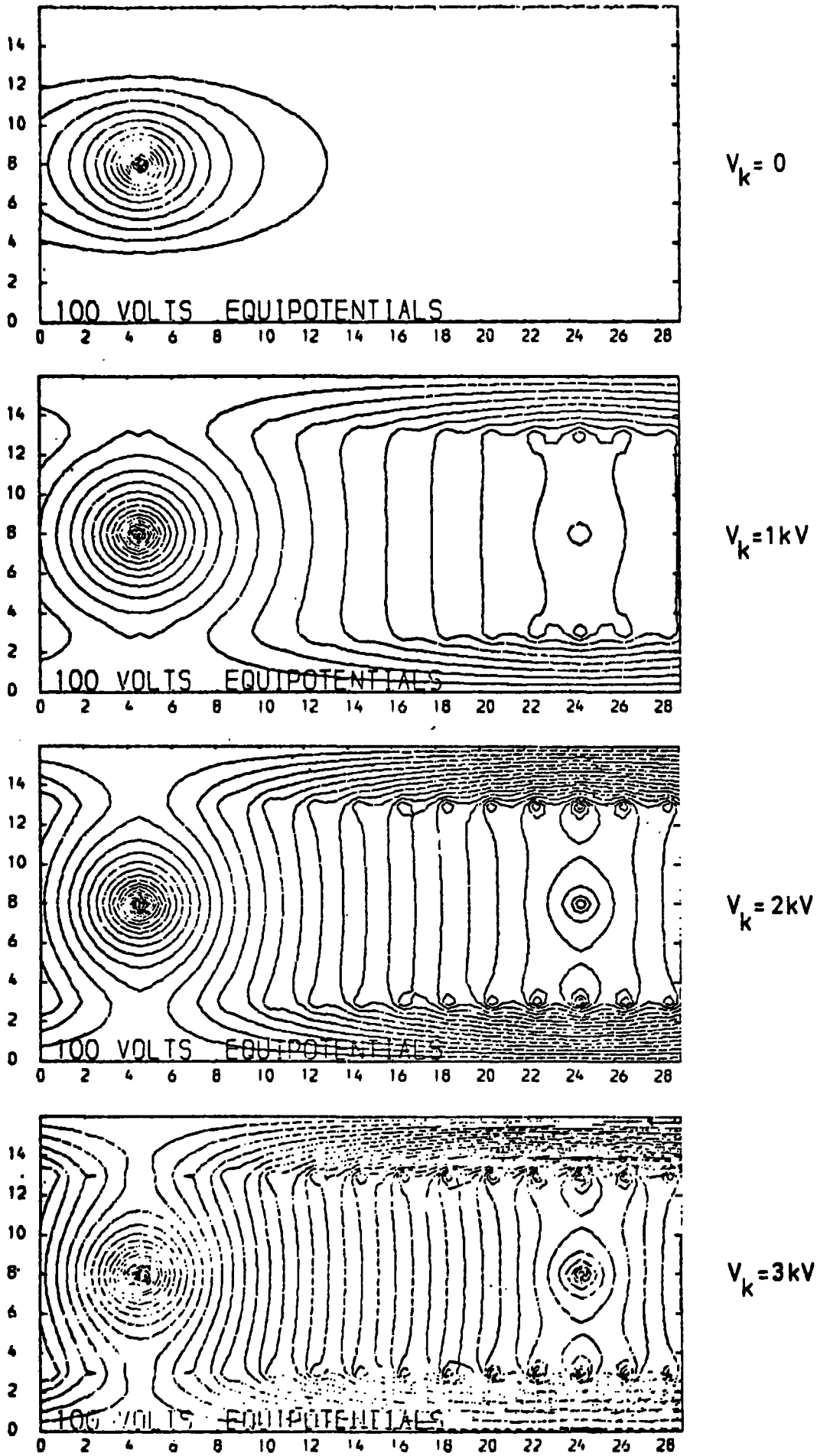

FIG. 5·24 CONTOURS FOR DIFFERENT DRIFT VOLTAGES.

The field near the potential wires increases from 1.92 kV/cm at V_k = 1000 volts to 4.4 and 6.7 kV/cm at V_k = 2000 and 3000 volts respectively i.e. with a ratio of 2.3 and 3.5 between the first V_k value and the second and between the first and the third respectively. These ratio were only 1.59 and 2.26 in the middle of the drift distance and 1.08 and 1.2 near the sense wire. This high increase in the field near the potential wires causes a high increase in the field between the drift wire plane and the earth plane. This also causes big non-uniformity in the field and increases the probability of breakdown. The average fluctuation near the potential wire are 1.6, 3.3 and 4.9 for V_k values of 1,2 and 3 kV respectively. On the other hand Wylie again concluded, from observing the field in the sense wire plane only, that no significant change was seen in the uniformity of the drift field with changing V_k.

On account of the above results, high V_k values were avoided in this work and the range of 1000-2000 volts for V_k was used.

5.6 CONCLUSIONS

The importance of the field shape in MWPC's and DC's is due to its big role in determining the process of events inside the chamber. The limitation of the high positive field to a narrow region around the sense wire provides the requirement of limiting the region of excitation and ionization to be around the sense wire. In DC's the uniform drift field in the drift region should not be high enough to produce excitation in that region. This may lead to the deterioration in energy resolution. Also the field between the drift wire plane and earth plane plays an important role in forming the field inside the chamber due to field penetration. It is thus vital to consider all the factors affecting the field inside the chamber when designs of MWPC's, DC's or GSC's are being considered.

Chapter 5 - References

1. Durham University NUMAC Service Doc. No. U 16 (1978). and Doc. No. U 48 (1978).

2. T. Tomitani, Nucl. Inst. & Meth. 100 (1972) 179.
F. Bourgeois and J.P. Dufey, CERN-NP Internal Report 73-11 (1973).

3. M. Comyn, Durham University, Internal Report N1-78-6 (1978).

4. M.P.R. Waligáraski, Nucl. Inst. & Meth. 109 (1973) 403.

5. G. Charpak et al, Nucl. Inst. & Meth. 80 (1970) 13.

6. P. Rice-Evans, Spark, Streamer, Proportional and Drift Chambers, (The Richelieu Press, London, 1974).

7. G. Charpak, Wire Chamber : A Reveiw and Forecast CERN-Report (1976)

8. P.Steffen and Vannucci, CERN-NP Internal Report 69-29 (1969).

9. A. Wylie, CERN NP Internal Report 74-7 (1974).

10. G.Charpak, Nucl.Inst. & Meth. 108 (1973) 413.

CHAPTER SIX

GAS SCINTILLATION COUNTERS

6.1 INTRODUCTION

In this chapter the main characteristics of gas scintillation counters (GSC) are analysed. The deisgn and arrangement of GSC's used in this part, in both the proportional and drift counter modes, were given in Chapter 2 as well as the characteristics of the photomultiplier tube used.

The characteristics under test in this chapter are the charge and light gain (tested with a GSPC), the plateau and energy resolution, and the pulse shape, i.e. its amplitude, rise time and width. Each of these characteristics was tested by varying several factors such as nitrogen concentration, sense wire radius etc. The aim of these tests was to optimize these parameters in order to make the chamber suitable for high count rate experiments with reasonable energy resolution.

The last section in this chapter is concerned with the high rate tests and the effect of high rates on the performance of the counter. The high intensity beam used to test the chamber was provided from an X-ray machine with a Co target and Fe filter. This beam of 6.9 keV was used as well as an Fe^{55} radioactive source of 5.9 keV.

6.2 CHARGE AND LIGHT GAIN

Gas scintillation counters provide two types of amplification :- Charge in the gas region and light in the photomultiplier. The contribution of each part to the characteristics of the chamber can be distinguished. The factors varied in this section are the sense wire voltage, the nitrogen concentration and the sense wire diameter.

The chamber used was the GSPC described in section 2.6.4. This chamber was used to eliminate the role of the drift field factor which would occur and complicate the process by the probability of producing light and charge if a GSDC had been used.

The charge pulse from one sense wire, through a 5000 pf capacitor, was fed to a charge sensitive preamplifier[1] then to an amplifier type NE-4658. A Tektronix-475 oscilloscope was used to measure the pulse amplitude. The light pulse from the photomultiplier was fed to a 1 dB attenuator (11% attenuation to prevent saturation in amplifier) then independently to the NE-4658 amplifier.

The charge pulse height produced by an X-ray source (Fe^{55}) was not sufficient to be detected, hence a heavy ionizing alpha source (Am^{241}) was used to provide a large enough charge pulse. The source was placed inside the chamber to avoid any absorption or scattering through the window. The measured pulse amplitudes were normalized to one by dividing by the primary pulse amplitude (at zero sense wire voltage).

6.2.1 Anode Voltage and Nitrogen Concentration

The charge and light gain are shown in Fig 6.1 and 6.2 respectively for different nitrogen concentrations. At low sense wire voltages the gain measurements are not very accurate due to the small values of pulse amplitudes which lead to high error in the gain measurements. This is due to limitations in reading small deflections on the oscilloscope.

Increasing the sense wire voltage increases the field around it and hence more excitation and ionization occur as a consequence of the increase in excitation and ionization the light and charge gain increase respectively. At constant nitrogen concentration , 4.4% for example, the exponential increases in charge and light gain differ in the starting points as shown in Fig 6.3. The light gain starts at below 200 volts

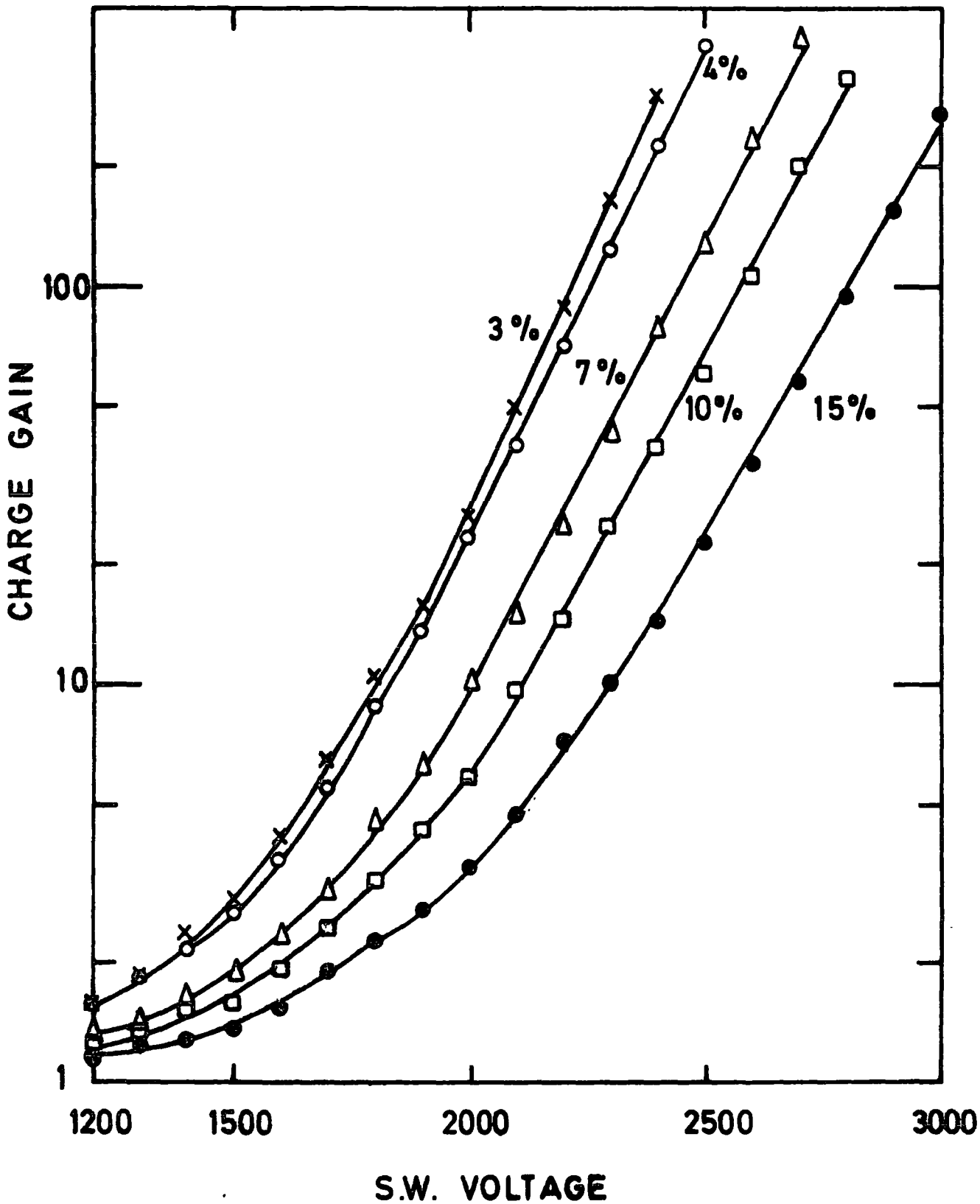

FIG. 6·1 CHARGE GAIN DEPENDANCE ON SENSE WIRE VOLTAGE AT DIFFERENT NITROGEN CONCENTRATIONS.

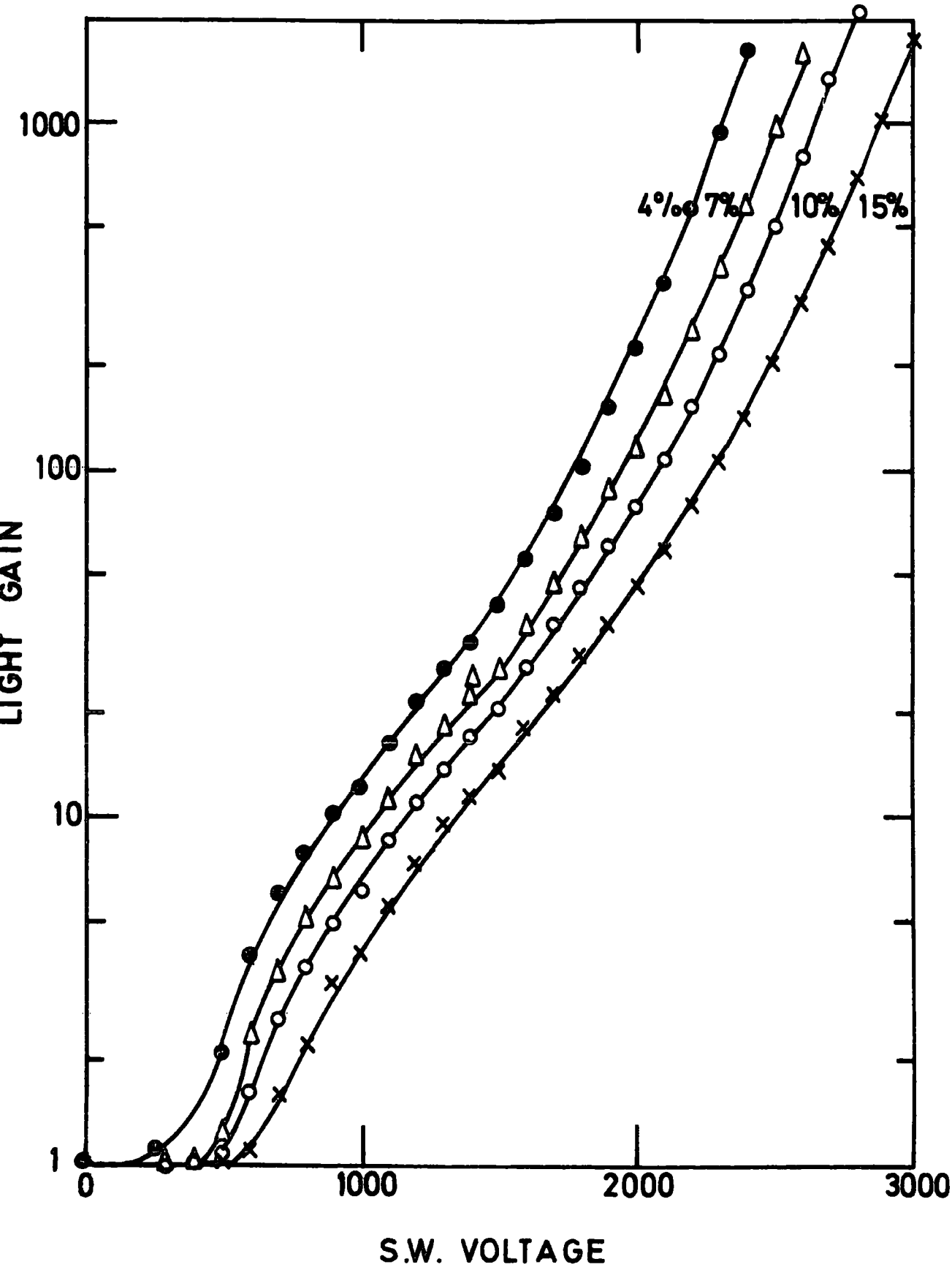

FIG. 6·2 LIGHT GAIN DEPENDANCE ON SENSE WIRE VOLTAGE AT DIFFERENT NITROGEN CONCENTRATIONS.

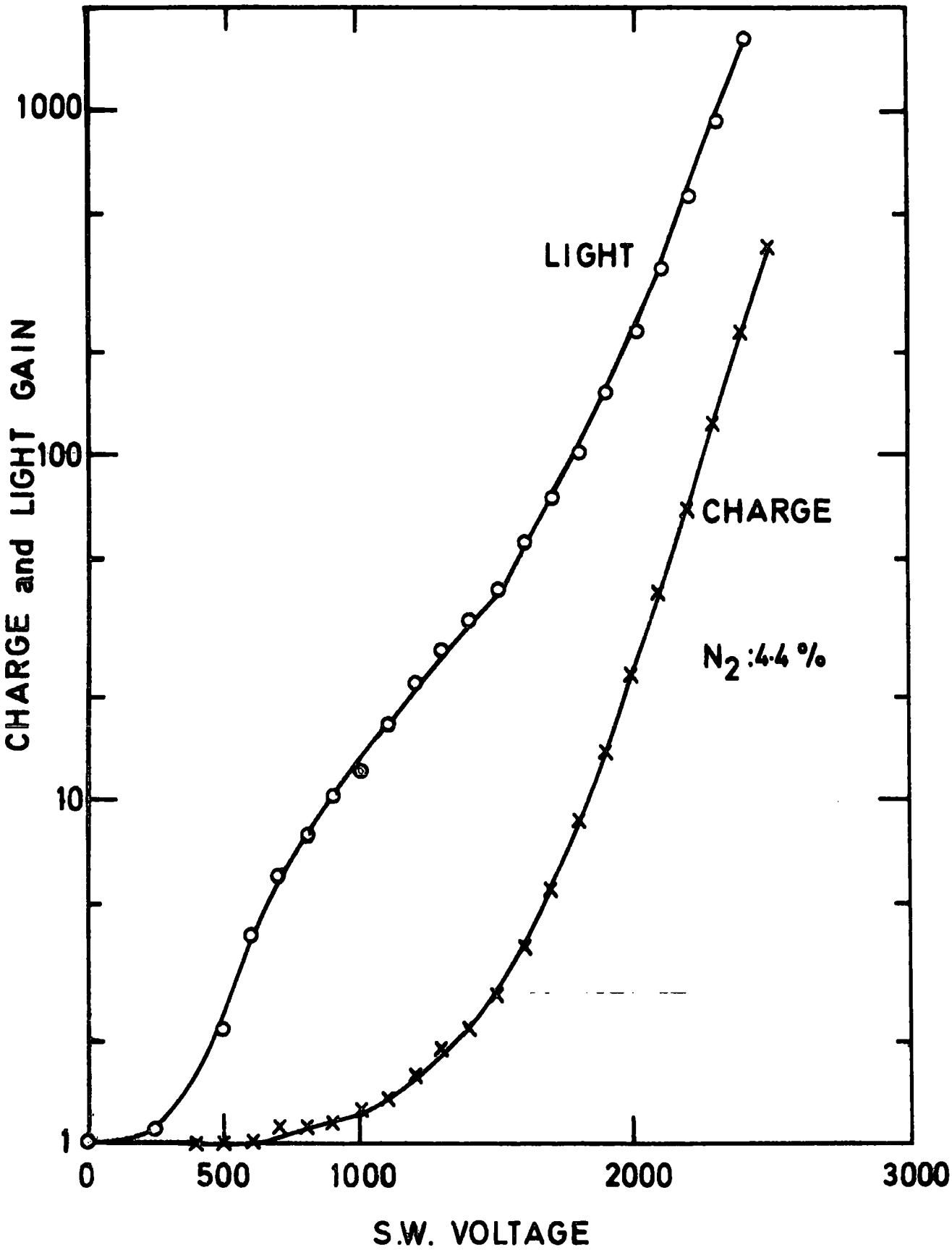

FIG. 6·3 CHARGE AND LIGHT GAIN AT 4·4 % NITROGEN CONCENTRATION.

while the charge gain starts well after it at 700 volts. Also the light gain is much higher than charge gain (factor of ∿7). The reason for the light amplification process starting earlier than the charge amplification process and having a higher gain is due to the excitation energy always being less than the ionization energy. Similar curves were obtained by Policarpo's[2] group for different nitrogen concentrations in argon at p = 965 torr in a GSPC. At 4.3% of nitrogen in argon the light-to-charge gain ratio was ∿3. This low ratio, compared to 7 in our case, can be due to the pressure factor and to the thin sense wire used, 140 μm in their chamber and 200 μm in our chamber.

The curves in Fig 6.1 and Fig 6.2 follow similar shape at different nitrogen concentration. At a constant anode voltage (2000 volts) the charge and light gain at different nitrogen concentration, taken from Fig 6.1 and Fig 6.2 respectively, were drawn in Fig 6.4. Both curves have a maximum around 1% ; it was at this concentration that the 3380 Å nitrogen band intensity was a maximum, as shown in Fig 3.4. Also, the fractional electron energy loss due to collisions is a maximum, see Fig 3.9, and this produces maximum light and charge. The maximum charge gain was 60 while the maximum light gain was 400. The actual light gain should be higher due to the undetected ultraviolet light. The loss in light gain due to the undetected ultraviolet is a minimum around 1% nitrogen concentration due to the drop in the 2200 Å argon band to a very low value, 10 arbitrary intensity unit compared to ∿ 250 for the 3380 Å nitrogen line. This was shown in Fig 3.4. At lower nitrogen concentration namely 0.1%, the 2200 Å argon band was 40 units and 3380 Å nitrogen line was 52 units.

The other result obtained from Figs 6.1 and 6.2 is the following: At constant charge gain, it was noticed that the light gain tends to be

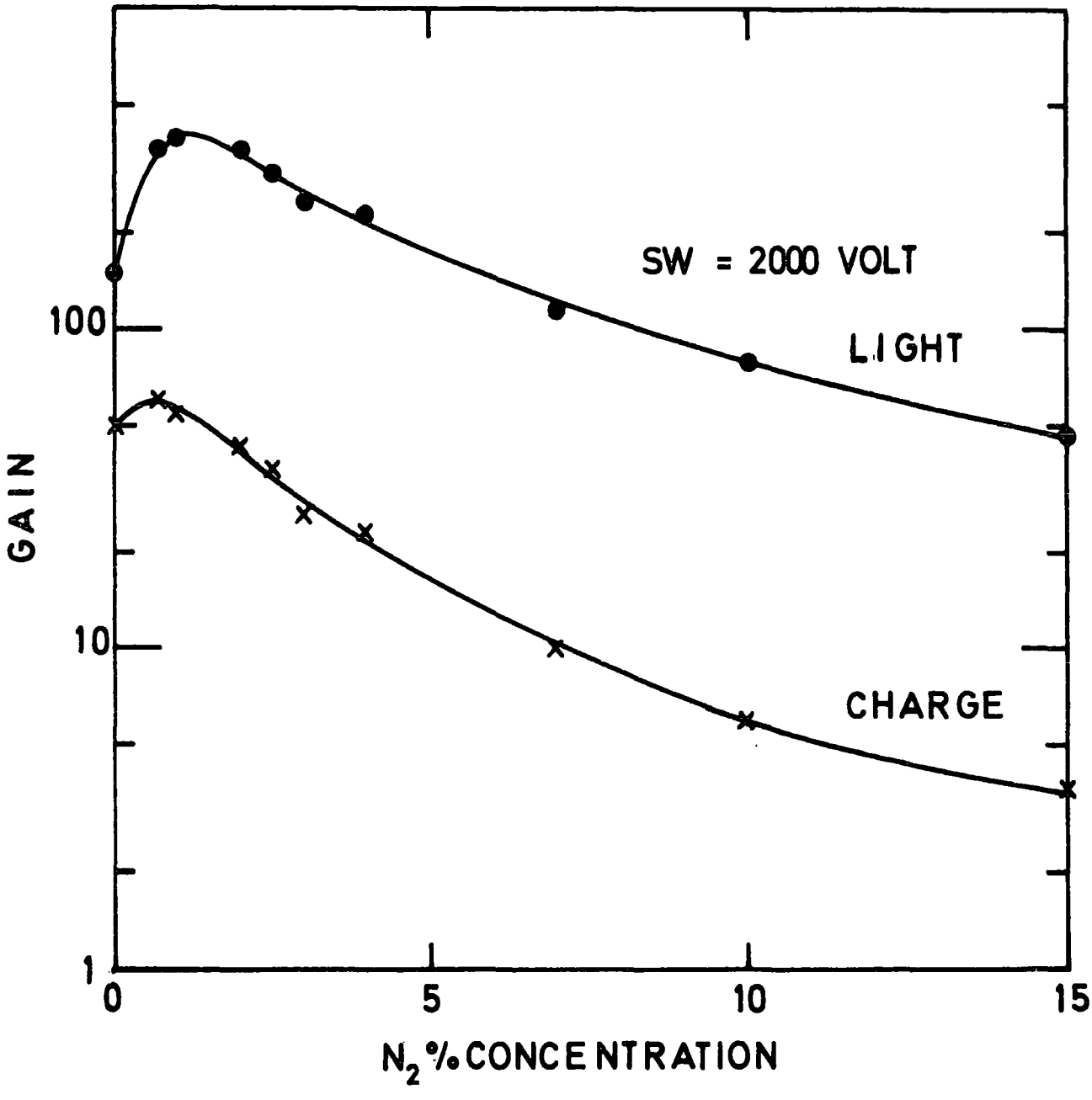

FIG. 6·4 CHARGE AND LIGHT GAIN DEPENDANCE ON NITROGEN CONCENTRATION AT SENSE WIRE VOLTAGE = 2000 VOLTS.

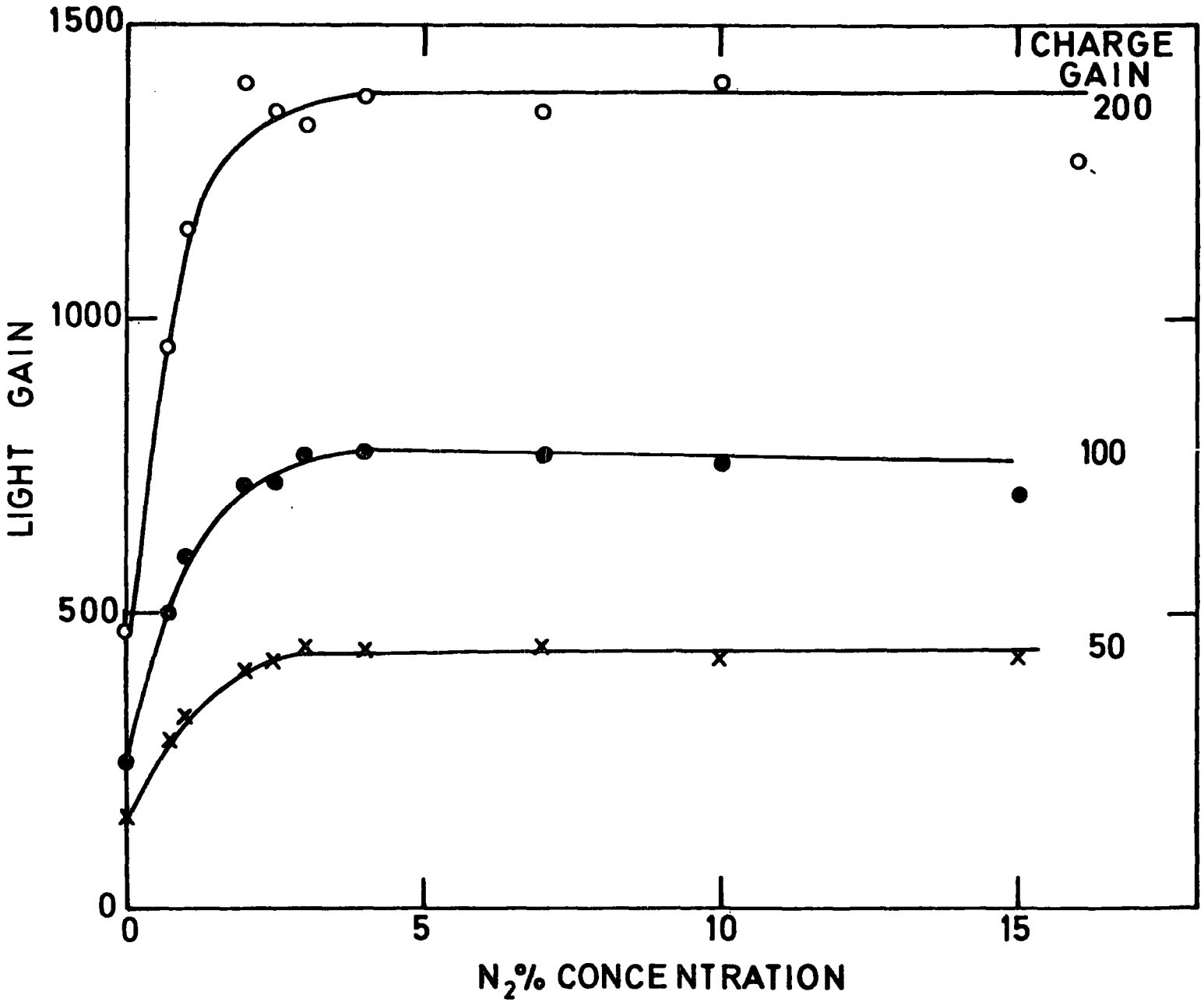

FIG. 6·5 LIGHT GAIN AT CONSTANT CHARGE GAINS.

constant at nitrogen concentrations higher than 4%. This is shown in Fig 6.5. The sense wire voltage required to give a charge gain of 50 was obtained from Fig 6.1 and the light gain corresponding to that voltage was deduced from Fig 6.2. The same procedure was repeated for the charge gains of 100 and 200 giving rise to curves of similar shapes. The ratios between the saturated light gain and charge gain are 8.8, 7.7 and 6.9 for the charge gain of 50, 100 and 200 respectively. This shows that at lower charge gain the probability of higher light output is better than that at higher charge gain due to less competition between excitation and ionization processes. From Fig 6.5 it was decided that a nitrogen percentage higher than 4% should be used with as low a charge gain as possible.

Several workers have measured the light and charge gains using GSC's with different gas mixtures. Conde and Policarpo[3] used pure argon and found that the ratio of threshold potentials for ion multiplications and light multiplications were higher than the ratio of the ionization potential of argon (15.7 eV) and the lowest excitation energy of argon (11.5 eV). The first ratio was between 3 and 5 depending on gas impurity, while the second was 1.37. They attributed the high light production to nitrogen impurities. In a later paper, Policarpo's group[2] confirmed the importance of small concentrations of nitrogen in an argon GSC. They also found that the pulse amplitude reaches a maximum at about 2.5% nitrogen. This value is not far from the result of Fig 6.4 if one considers the effect of pressure (970 torr in their case and 760 torr in our case) where, as was mentioned in Section 3.2.3, above 800 torr the intensity of the argon 1700-2000 Å region increases with pressure[4].

In comparing the light output from X_e, X_e-Ar and X_e-N_2 mixtures, Policarpo's group[5] observed that the maximum light output was obtained from Ar-X_e mixture of 3÷5% xenon concentration. The small percentage of

X_e is similar to the small percentage of nitrogen which produces maximum light output in argon-nitrogen mixture. They[6] showed the strong correlation between charge and light pulses in a pure X_e counter. Xenon has proved to be the best gas for light production, though very expensive; the same group found that in a X_e + 0.75% N_2 mixture the light output from 5.9 keV X-rays was about the same as that from higher energy gamma rays emitted by Cs^{137} using a NaI (Tℓ) crystal.

Other gas mixtures were used which produce large light pulses with very low charge gain such as the mixture used by Charpak et al[7] containing 48% Ar + 48% N_2 + 4% CO_2. This particular mixture has other characteristics in particular a drift velocity saturation with field which makes it favourable in two-dimensional localization detection of intense particle beams.

The choice of gas mixture for the production of light, by the electrons drifting in the field, with zero or very little charge amplification, is an important factor when it is required to avoid space charge effects with their limitations on high count rate experiments. In this work a mixture of argon and not less than 4% nitrogen was used.

6.2.2 Anode Wire Diameter

The effect of the sense wire diameter on the multiplication process in the chamber was discussed in section 4.5.2, and it was found that the multiplication factor increased as the wire diameter decreased according to the predicted relation 4.11.

The charge and light gain were measured for different sense wire radii, namely 200, 300 and 400 μm. The gas mixture used was Ar + 10% N_2 in the GSPC. Fig 6.6 shows these measurements and as expected the gain (charge and light) increased with decrease of the sense wire diameter. It was noticed that at constant charge gains, the light gain increases with

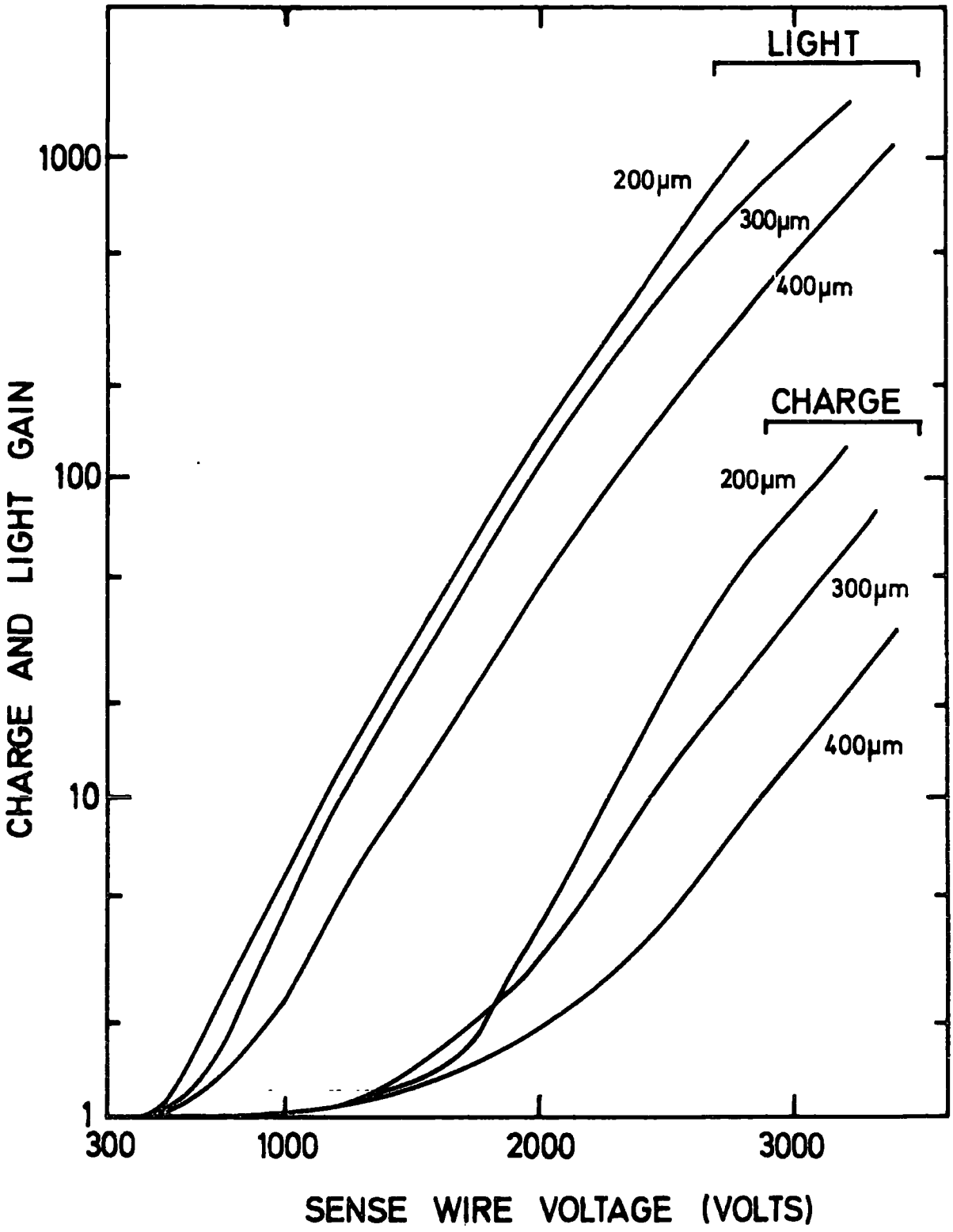

FIG. 6·6 CHARGE AND LIGHT GAIN FOR DIFFERENT SENSE WIRE DIAMETERS.

increasing the sense wire diameter. This is shown in Fig 6.7a for charge gains of 5,10, 20 and 30, the slope of the curves become steeper with increase of the charge gain. This is because the increase in charge gain, due to higher multiplication, leads in turn to higher excitation i.e. more light gain.

The increase of light gain with wire diameter can be explained according to eqn. 1.3.

$$E = \frac{V_a}{r \, \ell n(r_2/r_1)} \tag{1.3}$$

where r_2 and r_1 are the radii of the cylinder and the wire respectively and r is the distance from the wire. To produce the same charge gain, i.e. the same field, V_a is higher for higher wire radius as can be seen in Fig 6.6. Substituting the values of V_a from Fig 6.6, for each wire at a constant charge gain of 10 in eqn. 1.3 showed that the region of influence of the wires increases with increase of their diameter. Namely for wires of 200 μm, 300 μm and 400 μm, at a charge gain of 10, the distances (r) to produce this gain are in the ratio of 1, 1.19 and 1.52 respectively. The second factor affecting the light output is that the field very near to sense wires increases with decrease of the wire diameter This leads to a faster increase in charge production than light production. This can be seen in Fig 6.6 where the increase of charge gain with decrease of wire diameter is faster than the increase in light gain for example, at an anode voltage of 2.4 kV the charge gain increases by a factor of 4.43 when decreasing the wire diameter from 400 μm to 200 μm while light gain increases only by a factor of 2.8. This factor (the ratio between gain for 200 μm wire to that of 400 μm) increases with increasing anode voltage for the case

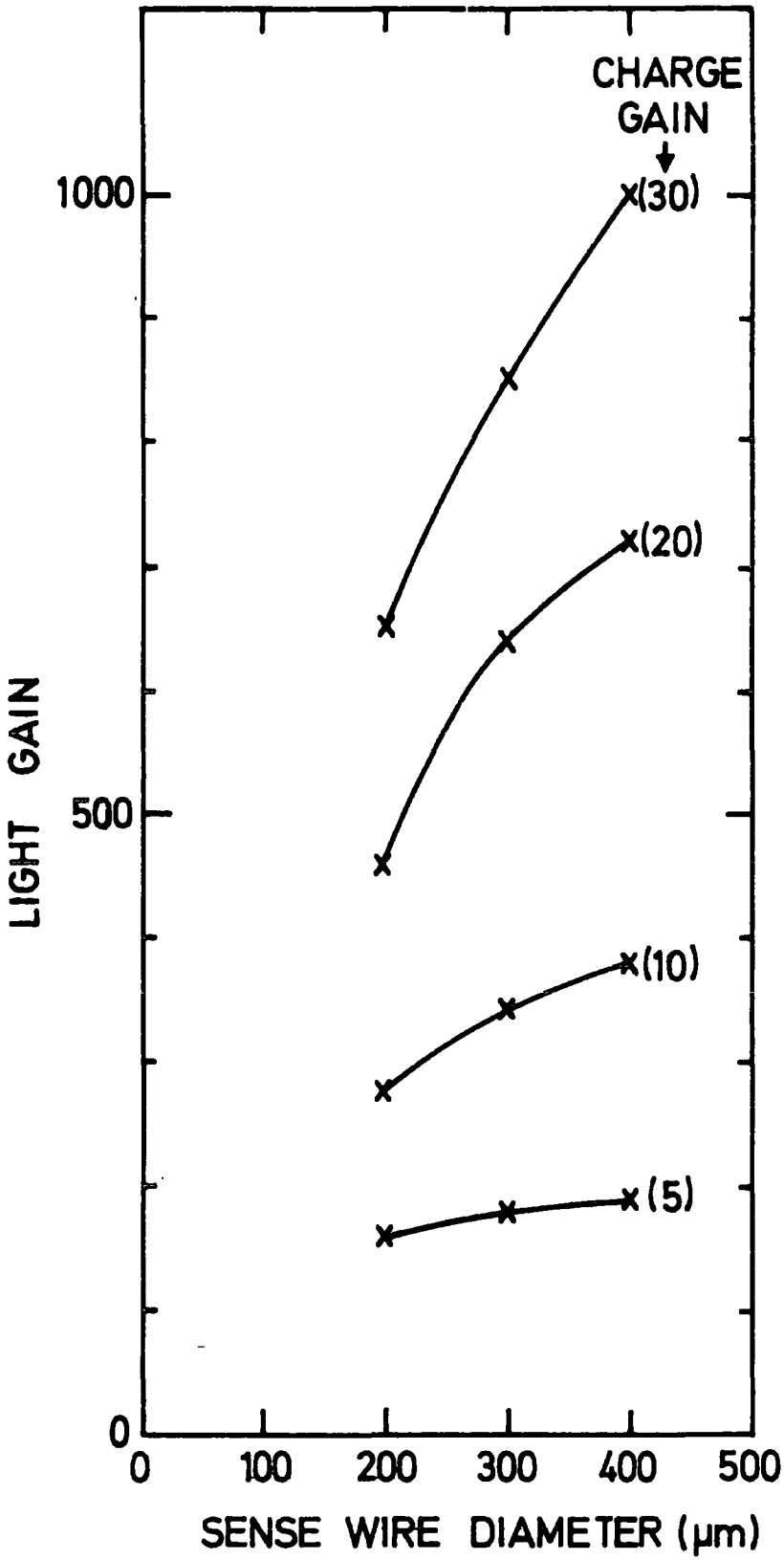

FIG. 6·7a LIGHT GAIN VARIATION WITH SENSE WIRE DIAMETER AT CONSTANT CHARGE GAINS.

of charge, but in the case of light it decreases with increasing anode voltage. This is shown in Fig 6.7b and c. This means that at high anode voltages, or at higher fields, the process of ionization is more frequent than the process of excitation. Hence with thicker wires one obtains a larger area of influence and a lower field. Both these factors produce more light output.

Conde et al[8] suggested an empirical relation between light output and electric field strength in a xenon filled parallel-plate GSPC. Musada et al[9] proved this relation to be in good agreement with the measured light in a liquid xenon cylindrical proportional scintillation counter. Also, they observed an increase in light gain with increase of anode wire diameter at constant charge gain similar to Fig 6.7a.

The study of factors affecting charge and light gain discussed in this section namely, anode wire diameter, anode voltage, and nitrogen concentration, shows that each has a considerable effect which can be treated independently of the other.

The increase of anode voltage caused an increase in charge and light gain but the charge gain increased faster than the light gain -see Fig.6.3,producing the serious disadvantage of space charge limitation. At constant charge gain it was found that the light gain reached saturation with less than 5% nitrogen. This saturated value was found to be about three times the light gain in pure argon for the three charge gain values (Fig 6.5). The same factor of increase in light gain, i.e. 3, was obtained when the charge gain was increased by a factor of 4 as shown in Fig 6.5, which shows that increase in nitrogen concentration is better as far as avoiding space charge effects are concerned. The wire diameter is another factor which can be changed without causing space charge effects- increasing the wire diameter by factor of 2 increased the light gain by

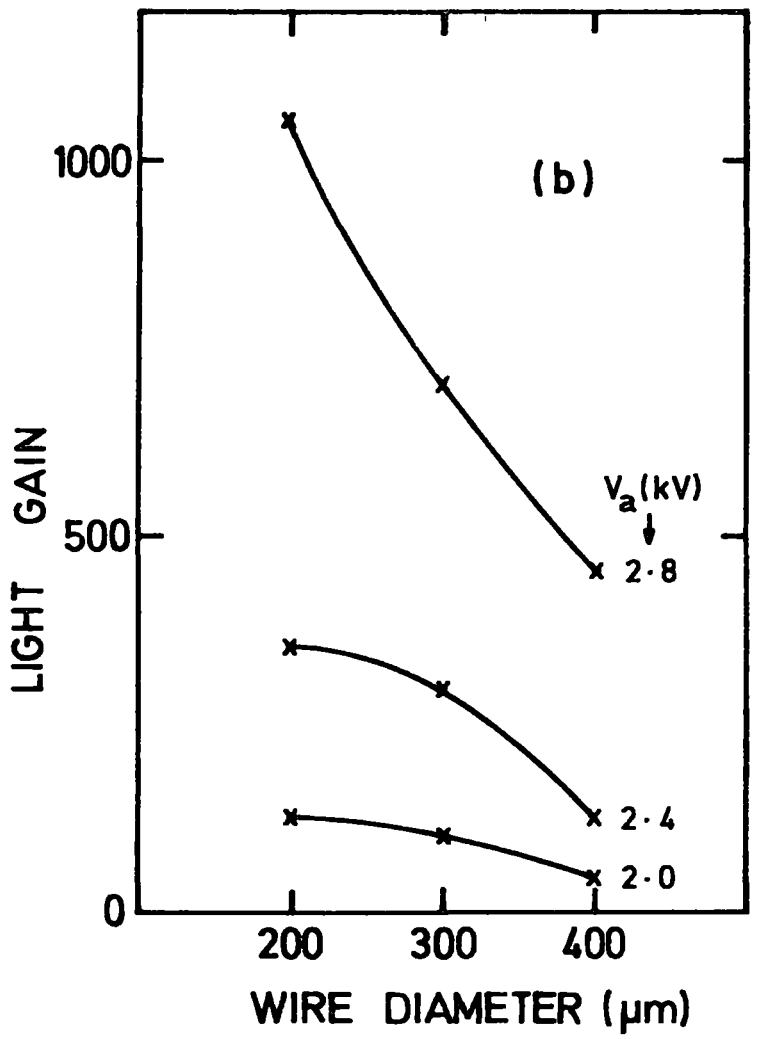

V_a (kV)	$M_{200\mu m}/M_{400\mu m}$ LIGHT	CHARGE
2	2·78	2·0
2·4	2·8	4·43
2·8	2·33	6·63

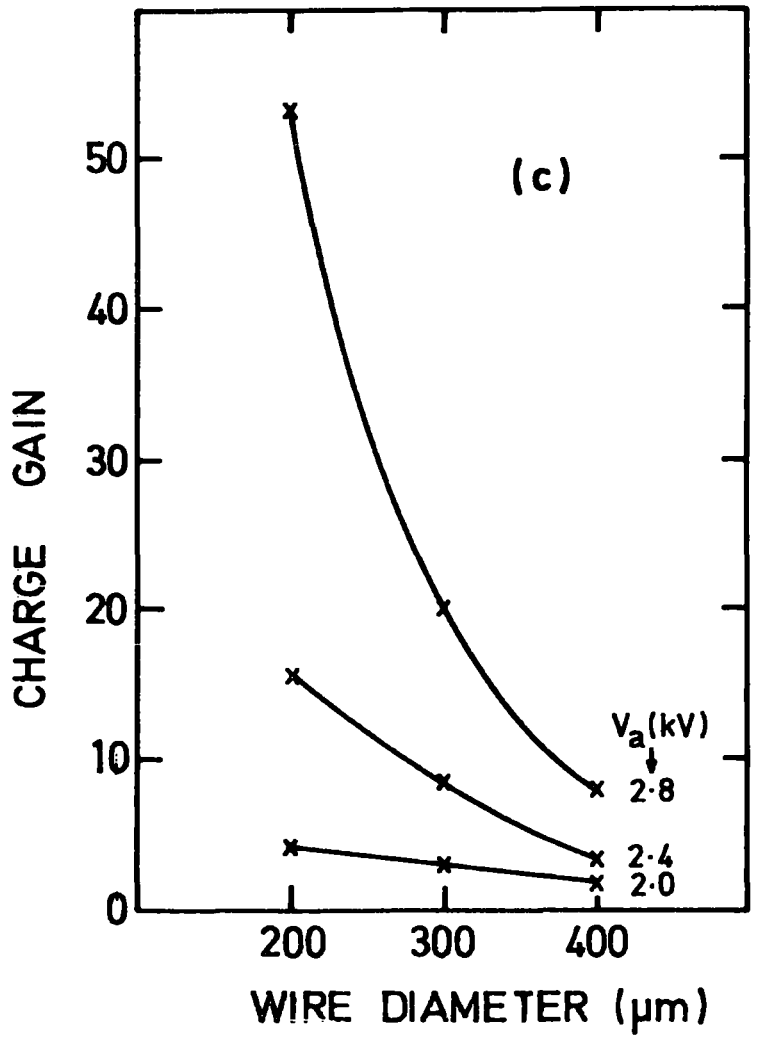

FIG. 6·7 THE CHANGE OF (b) LIGHT AND (c) CHARGE GAIN WITH ANODE WIRE DIAMETER FOR DIFFERENT ANODE VOLTAGES.

factor of 1.6 at a charge gain of 20 (Fig.6.7a), compared to the factor of 3 obtained from increasing nitrogen concentration only 5%.

6.3 PLATEAUS AND ENERGY RESOLUTION

The measurements of plateaus under different conditions give a good indication of the sensitivity of the counter and the effect on the sensitivity of different factors, such as drift voltage and nitrogen concentration. In this section the tests were carried out with the GSDC described in section 2.6.5. and the output pulse was taken from the photomultiplier tube. In most of the tests, measurements of energy resolutions were also taken.

The measurements of energy resolution at different anode voltages showed an improvement in energy resolution with increase of anode voltage. This is shown in Fig 6.8, where the energy spectra of an Fe^{55} radioactive source are shown for V_a = 2.85, 2.9 and 2.95 kV giving energy resolutions of 33%, 31% and 28% respectively. The improvement in the energy resolution with increasing V_a is due to the increase of the pulse amplitude and the consequent improvement in the signal-to-noise ratio, as shown in Fig. 4.12. It is worth mentioning that the energy resolution in the case of Am^{241} (5.5 MeV) was 8.6%.

6.3.1 The Drift Voltage (V_k)

The effect of increasing V_k on the plateau is shown in Fig 6.9. At low drift voltages, a high sense wire voltage is needed to reach the plateau. This is caused by penetration of the drift field into the area around the sense wire and it is more significant for high drift fields. This phenomenon was discussed in section 5.5.6 where, in the contour plottings, the radius of the zero equipotential around the sense wire decreased with increase of the drift voltage. Also, it was mentioned that the increase in the drift field caused a rapid increase in the field

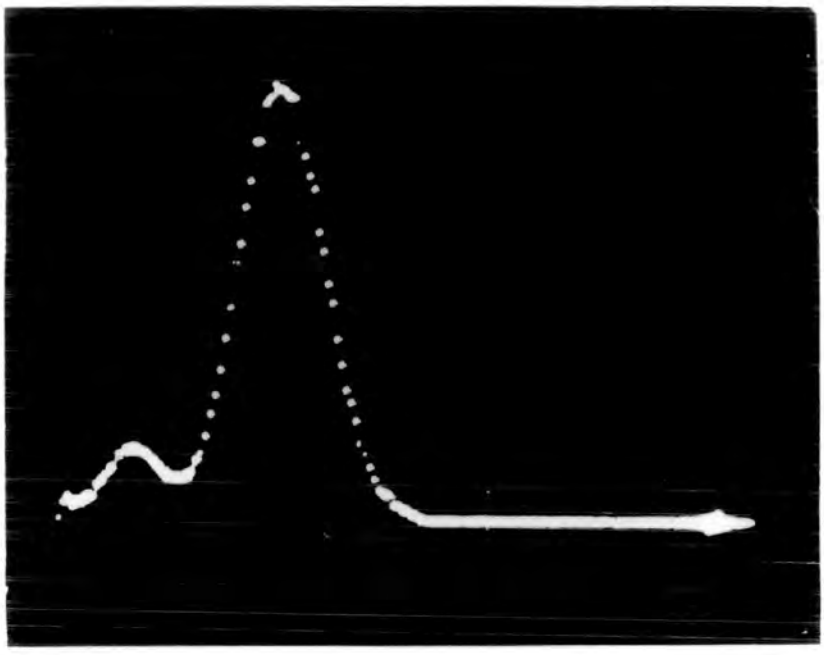

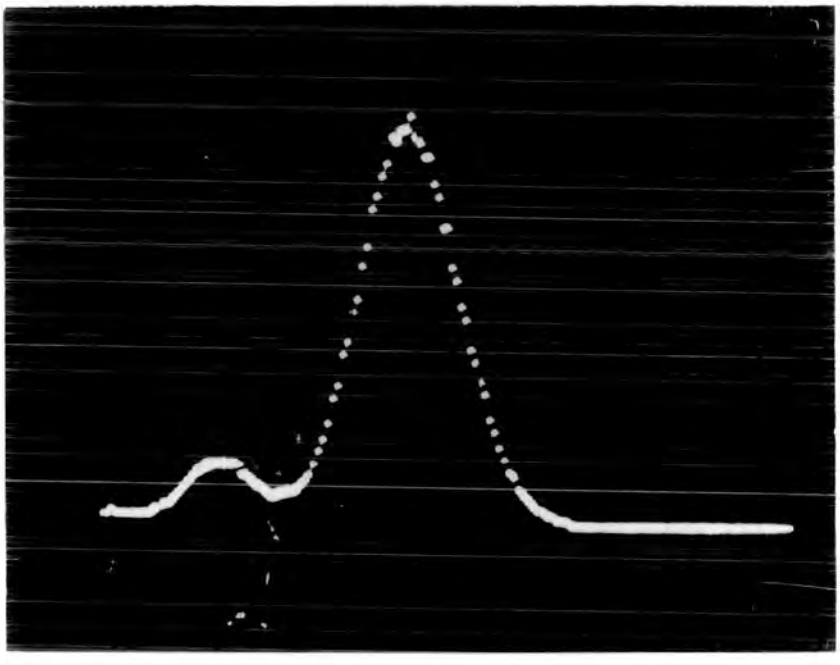

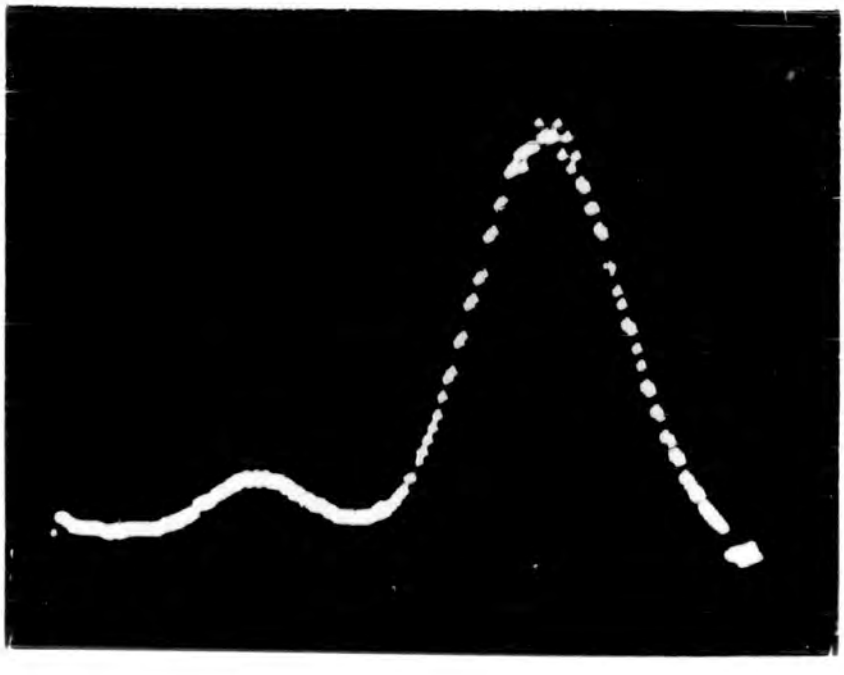

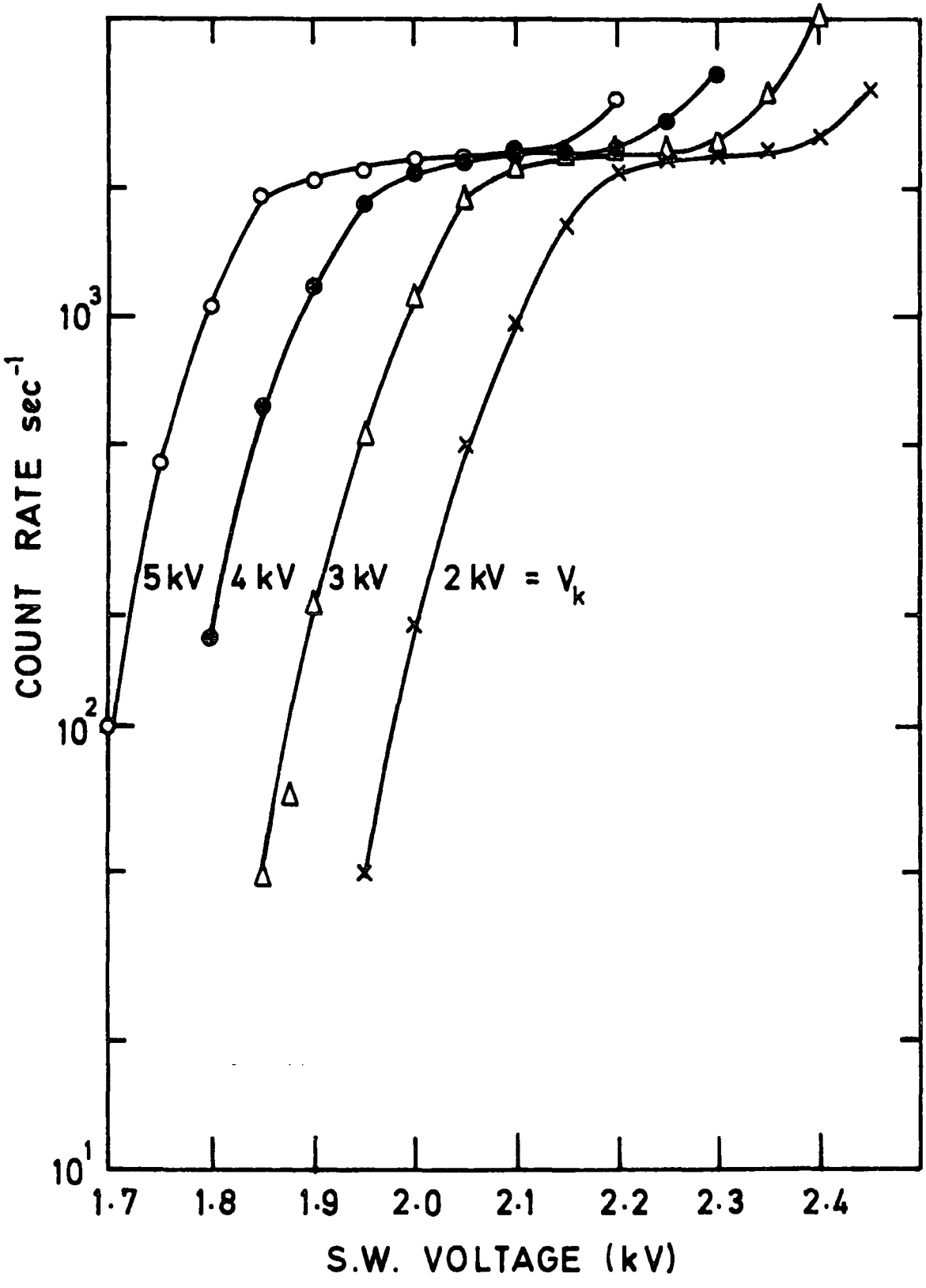

FIG. 6·9

PLATEAUS AT DIFFERENT DRIFT VOLTAGES

between the drift wire plane and the earth plane which may cause spurious pulses and undesirable breakdown.

The energy resolution was measured for the same mean pulse height value at different drift voltages. Table 6.1 gives the plateau range and the energy resolution for different values of V_k. The deterioration of energy resolution with increasing V_k can be attributed to the following reason.

TABLE 6.1

Plateau Width and Energy Resolution for Different Drift Voltages

V_{PM} = 1830 volts, N_2 = 4.6%

Drift Voltage kV	Range of Plateau (kV)	Energy Resolution %
2	2.2 - 2.4	29
3	2.1 - 2.3	30
4	2.0 - 2.2	36
5	1.9 - 2.1	42

The primary scintillation amplitude is independent of the field. When the drift is high enough, the drift region begins to emit light and the total amount of secondary light would depend on the position of the incident radiation track, thus leading to a deterioration of the energy resolution[10]. This can be shown by observing the fields produced at different drift voltages. For this particular chamber the drift fields at 2, 3, 4 and 5 kV are 0.59, 0.88, 1.18 and 1.47 kV/cm at drift distance of 3.4 cm. Field

values higher than 1 kV/cm are high enough to produce ionization and excitation. This value is within the field range around the sense wire which varies from 16 kV/cm to 1 kV/cm as shown in chapter five and in this region excitation is known to occur. Hence drift voltages of 4 and 5 kV i.e. drift fields of 1.18 and 1.47 kV/cm, are capable of producing excitation in the drift region and causing the deterioration of energy resolution as shown in Table 6.1.

From Table 6.1 one can see that similar plateau widths were obtained at different drift voltage values but the operating voltage increases with decrease of drift voltages.

High drift voltages, although they produced high drift velocities were avoided when a reasonable energy resolution was required. The value of 3 kV was used for this specific chamber since the energy resolution had not deteriorated significantly from the best value obtained at 2 kV.

6.3.2 Photomultiplier Voltage (V_{pm})

The tests described in this section were carried out with the passive network base for the photomultiplier tube described in section 2.4.2. The plateaus for three different photomultiplier voltages (V_{pm}) are shown in Fig 6.10. With low voltages a higher sense wire voltage was needed to operate in the plateau region. At high V_{pm} the pulse height increases, hence with a fixed discrimination level, the count rate increases for the same source position. This can be seen in Fig 6.10 for the values 1700 and 1800 V. The curve for 1900 V was taken with the source position slightly moved and caused the plateau to deviate from the pattern.

The variation of energy resolution with V_{pm} is shown in Table 6.2 The resolution was measured for the same mean pulse height value and this was achieved by varying the sense wire voltage appropriately.

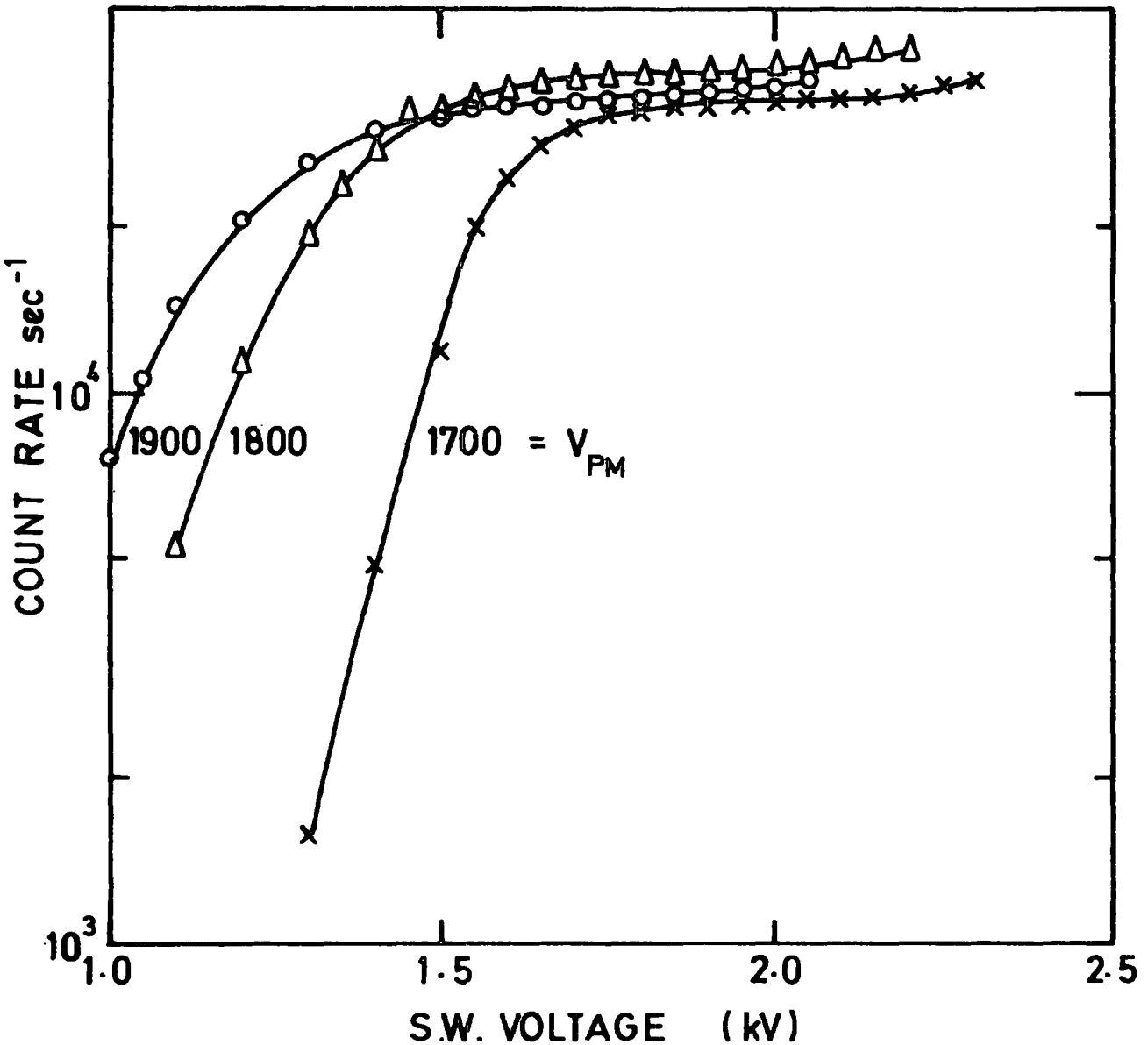

FIG. 6·10

PLATEAUS AT DIFFERENT PM VOLTAGES

TABLE 6.2

Plateau and Energy Resolution for Different Photomultiplier Voltages

V_k = 3 kV N_2 = 4.6%

V_{pm} (volts)	Plateau Starting Point (kV)	Energy Resolution (%)
1700	1.75	26
1800	1.65	27
1900	1.5	34

The deterioration of energy resolution at high V_{pm} values can be attributed to the photomultiplier noise at high voltages. The minimum value of V_{pm} recommended by the manufacturers is 1600 volts to ensure high light collection efficiency. Hence V_{pm} values in the region of 1700-1800 volts will be used in this work, unless other factors dictate higher values.

6.3.3 Nitrogen Concentration

The plateaus for different nitrogen concentration are shown in Fig.6.11. At high nitrogen concentrations high sense wire voltages were needed. This is because the electron collision total cross-section for nitrogen is higher than that for argon at electron energies less than 6 eV[11] and hence the energy loss by collision is higher, as given in Fig 3.9, and more field was then required. In the plateau region the count rate decreased with increasing nitrogen concentration. This was

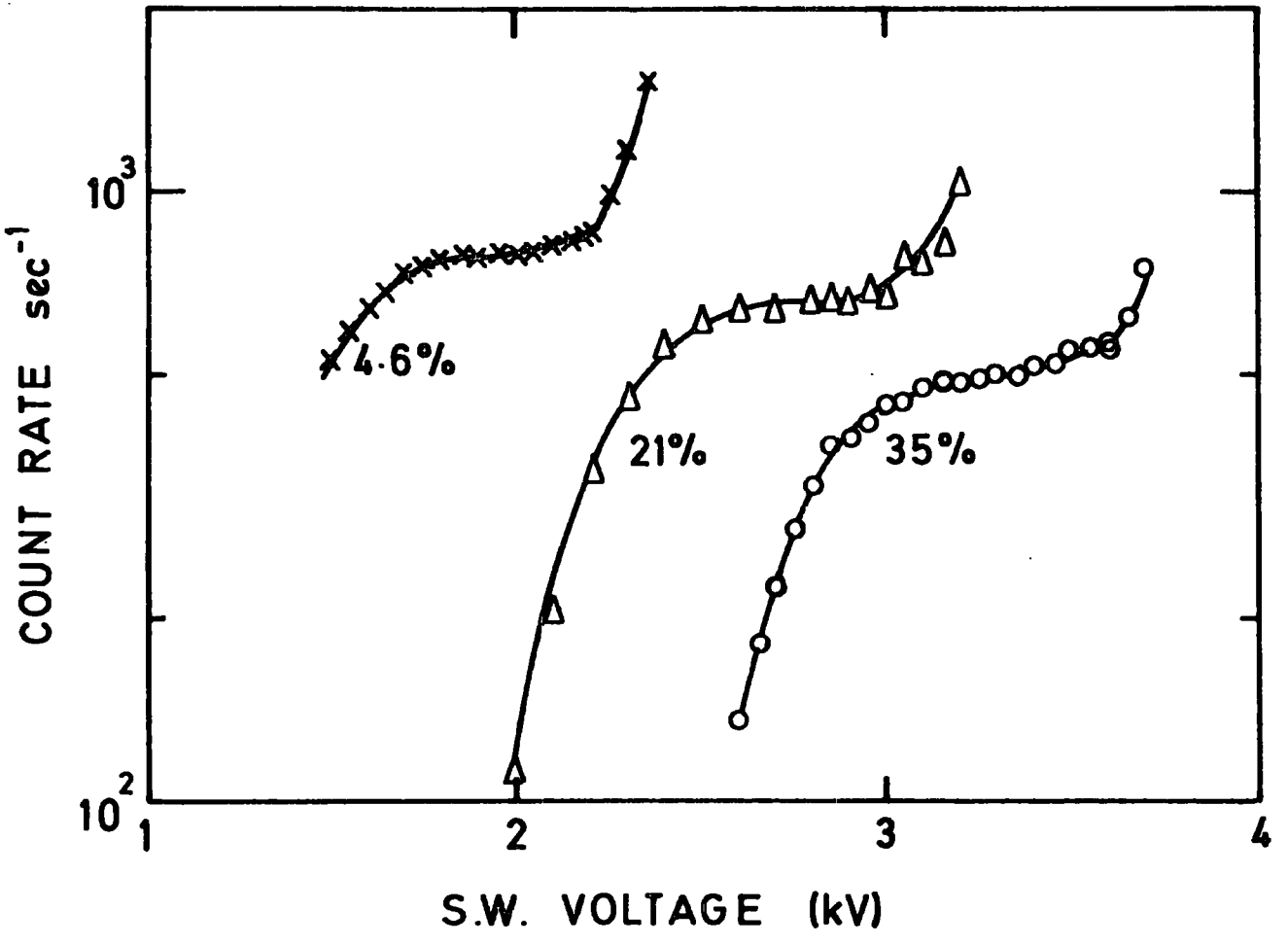

FIG. 6·11 DIFFERENT N_2 CONCENTRATIONS

caused by the use of a fixed discrimination level and the pulse heights which decreased with increase of nitrogen concentration. The plateau region and the energy resolution corresponding to different nitrogen concentrations are summarized in Table 6.3. The number of primary(n_p) and secondary(n_s) ion pairs/cm are also given.

TABLE 6.3

Plateau Width and Energy Resolution for Different Nitrogen Concentration

V_k = 3 kV V_{pm} = 1750 V

N_2 %	Plateau Region (kV)	Energy Resolution (%)	n_p $\left(\frac{\text{ion pairs}}{\text{cm}}\right)$	n_s $\left(\frac{\text{ion pairs}}{\text{cm}}\right)$
4.6	1.8 - 2.05	28	28.5	63.8
21	2.6 - 2.9	26	25.3	60.7
35	3.1 - 3.4	27	22.6	58.1

The values of n_p and n_s are calculated from eqn. 3.2 and Table 3.1. The slight deterioration in energy resolution with nitrogen percentage is expected as n_s drops by less than 5% in each case. The value of energy resolution at nitrogen percentage of 4.6% could be inaccurate due to the slight change in channel number of the P.H.A. From this table, it is clear that the nitrogen percentage has a very small effect on energy resolution but a considerable effect on the plateau, i.e. the increase in operating voltage.

6.3.4 Drift Wire-Earth Plane Separation (d) and The Geometry Factor

The decrease of d values has an effect on the plateau similar to that of increasing the drift voltage shown in Fig 6.8. This is caused by the field penetration from the drift wire-earth plane region into the drift region.

This effect of field penetration was shown in the equipotential contours, Fig 5.18. The effect of changing d on the plateau is shown in Fig 6.12. The plateau shifts to higher sense wire voltages as higher d values are used. This shift is comparable with that shown in Fig 6.9 for a drift voltage change from 2 to 3 kV. According to field calculations, given in chapter 5, high d values provide less fluctuation in field, particularly close to the drift wires (see Fig 5.17). At the same time high d values cause a decrease in the field over the major part of the drift region (see Figs 5.16 and 5.18,), and of course an increase in the chamber thickness causes a change in the solid angle. The solid angle depends on the source collimator diameter and the distance between the source and the sense wire. The change in the geometry factor affects the energy resolution. This was shown by varying the source collimator diameter and the d value. The increase of the diameter from 0.5 mm to 1.5 mm caused the energy resolution to increase from 27% to 31% for an Fe^{55} source. Similar results were obtained when drift wire-earth plane separations changed. The energy resolution changed from 30% to 32.5% when d increased from 7 to 11 mm.

The importance of the geometry factor has its impact on the lack of energy response linearity of the chamber and this is due to the fact that particles with different energies have different ranges, and the amount of light produced will depend on the particle range[12]. An improvement of

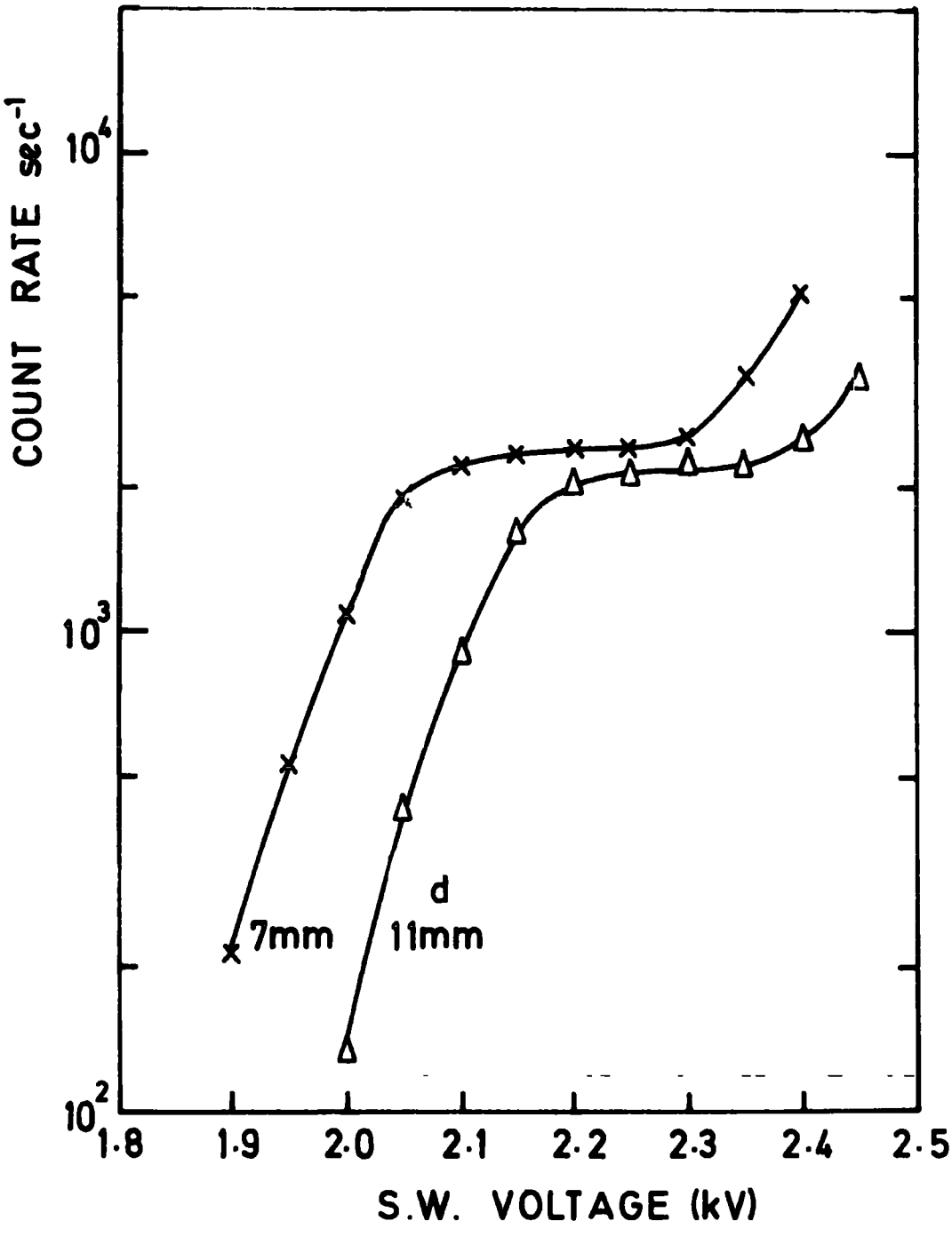

FIG. 6·12 PLATEAUS FOR DIFFERENT DRIFT-EARTHPLANE SEPARATIONS.

energy response linearity can be achieved by allowing the production of light to occur in a small volume of the counter. At the same time this will give an improved energy resolution.

6.3.5 Sense Wire Diameter

The effect of the sense wire diameter on the plateaus is shown in Fig 6.13 and summarized in Table 6.4

TABLE 6.4

Plateaus for Different Sense Wire Diameters

Wire Diameter (μm)	Plateau Width (volt)	Operating Voltage for Charge Gain of 11 (kV)	Light Gain
150	50	1.85	-
200	100	2.3	280
300	200	2.5	360
400	300	2.92	400

With thicker wires, it was clear that a higher sense wire voltage was needed to operate in the plateau region. This can be explained according to eqn. 4.6 where the multiplication factor increased as the wire diameter decreased. Hence to reach the same multiplication factor for larger wire diameters a higher voltage should be applied. The width of the plateau was increased with increase of the wire diameter. This is a phenomenon associated with the electronics and is due to the use of fixed discrimination level. The effect of discrimination level on the characteristics of the plateaus, i.e. operating voltage and width, is shown in Fig. 6.14. It is

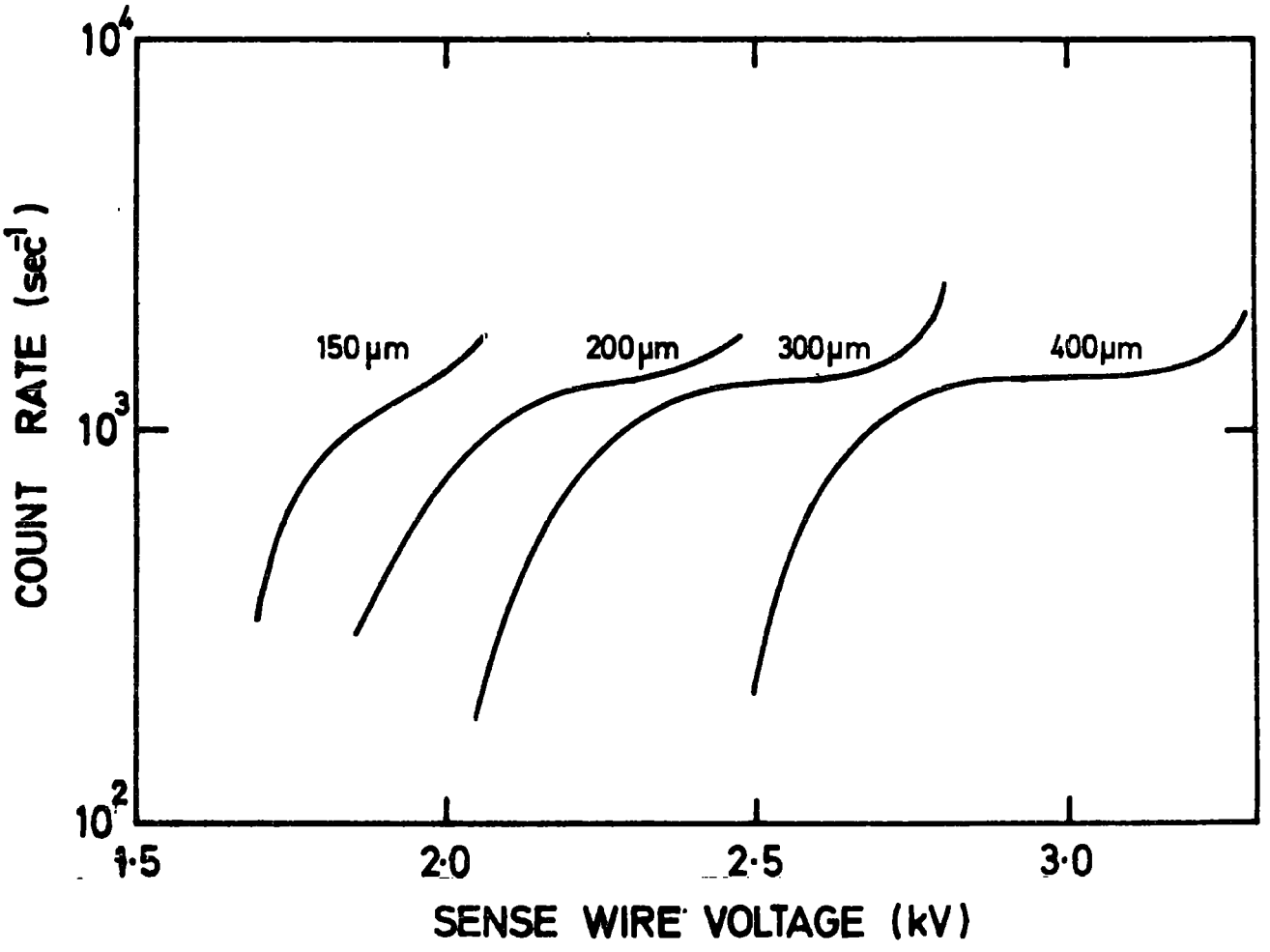

FIG. 6·13 PLATEAUS FOR DIFFERENT SENSE WIRE DIAMETERS.

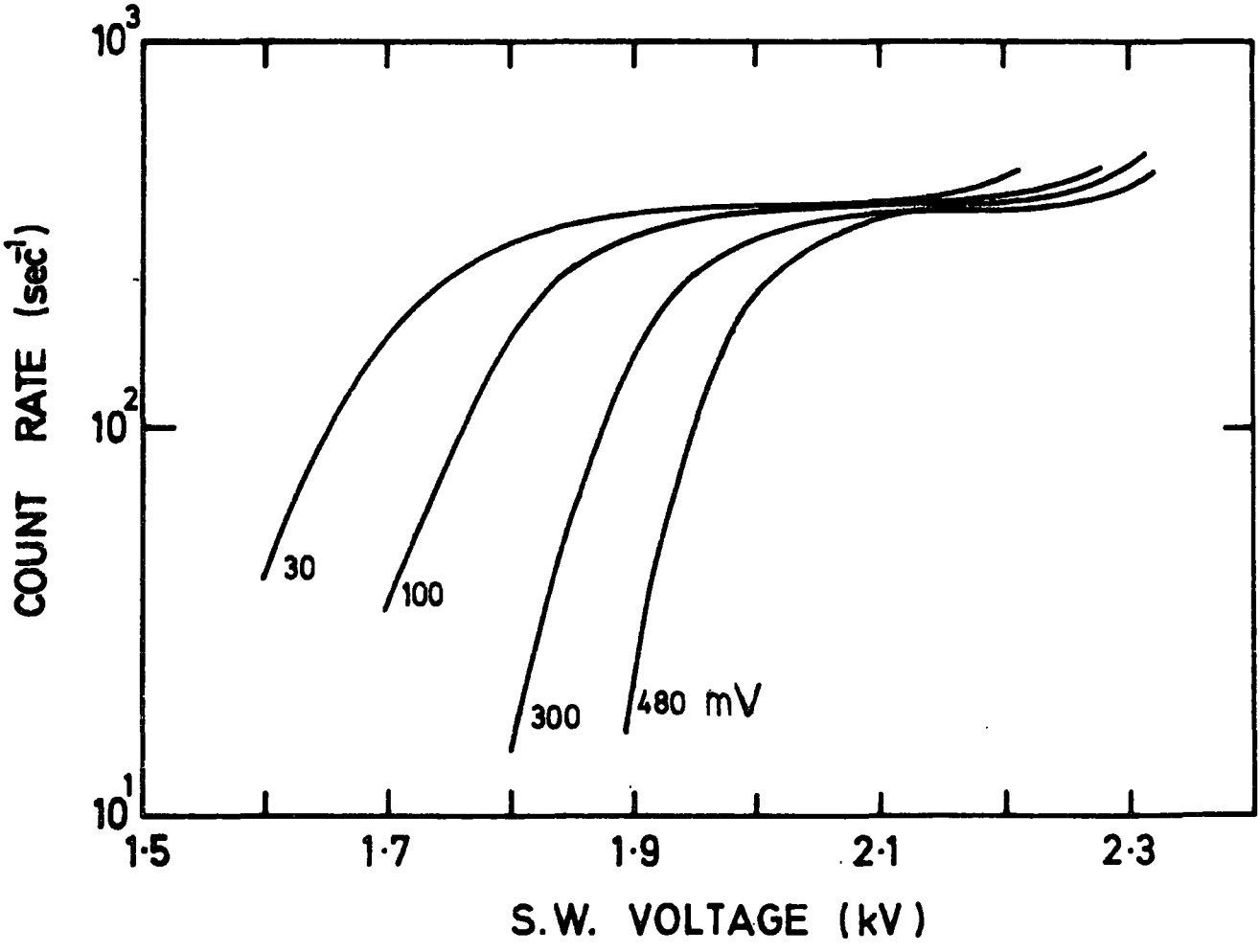

FIG. 6·14 EFFECT OF DISCRIMINATION LEVEL (mV) ON PLATEAU.

clear that a high discrimination level causes a considerable loss of pulses and hence a narrow plateau and high operating voltage are obtained. Comparing these results with those of Fig 6.13 it is clear that the fixed discrimination level used for that set of plateaus was high for small sense wire diameters.

Operating the chamber in the plateau region provided the same charge gain for different wire diameters. The operating voltages tabulated in Table 6.4 provided a charge gain of 11 for different wire diameters. These values were taken from Fig. 6.13. The charge and light gain values corresponding to each operating voltage (for the specific wire diameter) were taken from Fig. 6.6. The light gain was found to increase with increasing wire diameter at a fixed charge gain. This is given in Table 6.4.

The increase in light gain with higher anode wire diameter should lead to an improvement in energy resolution. This was observed by Policarpo et al[13]. Their energy resolution measurements showed that thicker wires provide better energy resolutions. A 0.9 mm anode wire diameter gave a very low energy resolution of 11.2% for 5.9 keV X-ray in a xenon filled chamber at 1115 torr. It is worth mentioning here that a NaI(Tℓ) crystal gave a resolution of 43% for the 5.9 keV X-ray from Fe^{55} [14] which is considerably worse than the 26% obtained and given in section 6.3.3.

6.4 THE PULSE SHAPE

As was mentioned earlier, the pulse produced in drift chambers is due to the movement of both electrons and ions formed in the avalanche. The high drift velocity of electrons, which are mostly produced around the sense wire, produces a pulse with a fast rise time of a few nanoseconds. The slow positive ions moving almost all the drift distance back to the cathode form the majority of the pulse which is a few microseconds in duration. A study of the pulse shape, i.e. the rise time, width and amplitude and the factors affecting the pulse shape provided a mean of optimizing it for high count rate experiments. For high count rate experiments, the pulse width should be made as small as possible, at the same time the energy resolution should not be allowed to deteriorate.

Chambers used in this section were GSDC's. The first was the one described in section 2.6.5. with D = 34 mm, s = 2 mm and anode wire of 200 μm. This chamber will be referred to as chamber one. Chamber 2 was similar except for D = 20 mm, s = 1 mm and anode wire of 400 μm diameter. The measurement of rise time was for 10% to 90% of the pulse, and the pulse width was taken as the total width measured from the base line.

6.4.1 Anode Voltage V_a

In this part the chamber used was chamber 2. The effect of the anode voltage on the pulse shape is shown in Fig 6.15. The data of this figure is summarized in Table 6.5

TABLE 6.5

Effect of Anode Voltage on Pulse Shape

V_a (kV)	Amplitude (mV)	Rise Time (nsec)	Width (nsec)
2.8	180	14	50
2.9	280	16	60
3.0	460	16	70

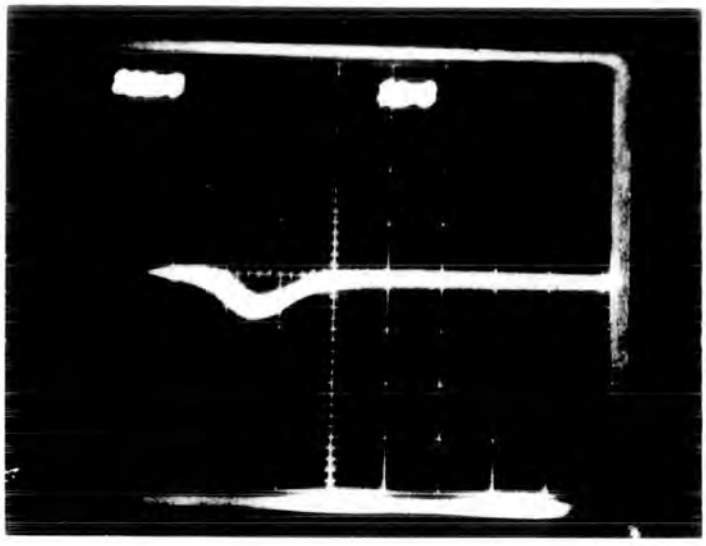

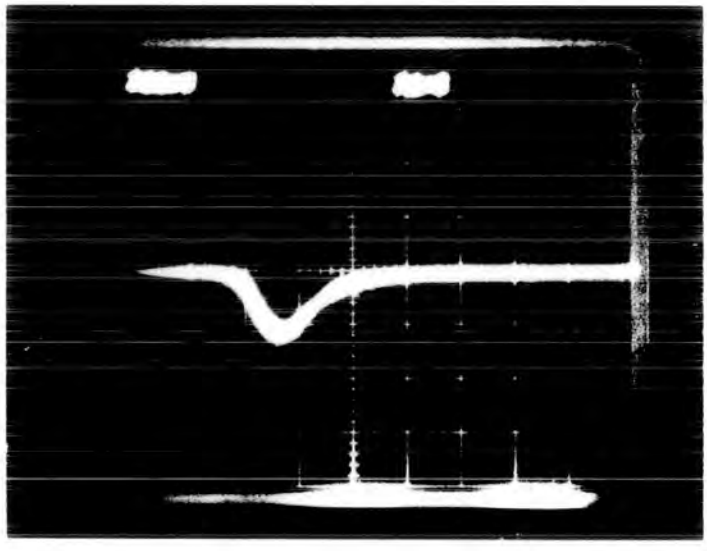

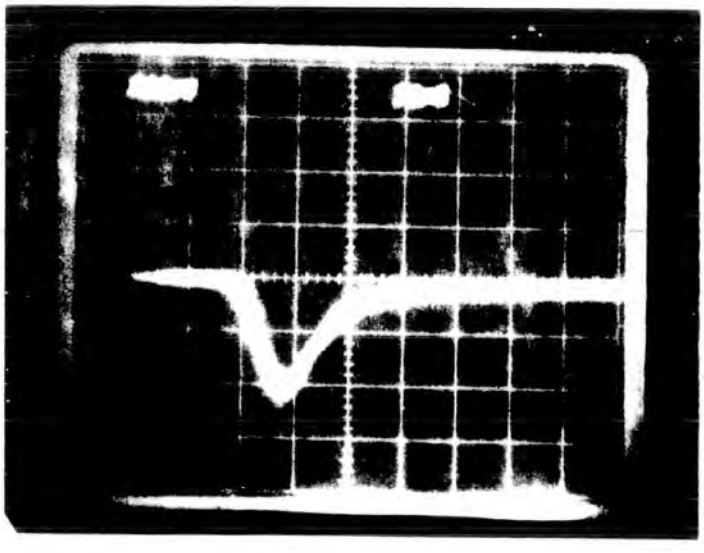

It is clear that increasing the anode voltage not only increases pulse amplitude, as expected due to increase in charge gain, but it also increases the pulse width at the same time. The increase in the width is mainly due to the increase in fall time of the pulse. Hence the movement of positive ions is the reason for increasing the pulse width. The major contribution of the positive ions to the signal is produced near the sense wire and as the increase of anode voltage causes an increase in the range of influence of the sense wire, positive ions take a longer time to escape from that region.

In the previous section it was found that the energy resolution improved with increase of anode voltages. This produces a conflicting requirement with the pulse width which increases with increasing anode voltage. Hence the choice of low anode voltage was made because it had another advantage of producing low charge gain.

6.4.2 The Drift Voltage V_k

Chamber 1 was used in the measurements of this part. The increase in the drift voltage causes an increase in the pulse amplitude. This is shown in Fig 6.16. In these measurements the sense wire voltage was reduced, when the drift voltage increased, in order to keep the field around the sense wire constant. In Fig 6.16 at drift voltages less than 1000 volts the field is not high enough to cause an increase in pulse amplitudes, but at higher drift voltages electrons gain more energy and diffusion becomes less effective. Both factors cause the increase in pulse amplitude.

The change in rise time with the drift voltage is shown in Fig 6.17. In the region of less than 1000 volts the rise time is constant in a similar manner to the pulse height observed in Fig 6.16. In higher fields however, an almost uniform drop in rise time occurs with increase of the

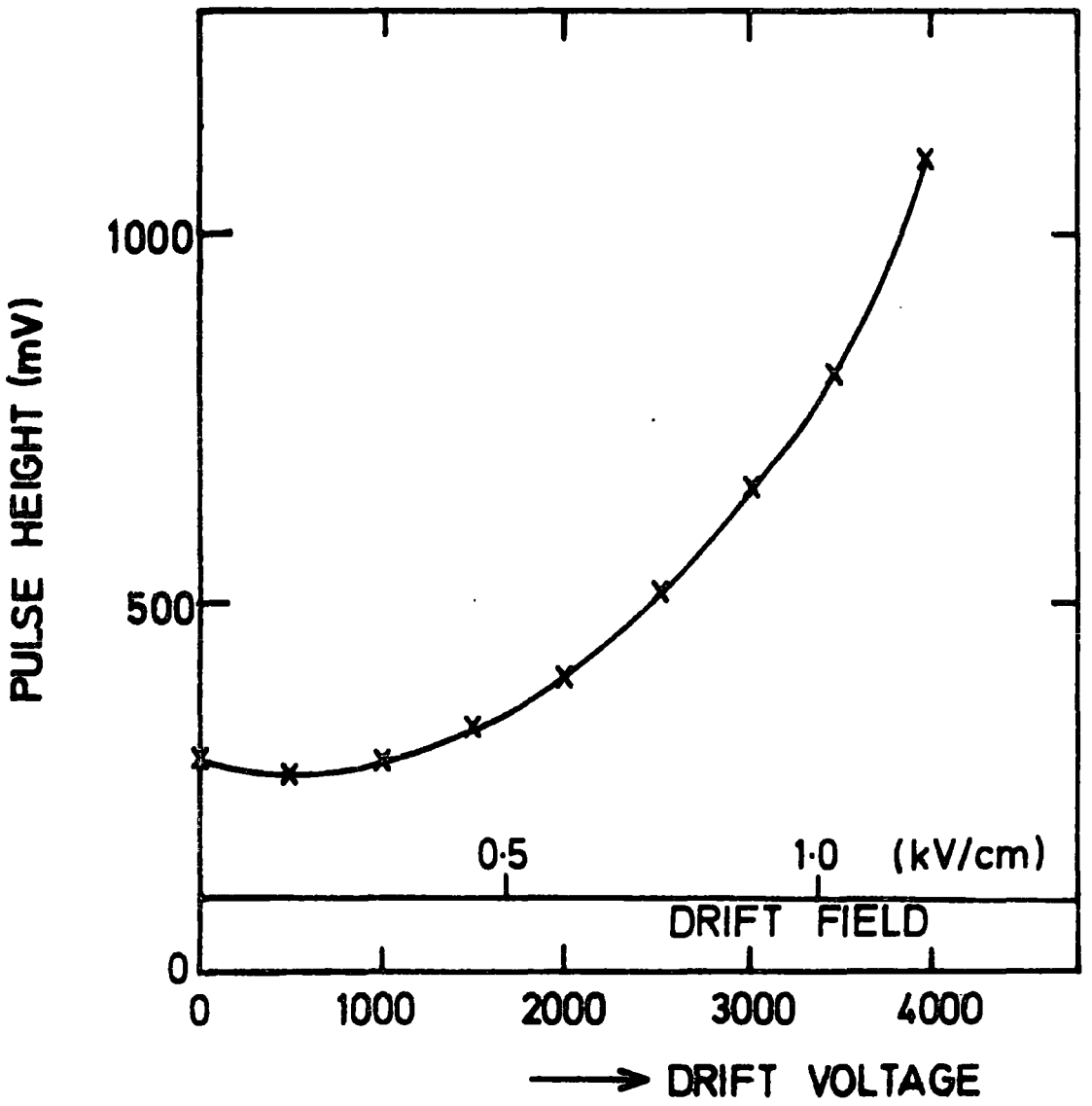

FIG. 6·16 PULSE HEIGHT DEPENDANCE ON DRIFT FIELD.

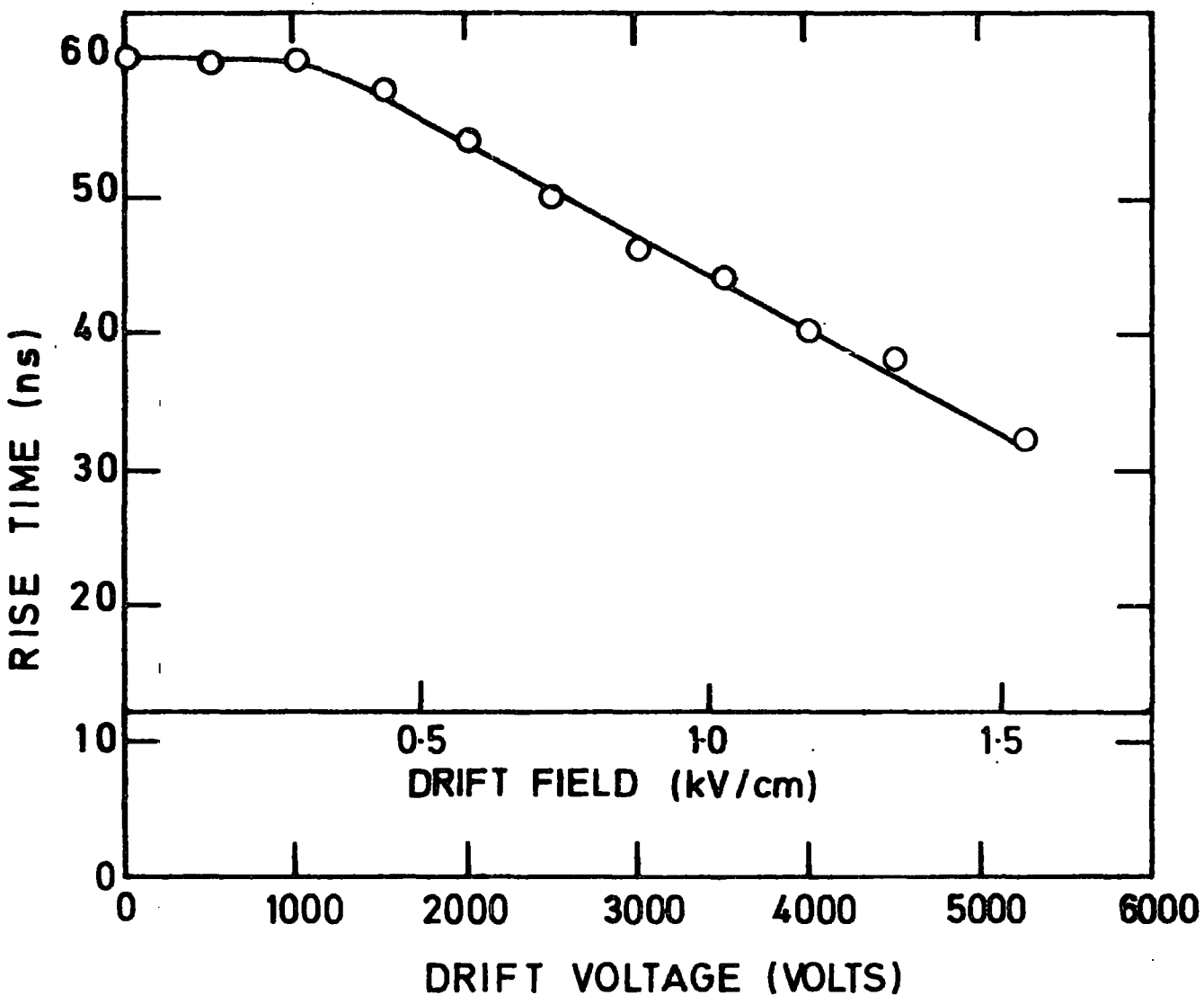

FIG. 6·17 EFFECT OF DRIFT FIELD ON THE PULSE RISE TIME.

field. It should be noted here that the difference in the rise time values of Fig 6.15 and Fig 6.17 is due to the differences between Chamber 2 and Chamber 1 used in the two sections.

A high drift voltage produces larger pulses with smaller rise time and this is favourable for fast removal of positive ions and high rate capability. At the same time a high drift field produces extra light gain, as mentioned in section 6.3.1, which cause a deterioration in energy resolution. Also, in high drift fields, the field around the potential wires increases much faster than anywhere else in the chamber and produces, as shown in section 5.5.6, a non-uniformity in the field around the drift wires and hence higher probability for breakdown. Moderate values of drift field (less than 1 kV/cm) were used in practice.

6.4.3 Source Position

The position of the source with respect to the sense wire has a considerable effect on the pulse shape and this is shown in Fig. 6.18. This set of readings was taken from Chamber 1. The width and rise time variations with source position are shown. The zero position indicates the sense wire position where the minimum should occur. The shift from this position is due to the use of an arbitrary zero on the measuring scale of the source position.

The increase of rise time, and pulse width, with increase of the distance (x) between the source and the sense wire is due to the dependence of diffusion on the drift distance. The drift time increases as x increases, hence according to eqn. 3.15, where $\sigma \propto \sqrt{t}$, diffusion increases with increase of x. The other factor which causes rise time to increase is the field. As shown in Chapter 5 the field inside the chamber is not totally uniform in the drift region, but gradually increases towards the sense wire. Also the drift velocity in argon-nitrogen mixtures increases with increase of

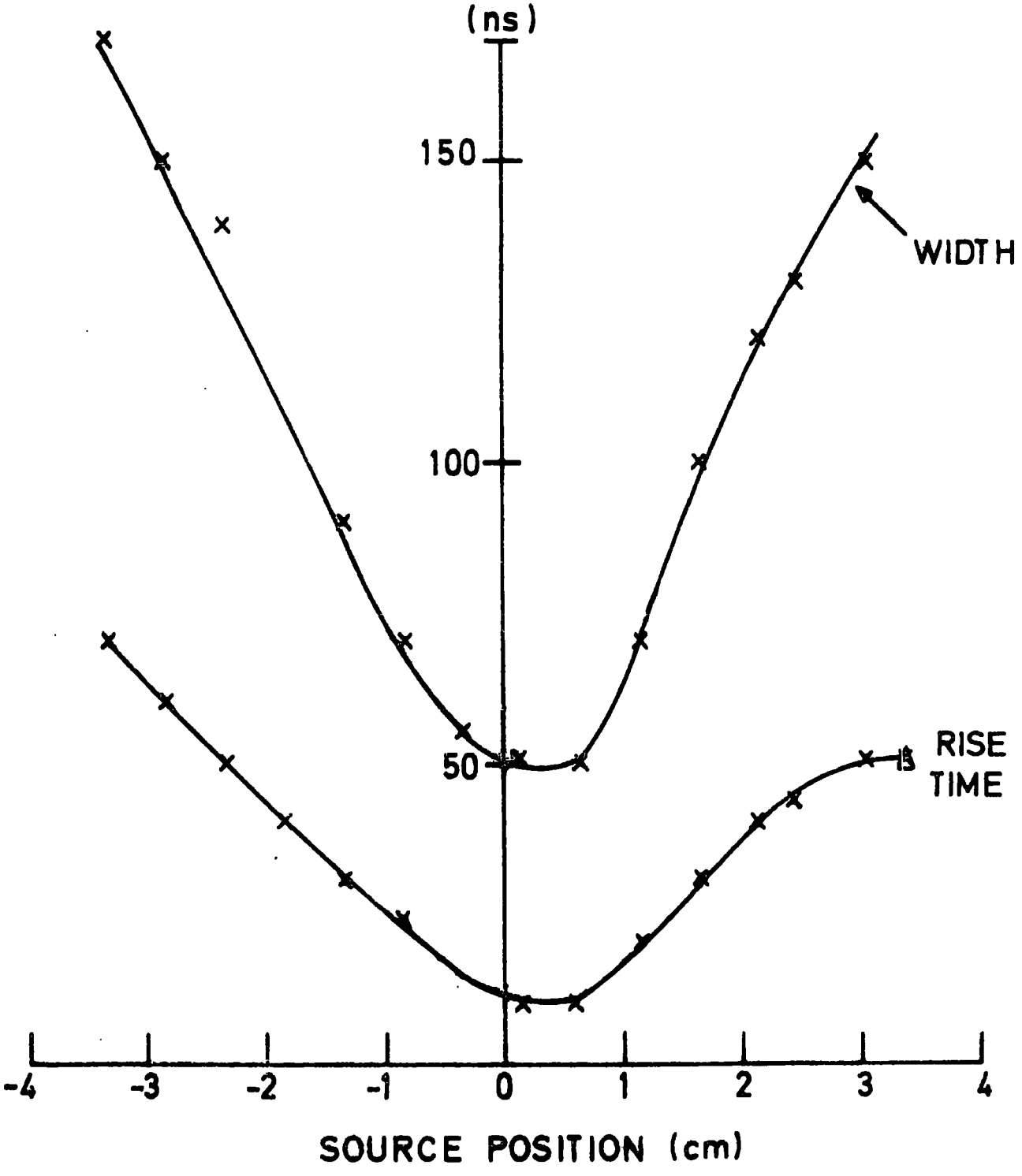

FIG.6·18 EFFECT OF SOURCE DISTANCE FROM THE SENSE WIRE ON PULSE WIDTH AND RISE TIME.

field. Hence as x decreases, the higher drift velocity and lesser diffusion produce pulses with faster rise times.

The dependence of the pulse amplitude on the source position is shown in Fig 6.19. The decrease of pulse amplitude as x increases can be attributed to the same cause as the rise time, i.e. lower drift field and higher diffusion. In Fig 6.19 the variation of pulse amplitude with source position is given for two drift voltages, 3 and 4 kV. The increase of pulse amplitude with the drift voltage is immediately obvious. Also the percentage decrease of amplitude with source position at the higher drift voltages is smaller. From position 0 to -3, Fig 6.19, the percentage of decrease is 53% for 4 kV while it is 63% for 3 kV. This shows that at higher drift fields, where the drift velocity is high, the effect of diffusion is less pronounced.

The effect of the source position on the pulse shape is mainly due to the non-saturated drift velocity and hence any small variation in the field causes a corresponding variation in drift velocity. Charpak et al[15], however, observed the opposite effect, namely a decrease in the pulse amplitude when x decreased. Other workers[16] also observed the same phenomenon. Charpak attributed this phenomenon, which was observed in an ordinary drift chamber, to space charge effects which are more significant in their chamber in which the sense wire diameter was only 20 μm compared to a diameter of 200 μm in our case.

The pulse shape variation with the source position is illustrated in Fig 6.20 using Chamber 2 with 10% of nitrogen. With the same chamber the measurement of energy resolution at different source positions, Fig 6.21, was carried out. The observed deterioration in energy resolution can be attributed to the solid angle variation, subtended to the photomultiplier tube, with the source position. It was shown earlier that

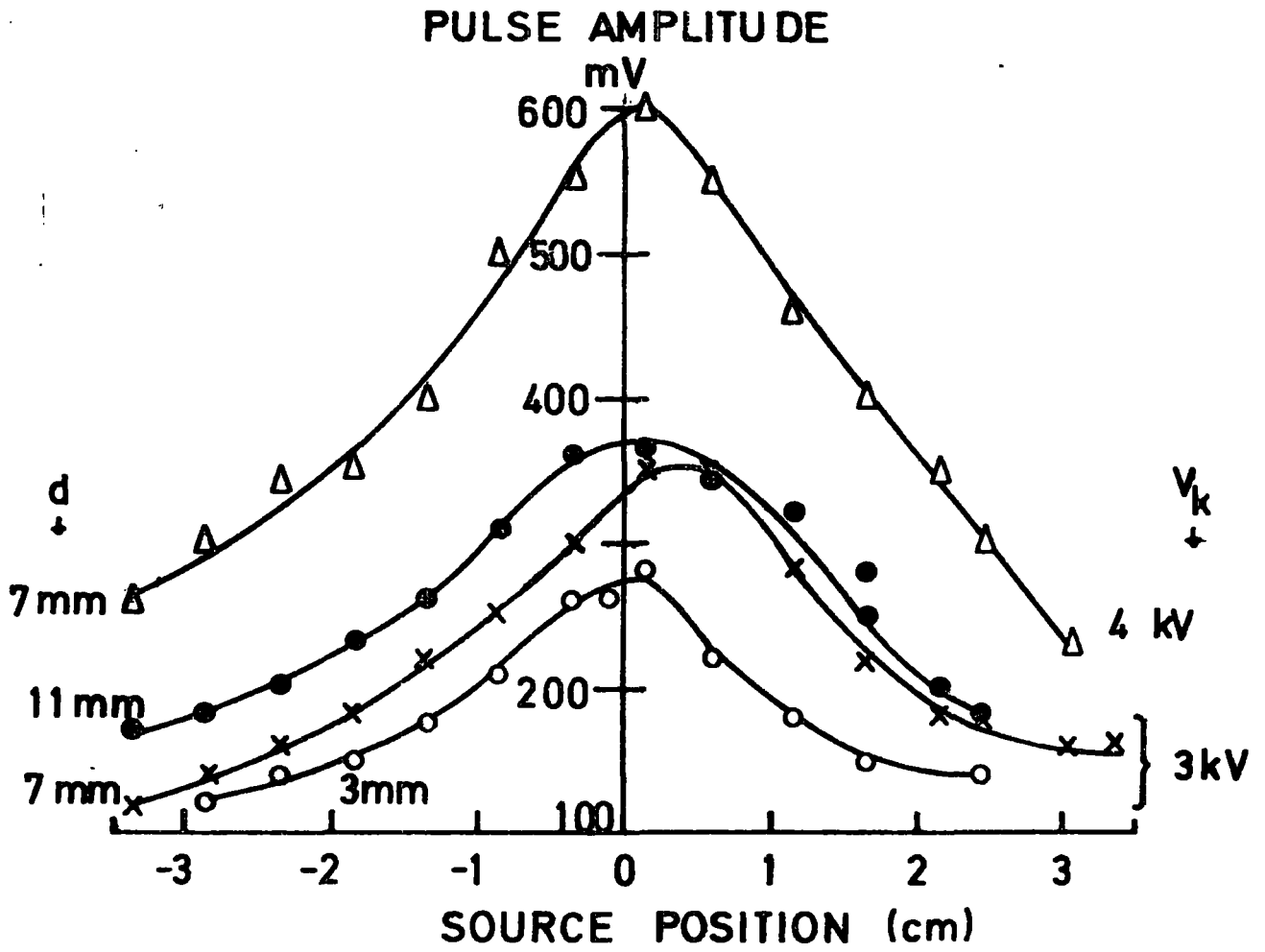

FIG. 6-19 EFFECT OF SOURCE POSITION ON PULSE AMPLITUDE.

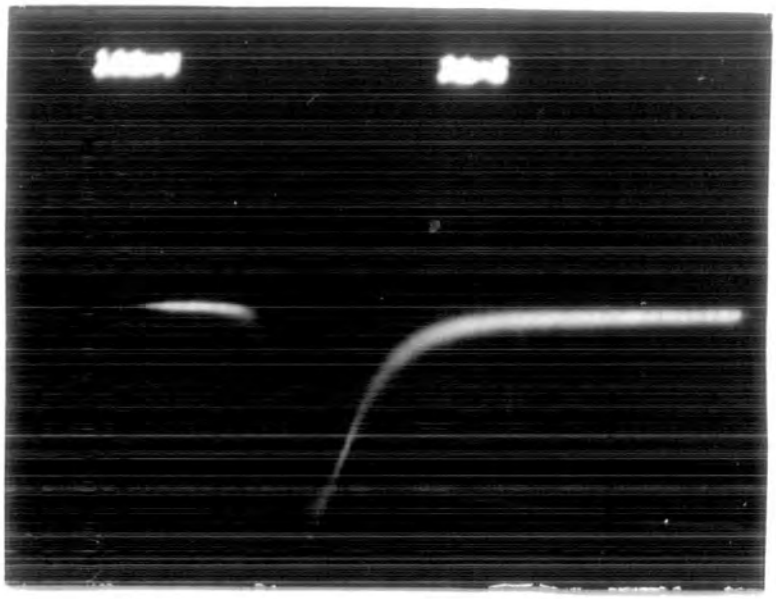

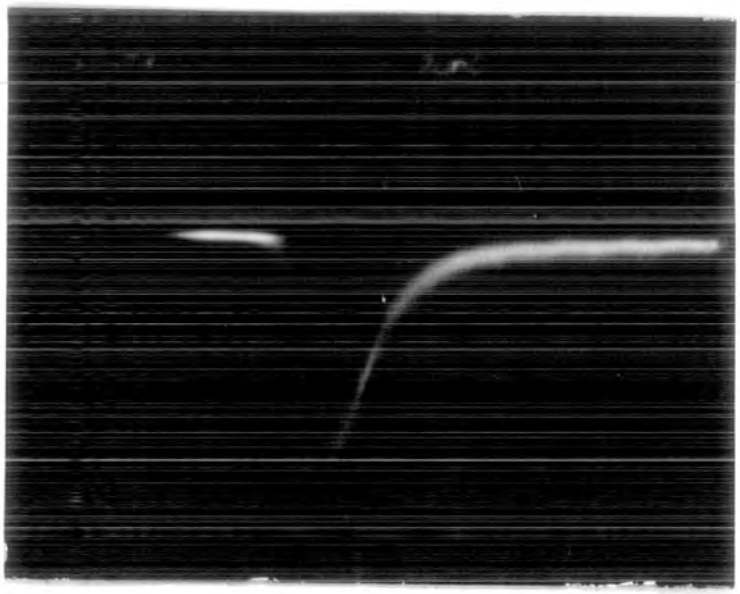

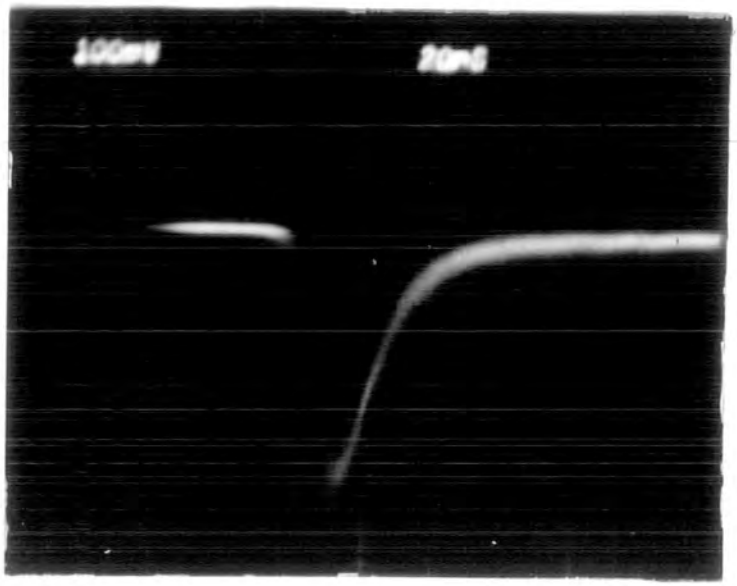
100mV
20mS

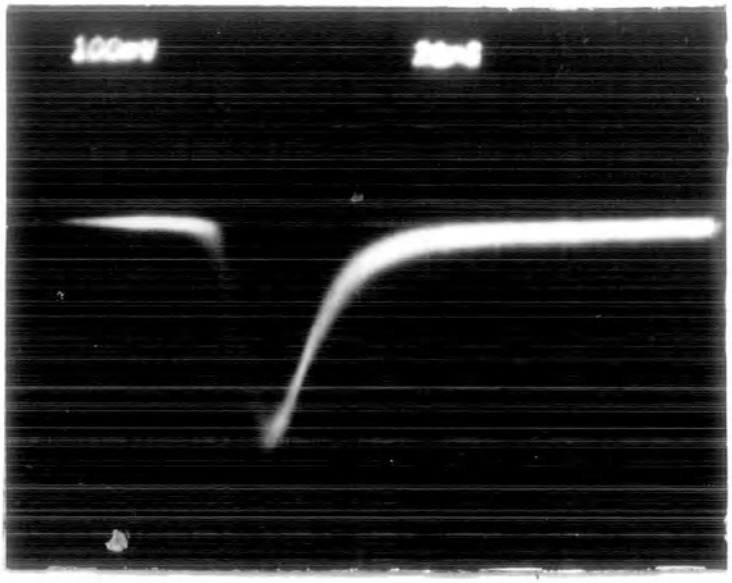
100mV
20nS

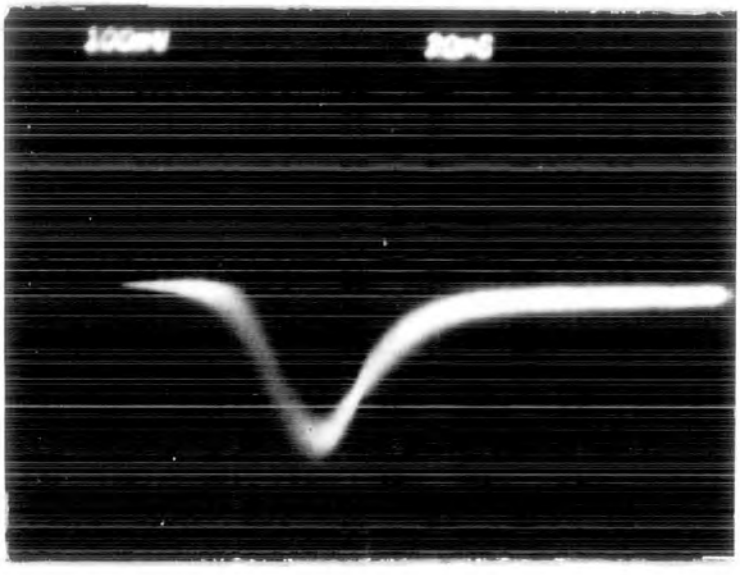
100mV
20nS

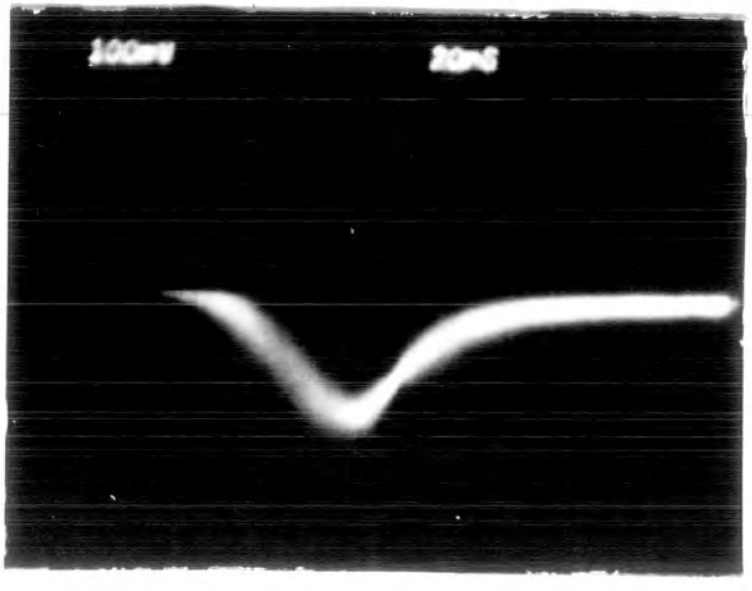
100mV
20nS

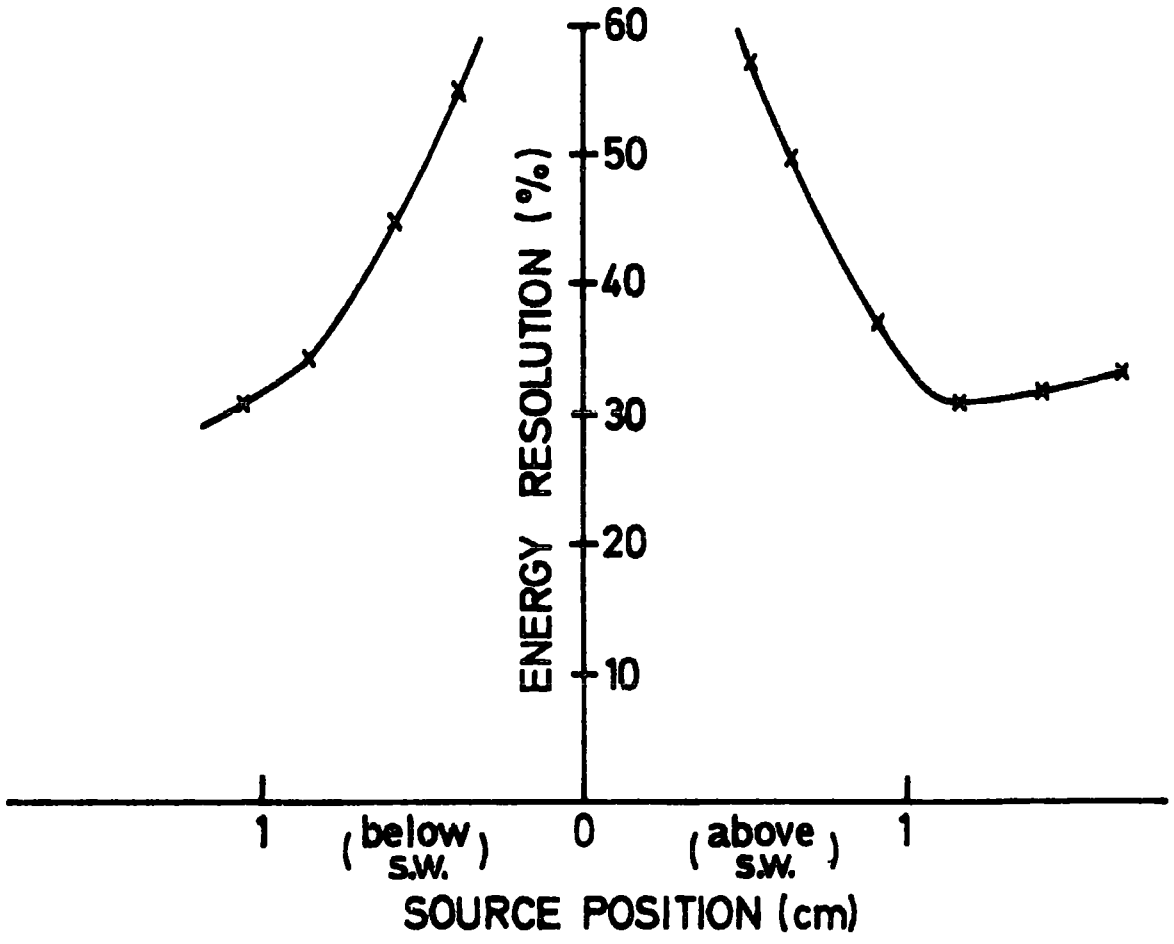

FIG. 6·21 EFFECT OF SOURCE POSITION ON ENERGY RESOLUTION.

good avalanche localization for example, by using a narrow collimator, produced good energy resolution. The same argument can be applied to the light received by the photomultiplier tube. At large solid angles, i.e. near the central axis of the tube, energy resolution is much worse than that at a distance from the centre.

Similar observations, i.e. drop in pulse amplitude, increase in pulse rise time and degradation of energy resolution with the source radial position, were reported by several workers. D.F.Anderson et al[17] succeeded in reducing the source position effect. In a parallel grid GSPC, filled with xenon, they used focusing rings. The stainless steel rings were converging concentric electrodes. They achieved a uniform response, i.e. no change in pulse amplitude or energy resolution, in a region covering 67% of the photomultiplier diameter. R.D.Andresen et al[18] used a GSPC filled with xenon. They observed a linear increase in the pulse amplitude with the solid angle subtended to the photomultiplier tube. Fenster et al[19] in their study of linearity and fatigue in photomultipliers showed that the incident angle of the beam on the photocathode, i.e. the radial source position, produced non-linearity in the photomultiplier output pulse.

6.4.4 Nitrogen Concentration

The variation of the pulse width with nitrogen concentration shown in Fig. 6.22, using Chamber 1. The width drops with increasing nitrogen concentration and reaches saturation with about 10% of nitrogen. This set of readings was taken at a constant pulse amplitude. This was achieved by increasing the sense wire voltage with increasing nitrogen concentration and in order to keep the drift velocity constant, the drift field was adjusted accordingly. The drop in pulse width with nitrogen concentration is due to the removal of long lived excited states (meta-

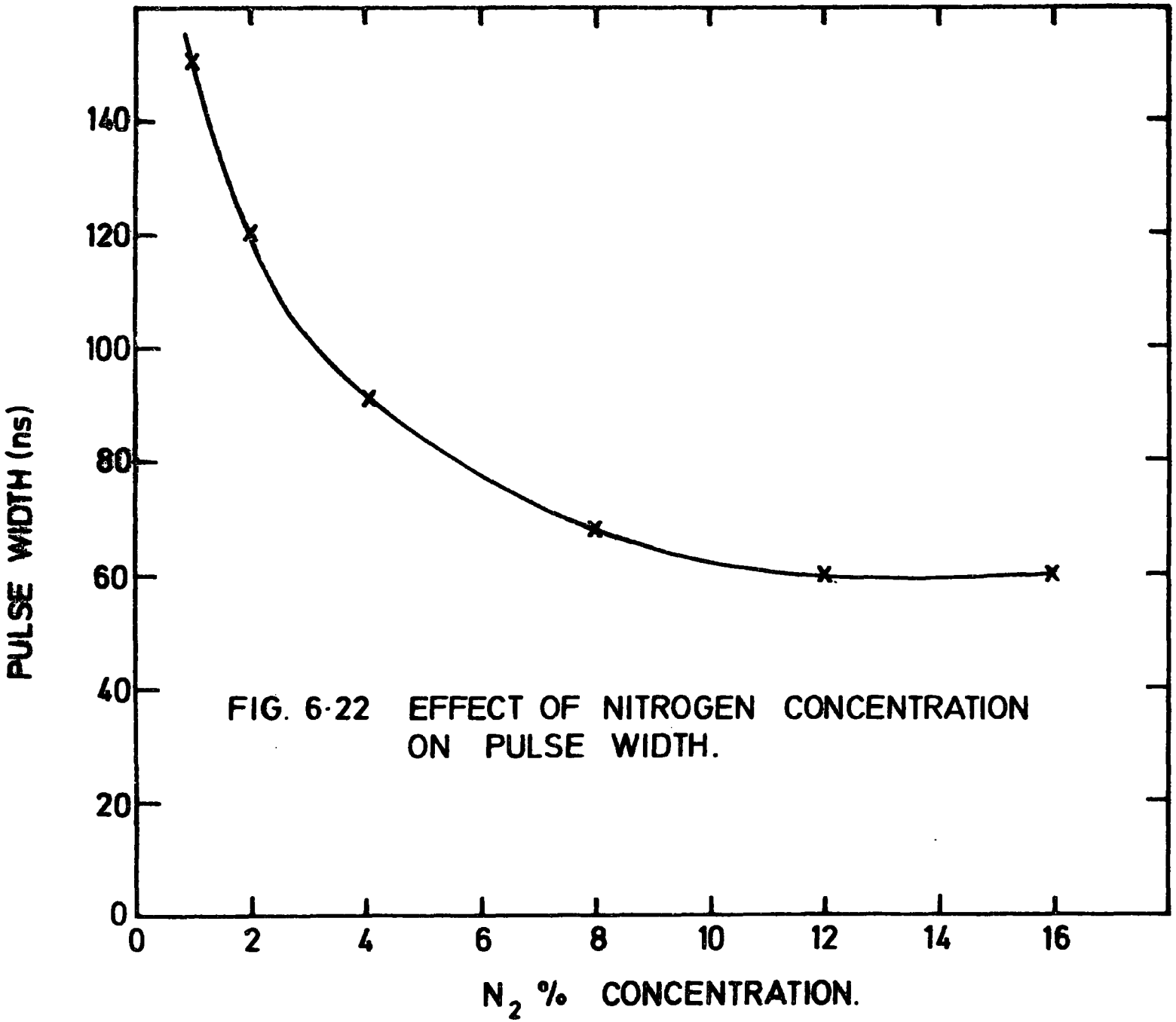

FIG. 6·22 EFFECT OF NITROGEN CONCENTRATION ON PULSE WIDTH.

stable) of argon by nitrogen.

Policarpo et al[2] investigated the variation of rise time of the primary scintillation pulse with nitrogen concentration. For the same reason, i.e. quenching ability of nitrogen, rise time was found to drop with nitrogen concentration and saturate at 10% nitrogen concentration and remain constant up to 100% N_2.

6.4.5 Drift Wire-Earth Plane Distance (d)

The effect of the drift wire-earth plane separation value (d) on the pulse shape was found to be as follows :- an increase in d causes an increase in pulse amplitudes Fig 6.19 as well as a decrease in pulse rise time. In Chamber 1 the maximum amplitude (near the sense wire) was found to be 275, 350 and 370 mV for d values of 3, 7 and 11 mm respectively. The rise time was found to be 30, 25 and 20 nanoseconds for d values of 3,7 and 11 mm at 10 mm from the sense wire. The change in amplitude and rise time can be attributed to the increase in field as d increases as computed in Chapter 5. These results are consistent with those observed in pulse amplitudes and rise times when the drift field was changed (see section 6.4.2).

Set against these improvements with large values of d is the fact that the geometry factor increases as d increases and this tend to degrade the energy resolution.

6.5 HIGH RATE TESTS

The high count rate tests on MWPC's given in Chapter 4, showed some serious limitations of the chambers. These limitations, namely dead time and space charge effects, are present in DC's as well. The characteristics of GSC's, discussed in earlier sections, are more promising for high rate experiments and this is shown in this section.

The two main problems in high rate experiments are the peak shift of the energy spectrum and the deterioration of energy resolution. The three main parts of the counter, namely the gas scintillator, the photomultiplier tube and the electronics, each contributes to this rate limitation. The contribution of each part was investigated separately while the contribution of the other two parts were kept at a minimum constant value.

6.5.1 Experimental Arrangement

The chamber used in this section was Chamber 2 mentioned in a previous section. It was GSDC with a thick sense wire (400 μm-diameter) for low charge and high light production. The drift distance, anode-drift wire plane separation and drift wire-earth plane separation were 2.0 cm, 6 mm and 3 mm respectively. These values were chosen in order to have a reasonably uniform field throughout most of the drift region.

The block diagram of the electronics used is shown in Fig 6.23. This set-up was similar to the one shown in Fig. 4.13 except that a fast amplifier and fast discriminator were used as well as a limiter and a stretcher.

The fast amplifier used in these tests was a LeCroy type 612 AM which has a set of 6 independent variable gain amplifiers with rise times of less than 3 nsec. Each of the six amplifiers has an adjustable gain, continuously variable over a range of 2.5 - 40. A gain of 40 was mainly used. Two simultaneous outputs are available for each input and hence

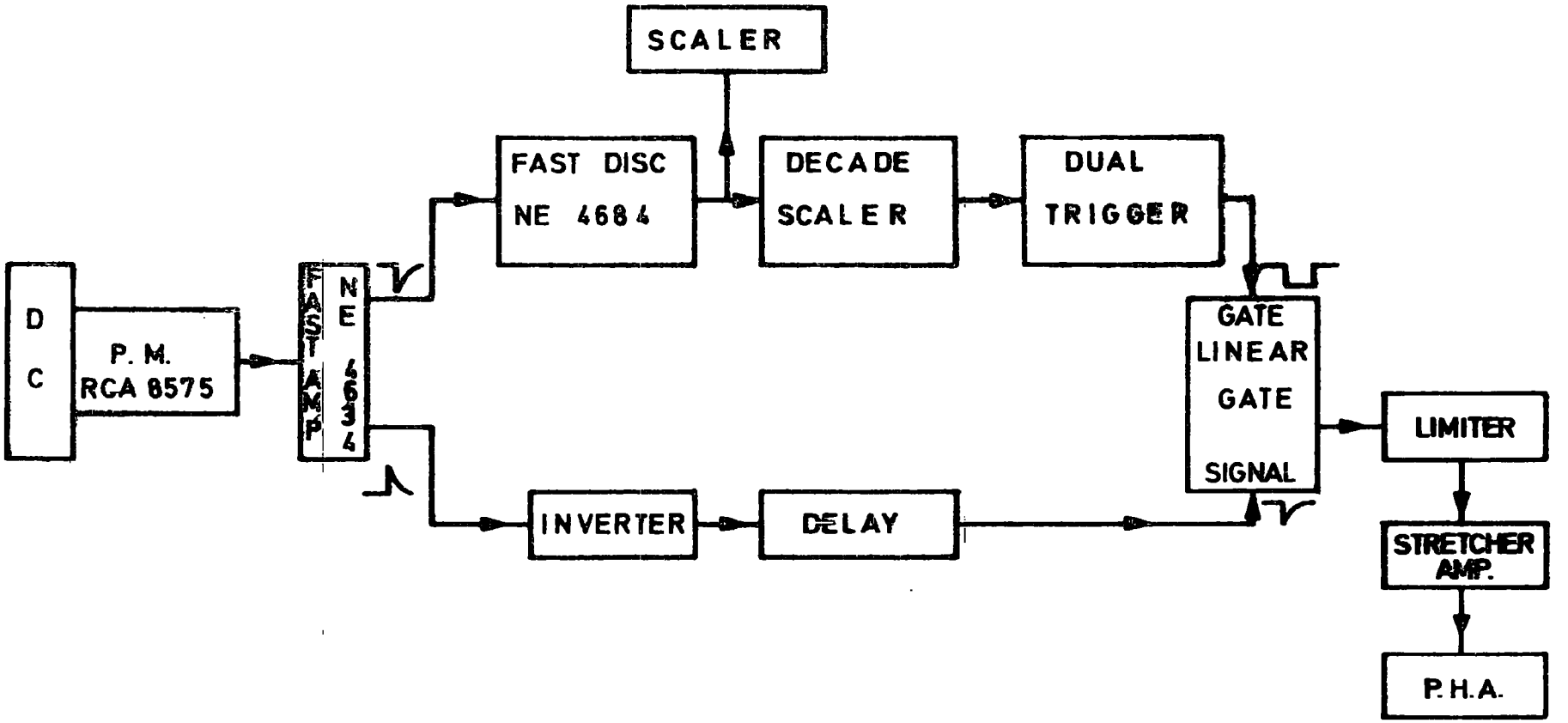

FIG. 6·23 THE BLOCK DIAGRAM OF THE ELECTRONICS

no inverter is needed with this amplifier.

A fast discriminator type NE-4684 was used. It provides three d.c. coupled simultaneous fast NIM outputs of 2.5 nsec rise time and 0.8 volt amplitude. The maximum rate of this unit is 110 MHz and its threshold range varies from 20 mV to 1 V. The minimum threshold was used throughout the tests.

The dual trigger TR 104S manufactured by EG & G provided the pulse with a width necessary to open the gate. The second output obtained from the fast amplifier was delayed through a delay box. The delay was adjusted to compensate for the propagation time in the three modules through which the pulse passed through before entering the gate. To allow the gate to open fully an extra 2 nsec delay was needed between the leading edge of the signal and the leading edge of the gate pulse (see Fig 6.24).

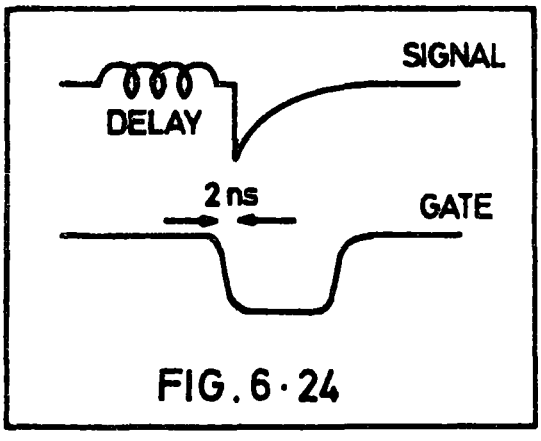

FIG. 6·24

The linear gate LG101 which was described in Chapter 4, has a different output impedance when it is open and when it is gated. The stretcher amplifier integrated the pulse and converted it to a form suitable for analysis by the PHA. The output impedance of the linear gate was in parallel with the input impedance of the stretcher. Hence the change in the output impedance of the linear gate changed the RC value of the stretcher (C is the integrating capacitor in the stretcher).

On account of this an EG & G AN104A limiter was buffered between the linear gate and the stretcher. The limiter provided the constant impedance for the stretcher and hence no base line shift occurred in the open or gated mode of the linear gate.

6.5.2 Effect of Electronics on Chambers Performance

The main limitations in high rate experiments are not only functions of the chamber itself as usually thought, but also functions of the processing electronics and the final counting system.

The role of electronics, in affecting the performance of GSC's, in high rate experiments, was initially observed with the amplifier used in the g-2 experiment[20]. Due to this amplifier's medium rate capacity, the peak shift was observed to appear at rate of 10^4 counts/sec onwards[21]. The fast amplifiers used in later work helped to minimize the effect of the amplifier bandwidth on the shift.

The pulse width from the dual trigger had an effect on the peak position and energy resolution. Although less signal width is desirable for high rate tests, it was noted that decreasing the pulse width caused a deterioration in the energy resolution and a shift in the peak position. Fig 6.25 shows the variation of energy spectrum of Fe^{55} with the variation of the pulse width. The energy resolution was measured from the FWHM of the photopeak and its position. Fig 6.26 shows the variation of energy resolution and peak shift with the gate width. The degradation of energy resolution and peak shift with decrease of the width was due to the loss of part of the signal when the gate width was smaller than the signal width as shown in Fig 6.24. The pulse width was then chosen at which the energy resolution reached a minimum and there was no peak shift, i.e. > 50 nsec.

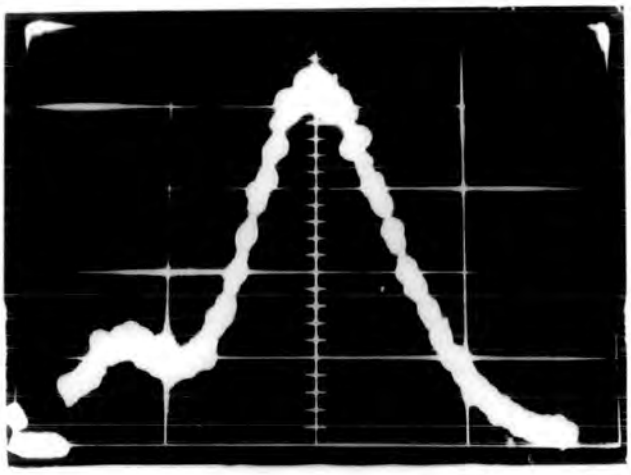

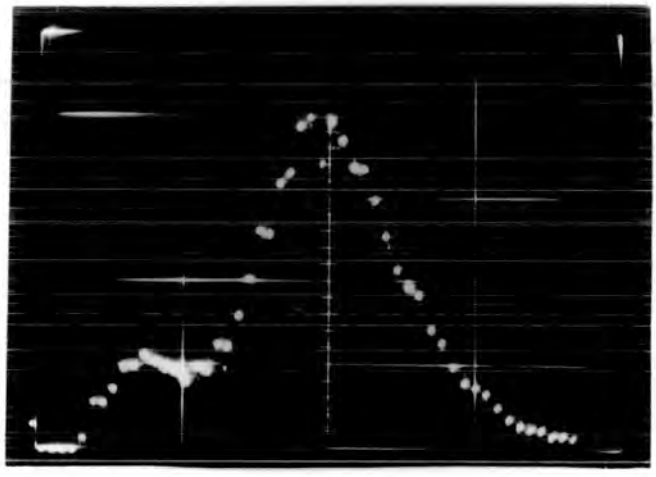

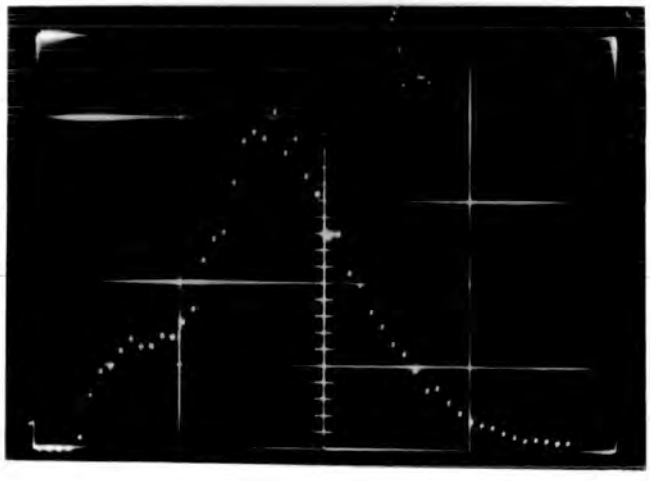

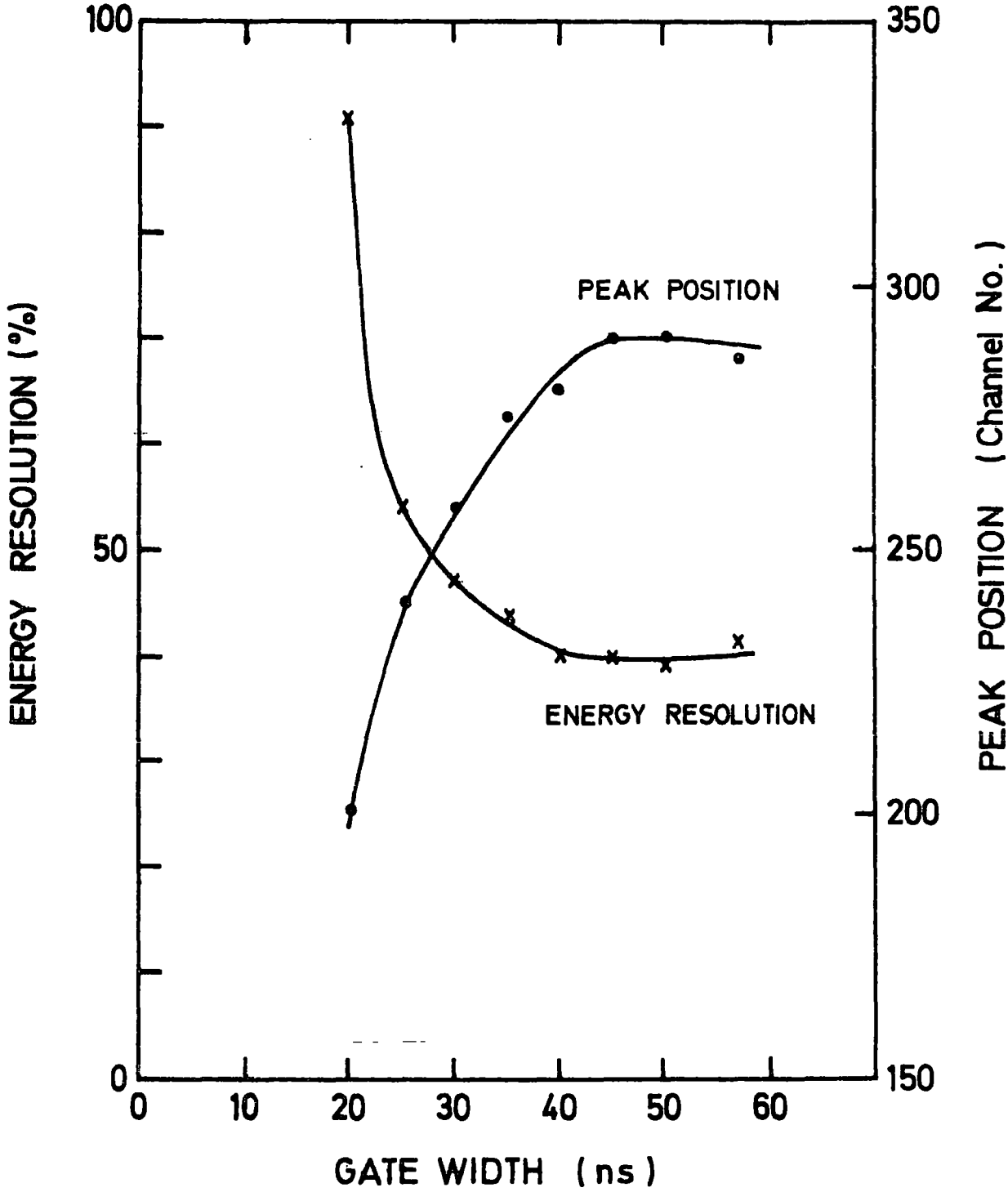

FIG. 6·26 GATE WIDTH EFFECT ON ENERGY RESOLUTION AND PEAK POSITION.

6.5.3 Peak Shift and Energy Resolution

As it was mentioned earlier, the effect of the electronics on the performance of the chamber was minimized by using a fast amplifier and a fast discriminator. The effect of photomultiplier tube on the shift was also minimized by using the active base network described in section 2.4.

To test the effect of the gas scintillators on the shift, the optimum values of the factors, studied earlier in this chapter, were used. The gas mixture used was Ar + 10% N_2 because the minimum pulse width was obtained from this mixture and due to its high light gain. The source position provided two conflicting factors namely the pulse width and the energy resolution. Decreasing the distance between the source and the sense wire gave a smaller pulse width but at the same time a fast deterioration in energy resolution. Hence a compromise was needed and a distance of 0.85 cm was used. The source of radiation used in this part was an X-ray machine which produced a 6.9 keV X-ray beam.

The shift in the peak position was investigated firstly by determining the plateau region of the chamber. Fig 6.27 and Fig 6.28 show two sets of plateaus at different X-ray beam intensities for two values of the photomultiplier voltage. No significant shift in the plateau can be observed up to a rate of $\sim$ 3 MHz for both values of V_{pm}. At the highest rate the plateaus start to fall at high sense wire voltages due to space charge effects inside the chamber. The shift is more pronounced at V_{pm} = 1800 than at 1650 volts. The reason for a larger shift at high V_{pm} values can be explained as follows. For high rate tests, a relatively low sense wire voltage was used in order to decrease the space charge effect inside the gas chamber. The low sense wire voltage required a high V_{pm} value which caused at high rates space charge effects in the photomultiplier itself and hence a drop in pulse height occurred.

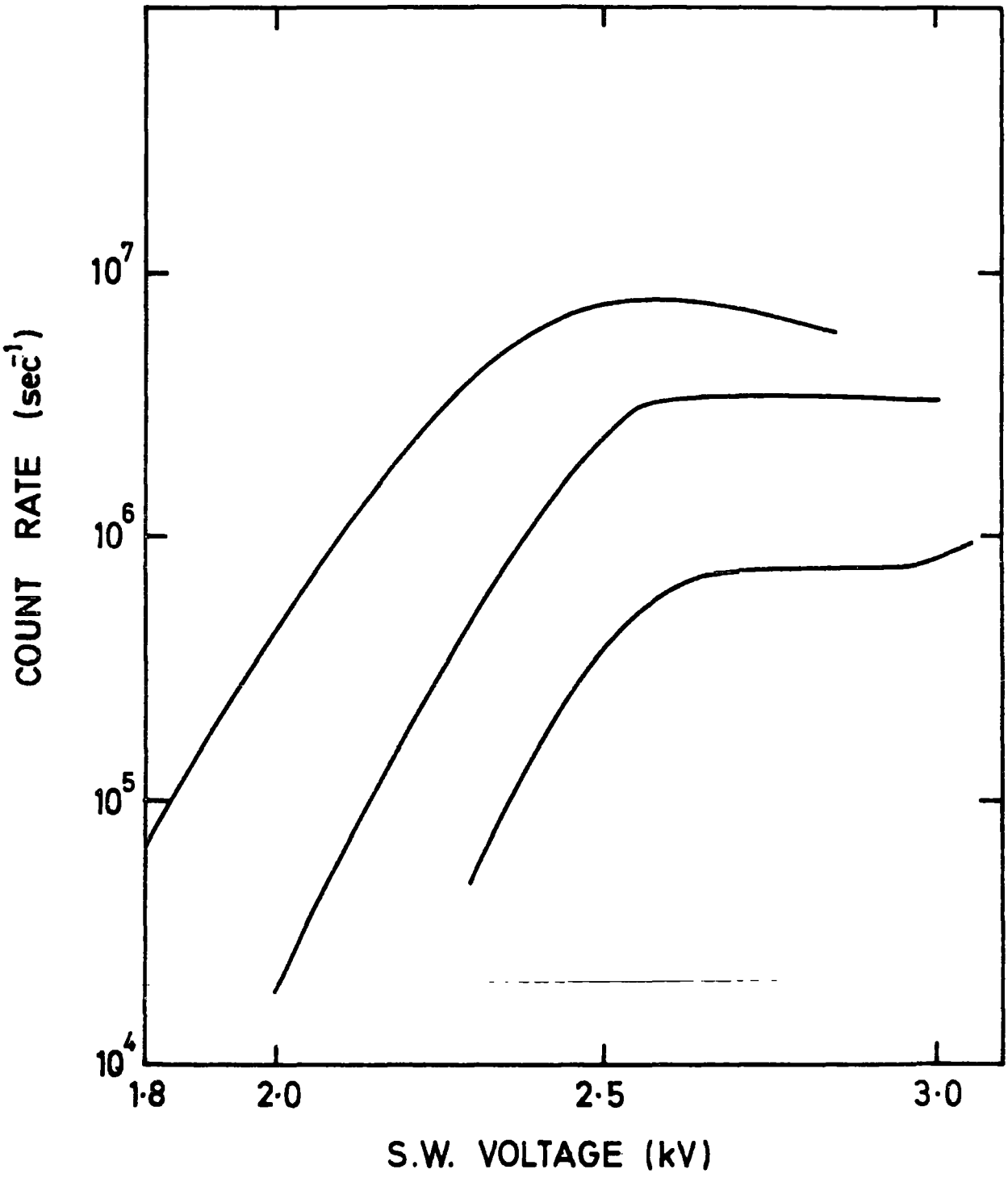

FIG. 6·27 PLATEAUS AT DIFFERENT RATES (V_{PM}=1650volts)

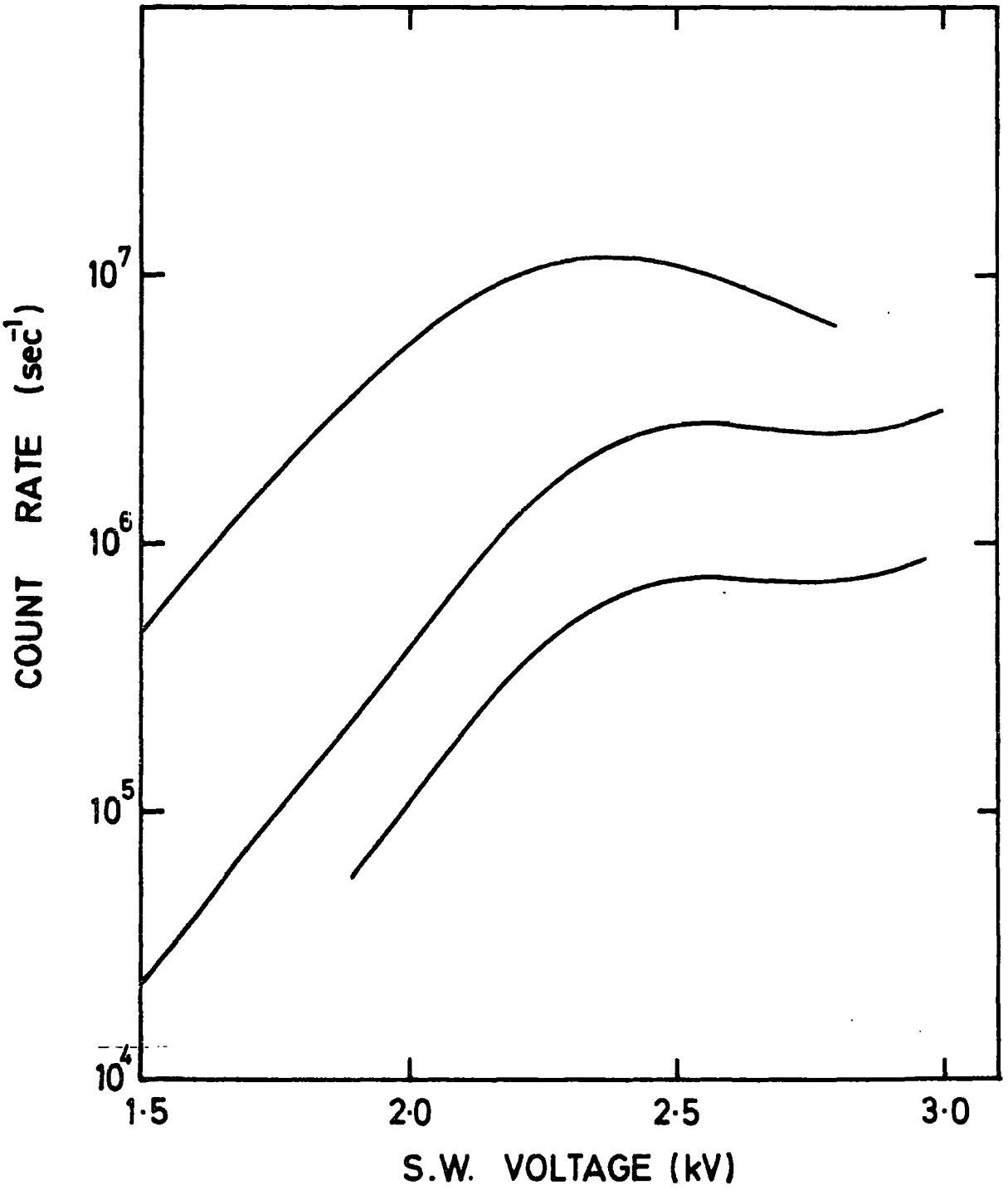

FIG. 6·28 PLATEAUS AT DIFFERENT RATES (V_{PM}=1800volts)

Using a value of 1650 volts for the photomultiplier voltage, the shift at different sense wire voltages (within the plateau region) was measured. The peak position, in channel number, versus the count rate is shown in Fig 6.29. It is clear in this figure that the shift increases, as expected, with increasing anode voltage. This is due to the increase in charge gain with increasing anode voltage. To show the strong relation between the charge gain and the shift, the values of the charge gain for the 400 μm wire was obtained from Fig 6.6 for the corresponding anode voltages shown in Fig 6.29. The shift percentage, defined in Eqn. 4.19, was obtained from Fig. 6.29. The relation between the shift percentage and the charge gain is shown in Fig 6.30 for two values of the rate and it is clear that the shift increases steadily as the charge gain increases. The strong relation between charge gain and shift percentage was also observed and measured by Policarpo[22]. Hence the charge gain, though very low, can be seen to produce a space charge at high rates.

The variation in energy resolution with the rate was observed. For the same anode voltages of Fig 6.29, the energy resolution was measured at different rates. This is shown in Fig 6.31. It is clear that the energy resolution deteriorates at high rates and contrary to the peak shift it deteriorates at low sense wire voltages. For example at a rate of 6 MHz the percentage deterioration in energy resolution at V_a = 3 kV is 29% while at 2.8 kV it increases to 37%. For the same values of V_a the peak shift percentage is 31% at V_a = 3kV but drops to 4.9% at 2.8 kV.

A compromise between two contradicting requirements for the anode voltage, namely less shift and less energy resolution, should be reached. The value of 2.9 kV was chosen because it produced only 10% shift in the peak at a rate of 8 MHz and the percentage deterioration in resolution

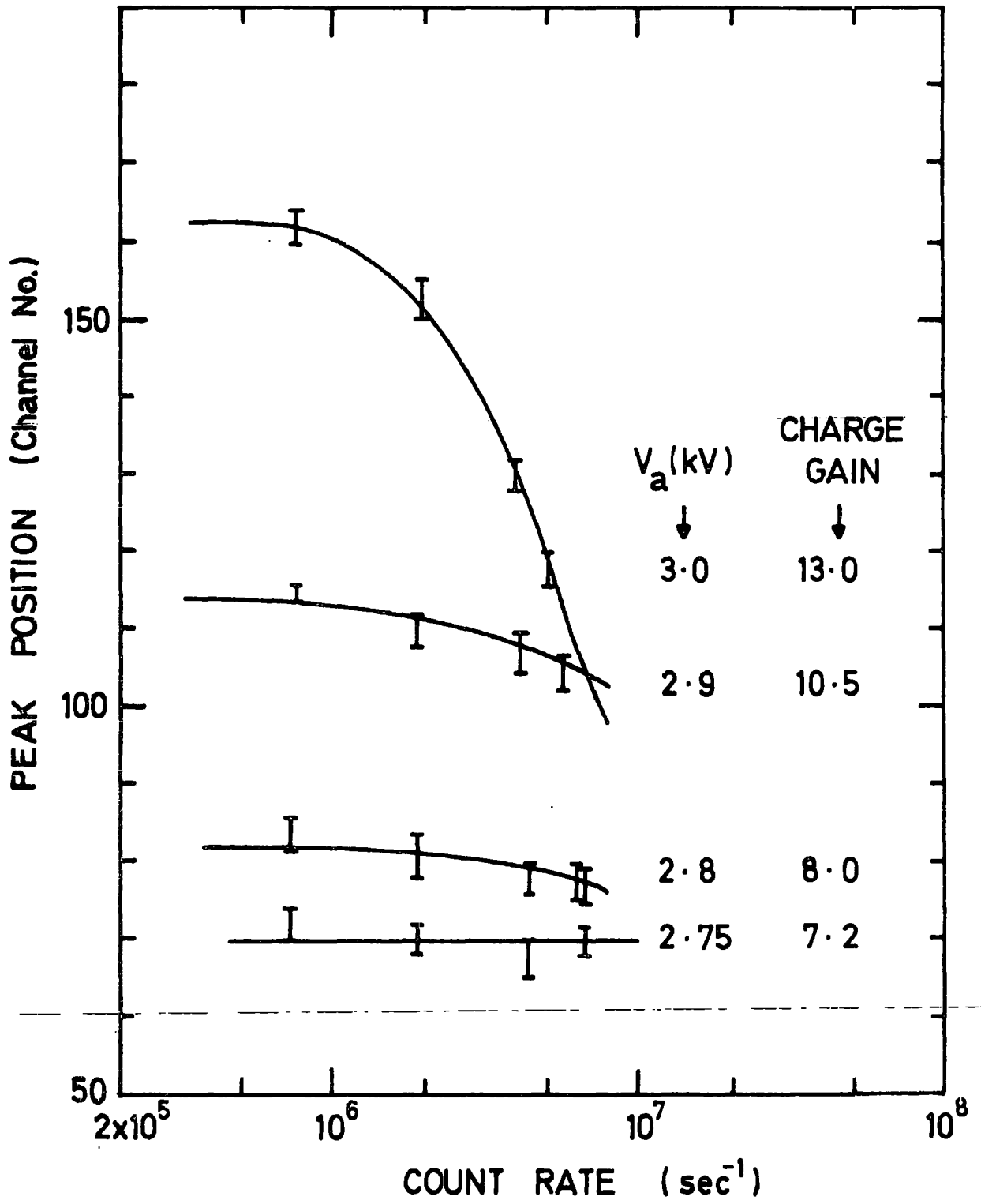

FIG. 6·29 PEAK SHIFT WITH RATES AT DIFFERENT SENSE WIRE VOLTAGES.

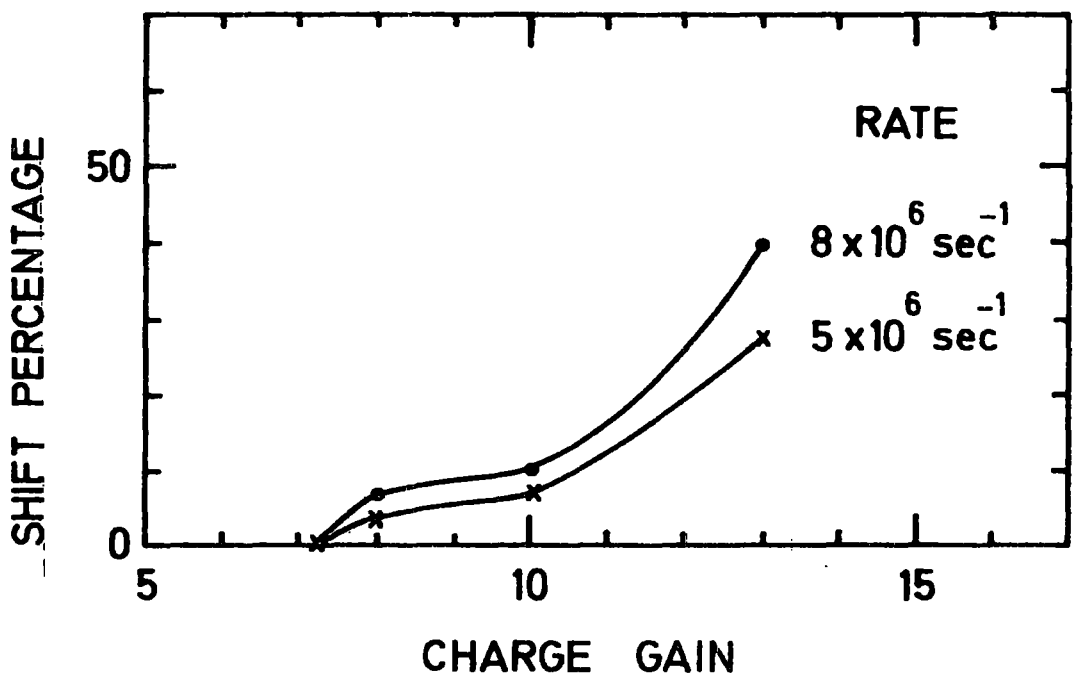

FIG. 6·30 CHARGE GAIN AND SHIFT PERCENTAGE FOR DIFFERENT RATES.

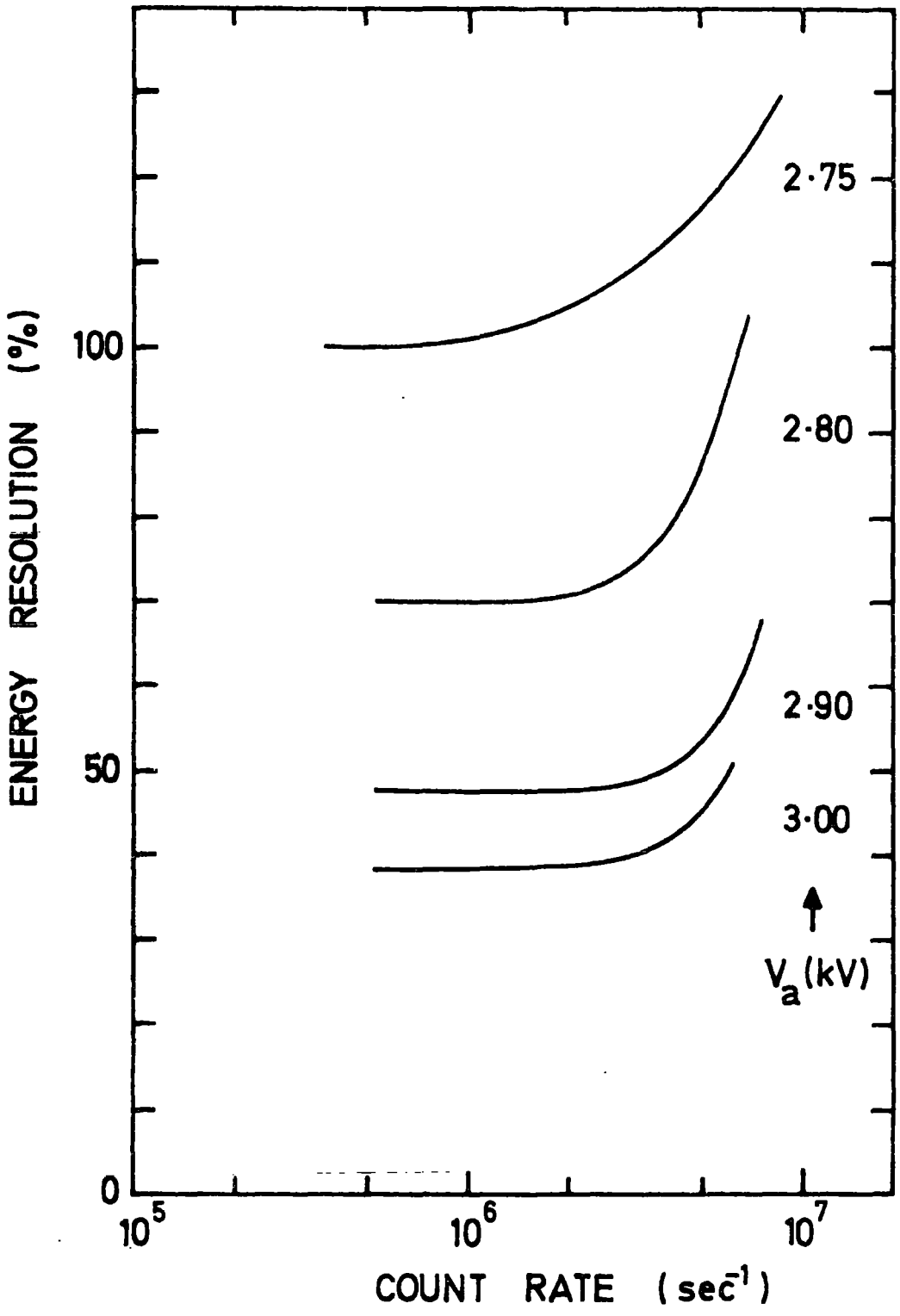

FIG. 6·31 EFFECT OF RATE ON ENERGY RESOLUTION AT DIFFERENT ANODE VOLTAGES.

was about 42%. At the lower rate of 6 MHz the shift was only 7.9% and the energy resolution deterioration drop off to 21%.

It should be noted here that the energy resolution at a low rate was not the best obtainable in the chamber due to choosing a source position which met other requirements, in particular a short pulse width.

The energy spectra at V_a = 2.9 kV, of the 6.9 keV X-ray line at different rates are shown in Fig 6.32. In these spectra the two main peaks, i.e. the photopeak and the escape peak, are seen in each spectrum. The peak shift can also be seen as well as the deterioration in energy resolution as the rate increased. As the rate increases it is obvious that another peak starts to appear at high channel number. These big pulses produced at high rates are due to pile-up of scintillation pulses. Attempts to reduce these pile-up pulses by decreasing gate width had the desired effect[23] but unfortunately energy resolution degrades as has been previously observed when the gate width was reduced.

The energy resolution of the chamber is in fact better than the measured value. This is due to external factors such as electronics and source collimations affecting the measurements. It is evident that a well collimated source contributes to the improvement of the energy resolution[24] and spatial resolution[25]. The use of large collimators and absorbers in this work, for different rates, degraded the measured values of energy resolution of the chamber due to the uncertainty of the position of the beam.

The highest rate obtained by Policarpo's group[22] was only 9×10^4 sec^{-1} in a xenon GSPC, 3% shift was observed at this rate and the deterioration in energy resolution was 14%. In a xenon filled GSDC, Charpak et al[26] obtained no change in chamber efficiency at 5×10^5 sec^{-1}. No shift or energy resolution deterioration were observed at a rate of 3 MHz in this work.

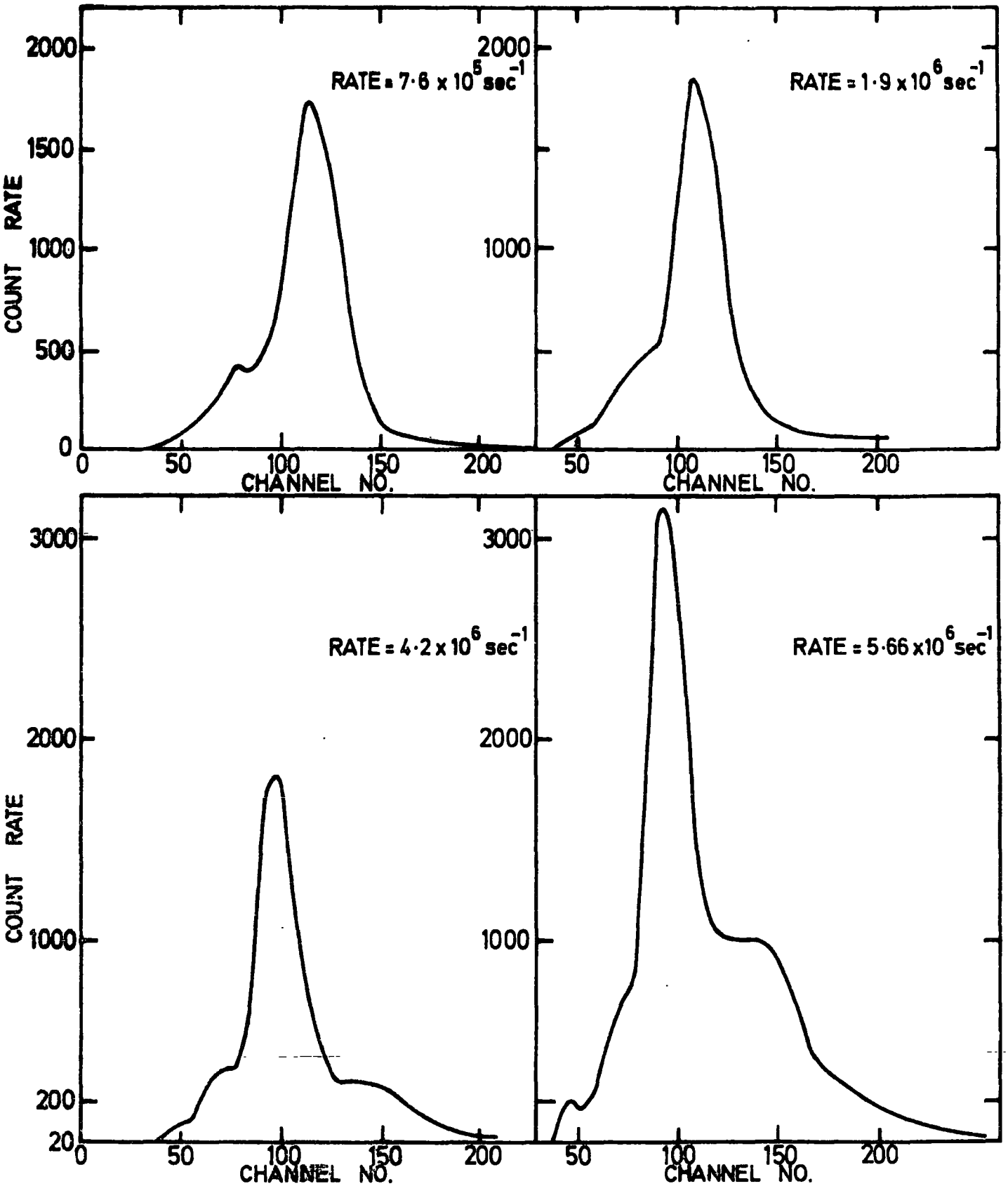

FIG. 6·32 ENERGY SPECTRA OF 6·9 keV X-RAYS AT DIFFERENT RATES.

6.6 CONCLUSIONS

The study of the factors affecting the performance of GSC's as high count rate detectors with reasonable energy resolution was presented in this chapter and can be summarized as follows : The conflict between low charge gain, to minimize space charge limitations, and high light output for good energy resolution, had to be compromised with more inclination towards low charge gain. It was found that for the same charge gain, the light gain increases with increase of two factors : nitrogen concentration reaching saturation above 5% and sense wire diameter. The factors which improve energy resolution are the increase of anode voltage V_a, the decrease of drift voltage V_k and the decrease of photomultiplier voltage V_{pm}. These, again, contradict with high rate requirements, i.e. low V_a to avoid space changes and high V_k to provide a high drift velocity.

Careful choice of chamber dimensions also helped to provide better performance. Thick sense wires produced better energy resolution though at the expense of the pulse amplitude which decreased with increasing wire diameter. Smaller drift distance (D) gave less diffusion and more uniform field.

The factors affecting pulse shape showed that increasing V_a increased the pulse amplitude but at the same time it increased the pulse width. On the other hand, increasing V_k increased the pulse amplitude and decreased the rise time. The distance of the source from the sense wire (x) played a big role in the pulse shape. Decreasing x decreased the pulse width (and rise time) and it increased the pulse amplitude but at the same time it deteriorated energy resolution. Concerning the nitrogen concentration, it was found that at constant drift velocity the pulse width decreased with increasing nitrogen concentration reaching saturation around 10%.

By choosing optimum values of the parameters the highest rate measured with the GSDC was 10^7 counts/sec (see Fig 6.28.). A shift of only 10% at a rate of 8×10^6 sec^{-1} was obtained. An energy resolution of 56% at a rate of 6×10^6 sec^{-1} were measured. These results are not the best that can be obtained from GSC's. Other factors which may produce better results will be discussed in the coming chapter.

Chapter Six - References

1. V. Radeka, I.E.E.E. Trans. Nucl. Sci. NS.21 (1974) 51.

2. A.J.P.L. Policarpo et al, Nucl. Inst. & Meth 55 (1967) 105.

3. C.A.N. Conde & A.J.P.L. Policarpo, Nucl. Inst. & Meth. 53 (1967) 7.

4. T.D.Strickler & E.T. Arakawa, J.Chem. Phys. 41 (1964) 1783.

5. C.A.N . Conde et al, IEEE Trans. Nucl. Sci. NS-15 (1968) 84.

6. A.J.P.L.Policarpo et al, Nucl. Inst. & Meth. 77 (1970) 309.

7. G. Charpak et al, IEEE Trans. Nucl. Sci. NS-23 (1976) 202.

8. C.A.N. Conde et al, IEEE Trans. Nucl. Sci. NS-24 (1977) 221.

9. K. Masuda et al, Nucl. Inst. & Meth. 160 (1979) 247.

10. C.A.N. Conde, Nucl. Inst. & Meth. 149 (1978) 685.

11. A. Von Engel, Ionized Gases (Clarendon Press, Oxford, 1965).

12. C.A.N. Conde, IEEE Trans. Nucl. Sci. NS-22 (1975) 104.

13. A.J.P.L. Policarpo et al, Nucl. Inst. & Meth. 96 (1971) 487.

14. D.W.Aitken, IEEE Trans. Nucl. Sci. NS-15 (1968) 10.

15. A. Breskin, G. Charpak and F. Sauli, Nucl. Inst. & Meth. 124 (1975) 189.

16. R. Browell, Ph.D. Thesis,- Durham University (1975).
K.A.Short, Ph.D. Thesis, - Durham University (1975).

17. D.F. Anderson et al, Nucl. Inst. & Meth. 144 (1977) 485.
IEEE Trans. Nucl. Sci. NS-25 (1978) 813.

18. R.D.Andersen et al, IEEE Trans. Nucl. Sci. NS-24 (1977) 810.

19. A. Fenster et al, Rev. Sci. Inst. 44 (1973) 689.

20. M. Comyn, Ph. D. Thesis, Durham University (1978).

21. S. Al-Dargazelli, T. Ariyaratne, J.M. Breare & B.C. Nandi, Durham University - Internal Report N1-78-7 (1978).

22. A.J.P.L. Policarpo et al, Nucl. Inst. & Meth, 97 (1971) 491.
M.A.F. Alves et al, Nucl. Inst. & Meth. 111 (1973) 413.

References cont'd.

23. T. Ariyaratne, Ph.D. Thesis, Durham University (1978).

24. S. Al-Dargazelli, T. Ariyaratne, J.M.Breare & B.C. Nandi Durham University - Internal Report N1-78-1 (1978).

25. S. Al-Dargazelli, Durham University -Internal Report N1-76-24 (1976).

26. G. Charpak et al, Nucl. Inst. & Meth. 126 (1975) 381.

CHAPTER SEVEN

CONCLUDING REMARKS AND FUTURE WORK

7.1 SUMMARY OF GSC's PERFORMANCE

The detailed study of this novel type of detector, the GSC, has revealed its versatile characteristics which are the combination of scintillation counter and wire chamber characteristics.

The aim of this study was mainly to establish the capability of this detector in high rate experiments and with a moderate energy resolution capability. Many detectors are excellent in one main characteristic and poor in others and it is fairly difficult to obtain detectors which have more than one useful main characteristic. This is mainly due to the requirements of each characteristic being inter-related and each of them can only be improved at the expense of the others. In this work compromises were usually reached in these conflicting requirements.

The measurements of drift velocity in argon nitrogen mixtures with the measurements of charge and light gain dictated the use of 10% nitrogen in the mixture. This produces maximum light output necessary for good energy resolution.

The study of the performance of MWPC's at high rates showed the limitation of the chambers which is mainly caused by the occurrence of space charges. The factors which cause the increase in space charge were minimized in the GSC's, in particular it was found advantageous to decrease the anode voltage and increase the anode wire diameter. One of the consequences of the space charge effect is the peak shift. To reduce the space charge effect, the most effective way was to decrease the charge gain to as low a value as possible. This however is the main reason for the degradation of energy resolution.

The calculations of the field distribution inside the chambers were very useful for improving the geometrical dimensions of the chamber, such as the cathode wire spacing and planes separation, and also for choosing the proper anode and drift voltages. From these calculations the conditions necessary to give the most uniform field were obtained ; at the same time high light production only in the proper region around the anode region was obtained.

The maximum rate obtained was 10 MHz and only 10% peak shift was observed at a rate of 6 MHz with an energy resolution of 56% for 6.9 keV X-rays. It should be noted here that at moderate rates of 100 kHz, 8.6% resolution was obtained for 5.5 MeV α-rays from Am^{241} and 30% for 5.9 keV X-rays from Fe^{55}.

7.2 APPLICATIONS OF GSC's:

Many applications are available for GSC's not only in physics, but in Astronomy, molecular biology and biophysics.

In astronomy and space environments, particle detectors must possess special characteristics. One of the main requirements of astronomy is a large sensitive area as well as a good energy resolution. The use of GSC's in astronomy is therefore feasible because not only due to the possibility of constructing big GSC's, but on the other hand a good energy resolution capability for soft X-rays, which is better than that of conventional wire chambers. Solid state detectors provide better energy resolution in the same energy range but the small size of these detectors makes GSC's a better proposition. The limitation on the size of GSC's is set by the photocathode size of the photomultiplier being used. This can be solved by using several photomultipliers or by replacing them by other photosensitive devices.

For space environments the main requirements from detectors are firstly economical size, weight and power, and secondly a good ability in rejecting background events. Though the performance of solid state detectors is unrivalled in laboratory systems, some of their operating requirements,particularly refrigeration, make their use difficult in space flight applications. On the other hand the GSC which does not suffer from these drawbacks, is a good candidate for this type of experiment. The second requirement can be achieved by rise time discrimination[1]. A charged particle produces a long track of ionization and consequently has a long signal rise time compared to the rise time of the electron cloud produced in the X-ray absorption process.

Another field of application for GSC's is through their capability of position localization. One dimension can be obtained from the drift time of electrons, i.e. the delay time between primary and secondary scintillation. The other by the charge division technique which utilizes a charge splitting electrode. The collected charge and total light amplitude provide heavy ions identification such as Xe^{136} and U^{238} ions, Cf^{252} fission fragments and Am^{241} α-particles. In radio-isotopic diagnostics where good energy and spatial resolutions are needed GSC's can replace other detectors. The energy range of gamma ray used in this field is 60 - 511 keV. With NaI(Tℓ) scintillators spatial resolutions of 9 and 6 mm were obtained with energies of 140 and 511 keV respectively[2]. At 140 keV semiconductor detectors provided spatial resolutions of about 3mm and energy resolution of 1%. On the other hand GSC's can provide a spatial resolution of a fraction of a millimeter[3-6] and an energy resolution better than that of solid scintillators. Comparing them with solid state detectors they are cheaper, bigger in size and provide better spatial resolution.

Detectors used for X-ray diffraction analysis in molecular biology require two main characteristics, namely high rate capability and good spatial resolution. A resistive-wire linear position sensitive detector was used by Faruqi and Huxley[7] to study structural changes in muscles during contraction at a molecular level. In order to obtain the required spatial resolution (∿ 100 μm) the detector was operated with a high gas gain. The high gas gain process caused "radiation damage" to the anode wire, and the use of lower gain degraded the spatial resolution. At a gas gain of 2000 a spatial resolution of 110 μm was achieved, while at a gain of 150 the resolution became 1 mm. The detector requirements for this type of experiment are a spatial resolution of about 0.5 mm in two dimensions and a capability to cope with 10 MHz peak rates. These two requirements are available from GSC's where spatial resolutions in the two dimensions of 0.3 and 0.5 mm were achieved[3,8] and also a rate of 10 MHz.

7.3 HIGH RATE APPLICATIONS

High rate experiments require an intense beam of radiation. Synchrotron radiation from an electron accelerator is now the most likely source of this radiation. It has the advantage, for many experiments, of being finally focussed and highly polarized. This relatively new source of radiation extends from wavelengths longer than those of visible light through to the ultraviolet and X-ray regions of the electromagnetic spectrum. The intensity and spectral continuity of this radiation are the two favourable parameters for X-ray spectroscopy of solids. The only source in the U.K. is the Synchrotron Radiation Source (SRS), at present under construction at the Daresbury Laboratory and it is planned to start commissioning in April 1980. The intensity of the SRS varies with the wavelength. The peak intensity of 5×10^{13} photons/sec occurs in the region 1-10 Å (10 - 1 keV). The horizontal angular aperture can be varied from less

than 1 mrad up to 40 mrad[9]. This well-focussed intense beam of variable frequencies is a typical source of EXAFS experiments.

EXAFS or Extended X-ray Absorption Fine Structure, which was known for a long time (1930) as Kronig oscillations, is a small perturbation on the gross elemental absorption curve. For isolated atoms the variation of the absorption coefficient with the energy of the X-ray photon is smooth except for the absorption edges. For the atoms in a solid, however, the variation of the absorption coefficient at energies just above an absorption edge shows a complex fine structure. This is attributed to the atoms surrounding the X-ray absorbing atom. The escaping electron wave, from the excited atom will be scattered by the surrounding atoms. The initial outgoing wave will add to it the new waves radiating from each scattering site. This addition of waves gives rise to the fine structure in the X-ray absorption spectrum. This oscillatory behaviour provides a key to the location of all the atoms that scattered the outgoing wave.

One of the problems in EXAFS experiments is the need for high accuracy. If the EXAFS amplitude is 10% of the absorption edge step (as in the case of copper), a 1% accuracy of the EXAFS amplitude determination would require a total count of 10^6. In order to obtain a sufficient number of points in a reasonable time it is necessary to obtain this number of counts in a time period of about 1 second. In extreme cases, such as carbon, the total detector counting rate must be as high as 5×10^7 sec^{-1}[10]. If the structure does not contain components with fine resolutions, excellent EXAFS data can be obtained with a total counting rate of $\sim 10^5$ sec^{-1}[10]. As for the energy resolution, EXAFS extend over a range of about 1 keV in energy and structure in the $\sim$10 eV range of resolution may be important[10]. At this stage no detector is capable of resolving energies to this high degree of accuracy and the well defined energy of the beam must be controlled by some form of monochromator.

The procedure of EXAFS experiments is such that the detector observes the fluoroscent X-ray emitted from the sample when exposed to incident exciting X-rays at energies just greater than that of the absorption edge of an element of interest. Monochromator beam (∿1 eV spread) passes into the sample. The actual energy selected by the monochromator can be varied by rotating the crystal in the monochromator. As the incident energy is varied past the absorption edge (usually K-edge) the EXAFS structure is observed both absorption (the more common technique) and in the emission of X-rays characteristics of the element. Since the K-edge is characteristic of each element, it is possible to measure the ordering around any given atom such as iron in haemoglobin or an element in an alloy, etc[11].

Up till now, the detectors used for EXAFS have been usually semiconductors. An array of nine silicon detectors, each with its own preamplifier and electronics was adapted by Goulding et al[10] for fluorescent EXAFS. Though silicon detectors are efficient in the 1-25 keV energy range, their high rate capability is limited to 2.5×10^5 sec^{-1} with an energy resolution of 3-4% for 5.9 keV X-rays[12]. The disadvantages of semiconductors, apart from their lack of high rate incapability, are their high cost and their small sensitive area. Increasing the area causes degradation of energy resolution due to the increase in detector capacity[13]. Hence GSC's can be used in this field with their high rate capability, cheap cost, large sensitive area and relative ease of operation.

Mössbauer spectroscopy is another field of application for the high rate capability of GSC's. Plastic scintillators and conventional MWPC's have been used, but again a comparison between them and GSC's shows the superiority of GSC's. MWPC constructed[14] specifically for Mössbauer spectroscopy was capable of 2×10^5 counts/sec in the region of 14.4 keV.

Peak shift deterioration of energy resolution accompanied the high rate. A plastic scintillator was capable of high rates of 20 MHz but the energy resolution was ∿ 40% in the 40-100 keV region. However, this detector is not suitable at less than 10 keV where the detector efficiency falls off very considerably. However, GSC's can provide a high rate capability and a moderate energy resolution in this energy range.

7.4 FURTHER DEVELOPMENTS AND FUTURE WORK

The good results obtained from GSC's in this work are not the best which can be achieved. Better results can be obtained with further developments of the chambers. One of the main factors which can improve the performance of the chamber is the gas mixture. It is well known that xenon with its highest light output, among other rare gases, provides better energy resolution. Alteration of the pressure is another factor which can be used. For example the absorption efficiency of argon at 1 atm x cm for 8 keV X-rays increased from 18% to 35% at 2 atm x cm. In comparison with xenon, its absorption efficiency increases from 83% at 1 atm/cm to 97% at 2 atm x cm[15] for the same photon energy. Although this is a simple way of increasing the efficiency, it brings with it some technical problems of high pressure operation.

A better photomultiplier tube can also contribute to improving the GSC's performance. A tube of the RCA 31000 M type with its wider range of spectral response than the RCA 8575 tube, used in this work, is becoming more popular among workers on GSC's. This type of tube detects more light particularly in the ultraviolet region and decreases the need to vary the other factors which influence the light production, especially factors which have unwanted side effects.

An improvement in the chamber design may reduce the variation of the pulse amplitude with the source position. This can be done by making

the chamber window at the side of the chamber so that the radiation beam line becomes at 90° with the photomultiplier axis.

The real assessment of the chambers performance will be to use it in a definite experiment. A high rate experiment,especially on EXAFS experiments, may show up more of the chamber capabilities and limitations The controlling factors can then be adjusted accordingly.

Chapter Seven - References

1. P. Gorenstein and S. Mickiewicz, Rev. Sci. Instr. 39 (1968) 816.
2. H.O.Anger, ISA Trans., 5 (1966) 311.
3. M.Mutterer et al, Nucl.Inst. & Meth. 144 (1977) 159.
4. K.P. Schelhaas et al, Nucl. & Meth. 154 (1978) 245.
5. V.I.Baskakov et al, Nucl.Inst. & Meth. 158 (1979) 129.
6. A.I.Alichanian et al, Nucl. Inst. & Meth. 158 (1979) 137.
7. A. R. Faruqi and H.E.Huxley, J.Appl. Cryst. 11 (1978) 449.
8. P. Gorenstein and K.Tapka, IEEE Trans. on Nucl.Sci. NS-24 (1977) 511.
9. K.R. Lea and I.H.Munro - DLNP - 1979.
10. F.S.Goulding et al, SSRL- Report No. 78/04 (1978).
11. Y. Farge, Physics Bulletin, March (1977) 114.
12. F.S. Goulding and D.A.Laudis, IEEE Trans. on Nucl.Sci.NS-25 (1978) 896.
13. R.D.Andresen et al, Astron. Astrophys. 53 (1976) 309.
14. Z. Pawlowski and W.Cudny, Nucl.Inst. & Meth. 157 (1978) 287.
15. A.R. Faruqi, The Rotation Method in Crystallography, (U.W.Arndt and A.J.Wonacott, (Eds), North-Holland publishing company (1977)).

ACKNOWLEDGEMENTS

The author would like to thank Professor B.H.Bransden and Professor A.W.Wolfendale for their support of this work and the use of laboratory facilities. Baghdad University is acknowledged for awarding the study leave and other aids during the work.

The greatest debt is to my supervisor, Dr. J.M.Breare, for his guidance, encouragement and assistance shown throughout this work. His invaluable friendship is deeply appreciated.

Special acknowledgements are to the Principal of St. Aidan's College, Miss I. Hindmarsh, Dr. M.Harvey and Dr. J. Turner, for their kindness and understanding. Members of the Senior Common Room in St. Aidan's College are deeply thanked for their hospitality and companionship shown during the author's stay in the College.

Past and present members of The Nuclear Instrumentation Group are thanked for their assistance,in particular Dr. B. Sitar, Dr.B.C.Nandi, Dr. M.Comyn and Dr.T.R. Ariyaratne. The technical support of Mr.J.Webster and Mr. R.McDermott is deeply acknowledged.

Mrs. S.Mellanby is thanked for the excellence of her typing. Mr. M.Lee, Miss D.Dixon and Miss J.Morgan are thanked for the photographs. Mrs.E.Johnston and Mr.N.Thompson are thanked for drawing the diagrams of this thesis.

Finally the author would like to express her deep gratitude to her devoted mother ; for her encouragement and support to achieve the completion of this work.